Development and test of a technology wind generator demonstrator with no insulation field coils applying high temperature superconductors

Zur Erlangung des akademischen Grades eines
DOKTOR-INGENIEURS
von der KIT-Fakultät für
Elektrotechnik und Informationstechnik
des Karlsruher Instituts für Technologie (KIT)

genehmigte
DISSERTATION
von

Dipl.-Ing. Fabian Schreiner

geb. in: Landau i.d. Pfalz, Deutschland

Tag der mündlichen Prüfung:	09.03.2022
Referent:	Prof. Dr.-Ing. Mathias Noe
Korreferent:	Prof. Dr.-Ing. Martin Doppelbauer

Danksagung

Vielen Dank an alle Kolleginnen und Kollegen, alle Freundinnen und Freunde und an meine Familie, die mich während meiner Zeit als Doktorand begleitet und unterstützt haben.

An erster Stelle möchte ich Herrn Prof. Dr.-Ing Mathias Noe für die Möglichkeit einer Promotion am Institut für Technische Physik danken. Der fachliche als auch organisatorische Austausch in regelmäßigen Treffen haben im erheblichen Maße zur Qualität dieser Arbeit beigetragen. Ganz besonders möchte ich mich auch für das mir entgegengebrachte Vertrauen bedanken. Die Möglichkeit zur Umsetzung eines größeren Hardware Projektes und das Präsentieren wissenschaftlicher Fragestellungen, auch im internationalen Umfeld, haben mich in meiner beruflichen und persönlichen Entwicklung gestärkt.

Weiter möchte ich mich bei Herrn Prof. Dr.-Ing Martin Doppelbauer bedanken, der in mehrfachen Treffen diese Arbeit begleitet hat, um wichtige Anregungen und Unterstützung hinsichtlich des Fachgebiets der elektrischen Maschinen zu geben. Insbesondere möchte ich mich für die Möglichkeit zur Nutzung des Motorprüffeldes am Campus Ost bedanken. An dieser Stelle auch ein besonderer Dank an die Kollegen die mich dort mit viel Geduld unterstützt haben.

Ganz besonders möchte ich all meinen Kolleginnen und Kollegen danken, die im Kleinen und Großen an dieser Promotion mitgewirkt haben. Mein besonderer Dank gilt Frau Dr.-Ing Yingzhen Liu für die vielen wertvollen fachlichen und auch persönlichen Gespräche und die tolle gemeinsame Projektarbeit. Sehr herzlich möchte ich an dieser Stelle auch den Kolleginnen und Kollegen Danke sagen, die in sehr enger Zusammenarbeit, fortlaufend bis zum Zusammenbau und Test des Prototypen mitgewirkt haben. Danke an Antje Drechsler, dass du dich voller Tatendrang mit mir an die konstruktive Auslegung gewagt hast und bis zum Schluss mit deiner Einsatzbereitschaft das Projekt bereichert und den Überblick behalten hast. Danke an Holger Fillinger für deine kontinuierliche Hilfe im Labor und der Beschaffung von Komponenten. Von deinem großen Wissens- und Erfahrungsschatz, besonders auch im Bereich der Vakuum- und Kryotechnik, konnte ich stets profitieren. Danke an Uwe Mirasch für deinen Einsatz bei der Entwicklung und Herstellung der supraleitenden Spulen. Erst durch deine langjährige Erfahrung in diesem Bereich, aber auch das kritische Hinterfragen und Einbringen von Verbesserungsvorschlägen, konnten wir so viele funktionstüchtige Spulen herstellen. Danke an Uwe Walschburger für deine Geduld bei der Umsetzung des theoretischen, konstruktiven Designs in einen praktischen, realen Prototyp. Du hast dich vieler kleiner und großer Änderungen

mit deinem handwerklichen Geschick angenommen und so eine Montage erst ermöglicht. Ich möchte nicht nur danke sagen, weil das Projekt ohne euch nicht möglich gewesen wäre, sondern auch besonders, weil ich mich zu jeder Zeit voll auf euch verlassen konnte.

Ein ganz besonderer Dank gilt natürlich auch meinen Eltern Rita und Norbert, die mich während meines Studiums, auch in finanzieller Hinsicht, stets unterstützt haben. Auch möchte ich meinem Bruder Florian danken, der immer Zeit hatte für fachliche Diskussionen insbesondere auf dem Gebiet der Thermodynamik.

Meinem Patenkind Salome möchte ich ebenfalls Danke sagen, weil du mir mit deiner fröhlichen und liebenswerten Art immer ein Lächeln ins Gesicht zauberst.

Liebe Kerstin, zu viele Dinge sind es für die ich dir dankbar bin, deshalb versuche ich es wie folgt zusammenzufassen: Danke für Dich!

Kurzfassung

Der steigende Bedarf an günstigen, erneuerbaren Energiequellen verursacht eine anhaltende Entwicklung hin zu Windkraftanlagen höherer Leistungsklassen. Generatoren dieser Leistungsklassen sind meist besonders schwer und weisen erhöhte Anforderungen bezüglich des Bauraums auf. Supraleitende Materialien mit ihrer hohen Stromtragfähigkeit und nicht vorhandenen Gleichstromverlusten, zeigen das Potential einer erhöhten Leistungsdichte von elektrischen Maschinen hinsichtlich Gewicht und Volumen. Diese Arbeit stellt deshalb die Entwicklung und den Test eines Generator-Technologiedemonstrators mit Felderregerspulen, bestehend aus Hochtemperatur-Supraleitern, vor. Für eine verbesserte elektrische und thermische Stabilität sind die supraleitenden Spulen als nicht-isolierte Spulen ausgeführt und verfügen deshalb über keine elektrische Isolation zwischen den Spulenwindungen.

Die grundsätzlichen Ausführungsformen supraleitender elektrischer Maschinen im Hinblick auf den Einsatz in Windkraftanlagen werden vorgestellt. Dabei werden insbesondere die Ausführung ferromagnetischer Komponenten, die Verwendung der supraleitenden Materialien im stationären und rotierenden Teil der Maschine als auch das kryogene Kühlsystem behandelt. Auf Grundlage dieser Vorüberlegungen wird das Design eines partiell supraleitenden Synchrongenerators mit stationären, supraleitenden Felderregerspulen und einer normalleitenden, rotierenden Drehstromwicklung gewählt. Das Statoreisen ist dabei als vom kryogenen System entkoppeltes warmes Eisen realisiert und sowohl Statoreisen als auch Rotoreisen sind als Luftspaltwicklungen ausgeführt und weisen keine ausgeprägten ferromagnetischen Nuten auf. Die Kühlung der supraleitenden Spulen und Subkomponenten erfolgt mittels eines direkten, leitungsgekühlten kryogenen Kühlsystems im Stator der Maschine.

Basierend auf der gewählten Ausführungsform der elektrischen Maschine wird ein detailliertes elektromagnetisches, thermisches und mechanisches Design eines Generator-Technologiedemonstrators erarbeitet. Hierbei wird nicht nur die Wechselwirkung der genannten physikalischen Domänen untereinander, sondern auch die grundsätzliche praktische Umsetzbarkeit berücksichtigt.

Im Rahmen dieser Arbeit kommen Hochtemperatur-Supraleiter von zwei verschiedenen Herstellern zum Einsatz, die beide hinsichtlich der Verwendung in den supraleitenden Spulen des Generators vorcharakterisiert werden. Insgesamt werden 14 supraleitende Generatorspulen hergestellt und erfolgreich bezüglich ihrer supraleitenden Eigenschaften und dem aufgrund der fehlenden Windungsisolation besonderen dynamischen Verhaltens in Flüssigstickstoff bei 77 K getestet.

Zusätzlich wird in einem speziellen labortechnischen Aufbau die leitungsgekühlte Anbindung von zwei Spulen für Temperaturen unterhalb von 77 K untersucht.

Zwölf Felderregerspulen werden zu einem sechspoligen Spulensystem mit sich ausbildenden, alternierenden magnetischen Polen zusammengefügt. Das Spulensystem, die Komponenten des kryogenen Kühlsystems, das Statoreisen sowie die mechanischen Stützstrukturen werden im Vakuumraum des Kryostaten installiert. In der kryogenen Umgebung im Stator des Generator Technologiedemonstrators wird das Spulensystem auf die angestrebte Betriebstemperatur von 30 K gekühlt und erfolgreich mit einem Nennstrom von 450 A betrieben.

Abstract

The increasing demand for low-cost, renewable energy sources is causing a continued trend toward wind turbines with higher power ratings. Generators with these power ratings are usually particularly heavy and have increased requirements in terms of volume. Superconducting materials, with their high current carrying capacity and no direct current losses, show the potential for increased power density per weight and volume of electrical machines. Therefore, this work presents the development and test of a generator technology demonstrator with field coils consisting of high temperature superconductors. For improved electrical and thermal stability, the superconducting coils are designed as no insulation coils and therefore do not use electrical insulation between the coil turns.

The general design approaches of superconducting electrical machines with respect to their use in wind turbines are presented. In particular, the design of ferromagnetic components, the use of superconducting materials in the stationary and rotating parts of the machine, and the cryogenic cooling system are discussed. Based on these preliminary considerations, the design of a partial superconducting synchronous generator with stationary superconducting field coils and a normal conducting rotating three-phase winding is chosen. The stator iron is realized as a warm iron decoupled from the cryogenic system, and both stator iron and rotor iron are designed as air gap windings without distinct ferromagnetic slots. The superconducting coils and sub components are cooled by means of a direct conduction cooled cryogenic cooling system in the stator of the machine.

Based on the chosen design approach of the electrical machine, a detailed electromagnetic, thermal and mechanical design of a generator technology demonstrator is elaborated. Here, not only the interaction of the mentioned physical domains among each other, but also the basic practical feasibility has to be considered.

High-temperature superconductors from two different suppliers are used in this work and both are pre-characterized with respect to their use in the superconducting coils of the generator. A total of 14 superconducting generator coils are manufactured and successfully tested in liquid nitrogen at 77 K regarding the superconducting properties and the special dynamic behavior due to the lack of winding insulation. In addition, the conduction-cooled linkage of two coils for temperatures below 77 K is investigated in a special laboratory setup.

Twelve field coils are assembled into a six-pole coil system with alternating magnetic poles. The coil system, the components of the cryogenic cooling system, the stator iron and the mechanical support structures are installed in the vacuum

chamber of the cryostat. In the cryogenic environment in the stator of the generator technology demonstrator, the coil system is cooled to the target operating temperature of 30 K and successfully supplied with a rated current of 450 A.

List of Symbols

α	Relative pole width	–
ΔT	Temperature difference	K
$\dot{Q}$	Heat flow	W
$\dot{Q}_{\lambda}$	Heat conduction	W
$\dot{Q}_{CL}$	Heat flow due to current lead	W
$\dot{Q}_{Conv}$	Convective heat transfer	W
$\dot{Q}_{cool}$	Cooling capability	W
$\dot{Q}_{J}$	Joule heating	W
$\dot{Q}_{opt}$	Optimized heat load due to current lead	W
$\dot{Q}_{Rad}$	Heat radiation	W
$\dot{Q}_{SP}$	Heat flow due to mechanical supports	W
$\dot{Q}_{total}$	Total heat load due to current lead	W
ϵ	Emissivity	–
ϵ_{Carnot}	Coefficient of performance of Carnot cycle	-
ϵ_{real}	Coefficient of performance of real refrigeration units	-
ϵ_{total}	Total emissivity	–
λ	Thermal conductivity	$\mathrm{W\,m^{-1}\,K^{-1}}$
λ_{hts}	Compound thermal conductivity of a HTS tape	$\mathrm{W\,m^{-1}\,K}$
μ	Magnetic permeability	$\mathrm{V\,s\,A^{-1}\,m^{-1}}$
μ_0	Magnetic vacuum permeability	$\mathrm{V\,s\,A^{-1}\,m^{-1}}$

μ_r	Relative permeability	–
ν	Friction angle	°
ω	Angular frequency	Hz
ρ	Electrical resistivity	$\Omega\,\mathrm{m}$
ρ_c	Contact resistivity	$\mu\Omega\,\mathrm{cm}^{-2}$
ρ_{hts}	Compound electrical resistivity of a HTS tape	$\Omega\,\mathrm{m}$
σ	Stefan-Boltzmann constant	$\mathrm{W\,m^{-2}\,K^{-4}}$
τ	Time constant	s
τ_p	Pole pitch	mm
τ_{slot}	Slot pitch	mm
θ	Angle of magnetic flux lines in relation to c axis	°
υ	Pitch angle	°
ϑ	Electrical angle	°
FOM	Figure of merit	-
A	Cross section	mm^2
A_a	Electrical loading of armature winding	$\mathrm{A\,m^{-1}}$
A_{opt}	Optimized cross section of a current lead	mm^2
B	Magnetic flux density	T
$B_{5\tau}$	99.3 % of steady-state magnetic flux density	T
$B_{\delta r}$	Radial component of the air gap flux density	T
$B_{\delta tooth}$	Magnetic flux density in a ferromagnetic tooth	T
$B_{\delta t}$	Tangential component of the air gap flux density	T
B_δ	Air gap flux density	T
B_τ	63.2 % of steady-state magnetic flux density	T
B_c	Critical magnetic flux density	T

$B_{steady-state}$	Steady-state magnetic flux density	T
c_{coil}	Coil heat capacity	$\mathrm{J\,kg^{-1}\,K^{-1}}$
c_p	Specific heat capacity	$\mathrm{J\,kg^{-1}\,K^{-1}}$
d_r	Outer rotor diameter	m
$d_{sidewall}$	Sidewall diameter	mm
E	Electric field	$\mathrm{V\,m^{-1}}$
E_c	Critical electric field	$\mathrm{V\,m^{-1}}$
E_{turn}	Turn-to-turn energy	J
f	Frequency	Hz
F_a	Axial force	N
f_L	Lorentz force	N
F_r	Radial force	N
F_t	Tangential force	N
H	Magnetic field strength	$\mathrm{A\,m^{-1}}$
h	Heat transfer coefficient	$\mathrm{W\,m^{-2}\,K}$
h_{PC}	Pancake height	mm
I	Electrical current	A
I_{coil}	Coil current	A
I_c	Critical current	A
I_{ex}	Excitation current	A
I_{opt}	Optimization current of a current lead	A
I_r	Radial current	A
I_{sp}	Supply current	A
I_s	Spiral current	A
j	Current density	$\mathrm{A\,m^{-2}}$

j_c	Critical current density	$\mathrm{A\,m^{-2}}$
j_e	Engineering current density	$\mathrm{A\,m^{-2}}$
L	Inductance	H
l	Length	mm
l_{ef}	Effective length	mm
l_{mpz}	Length of the minimum propagation zone	mm
L_s	Spiral inductance	H
M	Torque	N m
m	Mass	kg
n	Sharpness of the transition according to power law	–
N_{MLI}	Number of multi insultaion layers	–
N_{PC}	Pancake turns	–
n_{rot}	Rotational speed	$\mathrm{min^{-1}}$
P	Power	W
p	Pole pairs	–
P_{Carnot}	Carnot power	W
P_{el}	Electrical power	W
P_{real}	Practical electrical power of a cryocooler	W
P_{turn}	Turn-to-turn losses	W
R	Electrical resistance	Ω
R_c	Resistance of the central joint of a DPC	Ω
R_{dump}	Dump resistance	Ω
R_{int}	Resistance of the interconnection between two DPC	Ω
r_{in}	Inner pancake radius	mm
R_m	Reluctance	$\mathrm{A\,V^{-1}\,s^{-1}}$

r_{out}	Outer pancake radius	mm
R_{Par}	Parasitic resistive interconnection	Ω
R_r	Radial resistance	Ω
R_s	Spiral resistance	Ω
R_{th}	Thermal resistance	$\mathrm{K\,W^{-1}}$
T	Temperature	K
t	Time	s
$t_{5\tau}$	Time at 99.3 % of steady-state magnetic flux density	s
t_{τ}	Time at 63.2 % of steady-state magnetic flux density	s
T_a	Ambient temperature	K
T_{cold}	Temperature of cold system	K
T_{cs}	Temperature at cooling stage	K
T_c	Critical temperature	K
t_{delay}	Delay time defined by the time constant	s
T_{hot}	Temperature of hot system	K
t_{ramp}	Duration of a current ramp	s
T_{ref}	Reference temperature	K
$t_{steady-state}$	Time at steady-state magnetic flux density	s
t_{total}	Total time for charging process	s
th_{hts}	Thickness of a HTS tape	mm
U	Electrical voltage	V
U_c	Critical voltage	V
U_{ind}	Induced voltage	V
U_{phase}	Phase voltage	V
V	Volume	$\mathrm{m^3}$

w_{hts}	Width of a HTS tape	mm
w_{PCS}	Pancake side width	mm
w_{PC}	Pancake width	mm
w_{slot}	Slot width	mm
w_{tooth}	Tooth width	mm

List of Abbreviations

AC	Alternating current
Ag	Silver
CAGR	Compound annual growth rate
CC	Cryocooler
Cu	Copper
DC	Direct current
DD	Direct drive
DFIG	Doubly fed induction generator
DPC	Double pancake
EESG	Electrical excited synchronous generator
G10	Glass fiber reinforced plastic
GdBCO	Gadolinium barium copper oxide
H_2	Hydrogen
He	Helium
HTS	High temperature superconductor
LCOE	Levelized cost of energy
LN2	Liquid nitrogen
MgB_2	Magnesium diboride
MI	Metal insulation
MLI	Multilayer insulation
MPZ	Minimum propagation zone
NbTi	Niobium-titanium
Nb_3Sn	Niobium-tin
N	Neon
N_2	Nitrogen
NI	No insulation
NZPV	Normal zone propagation velocity
PC	Pancake
PMSG	Permanent magnet synchronous generator
ReBCO	Rare earth barium copper oxide
RRR	Residual resistance ratio
SC	Superconductor
SCG	Superconducting generators
YBCO	Yttrium barium copper oxide
1D	One-dimensional
2D	Two-dimensional
3D	Three-dimensional
1G	First generation

2G	Second generation

Contents

1 Introduction

1.1 Motivation and target

In 2019, the total global installed capacity for onshore and offshore wind turbines is 651 GW. Furthermore, the compound annual growth rate (CAGR) for onshore and offshore plants until 2050 is projected to be 7.2 % and 11.5 %, respectively [1, 2]. In order to reduce the levelized cost of energy (LCOE), not only more turbines but also larger wind turbines are being installed. Between 2000 and 2020, the average turbine capacity in the european union increased by a factor of four to a value of approximately 8 MW [3, 4]. In addition, work is already underway on offshore wind turbines with a rated output power of 14 MW and more [5–7]. However, higher power ratings inevitably lead to larger and heavier generators. Figure 1.1 shows the weight distribution for the tower head of a 6 MW wind turbine as direct drive 1.1 a) and with intermediate gearbox 1.1 b) [8]. Especially for direct-drive wind turbines, the large and heavy generators account for almost half of the total mass of the tower head. Direct-drive generators for wind turbines thus represent a promising application for superconducting materials with their high current-carrying capacity. The application of superconductors in wind turbine generators could allow an improvement of the power to weight and power to volume ratios, with further avoidance of high-maintenance gearboxes in the drive train. Furthermore, superconducting generators can reach theoretical efficiencies of more than 99 % [9] and a drastic reduction of materials such as copper or rare earths can be achieved with the implementation of superconducting technology [10].

High temperature superconductors of the second generation (2G HTS) have excellent current-carrying capacity at moderate temperatures and magnetic fields and are particularly suitable for use in electrical machines. However, 2G HTS are susceptible to local hot spots, which can lead to burnout and thus to the complete destruction of superconducting coils. With the so-called no insulation winding technique [11], passive self-protection of superconducting coils can be achieved to avoid such local hot spots. Electrical insulation between the coil turns is omitted to allow alternative current paths around a local defect. However, the additional resistive contacts between the turns also influence the dynamic behavior of the coils.

The target of this work is therefore the electromagnetic, cryogenic and mechanical design, as well as the construction and testing of a generator technology demonstrator with no insulation field coils.

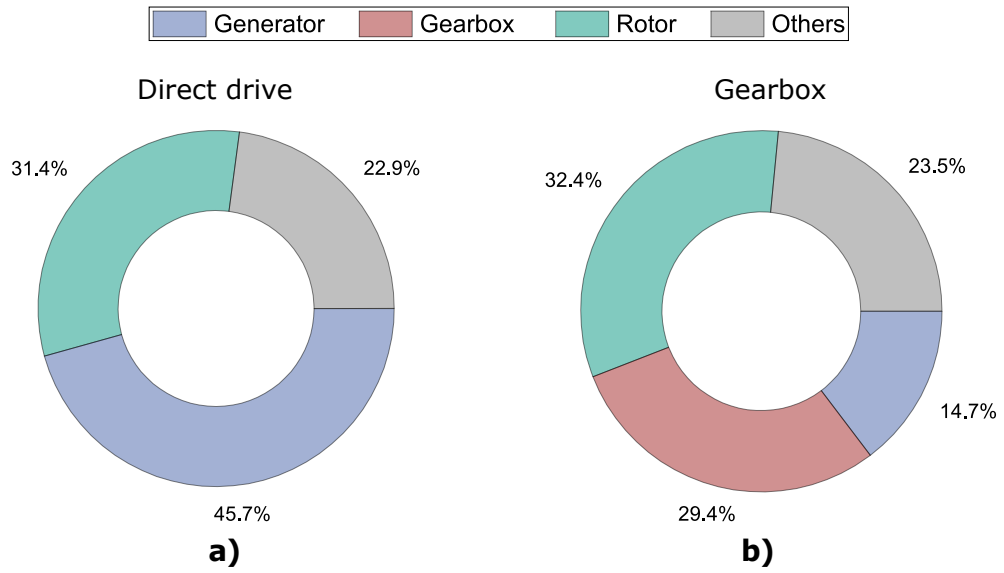

Figure 1.1: Distribution of the tower head mass for a 6 MW turbine [8]
a) Direct-drive drive train
b) Gearbox drive train

1.2 Structure of this thesis

In chapter 2, the most important technical superconductors for application in electrical rotating machines are presented. In particular, the architecture and critical parameters of second generation high temperature superconductors (2G HTS), which are used in this work, are described. Furthermore, the electrical and thermal stability limits of 2G HTS are discussed and the principle of no insulation coils (NI) as passive protection against thermal destruction of superconducting coils is introduced. In conclusion, the most important properties and definitions to characterize no insulation coils are given.

To address the impact of superconducting materials on the current technology of wind turbine generators, chapter 3 outlines the development in the wind industry and presents the state-of-the-art drive train and generator concepts. Based on the conventional technologies, the general design approaches of superconducting electrical machines are discussed. A classification is given regarding the use of ferromagnetic components with respect to a slotted or an air gap winding design, the configuration of partial or fully superconducting machines with stationary or rotating field coils, as well as the implementation of the cryogenic cooling system. Finally, partial and fully superconducting machines are compared with conventional direct drive permanent magnet synchronous generators (DD PMSG), as the most competitive conventional system.

In chapter 4 the electromagnetic, thermal and mechanical design of the generator technology demonstrator is presented. For the generator technology demonstrator, the concept of a partial superconducting synchronous generator with stationary,

superconducting, no insulation field coils and a rotating, normal conducting three-phase winding is chosen. Stator and rotor iron are designed as air gap windings and the superconducting coils in the stator are cooled by a direct conduction cooled cryogenic cooling system.

For the superconducting coils 2G HTS tapes from two different manufacturers are used. Therefore, in chapter 5, the architecture, critical parameters and turn-to-turn resistance of the superconductors are presented. Based on the pre-characterization of the superconductors, a coil design for the generator technology demonstrator is developed and the fabrication process is described. A total of 14 superconducting field coils are manufactured and tested in liquid nitrogen at 77 K, regarding their critical current and dynamic behavior. In addition, the stability of two coils at a current above the critical current is investigated. Furthermore, these two coils are tested in a special laboratory setup under conduction-cooled conditions at temperatures below 77 K. In particular, the turn-to-turn losses occurring in no-insulation coils during dynamic processes are investigated in more detail.

Chapter 6 describes the assembly and testing of the generator technology demonstrator. To build a six-pole coil system, 12 of the superconducting field coils are joined together and electrically connected in series. Firstly, the instrumentation and a preliminary test of the coil system in liquid nitrogen is presented. Then the superconducting coil system is assembled together with the cryogenic cooling system, the stator iron and the mechanical support structures in the vacuum chamber of the cryostat. Finally, the performance of the cryogenic cooling system is discussed and the superconducting coil system is tested at different temperatures under conduction cooled conditions regarding the critical current and dynamic behavior.

Chapter 7 summarizes the most important results of this work and discusses further possible investigations on the developed generator technology demonstrator. Furthermore, an outlook on future developments regarding the use of superconducting materials in rotating electrical machines is given.

2 Superconductors and superconducting coils

This chapter introduces the superconductors (SC) that are particularly important for technical applications and takes a closer look at the properties of the second-generation high-temperature superconductors considered in this work. In addition, the stability limits of high-temperature superconductors and their application in coils for electrically rotating machines, are discussed. Finally, the concept of no-insulation coils with their increased stability is introduced and their typical characteristics are explained.

2.1 Technical superconductors

Superconductivity is described as a physical phenomenon in which a material completely loses its direct current (DC) electrical resistance under certain conditions. A large number of superconducting materials are known as pure elements, alloys or compounds, but only a few are suitable for use in electrical energy applications due to their physical properties. In principle, superconductors can be classified with respect to their response to external magnetic fields, the underlying superconductor theory, the material or the critical temperature T_c. The critical temperature describes the temperature at which the superconducting state changes to the normally conducting state and represents a useful classification for technical applications. A distinction is made between low-temperature superconductors and high-temperature superconductors (HTS). This distinction is based on the historical assumption of the Bardeen-Cooper-Schrieffer [12] theory that superconductivity is not possible above approximately 30 K. After the discovery of materials with higher transition temperatures [13] they were classified as high temperature superconductors. It should be mentioned, that the boundaries for classification are not completely fixed and that there are also exceptions with regard to different definition criteria. Figure 2.1 shows the year of discovery of various superconducting materials with their corresponding critical temperature T_c [14].

Low-temperature superconductors

The most common low-temperature superconductors in technical applications are based on niobium alloys such as Niobium-titanium (NbTi) or Niobium-tin (Nb_3Sn)

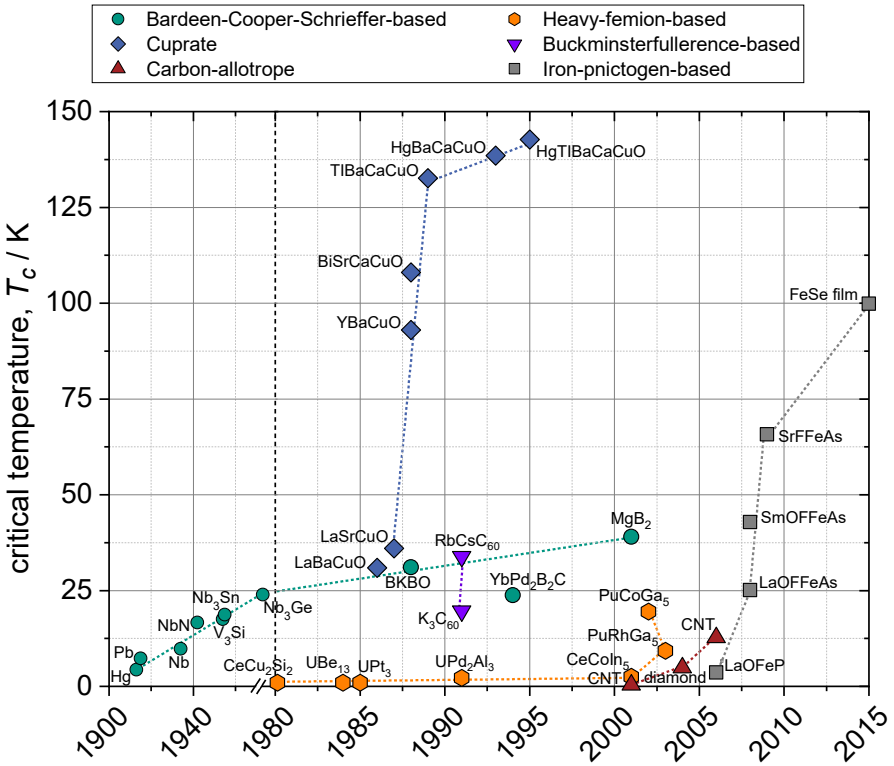

Figure 2.1: Year of discovery of various superconducting materials with their corresponding critical temperature between 1900 and 2015 (data from [14])

with a critical temperature T_c well below 20 K [15, 16]. Although the main area of application is in the sector of high-field magnets for research or medical imaging, designs of rotating machines with low-temperature superconductors can also be found [17–19]. However, the extremely low operation temperatures at around 4 K make the use of such materials for energy applications difficult. In contrast to the complex cryogenic cooling, this conductor material is characterized by relatively low costs compared to HTS. The costs of superconducting materials are usually given in $\$\,kA^{-1}\,m^{-1}$. Since the current-carrying capacity of superconducting materials is strongly dependent on external parameters such as temperature and magnetic field, these boundary conditions must be taken into account for a better cost comparison. The costs for NbTi at 4 K and 5 T are between 1 to $1.5\,\$\,kA^{-1}\,m^{-1}$, while the costs of Nb_3Sn at 4 K and 5 T range from 3 to $4\,\$\,kA^{-1}\,m^{-1}$ [20, 21].

High-temperature superconductors

The HTS suitable for technical applications can be basically divided into the compound of magnesium diboride (MgB_2), the so-called first generation (1G) and second generation (2G) HTS.

Although magnesium diboride belongs to the conventional and thus low-temperature

superconductors due to the mechanism of its superconductivity, this material can be assigned to the HTS with its relatively high transition temperature T_c of 39 K [15, 16]. Because of its ambiguous classification, magnesium diboride is also described in some literature as a medium-temperature superconductor. This superconductor can be produced as a round wire and can further be designed as a multifilament structure consisting of many single filaments with a smaller diameter compared to the total wire diameter. Because of its relatively low costs for a HTS, of around 20 \$ kA^{-1} m^{-1} at 20 K and 2 T [21], this conductor is viable for use in superconducting rotating machines. In addition, the multifilament structure allows a significant reduction of alternating current (AC) losses in the superconductor. However, the range of application in electrical machines is limited by the reduced current carrying capacity due to the relatively low T_c and the poor in-field performance, at temperatures of around 20 K and magnetic flux densities of 1 to 2 T.

The first generation of HTS consists of a bismuth strontium calcium copper oxide compound (BSCCO) and belongs to the group of high-temperature superconductors with transition temperatures of up to 108 K [15, 16]. Similar to magnesium diboride, these superconductors consist of a multifilament structure embedded in a silver alloy matrix. Although some superconducting electrical machines have been realized with this type of superconductor, the first generation is being more and more displaced due to the improved performance of the second generation of HTS. In addition, the high silver content in the matrix structure prevents a considerable further cost reduction towards more economically conductor prices.

Second generation high-temperature superconductors (2G HTS) show relatively high transition temperatures and excellent in-field properties. The critical temperature T_c of the most common 2G HTS is about 93 K [15, 16]. This superconductor class is particularly suitable for the high magnetic field loads occurring in electrically rotating machines. The superconducting layer consists of a rare earth barium copper oxide ReBCO compound. However, second-generation HTS can only be manufactured as tapes, which results in reduced torsional stability. These mechanical limits have to be taken into account during further processing into superconducting coils. Furthermore, the tape structure causes increased AC losses in an environment with time-varying currents or magnetic fields. The particularly good performance of 2G HTS is reflected in the cost which is usually quoted at 77 K and the self-field of the tape with approximately 0 T. In this work, a total of 1.2 km of 2G HTS tape from two different manufacturers is used, priced at 77 K and 0 T with 123 and 254 \$ kA^{-1} m^{-1} which is a typical cost range according to [22]. At 20 K and 2 T, costs between 55 and 85 \$ kA^{-1} m^{-1} are already achieved, due to the increased current-carrying capacity under these conditions.

Iron-pnictide-based superconductors with critical temperatures well above 30 K can also be classified as technical high-temperature superconductors. These materials still show lower critical temperatures, critical fields and current-carrying capacities in comparison with copper oxide-based superconductors, but could be potentially produced with a simplified and thus more economical manufacturing process [23]. However, since iron-pnictide-based superconductors are not

yet available as a commercial product, they will not be discussed further in this work.

2.2 2G HTS tapes

The generator technology demonstrator presented in this work applies only 2G HTS tapes, thus the technical properties of this superconductor are described in further detail in the following sections.

2.2.1 Architecture of HTS tapes

Due to their architecture, 2G HTS are also referred to as coated conductors. The tape consists of several layers of different thicknesses with a tape width between 2 mm to 12 mm. Figure 2.2 shows the typical structure of a coated conductor tape.

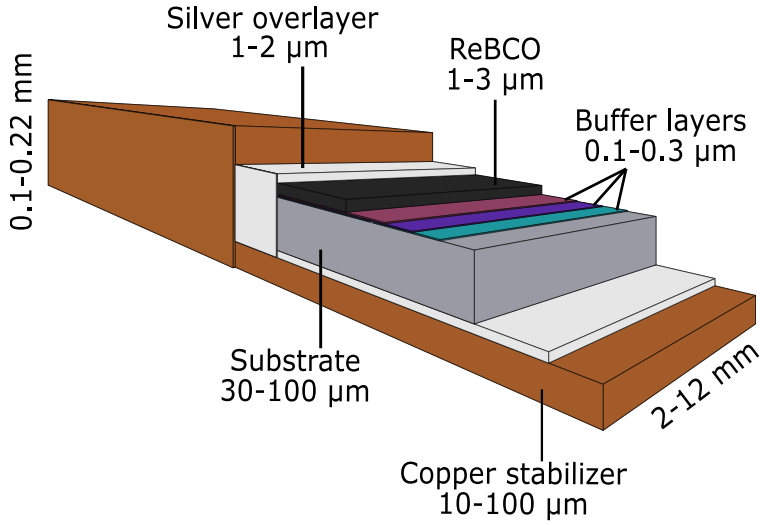

Figure 2.2: Typical architecture of a 2G HTS tape with the different layers

However, the architecture varies in detail depending on the manufacturer and production process [24–26]. The metallic substrate, which usually consists of Hastelloy^{TM} C276, can have a thickness of 30 µm to 100 µm and acts as a base and mechanical support for the remaining layers. To prevent chemical reactions or diffusion between the substrate layer and the superconductor layer, one or more buffer layers, with a thickness of a few hundred nanometers, are used as a barrier in between. In addition, the buffer layers contribute to achieve a suitable surface texture for the deposition of the superconducting layer. The current-carrying superconducting ReBCO layer is only a few micrometers thick. The rare earths used in most 2G HTS are yttrium or gadolinium, which is why these superconductors are also abbreviated as YBCO or GdBCO. For protection and

to ensure low contact resistance to the superconducting layer, the tape is coated with a 1 µm to 2 µm thin silver (Ag) layer. Depending on the application, a copper (Cu) layer on one or both sides of the tape, which serves as additional thermal and electrical stabilization, can be applied. The thickness of these copper layers can vary between 5 µm and 100 µm, resulting in a total thickness of HTS tapes in a range from 32 µm to 360 µm.

2.2.2 Critical parameters

In addition to the critical temperature T_c, the superconducting state is also limited by the two parameters of critical magnetic flux density B_c and critical current density j_c. These parameters influence each other and describe the range in which superconductivity is possible. Thus, for a given temperature T_1 and a given external magnetic field or a magnetic field caused by the superconductor itself B_1, only a certain critical current I_c exists. The basic relationship of these three quantities is shown in figure 2.3.

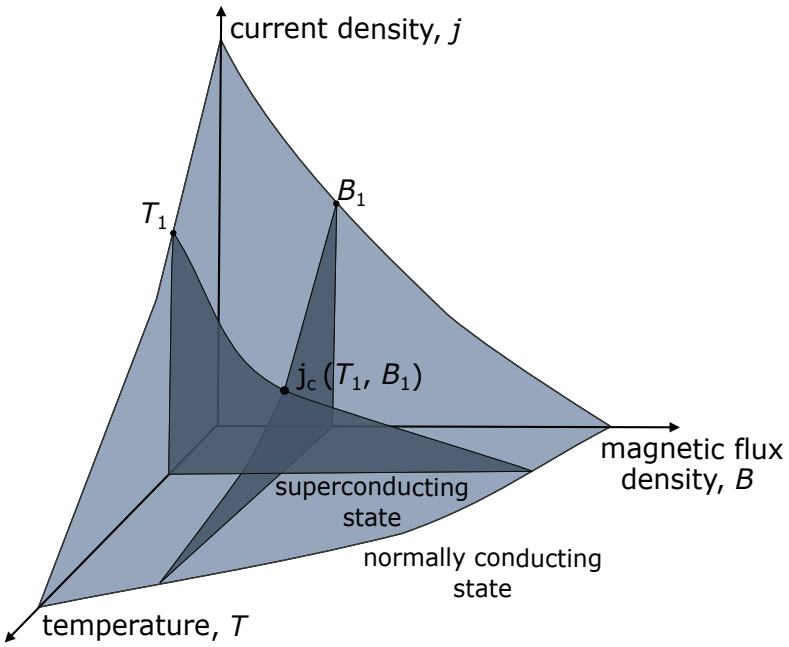

Figure 2.3: Critical parameters of the superconducting state

Starting from the critical current density at 77 K in self-field, the current-carrying capacity of a superconductor at different temperatures or magnetic flux densities can be described by the lift factor. While the lift factor at 77 K in self-field is defined as 1, it can reach values greater than 1 at constant magnetic field and decreasing temperature or values smaller than 1 at constant temperature and increasing magnetic field. Figure 2.4 shows the typical correlation of the lift factor of a 2G HTS tape for temperatures between 20 K and 77.5 K and magnetic flux densities between 0 T and 7 T according to the measured data from [27]. The data shown is recorded with the magnetic flux density B aligned perpendicular to the tape

surface. This corresponds to an alignment of the flux lines parallel to the c axis of the tape and is defined as an angle θ of 0°. The lift factor in this plot refers to the critical current of 144.9 A of a 4 mm tape at 77.5 K and 0 T. For example, the tape under consideration has a critical current of 858.16 A at 20 K and 1 T, resulting in a lift factor of 5.9.

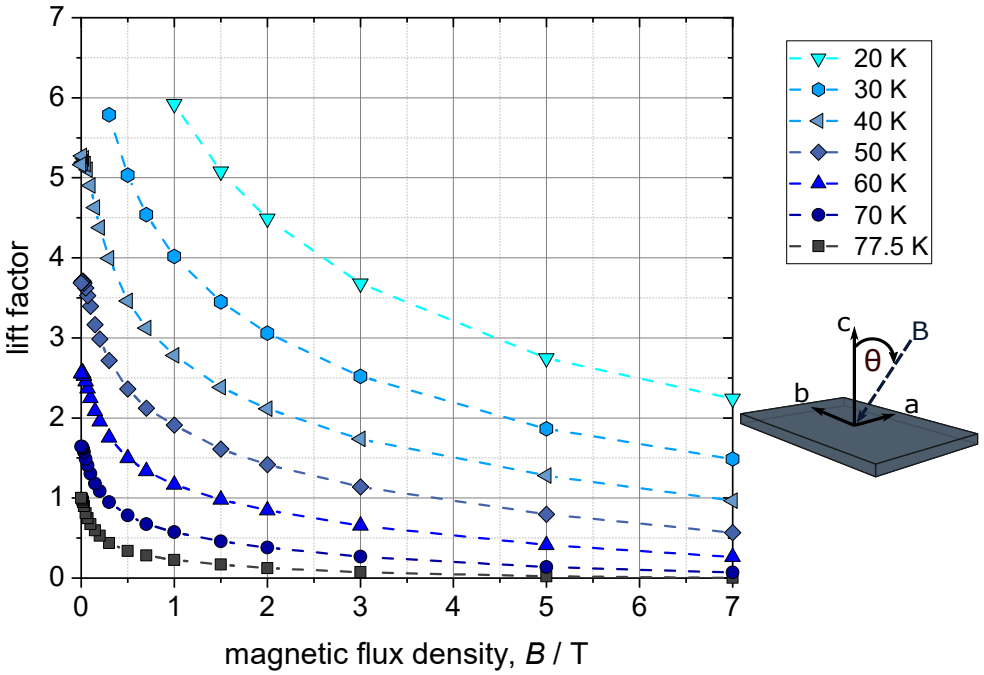

Figure 2.4: Measured lift factor of a 2G HTS tape sample at different temperatures and magnetic flux densities. The lift factor is defined as 1 with a reference point of 144.9 A at 77.5 K and 0 T. The magnetic flux density is aligned perpendicular to the tape surface which corresponds to $\theta = 0°$ (data from [27])

Due to their special structure, 2G HTS tapes exhibit significant anisotropic behavior. The reduction of the current carrying capacity depends not only on the magnitude of the magnetic flux density B but also on its orientation to the tape. While magnetic fields parallel to the tape surface have a reduced influence on the critical current I_c, magnetic flux perpendicular to the tape surface is usually the worst case in terms of current carrying capacity. Figure 2.5 shows the same tape sample already considered in figure 2.4. The data is recorded at a temperature of 77.5 K at magnetic flux densities with magnitudes between 0 T and 7 T and field angles between 0° and 240°. The lift factor is again related to the critical current of 144.9 A at 77.5 K and 0 T. In the case of a magnetic flux density of 0.1 T, the anisotropy of this tape can result in a difference between the minimum and maximum lift factor of 0.19. A typical model to describe the transition from the superconducting to the normally conducting region is the so-called power law [28]:

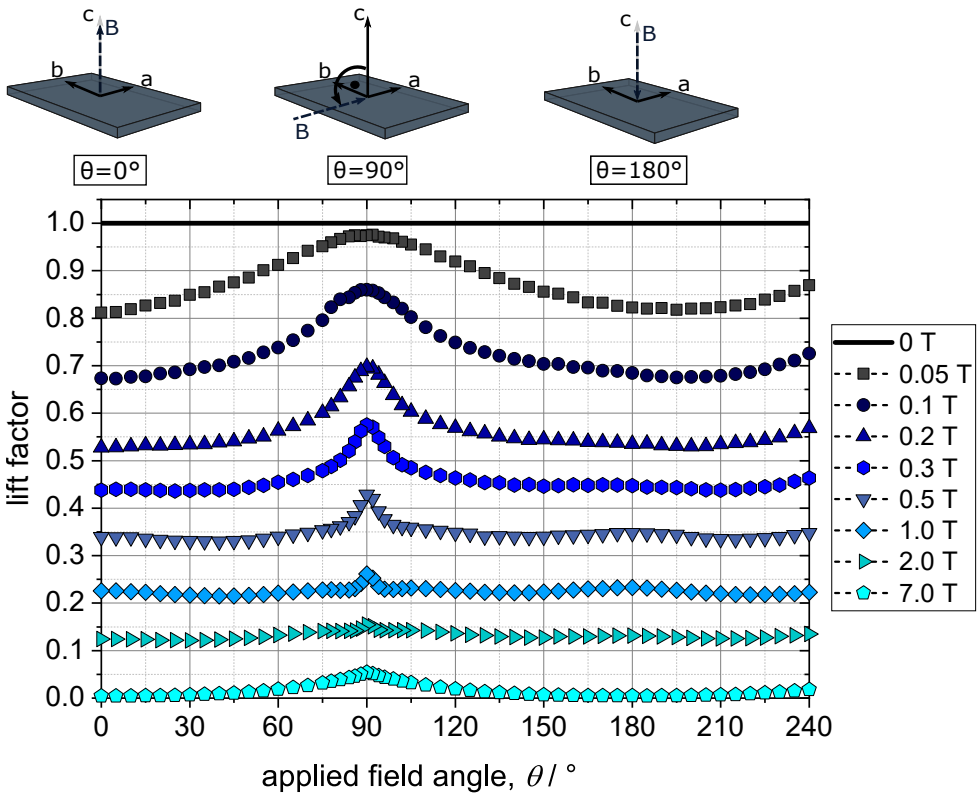

Figure 2.5: Measured lift factor of a 2G HTS tape sample at different magnitudes and orientation of magnetic flux density at a temperature of 77.5 K. The lift factor is defined as 1 with a reference point of 144.9 A at 77.5 K and 0 T (data from [27])

$$E(j) = E_c \cdot \left(\frac{j}{j_c}\right)^n \tag{2.1}$$

with the electric field E over the superconductor, the critical electric field E_c, the applied current density j, the critical current density j_c and the n-value, describing the sharpness of the transition from superconducting to normally conducting state.

The critical electric field E_c is usually set at 1 µV cm^{-1} for short HTS samples or 0.1 µV cm^{-1} for longer HTS lengths such as wound coils. To obtain the critical current I_c. The n-value depends on temperature and magnetic field and typically ranges between 10 to 40 [29]. Usual critical currents at 77 K in self-field are ranging between 400 A cm^{-1} and 600 A cm^{-1}, resulting in engineering current densities j_e of around 500 A mm^{-2} [27]. The performance of 2G HTS tapes continues to improve as demonstrated in [30], with a record J_e at 30 K and 3 T of up to 7068 A mm^{-2} reported. Table 2.1 summarizes the data of commercially available 2G HTS tapes from the most important manufacturers.

Table 2.1: Specifications of commercially available 2G HTS tape from different manufacturers

	Theva	Shanghai Superconductor	American Superconductor	SuperPower	Superconductor Technologies Inc.	SuNAM	SuperOx	Fujikura
country	Germany	China	USA	USA	USA	South Korea	Japan	Japan
max. I_c (77 K, sf) (A cm^{-1})	420	520	415	380	490	800	510	550
Lift factor (30 K, 3 T, Θ= 0°)	1.2 - 1.7*	2.4 - 2.5	1.3	2.8 - 3.1	1.9	0.5	2.4	1.3 - 1.8
Supercond. layer	GdBCO	YBCO	YBCO	YBCO	YBCO	GdBCO	GdBCO, YBCO	GdBCO
metallic substrate	Hastelloy C276	Hastelloy C276	Ni5W, Ni9W	Hastelloy C276	Hastelloy C276	Hastelloy C276	Hastelloy C276	Hastelloy C276
substrate thickness (µm)	50, 100	30, 50	50 - 75	30, 50	100	60, 105	40, 60, 100	50, 75
tape thickness (µm)	80 - 220	65 - 255	170 - 360	32 - 162	-	60 - 270	60 - 100	80 - 130
tape width (mm)	4, 6, 12	2 to 10	4.4, 4.8, 12	2, 3, 4, 6, 12	3, 4, 6, 8, 10, 12	4, 12	4, 6, 12	4, 12
max. piece length (m)	600	500	500	900	1000	150	600	500
References	[26, 27, 31]	[26, 27, 32–34]	[26, 27, 35–37]	[26, 27, 38, 39]	[26, 27, 40, 41]	[26, 27, 42, 43]	[26, 27, 44–46]	[26, 27, 47]

* Θ= 30° worst case for critical current

2.2.3 HTS stability

When using 2G HTS materials in rotating electrical machines, the critical limits shown in figure 2.3 must be considered for fault-free operation. However, local reduction of the j_c can be caused by various effects such as material defects, mechanical stress, locally increased magnetic flux densities or parasitic heat loads. Depending on the operating point, this can lead to a transition from the superconducting region to the normal conducting region. Due to the structure of the tapes, very high resistive areas can form locally, which in turn cause heat dissipation by the supplied current. As long as the underlying cooling system can absorb the heat generated, the system is in a state of equilibrium and can continue to operate. This equilibrium state of dissipated joule heat $\dot{Q}_J$ and cooling by conduction $\dot{Q}_\lambda$ and convection $\dot{Q}_{Conv}$ can be expressed by the following equation [48]:

$$\begin{aligned} \dot{Q}_J &= \dot{Q}_\lambda + \dot{Q}_{Conv} \\ j^2 \cdot \rho_{hts}(T) \cdot A \cdot l_{mpz} &= 2 \cdot \frac{\lambda_{hts}(T) \cdot A \cdot (T - T_a)}{l_{mpz}} \\ &\quad + h(T) \cdot (T - T_a) \cdot 2 \cdot (w_{hts} + th_{hts}) \cdot l_{mpz} \end{aligned} \tag{2.2}$$

with the current density j, the compound and temperature-dependent electrical resistivity of a HTS tape $\rho_{hts}(T)$, the temperature of the normal zone T, the cross section A, the length of the minimum propagation zone l_{mpz}, the compound and temperature-dependent thermal conductivity of a HTS tape $\lambda_{hts}(T)$, the ambient temperature T_a, the temperature-dependent heat transfer coefficient of the ambient medium $h(T)$, the width of the HTS tape w_{hts} and the thickness of the HTS tape th_{hts}.

If the cooling system is unable to remove the additional heat, the continuing temperature rise will force larger and larger areas beyond the critical limits of the superconductor. As a result, this can lead to a thermal runaway, abruptly transferring larger areas from the superconducting state to the normally conducting state, which is also referred to as a quench. The minimum size of a normal zone that leads to further propagation is described as minimum propagation zone (MPZ) and can be defined by its minimum length l_{mpz} using equation 2.2 [48]:

$$l_{mpz} = \sqrt{\frac{2 \cdot \lambda_{hts}(T) \cdot A \cdot (T - Ta)}{j^2 \cdot \rho_{hts}(T) - \frac{h(T) \cdot 2 \cdot (w_{hts} + th_{hts})}{A} \cdot (T - Ta)}} \tag{2.3}$$

The speed at which this normal zone propagates is called the normal zone propagation velocity (NZPV). The principle mechanism of a defect in the superconducting layer and the resulting normal conducting zone with conductive and convective cooling and the length of the minimum propagation zone is illustrated in figure 2.6.

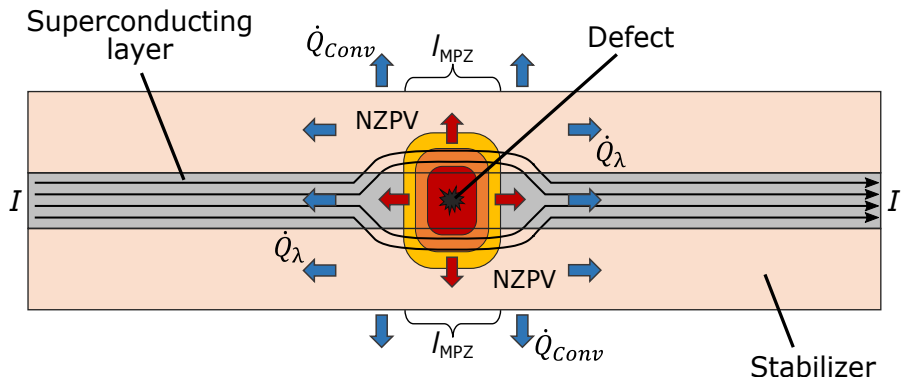

Figure 2.6: Illustration of the propagation of a normal zone in the superconducting layer caused by a defect. The 2G HTS tape is shown simplified with only superconducting layer and stabilization layer on both sides.

For a simplified representation, only the superconducting layer and a double-sided stabilization layer are shown.

The normal zone propagation velocity (NZPV) is a crucial parameter for the overall stability of a superconducting tape or superconducting application. With a fast NZPV, the resulting hot spot can quickly expand over larger areas. As a result, the heat can be better distributed and local hot spots with very high temperature peaks are avoided. Furthermore, the transition of large areas to the normal conductive state results in a larger total electrical resistance R. This reduces the current I that is continuously supplied and prevents increasing dissipation of heat. Due to their structure and physical properties, low-temperature superconductors usually have a normal zone propagation velocity (NZPV) of several $\mathrm{m\,s^{-1}}$ [49, 50]. With 2G HTS, the NZPV is only in the range of $\mathrm{cm\,s^{-1}}$ [51, 52], which leads to more localized hot spots with higher peak temperatures. If the temperature exceeds a value of 400 K, the tape is likely to undergo irreversible degradation or a burnout [53]. In 2G HTS coils with several hundred meters of wound tape, this leads to a complete destruction of the coil and represents a considerable challenge in the design of high-temperature superconducting coils. A possibility to improve the thermal and electrical stability is the addition of copper stabilization layers. This allows the electric current to bypass the defect in the superconductor via the resistive copper layer. However, in the event of a serious defect with hot spot development, stabilization layers can only delay the thermal runaway. Therefore, additional protection mechanisms are essential to prevent the thermal destruction of 2G HTS coils.

Quench detection and protection methods

In order to address a local thermal degradation or destruction, different approaches to the detection of hot spots in HTS coils are investigated [54].

A common method of monitoring a superconducting coil is a voltage measurement, which detects the voltages according to equation 2.1. For better sensitivity, inductive signal interference can be further reduced by a bridge-balance method. Thereby, the voltage between a central coil voltage tap and a potentiometer is measured and the inductive coil component is reduced by changing the potentiometer resistance. Another possibility is to co-wind the superconducting coil with a resistive, insulated metal tape. Due to the close magnetic coupling of the two tapes, inductive signal interference can be avoided [55]. Nevertheless, the low signal sensitivity in combination with the slow normal zone propagation velocity of HTS coils poses a challenge for voltage-based quench detection. A developing hot spot could reach high peak temperatures before a practically measurable voltage signal is detected. In addition, the environment, especially in electrically rotating machines, could present a further difficulty in terms of susceptibility to noise.
In [56] it is described how normal conducting zones can be identified by the change of the measured magnetic field due to current redistribution. While this method has much better signal sensitivity compared to voltage-based techniques, multiple hall sensor arrays must be used in larger HTS coils due to the slow normal zone propagation velocity. Another possibility is to cut the HTS tape lengthwise into two equal pieces, which form different magnetic fields when the current-carrying capacity of a strand is changed [57]. However, this basically requires the possibility to split the HTS tape in the given coil configuration. Another challenge for magnetic detection methods in electrical machines is the time-varying magnetic fields with regard to insensitivity to noise.
Furthermore, it is possible to detect a hot spot with an optical fiber that is embedded or co-wound with the superconductor. This detection method is based on the thermal expansion or thermally induced variation of strain caused by a local hot spot in the coil. Various approaches to this method are described in the literature [58–61]. While the basic signal sensitivity of this method is comparatively high, the signal amplification is decreased at temperatures below 20 K due to the reduced thermal contraction rate of the involved materials. Optical methods could be robust to electromagnetic and mechanical interference with respect for use in rotating machines, but rely on a possible invasive assembly of the optical fiber.
A non-invasive detection method is the approach of using acoustic signals. In this case, the HTS tape itself serves as a distributed temperature sensor, in which the change in an acoustic signal caused by an occurring hot spot is monitored. This makes it possible to achieve an accuracy of better than 1 K, while an additional co-winding is avoided [62, 63]. Although acoustic methods in principle have a low noise insensitivity, it is not yet clear whether such a method is robust against the noise occurring in rotating machines.
Another approach is to monitor the stray capacitance of a superconducting coil. This method is also a non-invasive detection variant, but is based mainly on the change of the permittivity of a cryogenic fluid into the gaseous state [64, 65]. Thus, this approach can only be used for superconducting coils that are directly cooled in a cryogenic bath. Although the signal sensitivity is promising, a susceptibility to transient electromagnetic fields is reported in [65].

Detection methods based on radio frequency also represent a promising non-invasive approach. Especially for environments with high mechanical and low-frequency electromagnetic noise, they could be an alternative to the aforementioned techniques [66, 67]. However, a test on practical HTS coils is still pending.

Table 2.2 lists the various approaches for quench detection with an evaluation in terms of signal sensitivity, invasiveness and noise insensitivity.

Table 2.2: Quench detection methods and their evaluation for use in superconducting rotating machines

Method	Signal sensitivity	Noise insensitivity	Invasiveness
Voltage-based	--	--	0
Magnetic-based	+	-	-
Optical-based	+	+	--
Acoustic-based	++	0	++
Capacitive-based*	++	-	++
Radio frequency-based	++	++	++

* only applicable in cryogenic liquids

If a quench is successfully detected, protective measures must be initiated to prevent a further uncontrolled rise in temperature. A first action is to stop the continuous current supply of the coil. Furthermore, the energy stored in the coil can be dissipated via a dump resistor R_{dump} connected in parallel. To avoid critical temperature peaks it is preferable to discharge the coil as quickly as possible via the dump resistor. However, this is limited by the inductance L and the dielectric strength of the coil [68, 69]. Another possibility is to enlarge the normally conducting areas and therefore the overall resistance of the coil by additional heating [70, 71]. The heating power can be provided by attached heaters. However, due to the slow normal zone propagation velocity in HTS coils, the individual elements must have a small distance to each other or be designed as continuous heating elements. Another approach to active protection is coupling-loss-induced quenching. An oscillating current causes coupling losses in the superconductor itself, thus eliminating the need for externally attached heating elements [72].

However, these approaches for protection against a thermal destruction of a HTS coil, need a quench detection at an early stage and immediate actively initiated countermeasures, resulting in a failure of the superconducting coils and thus to a possible shutdown of the electrical rotating machine. In addition, the basic applicability of the listed detection and protection measures in rotating machines with superconducting windings has not yet been verified. Therefore, the feasibility of a passive protection for superconducting coils in rotating machines is investigated in this work.

2.3 No insulation HTS coils for rotating machines

A simple way to wind 2G HTS tapes into a coil is in the form of a planar or pancake (PC) coil. In this process, the tape is wound continuously in only one plane, resulting in an increasing width of a pancake side w_{PCS} with an increasing number of pancake turns N_{PC}. The minimum height of the pancake h_{PC} corresponds to the width of the superconductor tape used. To further increase the total number of turns of a coil, several such pancakes can be stacked on top of each other. A configuration of only two pancakes is called a double pancake (DPC). In the case of a superconducting rotating machine, a simple solenoid coil geometry is usually not sufficient. The coil shape is similar to a racetrack with pronounced straight coil sides corresponding to the effective length l_{ef} of the rotating machine. To avoid degradation of the superconductor, the inner radius r_{in} and outer radius r_{out} in the curved part of the racetrack must be bigger than the minimum bending radius of the HTS tape. Figure 2.7 shows a sketch and a cross-sectional view of a pancake in racetrack shape with the most important parameters.

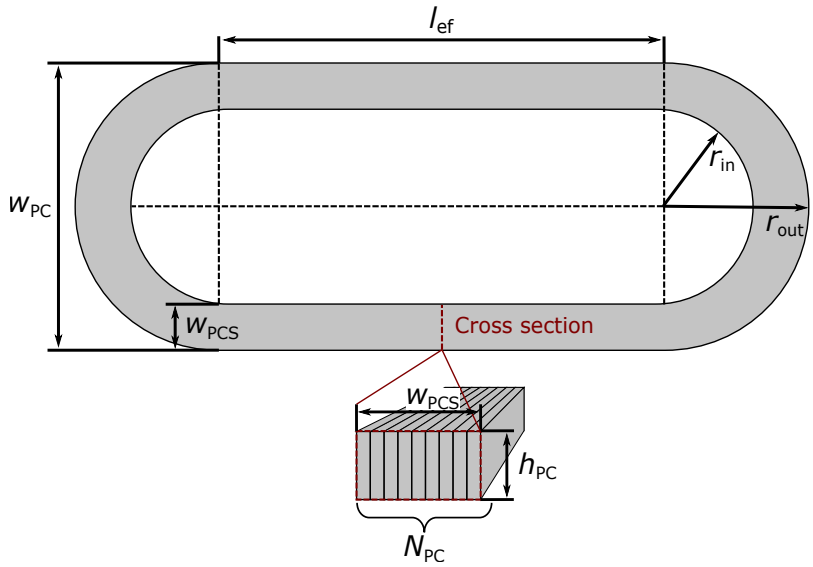

Figure 2.7: Sketch with cross-sectional view of a pancake in racetrack shape wound with 2G HTS tape

As with conventional coils, the individual turns of HTS coils are usually electrically insulated from each other. In [11], an HTS coil without insulation between the superconducting tapes is presented for the first time. This is possible because the superconductor in steady state condition is a zero resistance path for the current compared to the resistive turn-to-turn contacts. The omission of an insulation allows additional current directions between the coil turns. In this work, the actual superconducting coil path, which is responsible for the generation of the magnetic flux density, is called the spiral path and the alternative turn-to-turn paths are called radial path. Figure 2.8 a) shows how only a spiral current I_s can flow in an insulated coil, while radial currents I_r between the individual turns are also

possible in a no-insulation (NI) coil, illustrated in 2.8 b). The alternative turn-to-turn connections in a NI coil allow both current and heat to escape the spiral path in the event of a local defect. This avoids forcing the coil current through a defect, which can prevent local hot spots with very high peak temperatures. Compared to the active protection mechanisms from section 2.2.3, no insulation coils can have passive self-protection against thermal destruction [11, 73–75].

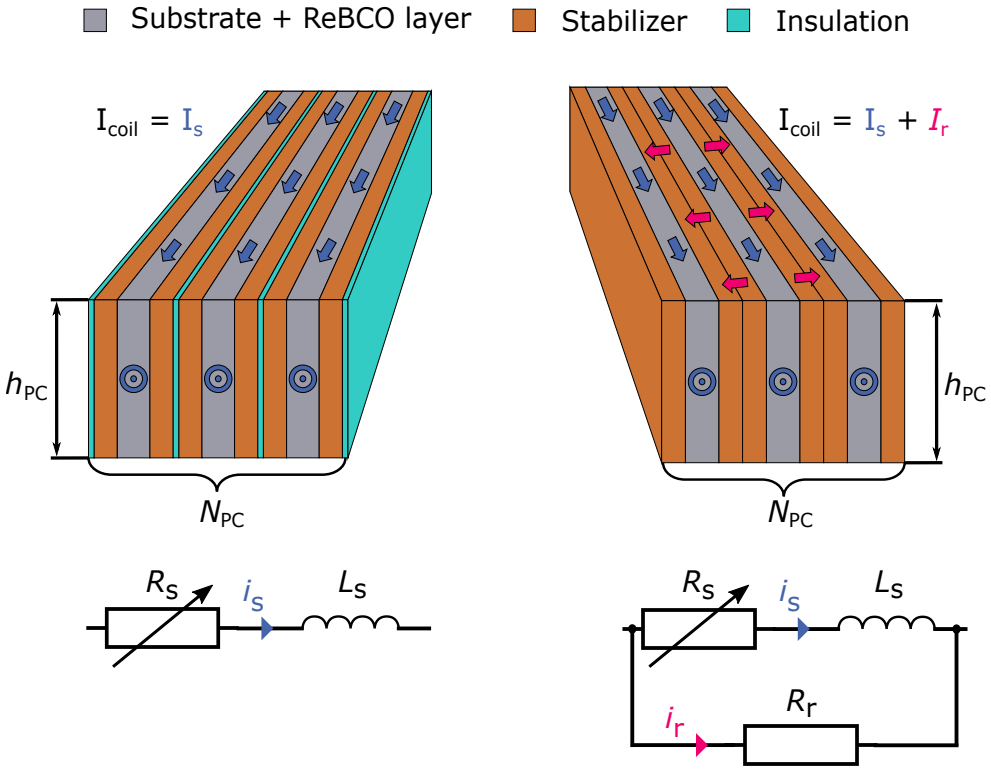

a) Insulated coil **b)** No insulation coil

Figure 2.8: a) Illustration of an insulated coil with currents in spiral direction and corresponding simplified equivalent circuit diagram. b) Illustration of a no-insulation coil with currents in spiral and radial direction and corresponding simplified equivalent circuit diagram

Charging and discharging delay

An insulated coil can be described with a series-connected coil inductance L_s and a resistor R_s on the spiral path as shown in figure 2.8 a). The spiral resistance R_s is zero for perfect superconductivity. A no-insulation coil can be expressed in simplified terms with a resistor R_r connected in parallel to the spiral path in the equivalent circuit as expressed in 2.8 b). The radial resistance R_r sums the resistive contacts between the turns in the radial direction. Due to the additional current paths, the dynamic behavior of a no insulation coil exhibits a delay in the developing or decaying magnetic field. This delay can be represented by the universal time constant τ with the following relation:

$$\tau = \frac{L_s}{R_r} \tag{2.4}$$

The duration τ describes the time after a step response, which is required to reach 63.2 % of the current, voltage or magnetic flux density steady state values. According to [76], the time constant is determined, as it is described in figure 2.9 and the following equations:

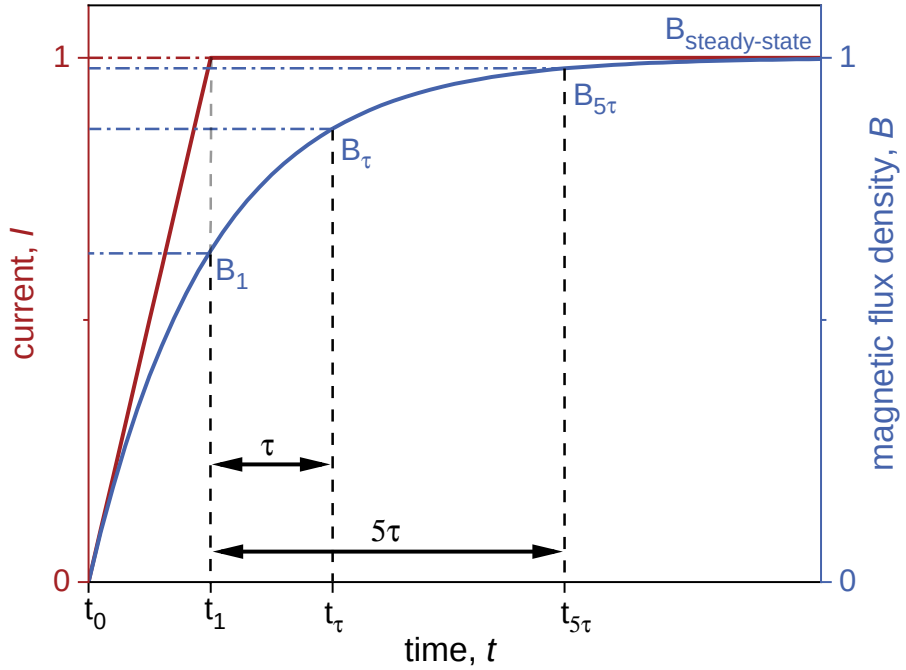

Figure 2.9: Illustration for the determination of the time constant of no insulation coils at an arbitrary current ramp with delayed magnetic flux density

$$\tau = t_\tau|_{B_\tau} - t_1|_{B_1} \Rightarrow \begin{cases} t_1 & = t_0, \text{for current step} \\ B_1 & = B(t_1) \\ B_\tau & = B_1 + 0.632 \cdot (B_{steady-state} - B_1) \end{cases} \tag{2.5}$$

$$5 \cdot \tau = t_{5\tau}|_{B_{5\tau}} - t_1|_{B_1} \Rightarrow \begin{cases} t_1 & = t_0, \text{for current step} \\ B_1 & = B(t_1) \\ B_{5\tau} & = B_1 + 0.993 \cdot (B_{steady-state} - B_1) \end{cases} \tag{2.6}$$

Usually, superconducting coils are excited with a defined current ramp of a few amperes per second. Thus, the time constant τ describes the time required to reach 63.2 % of the difference between the magnetic field in the steady-state and the field at the end of the ramp. A more practical quantity for the operation of superconducting magnets is the fivefold time constant, since the generated field

corresponds with 99.3 % almost to the field in the steady-state. The total time t_{total} needed to sufficiently charge or discharge a no insulation coil is therefore a combination of the duration for the current ramp t_{ramp} and the delay t_{delay}, defined by the time constant.

$$t_{total} = t_{ramp} + t_{delay} \tag{2.7}$$

Turn-to-turn resistance and losses

According to equation 2.4, the resistance in the radial direction R_r significantly influences the dynamic behavior of no insulation coils. It represents the sum of the resistive contacts between the turns and can be defined for racetrack coils as follows [77, 78]:

$$R_r = \sum_{i=1}^{N_{PC}-1} R_i = \sum_{i=1}^{N_{PC}-1} \rho_c \cdot \left(\frac{1}{2 \cdot \pi \cdot r_i \cdot w_{PCS}} + \frac{1}{2 \cdot l_{ef} \cdot w_{PCS}} \right) \tag{2.8}$$

with the radial resistance per turn R_i, the radius per turn r_i ranging between $r_{in} \leq r_i \leq r_{out}$ and the contact resistivity ρ_c defined as the contact resistivity per contact area and usually given in $\mu\Omega\,\mathrm{cm}^{-2}$.

The contact resistivity ρ_c between two HTS tapes depends on various parameters such as surface properties like oxidation and roughness, contact pressure, temperature, mechanical and thermal cycling and also on the layer structure of the HTS tapes involved [79, 80]. The values can vary considerably from only $5\,\mu\Omega\,\mathrm{cm}^{-2}$ to almost $10\,\mathrm{m}\Omega\,\mathrm{cm}^{-2}$ [79–86]. The contact resistivity is determined directly by contact measurements of short tape samples or indirectly, according to equation 2.4, via the measured time constant τ and the inductance L of a coil. In principle, a low resistance value, enables better passive protection mechanism of a no insulation coil but also result in very large delays t_{delay}. For this reason, attempts are made to artificially change the contact resistivity. One method is the so-called metal insulation (MI) coil, in which the resistance in the radial direction is increased by co-winding with a metal tape [87]. Another possibility is the partial insulation coil, in which only part of the turns are insulated from each other, thus also increasing the total radial resistance [88].

During dynamic operation, the current flowing in the radial direction I_r of a no insulation coil causes additional losses due to the resistive turn-to-turn contacts. These losses, which are called turn-to-turn losses P_{turn}, occur over the entire period from the start of a current ramp at t_0 until the steady-state condition $t_{steady-state}$. The total energy dissipated in the coil E_{turn} can thus be described as follows [89]:

$$E_{turn} = \int_{t_0}^{t_{stead-state}} P_{turn}(t), dt = \int_{t_0}^{t_{stead-state}} I_r^2(t) \cdot R_r, dt \tag{2.9}$$

Figure 2.10 shows the typical waveforms of the spiral I_s and radial I_r currents for a common current ramp of the supply current I_{sp}. The spiral current has the same curve as the magnetic flux density of the coil, since both values are directly linked via the proportionality factor of the coil turns N_{PC}. The radial current and thus the dissipated turn-to-turn losses P_{turn} show a peak at the end of the current ramp at the time t_1. Subsequently, the radial current decays and larger parts of the total current are transferred to the spiral path. The area under the radial current curve represents the dissipated energy during the ramping process, which depends on the slew rate and the current magnitude. With steeper slew rates and higher supply currents, the turn-to-turn losses also increase, which must be taken into account during the operation of NI coils.

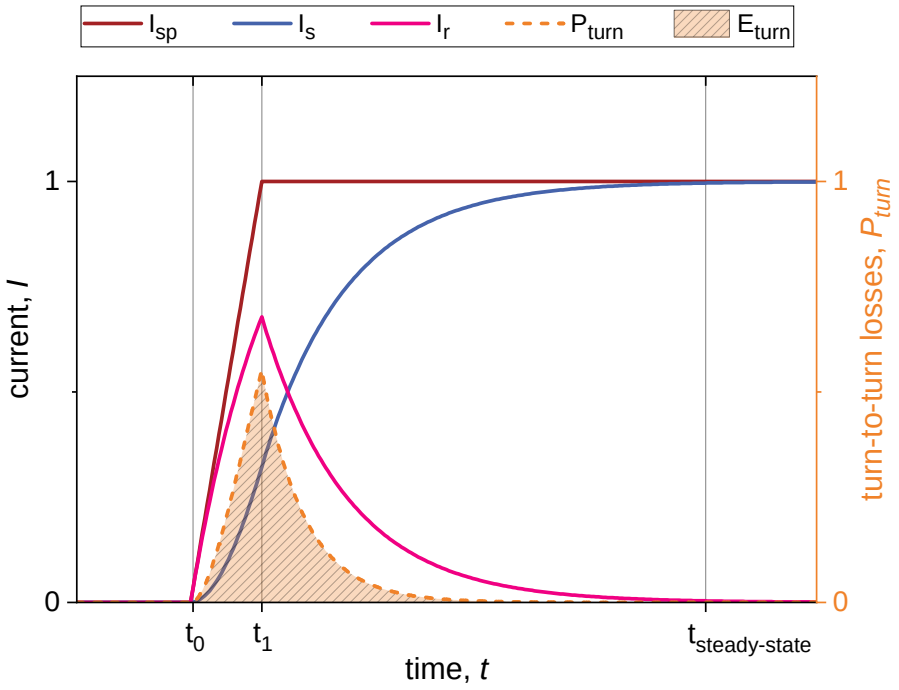

Figure 2.10: Characteristic waveform of the spiral and radial current in an NI coil at a supply current with a given ramp. The area under the turn-to-turn losses represents the total dissipated energy in the coil

3 Conventional and superconducting wind turbine systems

This chapter is intended to provide the basis of a suitable comparison with superconducting wind turbine systems. Therefore, the most common wind turbine systems and the future development in terms of power ratings are presented first. In a second step, the special features of superconducting wind turbines and their classification are discussed, and finally a comparison with conventional systems, in particular with regard to power density, is made.

3.1 Development in the wind industry

The share of renewable energy in primary energy is continuously increasing. According to [90], the global share of renewables for the generation of electricity grew by almost 7 % in 2020. Wind power generation, both onshore and offshore, is therefore becoming more important. Figure 3.1 shows the installed cumulative global capacity from 2000 to 2019 [1] and a forecast according to the data of [2] for the year 2050. In 2019, the total installed capacity was 651 GW. The compound annual growth rate (CAGR) for the past and forecast period is given. The growth in installed offshore capacity with 38.5 % and 11.5 % for both periods, is greater than the growth in onshore capacity. The complex and costly transport, installation and maintenance of offshore turbines is contrasted by the advantages of more continuous and stronger winds [91, 92]. While full load hours of up to 3200 h are possible for good onshore sites, offshore wind farms with a correspondingly good location can reach up to 4500 h [93].

Furthermore, it is possible to realize even larger wind turbines than onshore. The share of wind energy generated offshore will therefore gain in importance in the future. A measure to quantify the cost of electricity for certain generation types is the so called levelized cost of energy (LCOE). The sum of the total costs over a lifetime is divided by the sum of the electrical energy generated. The costs consist of the investment expenses, the operation and maintenance expenses and, in the case of non-renewable energy sources, the fuel expenses. For onshore generation, the levelized cost of energy ranges from

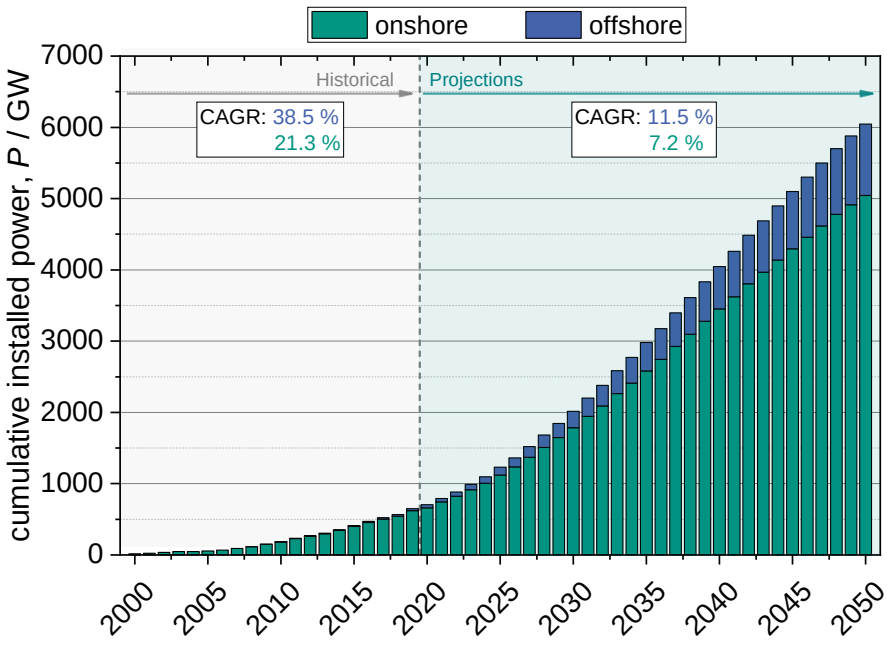

Figure 3.1: Cumulative installed global onshore and offshore windpower (data from[1, 2])

3.99 Eurocent $kW^{-1}\,h^{-1}$ to 8.23 Eurocent $kW^{-1}\,h^{-1}$. In the offshore sector, the margin is 7.79 Eurocent $kW^{-1}\,h^{-1}$ to 13.79 Eurocent $kW^{-1}\,h^{-1}$ [93]. Efforts are ongoing to further reduce these margins. A promising approach to further reduce the levelized cost of energy is the installation of turbines and plants with larger capacity [94]. There is a clear trend among manufacturers towards increasingly powerful systems. Figure 3.2 shows the development of the average offshore turbine capacity and wind farm size in the European Union over the last 20 years [3, 4]. The average onshore and offshore installed turbine capacity in the European Union in 2020 was 3.3 MW and 8.2 MW, respectively [95]. Several manufacturers are already working on turbine models with rated powers beyond 10 MW as it is stated in subsection 3.2.3.

According to [96], the fundamental relationship of the output power P of an electrical machine can be described as follows:

$$P = \pi^2 \cdot \alpha \cdot A_a \cdot B_{\delta,max} \cdot d_r^2 \cdot l_{ef} \cdot n_{rot} \tag{3.1}$$

with the relative pole width α, the electrical loading of the armature winding A_a, the maximum air gap flux density $B_{\delta,max}$, the outer rotor diameter d_r, the effective length l_{ef} and the mechanical rotational speed n_{rot}.

This results in three basic approaches for increasing the power of an electrical machine: The increase of the electrical loading and thus of the magnetic fields of the machine A_a and $B_{\delta,max}$, enlarging the construction volume d_R and l_{ef} or

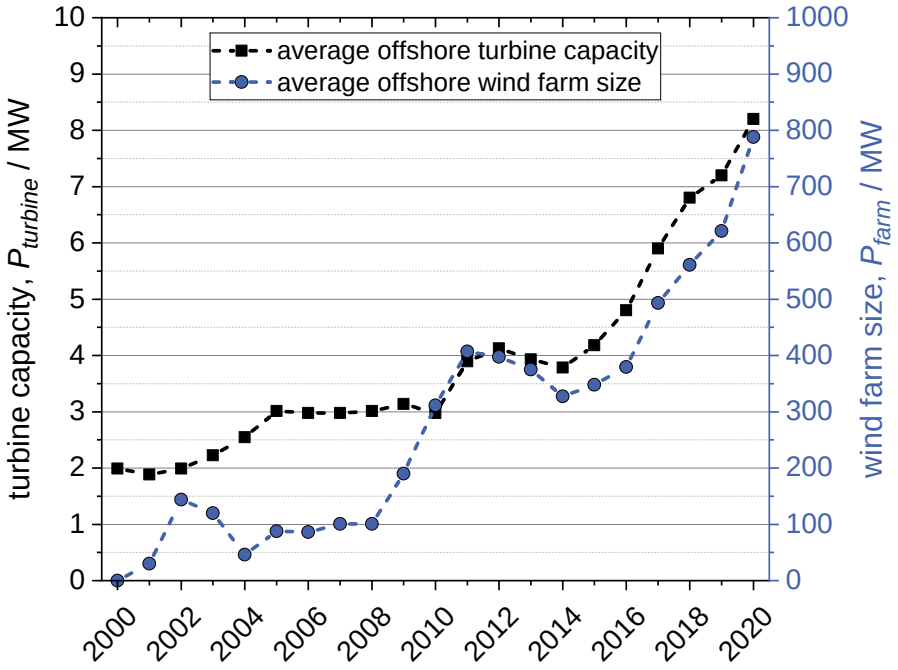

Figure 3.2: Average turbine capacity and wind farm size in the European Union (data from [3, 4])

increasing the rated rotational speed n_{rot}. In conventional electrical machines, the increase in rated power due to the influence of electrical loading is restricted by the physical limits of the ferromagnetic and resistive current-conducting materials. The application of superconducting materials with their very high current-carrying capacity enables designs that are beyond the electrical loading and magnetic flux density limits of conventional rotating machines. The extended design scope for electrical loading by superconductors enables wind turbines with reduced construction volume, weight and mechanical rotational speeds.

3.2 Conventional wind turbine systems

3.2.1 Drive train

According to equation 3.1, the nominal speed plays a central role for the design of the generator of a wind turbine. The ratio between the mechanical rotor speed n_r and the frequency of the electrical system f is defined by the number of magnetic poles in the electrical machine [97].

$$n_r = \frac{f}{p} \tag{3.2}$$

with the mechanical rotational speed n_r, the electrical frequency f and the number of pole pairs p.

The generator speed is determined by the design of the drive train, which can be divided into the two basic concepts of an intermediate gearbox or a direct drive coupling.

Gearbox

The rotational speed of the rotor blades of a multi-megawatt wind turbine is usually in the range of $6\,\mathrm{min}^{-1}$ to $20\,\mathrm{min}^{-1}$. In systems with gearboxes, these very slow rotational speeds are converted into rotational speeds more suitable for conventional generators. Typical gear ratios for high-speed generators consist of three to four gear stages and thus achieve generator speeds of $900\,\mathrm{min}^{-1}$ to $2000\,\mathrm{min}^{-1}$, which results in smaller and lighter generators [97]. However, this means that the gearbox has to absorb the high torques that occur and is therefore a mechanical wear part that has an increased susceptibility to errors and requires enhanced maintenance [98]. For the offshore sector in particular, the increased maintenance effort represents an additional challenge [99]. So-called medium speed systems offer a compromise by avoiding the maintenance-intensive high-speed gear stages. Generator speeds of $150\,\mathrm{min}^{-1}$ to $500\,\mathrm{min}^{-1}$ are usually achieved with only one to two transmission stages. But this also requires larger and heavier generators [100]. Moreover, the gear units themselves are sub components with increased space and weight requirements.

Direct drive

In direct drive (DD) configurations the shaft of the rotor blades is directly connected to the shaft of the rotor of the electrical rotating machine, resulting in very low mechanical rotational speeds for the electrical system. In order to obtain an acceptable frequency of the electrical system, the generator must be designed according to equation 3.2 with a significantly higher number of magnetic poles as the gearbox driven machines. The required number of poles of the electric machine consequently leads to an increase in the generator volume, weight and capital cost [101]. However, this is compensated by a more efficient and reliable gearless drive train. In addition, especially turbines with a power class of 7 MW and more achieve similar weights compared to combinations of high-speed generators with intermediate gearboxes [97].

3.2.2 Induction generators

In order to utilize the widest possible range of wind speeds, the resulting frequency fluctuations of the electrical system must be adapted to the fixed grid frequency

using appropriate converter systems. Due to the rapid advances in inverter technology, such variable speed systems are, especially for higher power ratings, today's standard. Thus, the individual components consisting of mechanical coupling, generator and inverter must be considered as a complete system. In principle, it is possible to connect induction generators to the grid by means of a full power inverter or a partial power inverter. However, the concept of the doubly-fed induction generator (DFIG) with a partial power converter is the most common drive train concept for induction generators.

Doubly fed induction generator

Induction generators represent a cost-effective alternative to the synchronous machines. Since these machines are usually designed as fast rotating generators, a gearbox with a corresponding transmission ratio is required. In the case of a doubly-fed induction generator (DFIG) system, the rotor windings are connected to the inverter either by means of slip rings or a rotating transformer. The basic configuration of a DFIG system is shown in figure 3.3. The stator is connected directly to the grid. This particular design allows the use of a simplified partial inverter that is only designed for about 30 % of the generator's rated power. However, this also limits the speed regulation by 30 % of the synchronous rotational speed [102]. In addition, the system enables independent active and reactive power regulation, similar to a synchronous generator [97]. In systems with full converters, the wind turbine is virtually decoupled from the grid by the converter. Due to the direct coupling of the stator to the grid, the doubly-fed induction generator is particularly susceptible to fault events [103].

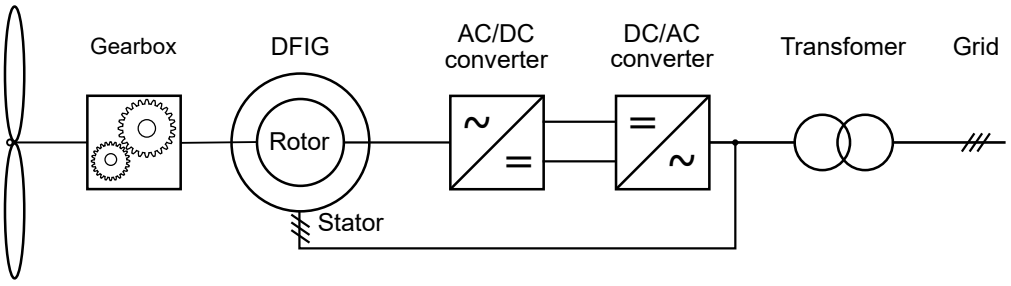

Figure 3.3: Doubly-fed induction generator wind turbine system

3.2.3 Synchronous generators

Synchronous generators in wind turbines are typically designed together with full power converters. The converter must therefore be able to carry the entire rated generator power, resulting in more complex and larger converter systems. However, the use of a full power converter allows speed control over a wide range. Synchronous machines can be realized with a gearbox or as a direct drive.

In particular, in the case of direct drive, the full inverter allows the generator frequency to be adapted to the grid frequency, thus keeping the number of pole pairs of the generator within an acceptable range. With regard to their excitation systems, synchronous machines can be divided into electrical excited synchronous generator (EESG) and permanent magnet synchronous generator (PMSG).

Electrical excited synchronous generator

For electrical excited generators, field coils are employed which are excited with direct current (DC) to generate the magnetic flux density in the air gap. The supply of the field coils on the rotor therefore requires slip rings or a rotating rectifier and causes additional losses in the coils. However, the electrical excitation of the rotor coils allows additional control for the adjustment of different operating points [102]. The three-phase stator coil system is coupled to the grid via the full power converter. Figure 3.4 shows the basic structure of the electrical excited synchronous generator (EESG). Especially as a direct drive, this machine concept means particularly heavy and large generators not at least because of the additional copper windings on the rotor. Electrical excited synchronous generator are generally 50 % heavier than corresponding generators with permanent magnets and face major challenges in terms of scalability to high machine outputs in the range of 10 MW and more [97].

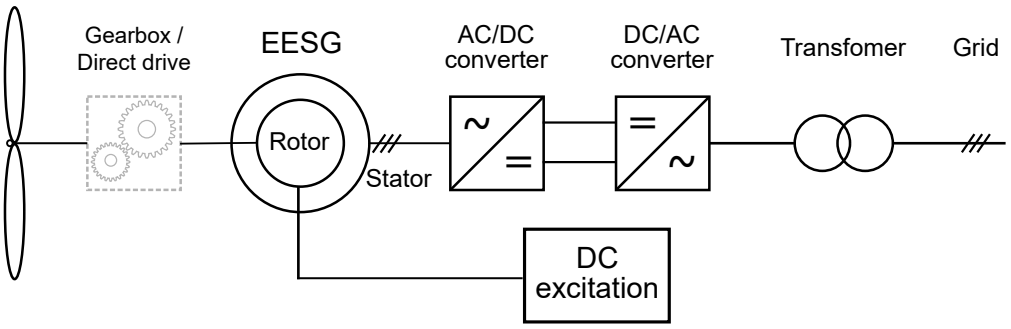

Figure 3.4: Electrical excited synchronous generator wind turbine system

Permanent magnet synchronous generator

The stator of the permanent magnet synchronous generator (PMSG) is basically similar to the electrical excited synchronous generator and is also connected to the grid via a full power converter in order to ensure the widest possible speed control range. The rotor, however, has permanent magnets to generate the magnetic flux density in the air gap. This eliminates the need for excitation devices, which makes these systems particularly low-maintenance [97]. The basic configuration is presented in figure 3.5. In addition, the losses of the copper exciter coils required for electrical excited synchronous generators are eliminated. At

present, permanent magnet synchronous generators (PMSG) represent the wind turbine generator class with the highest power density and at the same time very high efficiency and reliability, especially when designed as a direct drive [104]. Nevertheless, the high material requirement for rare earths and their volatile price in the past [105] represent a considerable cost item, which also makes PMSG the generator class with the highest capital cost at present [106].

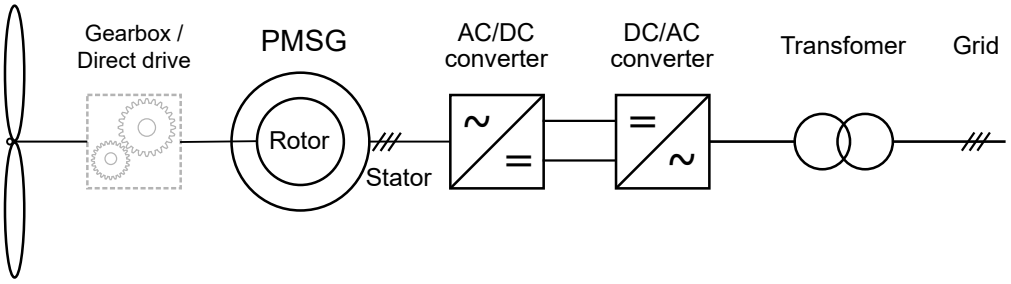

Figure 3.5: Permanent magnet synchronous generator wind turbine system

Market share and current turbine power ratings

Figure 3.6 shows the respective share of installed drive train technologies according to [10]. Whereas in the past, due to their low-cost and simple design, asynchronous machines, and in particular doubly-fed induction generators, accounted for the majority of installed offshore drive trains, a continuous decline in this technology is forecast for the coming decades. According to [10], permanent magnet synchronous generators (PMSG) will play an important role in the planning of new offshore wind farms. While high-speed geared drive trains will also play a minor role, medium-speed gears and direct-drive PMSG in particular are expected to account for an increasing share. Thus, there is a trend not only towards turbines with higher rated power, but also toward less complex mechanical drive trains and therefore towards larger and heavier generators.

In addition, table 3.1 lists the turbine models of the three largest wind turbine manufacturers with the highest rated outputs to date. Both prototype models with rated outputs well above 10 MW and their predecessor models ready for the market are shown. It can be seen that the use of turbines in the double-digit power range will already be possible in the near future.

It is also apparent that turbines in this power class are planned exclusively as permanent magnet synchronous generators (PMSG). Although the medium-speed drive train could play an important role in the future, superconducting generator concepts will be compared with the direct-drive PMSG in this work. The major disadvantage of having the largest and heaviest generators in direct-drive solutions can be overcome by using superconducting technologies. Thus, the use of superconductors could not only keep the simplified direct-drive trains, but at the same time enable greatly reduced generator sizes and masses.

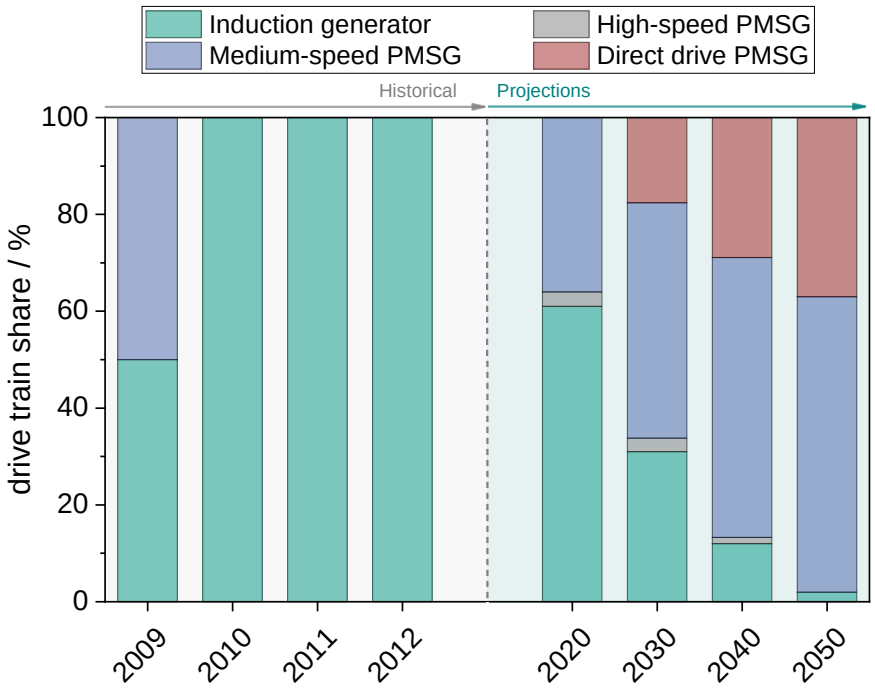

Figure 3.6: Share of different drive train technologies in the German offshore market (data from [10])

Table 3.1: Current turbine models with the highest power rating

Turbine	Power rating	Drive train	Generator type	Status	Ref.
SG 8.0-167 DD	8 MW	DD	PMSG	market-ready	[107]
SG 14.0-222 DD	14 MW	DD	PMSG	prototype (2021)	[5]
Haliade 150-6 MW	6 MW	DD	PMSG	market-ready	[108]
Haliade X-14 MW	14 MW	DD	PMSG	prototype (2020)	[6]
V164-10.0 MW	10 MW	medium speed	PMSG	market-ready	[109]
V236-15.0 MW	15 MW	medium speed	PMSG	prototype (2022)	[7]

3.3 Superconducting wind turbine systems

One of the first designs for a superconducting rotating machine can already be traced back to 1966 [110]. Since then, a number of design studies, prototypes and even real scale machines have been developed and presented. Due to the special conditions and requirements in direct drive wind turbines, increased research activity can be observed regarding the use of superconducting materials in such

systems. For superconducting generators (SCG) as well as for conventional machines with copper windings or permanent magnets, fundamental other machine topologies with axial or tangential directed magnetic flux directions are proposed. However, only radial flux machines will be discussed in this thesis. Nevertheless, the use of superconductors can also lead to new design approaches for radial flux machines.

3.3.1 General design approaches

In addition to the design requirements due to the necessary cryogenic cooling, special design options for electrically rotating machines regarding the usage of ferromagnetic materials and the stator and rotor configuration are feasible.

In wind power generators, the magnetic flux is mainly directed through ferromagnetic materials to keep the reluctance R_m of the magnetic circuit low. However, the use of these materials also represents an increase in weight and thus directly influences the power density of the overall system. The basic arrangement possibilities of the ferromagnetic material for conventional and superconducting machines are shown in figure 3.7.

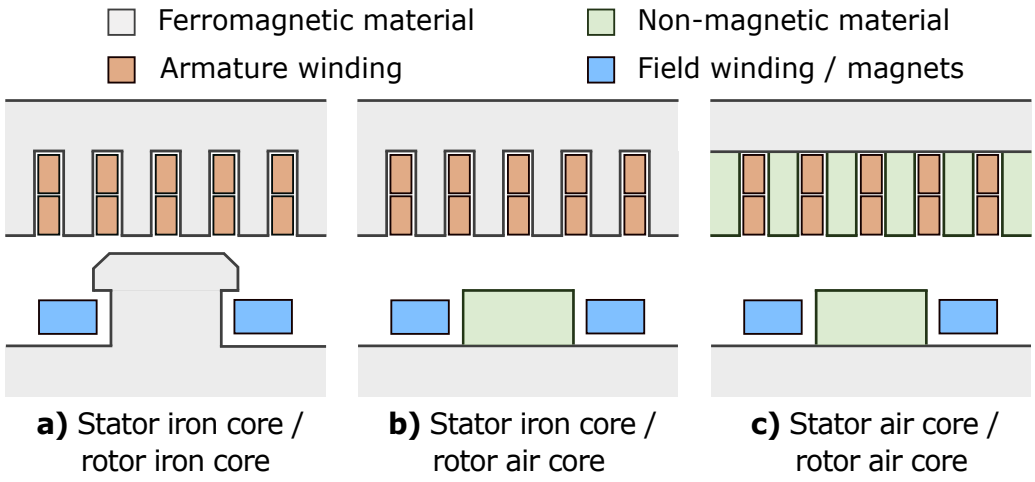

Figure 3.7: Different machine topologies applying ferromagnetic materials

In figure 3.7 a) a typical configuration of a electrical excited synchronous generator is shown. The armature winding is embedded in a slotted ferromagnetic structure while the excitation winding is arranged around a magnetic pole. This machine type is therefore defined as a salient pole machine. The pronounced pole shoe enables a reduction of the number of turns of the excitation winding and in addition absorbs a major part of the occurring electromagnetic forces, due to the resulting low field exposure of the winding.

Figure 3.7 b) represents a typical configuration of a permanent magnet synchronous generator. It is possible to embed the permanent magnets in the ferromagnetic

material or to mount the magnets directly on the surface of the iron while the armature winding is still embedded in a slotted structure.

In figure 3.7 c) a so called air gap or air core design is shown, where no slotted ferromagnetic structures are applied. This configuration uses either no iron or only a back iron topology to reduce leakage flux. While an air gap winding is usually not suitable for conventional machines due to the increased number of winding turns required, superconducting materials with their enhanced current-carrying capacity make this type of winding topology feasible. The absence of iron teeth makes it possible to build generators that are lighter and not limited by the iron saturation of the teeth, enabling designs even beyond the actual common air gap flux densities. By eliminating the slot, a much more homogeneous distribution of the magnetic flux density in the air gap with fewer harmonics is achieved and thus a more sinusoidal fundamental wave is formed. As a result, the torque ripple can be reduced by approximately 90 % compared to similar machine topologies [111]. Further a back iron topology allows a simpler thermal separation to the cryogenic temperature region and can thus be designed as a warm iron. Nevertheless, cold iron designs with ferromagnetic materials at cryogenic temperatures are also possible, but it must be taken into account that this configuration causes additional thermal mass and iron loss at the cryogenic level. Data for typical ferromagnetic materials in machine applications regarding permeability and losses at cryogenic temperatures can be found in [112, 113].
However, applying air gap windings results in increased mechanical and electromagnetic stress on the superconductor. In an air gap winding, the majority of the magnetic flux density is no longer conducted via the iron teeth, which causes a much higher field exposure to the windings of the machine. As a result, the electromagnetic forces are not only acting on the iron, but also have a stronger impact on the armature and field winding [114]. Therefore, both windings must be mechanically supported with additional non-magnetic support structures. Due to the lack of iron and the resulting increased reluctance R_m, more ampere-turns are required for the same air gap flux densities. In addition, according to section 2.2, the higher fields reduce the current-carrying capacity of the superconductor, which can lead, depending on the machine design, to 1.5 times to 34 times more superconducting material [111, 114–117]. Therefore, air gap windings enable promising design approaches with regard to reduced weight, lower harmonics and cryogenic system complexity but pose a particular economic challenge due to the high amount of superconductors.

In conventional wind generators, the stator houses the three-phase armature winding and the field windings or permanent magnets are usually found in the moving part of the machine as it is illustrated in figure 3.8 a). Thus, as already mentioned, for a permanent magnet synchronous generator no rotating excitation system is required. With electrical excited synchronous generators, only the direct current (DC) excitation power of the field coils and not the entire AC generator power must be transmitted. This avoids large slip rings or brush-less excitation systems on the rotating shaft. Furthermore, for an excitation system with brushes an additional slip ring is required when connecting a three-phase system which

has to withstand higher voltage ratings. As a result, the slip ring excitation system can be simplified by placing the field coils on the rotor. Moreover, the design of the stationary armature winding in terms of insulation, cooling and mechanical support is simplified.

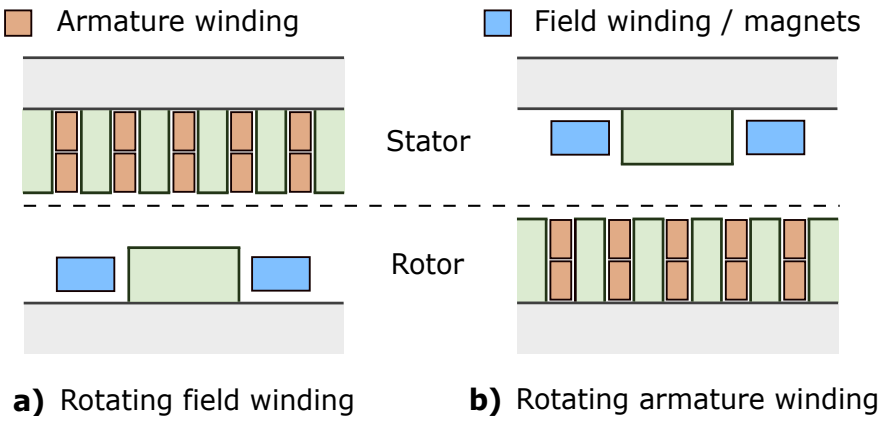

Figure 3.8: Rotating field winding and rotating armature winding concepts

For superconducting generators, rotating superconducting materials imply the need for a rotating cryogenic cooling system. In [118] it is claimed that the realization of a rotating cryogenic system represents a greater effort than applying a rotating armature system. In addition, a stationary cryogenic cooling system can be based on already proven technologies in medical imaging. Therefore, some designs with stationary field coils and a rotating armature winding as it is shown in figure 3.8 b) were presented [17, 18, 119–121]. Especially for small superconducting machine prototypes, this machine configuration is an interesting alternative due to the simplified cryogenic system. However, a rotating armature winding is also a viable alternative for large machine outputs. For slow rotating machines such as direct-drive wind generators the slip ring system for rotating armature winding is already technically feasible. In [19], a system based on a hydro power generator for a 10 MW wind turbine at a speed of 10 min is introduced, that shows losses of just 4.6 kW with a brush-life of over 5 years. Nevertheless, machine designs with a rotating cryogenic system have already been presented and technically implemented even for higher power ratings. For the coupling between the stationary and the rotating part of the cooling system, rotating seals based on a ferrofluid are used [122, 123]. Thus, the design with rotating field coils and cryogenic system represents the larger part of the investigated superconducting machines.

3.3.2 Partial and fully superconducting generators

Superconducting rotating machines can be further divided into partial and fully superconducting machines. In a partial superconducting machine, preferably only the field coils or the permanent magnets are superconducting, while the armature

winding is still made of normal conducting material such as copper. In fully superconducting machines, the armature winding is additionally superconducting.

According to section 2.2, superconducting materials do not show DC resistance as long as they are operated below their critical parameters. The use of superconducting field coils excited with DC, which corresponds to an electrical excited synchronous generator, therefore represents the majority of the investigations published. American superconductor developed the design of a 10 MW superconducting generator and tested a full-scale HTS field coil at 77 K and 30 K [124]. The Innwind project investigated possible generator designs for the 10 MW and 20 MW power classes including a superconducting machine concept. A magnesium diboride (MgB_2) coil consisting of 10 double pancakes and a ReBCO coil consisting of three single pancakes were tested under different temperature conditions [125, 126]. In the SupraPower project, the design of a 10 MW generator with MgB_2 field coils was presented. The coils were cooled to the operating temperature of approximately 20 K in a modular cryostat setup. Two full scale coils including the cryogenic cooling system were mounted on a rotating test rig called the magnetic rotating validator [127]. In 2018, the EcoSwing project succeeded in connecting the first superconducting wind generator to the grid. The direct-drive generator with a rated power of 3.6 MW has 40 HTS field coils mounted on its rotor. The superconducting coils are cooled by a total of nine co-rotating coldheads to the operating temperature of approximately 20 K. In total, the generator was able to deliver 600 MW h of power to the grid over a operating period of 650 h, thus raising the technology readiness level of partial superconducting wind generators to a value between six and seven [128, 129].
In addition to the use of superconducting field coils, the excitation field can also be generated by superconducting permanent magnets. In [130, 131] it is reported how magnetic fields are trapped in superconducting bulks or stacked tapes to act as permanent magnets reaching maximum values of almost 18 T. The use of such technologies in superconducting rotating machines corresponds to the machine concept of a permanent magnet synchronous generator. Although in principle very high magnetic flux densities and the omission of a rotating excitation system would be possible, the application of this technology in rotating machines still faces major challenges. Magnetization must take place via an external magnetic field generated by the armature winding or a separate coil in the cryogenic state. In addition, the superconducting permanent magnets experience a continuous degradation of their generated magnetic flux due to the time-varying fields in rotating machines [132]. Some conceptual design studies on wind generators with superconducting permanent magnets have been carried out [133, 134] and a few small prototype machines have been presented [135, 136].

With the additional use of superconducting materials in the armature winding, electrically rotating machines with extremely high efficiencies and power densities are theoretically possible. Since in such machines both stator and rotor must have a cryogenic cooling system, only the configuration of a rotating superconducting field winding or respectively magnets and a stationary armature winding is practical for a fully superconducting machine. The greatest challenge in the

implementation of superconducting armature windings is the alternating current (AC) losses that occur in the cryogenic system [9]. Thus, for a technical realization, a conductor with reduced AC losses must be selected. One possibility is the use of magnesium diboride (MgB_2) which, due to its thin multi-filament structure, has much lower AC losses than wide and flat ReBCO tape. To keep the AC losses of ReBCO tapes as low as possible, particularly narrow tapes with a width of only 2 mm can be used. Furthermore, a multi-filamentary structure can be applied to the tape by laser scribing [137]. Another approach is to design the cryogenic systems for the stator and rotor separately and thermally insulated from each other. This not only offers the possibility of different cryogenic operating temperatures, but also of selecting conductor materials for the stator and rotor that are better suited to the respective requirements [138]. Although some design studies of fully superconducting wind generators have been presented, a working prototype has not yet been reported. Nevertheless, due to the high potential of fully superconducting machines, a growing research interest can be observed.

Figure 3.9 summarizes the different possible concepts of superconducting machines according to the aforementioned design approaches and highlights the machine type which is investigated in this thesis.
A partial superconducting machine with stationary superconducting field coils and a normal conducting three-phase rotating armature winding is further investigated in this work. The stator and rotor windings are designed as air gap windings with a back iron. Although fully superconducting machines have great potential in terms of power density, such a design presents significant challenges in terms of designing and realizing a prototype since this approach is still at an earlier stage of development. Rather, as a first step, a division into sub-topics, such as the investigation of a prototype coil with respect to AC losses or a only theoretical design of such machines, is more promising. Additionally, a decision is made to investigate an air gap winding concept because of the promising design approaches regarding reduced weight, lower harmonics and reduced cryogenic system complexity. Furthermore, a concept with stationary superconducting excitation coils allows the investigation of a prototype machine without the need for a complex rotating cryogenic cooling system. Moreover, for space reasons, the selected cooling concept of direct cryogenic cooling presented in more detail in subsection 3.3.3 can only be practically realized on a rotor, for generators of higher power classes and with rotor diameters of several meters.

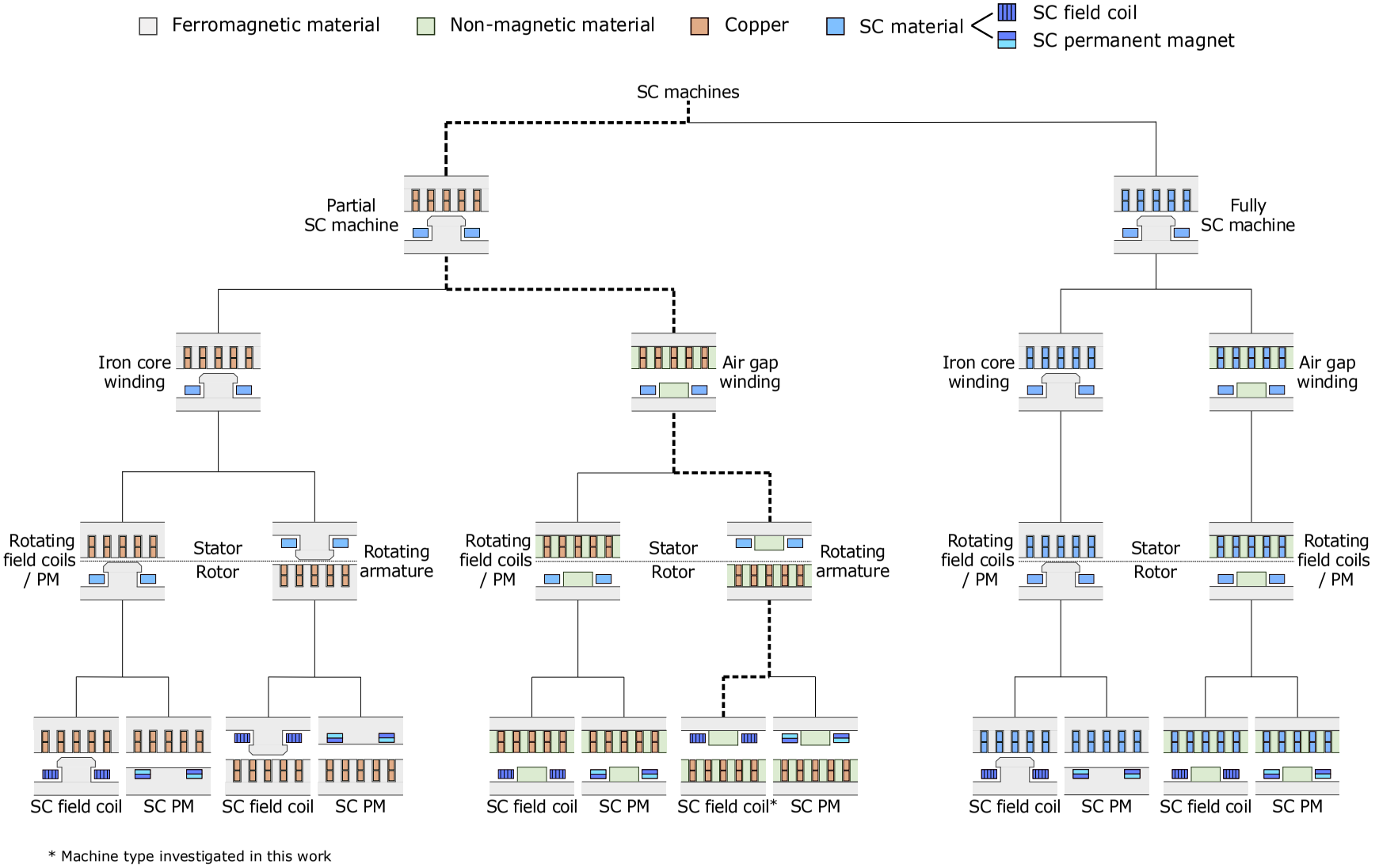

Figure 3.9: Design concepts of partial and fully superconducting machines

3.3.3 Cryogenic cooling concepts

Cryogenic cooling can basically be divided into two major approaches of an open and closed cooling cycle. Firstly, an open cooling cycle uses the latent heat of vaporization to evaporate a cryogenic fluid at its boiling point in an isothermal process. The produced vapor is released directly into the atmosphere. If the system continues to exchange heat with the gas, the change in enthalpy can also be used for cooling until the gas reaches room temperature. A typical example of an open cooling cycle is the AmpaCity project, where a superconducting transmission line is cooled with evaporating liquid nitrogen [139]. However, for handling reasons and depending on the respective requirements, an open cooling cycle is not suitable for every application. Furthermore, a continuous supply of cryogenic fluid must be ensured, which is a particular challenge for remote offshore systems.

In table 3.2 cryogens and their physical cooling properties which are basically suitable for the required temperature range in rotating superconducting machines are listed [140].

Table 3.2: Physical cooling properties and evaluation of cryogens suitable for cooling of superconducting rotating machines (data from [140])

	Helium (He)	Hydrogen (H_2)	Neon (N)	Nitrogen (N_2)
Physical cooling properties				
Boiling point (K)[1]	4.22	20.34	27.06	77.24
Latent heat of vaporization ($kJ\,kg^{-1}$)	20.82	445.9	24.56	198.9
Enthalpy difference vapor ($kJ\,kg^{-1}$)[2]	1542.7	3509.0	282.96	234.6
Evaluation for use in superconducting rotating machines				
Temperature	-	++	++	--
Cooling capacity	-	++	--	+
Safety	0	--	0	0
Cost	--	++	-	++

[1] At atmospheric pressure
[2] Boiling point to room temperature at 300 K

Further, the cryogens are evaluated regarding their application in superconducting rotating machines in terms of cooling properties, safety and cost. Due to the increased magnetic flux density in electrical machines and the resulting reduced current carrying capacity of superconducting materials, hydrogen (H_2) and neon

(N) with boiling temperatures at about 20 K and 27 K represent the most suitable candidates in terms of temperature range. Although the current carrying capacity of HTS is significantly greater at the helium (He) boiling temperature of approximately 4 K, the very low temperatures also represent increased demands on the cryogenic cooling system in terms of insulation and efficiency. The boiling temperature of nitrogen (N_2) is the least suitable due to the greatly reduced current carrying capacity at high field exposure at this temperature. In terms of cooling capacity, hydrogen has the greatest potential with a very large latent heat of vaporization, while nitrogen can still absorb less than half of the energy at its boiling point. Helium and neon both have a relatively low latent heat of vaporization, but neon also requires much less energy for the enthalpy change when heated further to room temperature. All cryogens exhibit a liquid to gas expansion ratio of 700 or more and therefore require safety measures to prevent a sudden increase in pressure. In addition, hydrogen has an increased risk of explosion. At only a few cents per liter, nitrogen and hydrogen represent a very cost-effective cryogenic cooling option, while neon and helium are significantly more expensive.

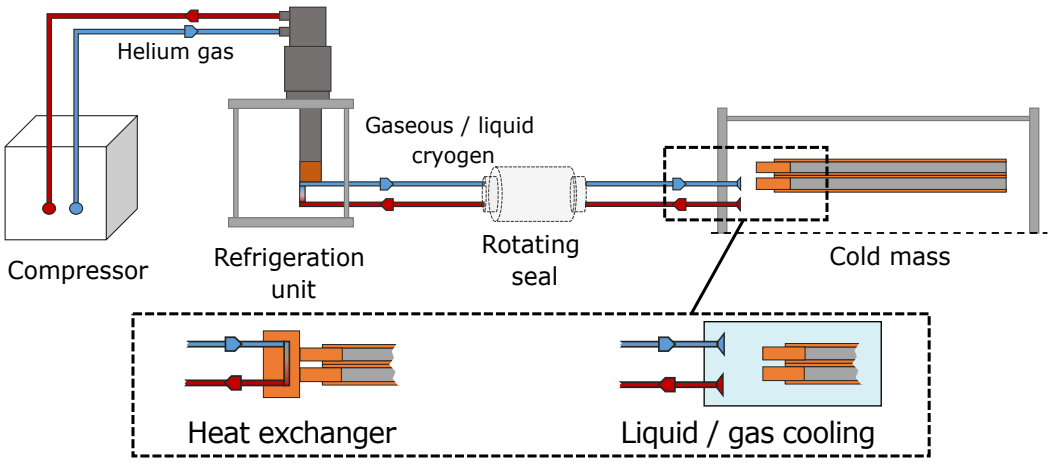

a) Remote cryogenic cooling

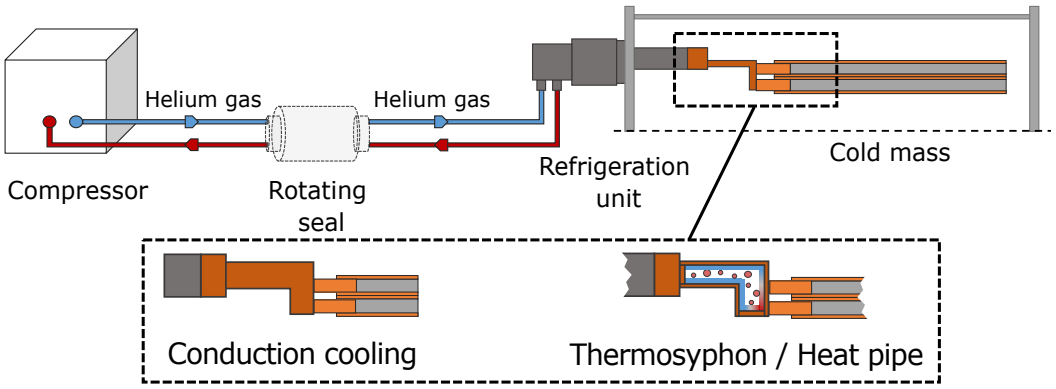

b) Direct cryogenic cooling

Figure 3.10: Remote and direct cryogenic cooling concept

A more suitable approach for cryogenic cooling of most superconducting rotating machines is a closed cooling cycle. In this case, the cryogenic fluid is not evaporated to the atmosphere or no cryogenic fluid is used in the cooling process at all. Closed cooling cycles can be further divided in a remote or direct cryogenic cooling concept [141].

In remote cryogenic cooling, heat is removed from the generator with a gaseous or liquid cryogen. To ensure closed-loop operation, the gas produced or warmed up is re-liquefied via a refrigeration unit that is located separately from the actual cold system. The components to be cooled can be in direct contact with the cryogenic gas or fluid or thermally connected by means of a heat exchanger. The basic configuration of a cryogenic remote cooling concept is shown in figure 3.10 a).
In direct cryogenic cooling, as it is illustrated in figure 3.10 b), the refrigeration unit is located close to the mass to be cooled while the compressors based on oil lubrication are still separated from the actual cold system. A thermal connection between the cold finger of the refrigerator and the cold mass is achieved by a conductive connection through materials with good thermal conductivity. In addition, thermosyphons or heat pipes specially designed for cryogenic temperatures [142] can be used for better thermal connection.

For compact machines where the space of a direct installation of the refrigeration unit is limited, the remote cooling concept is preferred. However, this requires an additional cryostat for the separate refrigeration unit and the supply lines to the actual system, which can lead to an increased heat input into the cryogenic environment. In case of fast rotating cryogenic systems, a remote concept is also more suitable, since the cooling performance of the rotating refrigeration units can be reduced by the high rotational speeds. However, the rotating seal in this cooling concept must also be designed for the cryogenic temperatures of the passing gases or fluids [122].
For large rotating machines, such as direct drive wind generators, a direct cooling concept can be implemented due to the increased installation space available. In the case of a rotating cryogenic system, the operation of the refrigeration units is only slightly affected by the slow rotational speeds. Helium gas circulates between the compressor and the refrigeration unit and is alternately compressed and expanded. Since the cryogenic temperatures only occur directly at the refrigeration unit and the helium gas stays above cryogenic temperatures, such systems are classified as cryogen-free. As a result, no rotating seals specially designed for cryogenic temperatures are needed.

In this work, a direct, cryogen-free cooling concept is chosen, in which the thermal connection is realized by conduction cooling. A more detailed description of the cryogenic system design for the machine prototype under consideration is given in section 4.2.

3.4 Comparison of conventional and superconducting wind turbine systems

Partial and fully superconducting generators are compared only with direct drive (DD) permanent magnet synchronous generators (PMSG) in the following, since superconductors can enable simplified drive trains and compact and lightweight generators at the same time. The use of superconducting materials in wind generators offers several advantages over conventional generator technology. While permanent magnet synchronous generators achieve rated efficiencies of almost 98 %, superconducting machines can even achieve theoretical efficiencies of over 99 % due to the elimination of copper losses [9]. However, the superconducting components must be kept continuously at cryogenic temperature, since it is not feasible to switch the cryogenic cooling system on and off quickly. Thus, the cryogenic system also causes losses in weak or no wind situations. It should also be mentioned that the only large-scale superconducting wind generator to date achieves a rated efficiency of just 92 %. In [129] it is reported that the low efficiency is caused by a design decision towards lower costs.

Another aspect in the comparison with permanent magnet synchronous generators is the consumption of rare earths. As with permanent magnets, the production of superconducting tapes also requires these raw materials. While permanent magnets mainly use neodymium and dysprosium, second-generation HTS tapes, for example, consist mainly of Yttrium. A comparison between direct drive permanent magnet synchronous generators and direct drive superconducting generators (SCG) regarding these materials is given in [10] and listed in table 3.3. Moreover a future consumption with a calculated improvement in the manufacturing process of permanent magnets is considered. Due to the fact that the superconducting layer of HTS tapes is only a few micrometers thick, direct drive superconducting generators require only 0.2 % of rare earths compared to direct drive permanent magnet synchronous generators, even assuming future optimized production of the permanent magnets.

Table 3.3: Demand of rare earths in direct drive permanent magnet synchronous generators and direct drive superconducting generators (data from [10])

Generator type	Mineral	2013 ($kg\,MW^{-1}$)	2025 ($kg\,MW^{-1}$)	2050 ($kg\,MW^{-1}$)
DD PMSG	Neodymium	201.5	162.5	130.0
	Dysprosium	15.0	11.7	11.7
DD SCG	Yttrium	0.3	0.3	0.3

The main advantage of using superconducting technologies in wind power systems is the increased power density of the generators. In order to better quantify the improved power density, an extensive literature review is performed regarding

the design data of direct drive permanent magnet synchronous generators and direct drive partial and fully superconducting generators. The data collected on the three different generator types is summarized in table 3.4. The rated torque as a function of the generator mass and volume for the three different types is shown in the figures 3.11 and 3.12 respectively. It can be seen that the values for torque per mass and torque per volume can vary greatly depending on the generator design. For example, even a permanent magnet synchronous generator (PMSG) design achieves a maximum value of 49.76 kN m t^{-1}. Nevertheless, the PMSG have an average value of about 35 kN m t^{-1}, while the partial superconducting generators show an average value of 79 kN m t^{-1}, which is more than twice as high. The difference in the torque to volume ratio is even more significant, at 92 kN m m^{-3} and 444 kN m m^{-3} respectively. By using superconducting materials also in the armature winding, the torque-to-weight ratio can be more than doubled again to an average value of 204 kN m t^{-1} compared to partial superconducting machines. The design with the highest rated power of 20 MW has a mass of only 167.5 t. The torque to volume ratio for fully superconducting generators (SCG) is 736 kN m m^{-3} on average and cannot be increased to the same extent as the torque to weight ratio compared to partial SCG.

However, such scaling effects only occur with turbines of higher power classes. In [143] it is reported that a higher power density compared to conventional turbines is only achieved with power classes of more than 3 MW. It is further stated that a possible break-even point is expected only at power classes of 6 MW and higher.

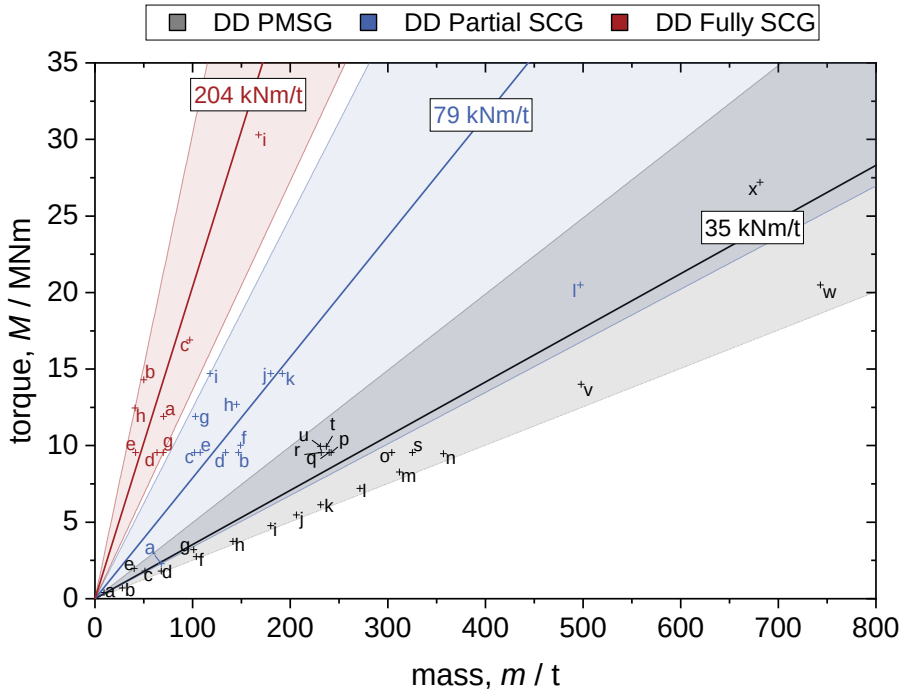

Figure 3.11: Rated torque as a function of generator mass for direct drive permanent magnet synchronous generators, partial and fully superconducting generators from table 3.4

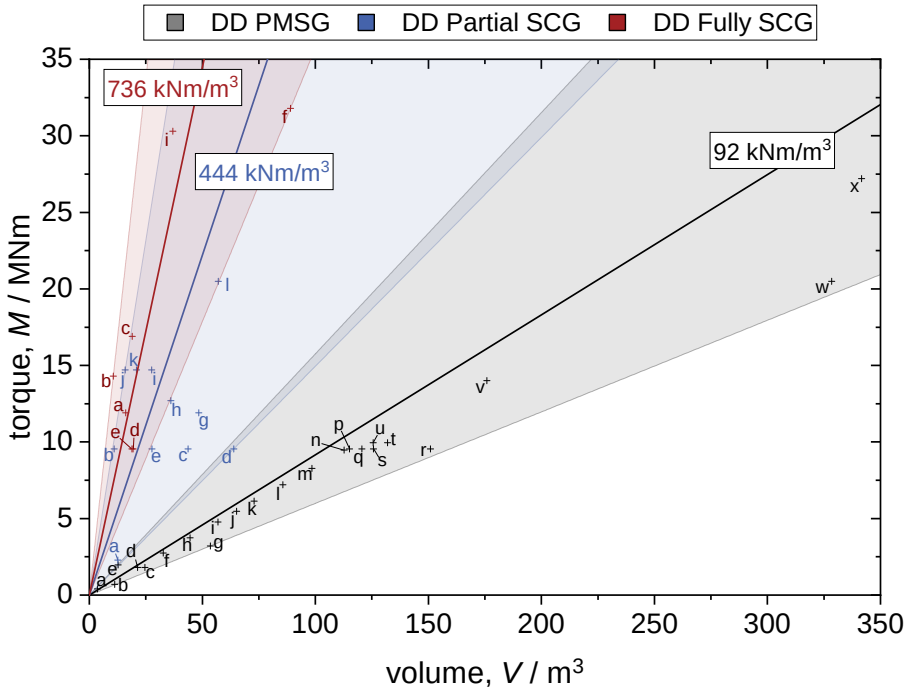

Figure 3.12: Rated torque as a function of generator volume for direct drive permanent magnet synchronous generators, partial and fully superconducting generators from table 3.4

Table 3.4: Data from direct driven PMSG, partial and fully superconducting wind generators

	Power (MW)	Torque (MN m)	Speed (min)	Mass (t)	Volume (m^3)	Armature/field winding	Torque per mass ($kN\,m\,t^{-1}$)	Torque per volume ($kN\,m\,m^{-3}$)	Ref.
					DD PMSG				
a)	0.75	0.25	28.60	9.37	3.61	Cu/PM	26.68	69.30	[144]
b)	1.50	0.70	20.50	27.92	11.22	Cu/PM	25.07	62.37	[144]
c)	3.00	1.80	16.00	51.06	24.54	Cu/PM	35.25	73.34	[144]
d)	3.00	1.80	15.92	67.83	21.35	Cu/PM	44.23	140.53	[143]
e)	2.00	1.97	17.90	40.20	12.70	Cu/PM	49.76	157.58	[143]
f)	4.00	2.75	13.89	103.63	32.67	Cu/PM	38.60	122.42	[143]
g)	5.00	3.20	14.80	101.05	53.49	Cu/PM	31.67	59.83	[144]
h)	5.00	3.75	12.73	141.32	44.58	Cu/PM	35.38	112.15	[143]
i)	6.00	4.78	11.98	180.18	56.93	Cu/PM	33.30	105.40	[143]
j)	7.00	5.48	12.21	206.38	65.20	Cu/PM	33.92	107.36	[143]
k)	8.00	6.13	12.46	231.13	72.90	Cu/PM	34.61	109.74	[143]
l)	9.00	7.20	11.94	271.32	85.67	Cu/PM	33.17	105.04	[143]
m)	10.00	8.23	11.54	311.94	98.46	Cu/PM	32.06	101.56	[143]
n)	11.00	9.47	11.09	356.95	112.69	Cu/PM	30.82	97.61	[143]
o)	10.00	9.54	10.00	304.00	-	Cu/PM	32.89	-	[145]
p)	10.00	9.55	10.00	241.97	115.15	Cu/PM	39.47	82.94	[144]
q)	10.00	9.55	10.00	240.00	120.64	Cu/PM	39.79	79.16	[101]
r)	10.00	9.55	10.00	231.70	150.96	Cu/PM	41.22	63.26	[115]
s)	10.00	9.55	10.00	325.00	125.66	Cu/PM	30.77	79.58	[146]
t)	10.00	9.95	9.60	236.97	131.95	Cu/PM	41.99	75.41	[147]
u)	10.00	9.96	9.60	231.00	125.54	Cu/PM	43.12	79.33	[148]
v)	14.00	14.00	10.00	498.00	175.93	Cu/PM	28.11	79.85	[146]
w)	15.00	20.50	7.00	743.00	328.43	Cu/PM	27.59	62.42	[149]
x)	20.00	27.20	7.00	681.20	341.62	Cu/PM	39.93	79.62	[144]
					DD Partial SCG				
a)	3.60	2,29	15,00	68.00	12.61	Cu/HTS	33.70	181.56	[129]
b)	10.00	9.54	10.00	147.00	11.03	Cu/HTS	64.90	864.84	[145]
c)	10.00	9.55	10.00	102.00	43.72	Cu/HTS	93.63	218.45	[150]
d)	10.00	9.55	10.00	133.80	63.90	Cu/HTS	71.38	149.45	[115]
e)	10.00	9.55	10.00	107.80	27.76	Cu/HTS	88.59	344.03	[115]

Table 3.4: Data from direct driven PMSG, partial and fully superconducting wind generators

	Power (MW)	Torque (MN m)	Speed (min)	Mass (t)	Volume (m^3)	Armature/field winding	Torque per mass ($kN\,m\,t^{-1}$)	Torque per volume ($kN\,m\,m^{-3}$)	Ref.
f)	10.50	10.02	10.00	149.09	-	Cu/HTS	67.21	-	[151]
g)	10.00	11.90	8.00	103.00	48.40	Cu/HTS	115.53	245.84	[152]
h)	12.00	12.70	9.00	145.00	36.03	Cu/HTS	87.59	352.48	[153]
i)	12.30	14.70	8.00	118.00	27.65	Cu/HTS	124.58	531.72	[154]
j)	12.30	14.70	8.00	180.00	15.87	Cu/HTS	81.67	926.54	[155]
k)	12.30	14.70	8.00	192.00	20.79	Cu/HTS	76.56	707.21	[155]
l)	15.00	20.5	7.00	497.00	57.02	Cu/HTS	41.25	359.52	[149]
					DD Fully SCG				
a)	10.00	11.90	8.00	70.10	16.12	HTS/HTS	169.76	738.38	[156]
b)	15.00	14.30	10.00	50.00	10.60	HTS/HTS	286.00	1348.69	[157]
c)	15.00	16.90	8.50	97.20	18.94	HTS/HTS	173.87	892.11	[138]
d)	10.00	9.55	10.00	63.60	19.35	MgB_2/HTS	150.16	493.48	[115]
e)	10.00	9.55	10.00	41.65	18.85	MgB_2/HTS	229.29	506.64	[158]
f)	20.00	31.80	6.60	-	89.04	MgB_2/HTS	-	357.15	[159]
g)	10.00	9.55	10.00	70.00	-	MgB_2/MgB_2	136.43	-	[160]
h)	10.00	12.46	8.00	41.00	-	MgB_2/MgB_2	303.78	-	[161]
i)	20.00	30.30	6.30	167.50	37.00	MgB_2/MgB_2	180.90	818.87	[162]

4 Design of a 10 kW generator technology demonstrator

In the following chapter, the electromagnetic, thermal and mechanical design of the generator technology demonstrator developed in this work is presented. Figure 4.1 shows an illustrated sectional view of the demonstrator with its main components. According to section 2.3 and 3.3, the generator can be classified as a partial superconducting synchronous generator with stationary superconducting field coils and a rotating, normally conducting armature winding. Furthermore, the superconducting field coils are designed as no insulation windings. The superconducting components are cooled by a direct, conduction cooled cryogenic cooling system in the stator of the machine. In addition, it is an air gap winding with a warm stator and rotor back iron and no distinct ferromagnetic teeth.

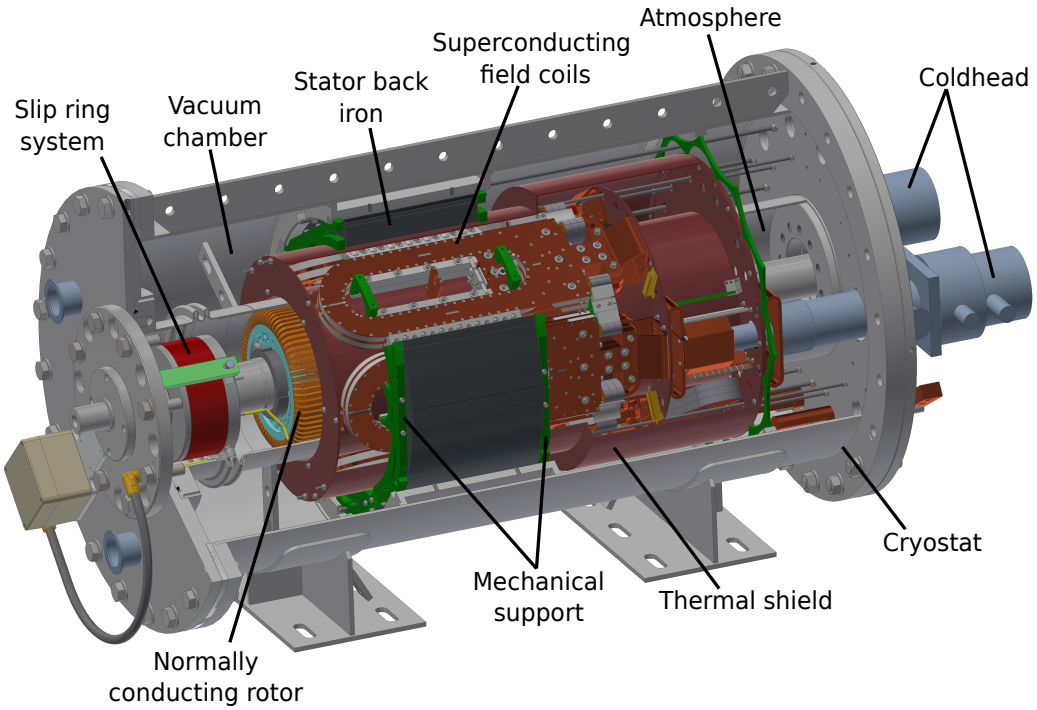

Figure 4.1: Illustrated sectional view of the generator demonstrator with its main components

4.1 Electromagnetic design

A basic electromagnetic design of the 10 kW generator demonstrator was first introduced in [163]. The first design proposal is based on a DC machine with a superconducting coil design using 4 mm wide HTS tape. In table 4.1 the main design parameters of the former design are listed.

Table 4.1: Main parameters of the generator design from [163]

Parameter	Value	Unit
Rated power	10	kW
Rated voltage	230	V
Rated stator excitation current	147	A
Rated speed	389	min
Rated torque	250	N m
Pole pairs	3	–
Superconducting pancakes per pole	4	–
Superconducting tape width	4	mm
Total length superconducting tape	3.2	km
Outer diameter stator iron	486	mm
Thickness stator iron	30	mm

The machine design is in principle based on the originally presented design, with a six-pole superconducting field coil system in the stator of the machine. However, the design of the generator technology demonstrator presented in this work features fundamental changes with regard to the used HTS tape and the machine type, which is modified to a partial superconducting synchronous machine. The HTS is changed to a 12 mm wide tape due to the following reason. The decision to a larger width of the superconducting tape is decreasing the number of windings. While the former design was using four pancake windings per stator pole, the revised design consists of two pancake windings per pole. This decreases the length of tape in the superconducting coils from 3.2 km to 1.2 km and therefore the manufacturing effort for the superconducting coils. To reach the same flux density distribution in the machine, the lower winding number has to be compensated by a higher excitation current I_{ex} supplied to the stator system. Since the machine design is based on an almost stationary stator field and the superconducting coils are supplied by a DC current, AC losses in the HTS tapes are negligible. In [164, 165] the effect of lower AC losses in the superconductors at smaller tape widths is explained, but due to the generally stationary field conditions a design with a larger tape width is chosen.

The normally conducting rotor is a special design manufactured from the company *Antriebssysteme Faurndau* [166] and an illustrative sectional view of its main components is given in figure 4.2. The three-phase system of the rotor is electrically contacted with the stationary part via slip rings. It is designed as a Y-connection with 3 parallel groups and the coils are arranged as double layer windings. The rotating part of the machine is located on the atmospheric side in the inner bore of the stator cryostat and no additional cooling system is provided. The rotor shaft is supported by a floating bearing and a locating bearing, which are attached to the two cryostat lids respectively. The rotor back iron has a maximum outer diameter of 190 mm over the effective length l_{ef} of the machine. Towards the coil terminals, the diameter of the iron is gradually reduced. The normal conducting rotor windings are fixed with non-magnetic mechanical supports.

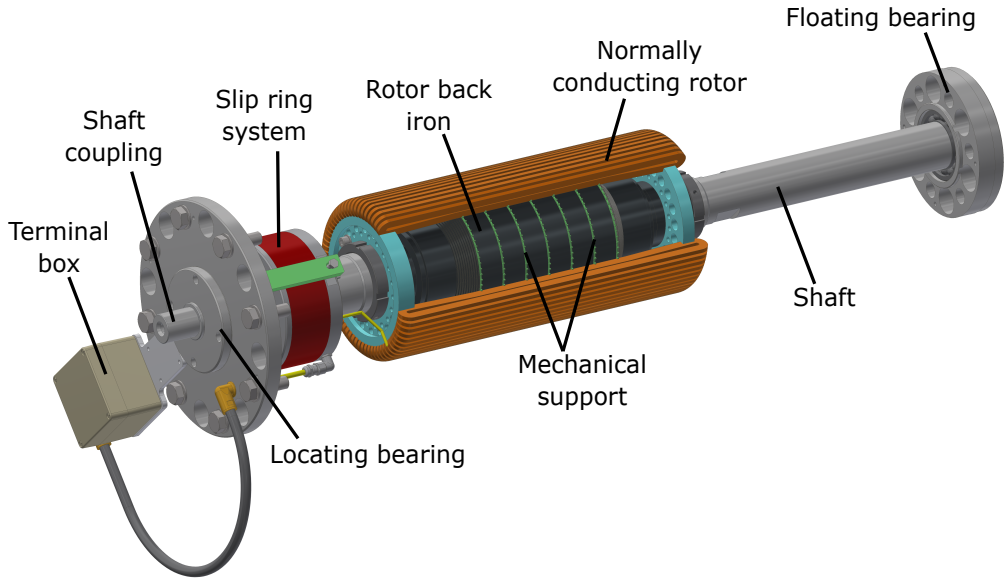

Figure 4.2: Illustrated sectional view of the rotor with its main components

A cross-sectional view of the electromagnetic design of the generator with its main components is shown in figure 4.3. The superconducting field coils are located in the stationary part of the machine and are described in more detail in chapter 5. Accordingly, the outer and inner cryostat walls are encompassing a vacuum atmosphere with the superconducting stator system inside. To minimize leakage flux and improve the machine performance a stator back iron with a thickness of 40 mm and a total length of 240 mm is guiding the magnetic flux of the stator. The stator iron is designed as stacked sheets with the designation M235-35A and is realized as a warm iron, since it is attached to the room temperature region of the system. Nevertheless, the iron can be located inside the cryostat, to avoid that the outer cryostat wall is interrupting the overall magnetic circuit and is increasing the reluctance R_m. Furthermore, the six-pole coil system is surrounded by a thermal shielding and a multilayer insulation (MLI) to reduce the radiative heat load. A further description of the thermal shield with MLI can be found in subsection 4.2.4.

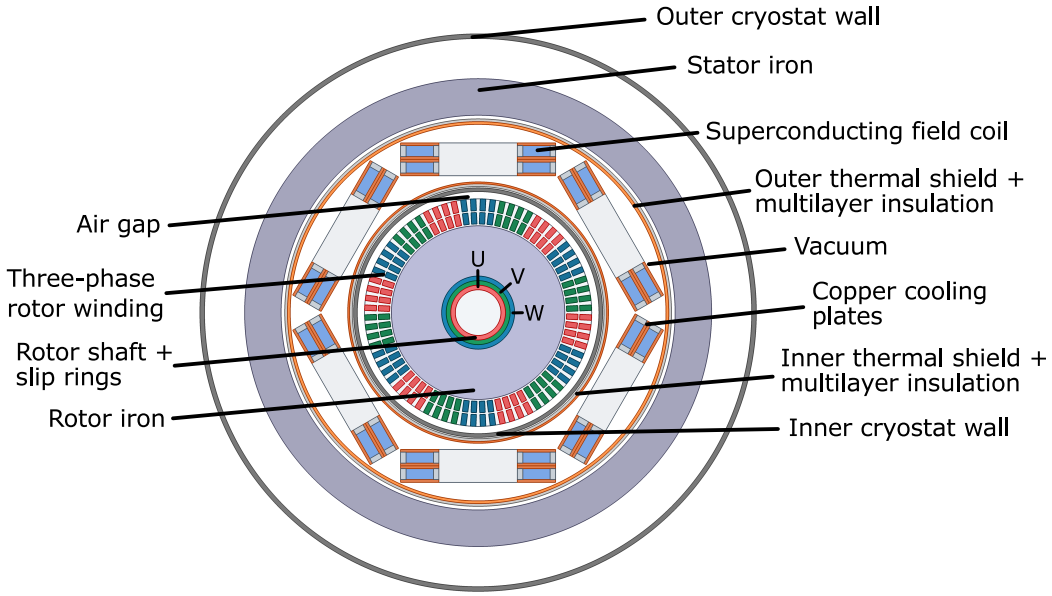

Figure 4.3: Cross-sectional view of electromagnetic design of the generator demonstrator

In figure 4.4 the radial magnetic flux density $B_{\delta r}$ and the tangential magnetic flux density $B_{\delta t}$ in the middle of the air gap for the rated excitation current I_{ex} of 450 A are plotted.

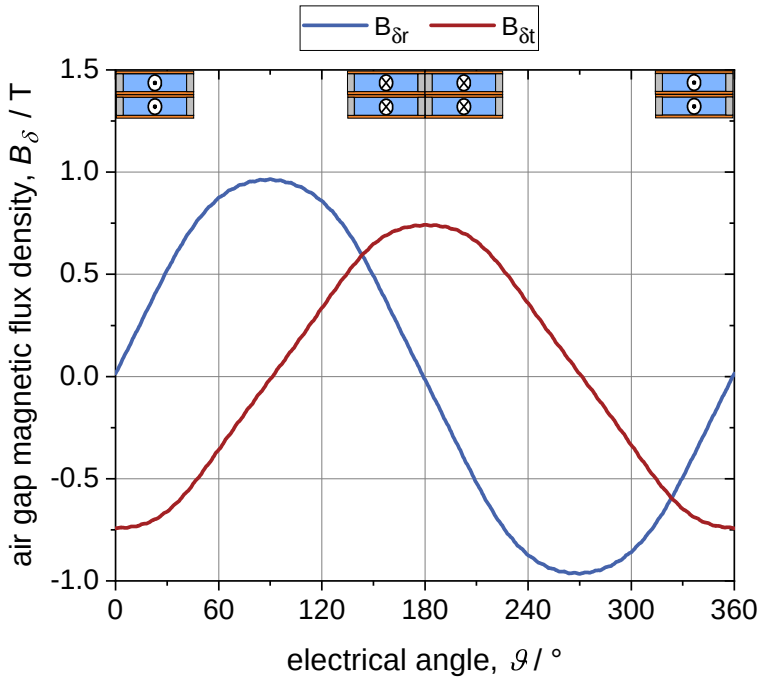

Figure 4.4: Radial and tangential magnetic flux density in the middle of the air gap at rated excitation current plotted over two poles

To reach the required performance of the generator with the changed stator system, the magnetic flux density distribution in the machine and especially the magnetic flux density in the air gap B_δ have to be similar to the former design. The electromagnetic calculations for the generator demonstrator are based on a two-dimensional (2D) transient finite element model, solved with the software *Ansys Maxwell* [167]. The flux density is depicted over two stator poles with an average rated flux density of 0.63 T.

In figure 4.5 a) the phase voltage U_{phase} is plotted at variable excitation current and constant rated rotational speed n_{rot} of 389 min under no load conditions. Up to the rated excitation current I_{ex} of 450 A, an almost linear increase of the voltage according to the air gap line is observed. The linear increase shows a relatively small slope due to the large distance between the stator and rotor coils of 28 mm. At higher excitation currents, the saturation of the ferromagnetic components becomes noticeable. Additionally, the phase voltage is plotted in figure 4.5 b) at variable rotational speed and different excitation currents from 150 A to 750 A.

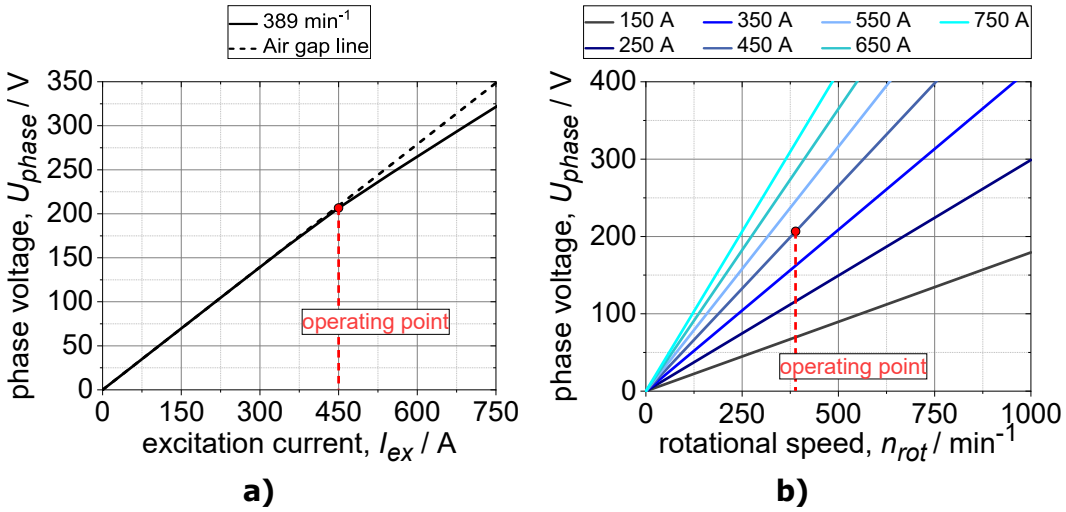

Figure 4.5: Simulated phase voltage under no load
a) Simulated phase voltage at constant rated rotational speed of 389 min and variable excitation current
b) Simulated phase voltage at different excitation currents and variable rotational speed

The rated torque M is 250 N m at a rated rotational speed n_{rot} of 389 min. The torque and induced voltages in the normally conducting three-phase system under rated load conditions are shown in figures 4.6 a) and 4.6 b), respectively. According to [168] the simulated peak to peak torque ripple is 0.07 % which can be attributed to the air gap winding design and the very low harmonics.

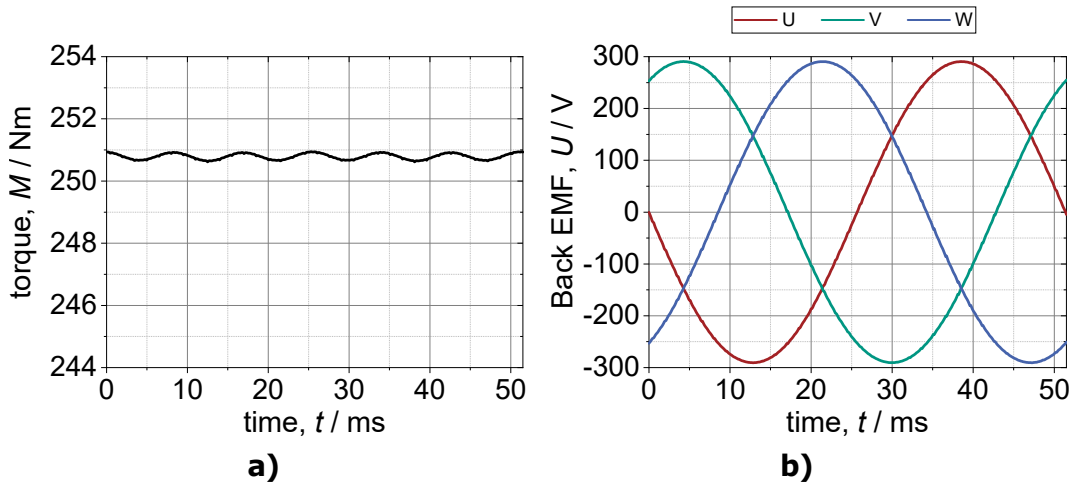

Figure 4.6: Simulation results under rated load conditions
a) Torque
b) Back EMF

A summary of the electromagnetic design parameters for the stator and rotor of the 10 kW generator demonstrator is given in table 4.2.

Table 4.2: Electromagnetic design parameters of the generator demonstrator

Parameter	Value	Unit
Stator		
Cryostat length (with coldheads)	1538	mm
Cryostat inner diameter	265	mm
Cryostat outer diameter	610	mm
Stator iron length	240	mm
Stator iron inner diameter	432	mm
Stator iron outer diameter	512	mm
Pole pairs	3	–
Superconducting pancakes per pole	2	–
Effective length	240	mm
Physical air gap	3.5	mm
Distance stator to rotor coils	28	mm
Average air gap magnetic flux density	0.63	T
Rated excitation current	450	A
Rotor		
Rotor length	1419	mm
Rotor inner diameter	194	mm
Rotor outer diameter	258	mm
Rotor iron inner diameter	80	mm
Rotor iron outer diameter	190	mm
Shaft outer diameter	80	mm
Rated torque	250	N m
Rated speed	389	min
Rated voltage	354	V
Rated current	16.3	A
Inductance	8.91	mH
Winding resistance	0.815	Ω
Inertia	0.783	$kg\,m^2$
Number of coils	72	–
Turns per coil	20	–
Coils per pole and phase	4	–

4.2 Cryogenic system design

Due to the higher magnetic field exposure of the HTS in electrical machines, a temperature range of 20 K to 30 K is usually selected in the design [169, 170]. To reduce the heat load at this temperature level, part of the heat is dissipated at an intermediate stage of about 77 K. The described cooling system is a direct conduction cooled cryogenic concept as presented in subsection 3.3.2.

In the following, the main types of heat input into the cryogenic system of the superconducting machine are discussed. The heat load by convection $\dot{Q}_{Conv}$ can be neglected due to the vacuum in the cryostat. The heat loads can be divided into inputs caused by the current leads of the system $\dot{Q}_{CL}$, by the mechanical support system $\dot{Q}_{SP}$ and by thermal radiation $\dot{Q}_{Rad}$. To realize a closed DC circuit, two current leads are required. This doubles the heat input caused by the current leads. The total heat load due to the mechanical structures is the sum of the individual support structures in the system. Thus, the total heat input to be dissipated at the first and second cooling stages is:

$$\begin{aligned} \dot{Q}_{77K} &= 2 \cdot \dot{Q}_{CL_{77K}} + \sum_{i=1}^{n} \dot{Q}_{SP_{77K},i} + \dot{Q}_{Rad_{77K}} \\ \dot{Q}_{30K} &= 2 \cdot \dot{Q}_{CL_{30K}} + \sum_{i=1}^{n} \dot{Q}_{SP_{30K},i} + \dot{Q}_{Rad_{30K}} \end{aligned} \tag{4.1}$$

Figure 4.7 shows an illustration of these heat flows in the first and second cooling stages of the cryogenic system.

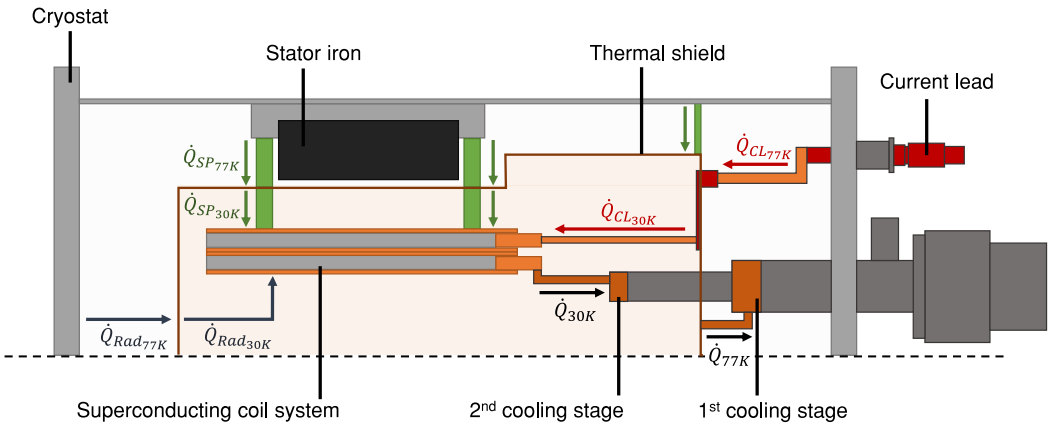

Figure 4.7: Different heat loads to the cryogenic system

4.2.1 Cryogenic cooling

The cooling requirements of superconducting electrical machines regarding cooling power and the temperature range between 20 K to 30 K are best met by Gifford-McMahon (GM) coolers [171], therefore only this type of cryocooler is considered in this work. This cryocoolers usually have a two-stage cooling system.

The theoretically maximum achievable efficiency of a thermodynamic cycle is described by the Carnot cycle and defined as the coefficient of performance ϵ_{Carnot} [172]:

$$\epsilon_{Carnot} = \frac{\dot{Q}}{P_{Carnot}} = \frac{T_{cold}}{(T_{hot} - T_{cold})} \tag{4.2}$$

with the heat extracted from the cold system $\dot{Q}$, the Carnot power P_{Carnot}, the temperature of the cold system T_{cold} and the temperature of the warm system T_{hot}.

Assuming T_{hot} = 300 K as the warm ambient temperature and T_{cold1} = 77 K and T_{cold2} = 20 K as the temperature of the first and second cooling stage, the coefficient of performance is:

$$\epsilon_{Carnot_{77K}} = \frac{77\,\mathrm{K}}{(300\,\mathrm{K} - 77\,\mathrm{K})} = 0.345 \tag{4.3}$$

$$\epsilon_{Carnot_{30K}} = \frac{30\,\mathrm{K}}{(300\,\mathrm{K} - 30\,\mathrm{K})} = 0.111 \tag{4.4}$$

Using the coefficients of performance of the two cooling stages in equation 4.2 results in:

$$P_{Carnot_{77K}} = 2.9 \cdot \dot{Q}_{77K} \tag{4.5}$$

$$P_{Carnot_{30K}} = 9 \cdot \dot{Q}_{30K} \tag{4.6}$$

The Carnot cycle represents an idealized thermodynamic cycle without consideration of further irreversible processes. In order to determine the practical electrical input power of a cryocooler system, the coefficient of performance must be multiplied the figure of merit f_{FOM}:

$$\epsilon_{real} = \epsilon_{Carnot} \cdot f_{FOM} \tag{4.7}$$

In [173] it is stated that the figure of merit of GM coolers mainly depends on the refrigeration power of the system. Assuming that the prototype to be developed has a total heat load in the cryogenic system of less than 100 W, a figure of merit of about 5 % can be achieved. As a consequence, ϵ_{real} and the actually required electrical power P_{real} at the two cooling stages are:

$$\epsilon_{real_{77K}} = 0.345 \cdot 0.05 = 0.0172 \tag{4.8}$$

$$\epsilon_{real_{30K}} = 0.111 \cdot 0.05 = 0.0056 \tag{4.9}$$

$$P_{real_{77K}} = 57.92 \cdot \dot{Q}_{77K} \tag{4.10}$$

$$P_{real_{30K}} = 180.0 \cdot \dot{Q}_{30K} \tag{4.11}$$

For the cryogenic cooling system, this results in the total required electrical power at room temperature level with:

$$\begin{aligned} P_{el_{300K}} &= \epsilon_{real_{77K}} \cdot \dot{Q}_{77K} + \epsilon_{real_{30K}} \cdot \dot{Q}_{30K} \\ &= 57.92 \cdot \dot{Q}_{77K} + 180.0 \cdot \dot{Q}_{30K} \end{aligned} \tag{4.12}$$

With 1 W of heat input at a temperature level of 77 K, almost 58 W of electrical power is needed at room temperature. In addition, at a temperature level of 30 K, approximately 180 W of electrical power must be provided.

This results in the necessity of reducing the heat input into the cryogenic system and retaining the heat at intermediate temperatures in order to achieve a sufficient overall efficiency of superconducting machines.

4.2.2 Current leads

The current lead forms the electrical link between the ambient temperature and the cryogenic system. However, an electrical DC connection also means a thermal bridge between the two temperature levels. Therefore, the current lead usually has one of the largest shares of heat input into the cryogenic system of an electrical machine [174]. There are different design approaches for current leads depending on the type of the system. At first, the conduction cooled current lead is considered, where the hot and cold ends are connected with an electrically and thermally conductive material.

Conduction cooled current leads

Superconducting applications in power engineering often require the feeding of high electrical currents I from room temperature to cryogenic temperature. The transport of high currents in a resistive material results in Ohmic losses in the form of Joule heating according to the following equation:

$$\dot{Q}_J = R(T) \cdot I^2 = \frac{\rho(T) \cdot l}{A} \cdot I^2 \tag{4.13}$$

with the temperature dependent electrical resistance $R(T)$, the temperature dependent specific electrical resistivity $\rho(T)$, the length of the current lead l, the cross section of the current lead A and the electrical current I.

The Joule heating increases with increasing length and decreasing cross section of the current lead. In contrast, the conductive heat transfer $\dot{Q}_\lambda$ decreases with greater length and smaller cross section according to the Fourier law:

$$|\dot{Q}_\lambda| = \frac{|\Delta T|}{R_{th}(T)} = \lambda(T) \cdot A \cdot \frac{|\Delta T|}{l} \tag{4.14}$$

with the temperature dependent thermal resistance $R_{th}(T)$, the temperature dependent thermal conductivity $\lambda(T)$, the cross section A, the temperature difference between the warm and cold end ΔT and the length l.

To reduce the heat load into the cryogenic environment, the minimum of the sum of the Joule heat $\dot{Q}_J$ and the heat conduction $\dot{Q}_\lambda$ must be determined. The design of the geometry ratio regarding the length and the cross section of the current lead for a given current and material represents an optimization problem. Under the assumption of an adiabatic current lead along its length and establishing the energy balance of the heat flows from equation 4.13 and 4.14, the following equation, according to [173], is obtained for the optimized geometry ratio of length to cross section:

$$\left(\frac{l}{A}\right)_{opt} = \frac{1}{I \cdot \sqrt{2}} \cdot \int_{T_{cold}}^{T_{hot}} \frac{\lambda(T)}{\sqrt{\int_T^{T_{hot}} \rho(\tau) \cdot \lambda(\tau) \cdot d\tau}} \cdot dT \tag{4.15}$$

Equation 4.15 shows that an optimum geometric ratio for a given temperature of the warm end T_{hot} and cold end T_{cold} of the current lead can be only achieved for a specific current I. Due to the temperature-dependent material data, the solution of this optimization problem can be only solved analytically with simplifications.

In order to be able to build compact current leads, materials with good electrical conductivity such as copper are often used. The electrical and thermal conductivity of copper depends on the purity, which is expressed by the residual resistance

ratio (RRR) [29]. For the following calculations, a standard copper with a residual resistance ratio of 50 is considered. Figure 4.8 shows the specific electrical resistance ρ and the thermal conductivity λ of Cu RRR 50 over a temperature range from 4 K to 300 K [175]. The behavior of material data below 100 K, especially the thermal conductivity, makes it necessary to solve the above equations for this temperature range with numerical methods. To solve the optimization problem, a 1D model based on the finite difference method is developed using the software *Matlab* [176].

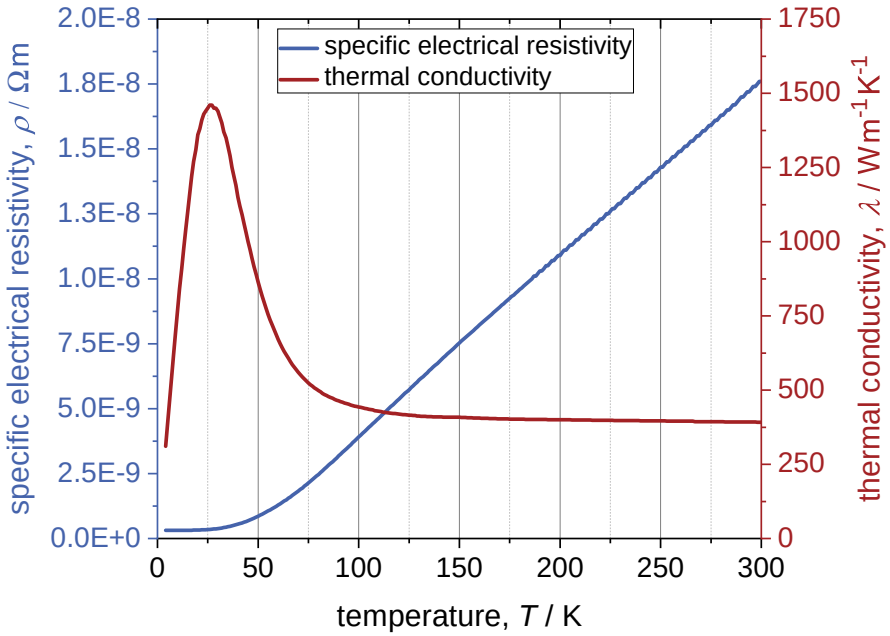

Figure 4.8: Specific electrical resistance and thermal conductivity as a function of the temperature of Cu RRR 50 [175]

The length of the current lead is determined by the structural dimensions of the generator design. For the connection between the room temperature environment at the cryostat lid and the temperature level of the first cooling stage, a length of 170 mm is assumed. The distance between the first cooling stage and the second cooling stage is set as 360 mm. The temperatures of the first cooling stage T_{cs1} and the second cooling stage T_{cs2} are assumed to be 77 K and 30 K respectively. According to equation 4.15, an optimum cross section A_{opt} for the given temperatures and lengths can only be determined for a certain electric current. For the design it is therefore necessary to consider which heat loads due to the current leads can be expected for the combination of the optimized current I_{opt} and the actual injected current I_{ex}. In the development of a superconducting generator prototype, it therefore makes sense to consider the designed operating current of 450 A and the critical current of approximately 700 A to be expected in the superconducting stator system. The critical currents of the superconducting coils and the entire stator system are explained in more detail in chapter 5. This results in four possible combinations. The combinations with the optimized

geometry ratio of length and cross section area and optimized heat input at 77 K and 30 K, are listed in table 4.3.

Table 4.3: Current lead combinations

Combination	I_{opt} (A)	I_{sp} (A)	T_{cs} (K)	l (mm)	A_{opt} (mm^2)	$\dot{Q}_{opt}$ (W)
A 1	450	450	77	170	21.67	19.12
			30	360	22.52	3.91
A 2	450	700	77	170	21.67	42.41
			30	360	22.52	7.45
B 1	700	450	77	170	33.89	22.32
			30	360	35.70	4.74
B 2	700	700	77	170	33.89	29.74
			30	360	35.70	6.09

To close the electrical supply circuit for the superconducting coil system, two current leads are required. Figure 4.9 shows the total heat load per cooling stage caused by the complete current lead system.

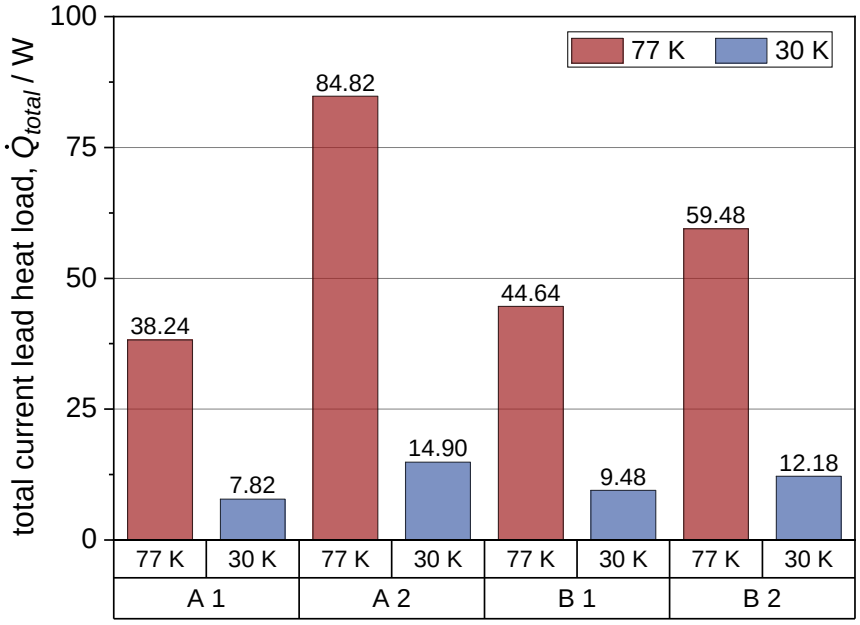

Figure 4.9: Total heat load at the first and second cooling stage due to the different current lead combinations

Version A 2 with a heat input of almost 85 W at the first cooling stage requires too much cooling power to ensure thermal equilibrium. As a result, an optimization

to the operating current of the machine with 450 A excludes tests near the critical limit of the superconductor system. In order to be able to carry out tests close to this critical limit, the current leads are designed for an electrical current of 700 A. This results in combination B for the generator prototype design. With this design, the losses are kept within acceptable limits when operating at both 450 A as in case B 1 and 700 A in case B 2.

Binary current leads

Section 4.2.1 shows why the reduction of heat input is essential, especially at low cryogenic temperature regions. The heat leakage caused by the current leads to the lowest cryogenic temperature level $\dot{Q}_{CL_2}$ can be greatly reduced by the intermediate cooling stage, but still represents a high load for the refrigeration system. A further reduction of the heat input can be achieved by using so-called binary current leads [177–179]. Binary current leads consist of a resistive part and a superconducting part which is used at temperatures below the critical temperature T_c. The physical properties of HTS, with no electrical DC resistance below T_c but at the same time a relatively high thermal resistance, are used.

The electrical connection between the first and the second cooling stage is realized with three parallel HTS tapes. The tapes are soldered at their ends to the electrical connection system to ensure good electrical contact and to close the electrical circuit. Figure 4.10 shows the HTS current lead between the two cooling stages.

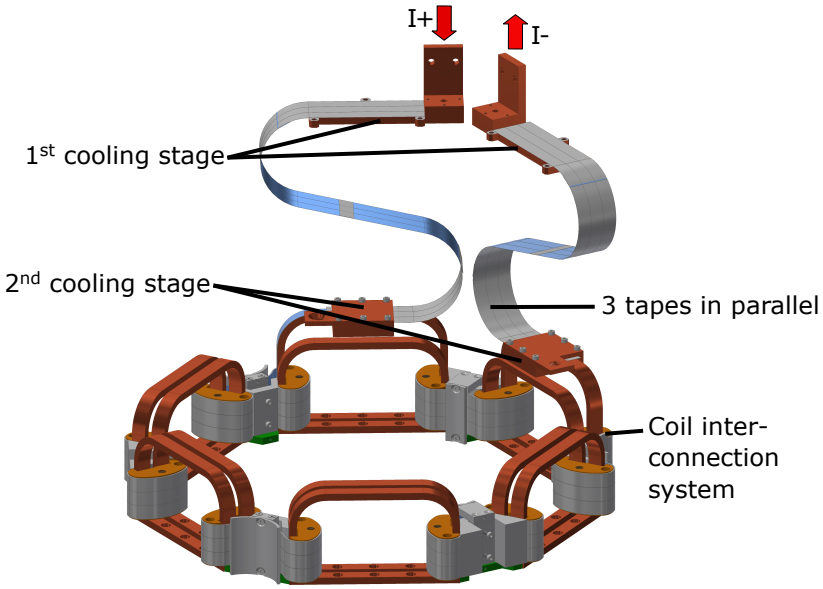

Figure 4.10: HTS current lead between the first and second cooling stage

The average critical current I_c of each tape used in the parallel connection is about 650 A at 77 K in self-field. Assuming that the stray field of the coils in this area has only a minor influence on the current carrying capacity of the tapes and that the soldered contacts allow a homogeneous current distribution in the parallel

connection, an operation far below the average critical current of each tape should be achieved. With a supply current I_{ex} of 450 A and 700 A, each tape is loaded with 23.08 % and 35.90 % of its critical current respectively. Due to the lack of Joule losses $\dot{Q}_J$ in the HTS part of the current lead, only heat according to equation 4.14 is introduced into the system of the second cooling stage. As described in chapter 2, the substrate layer and the copper stabilization layer, with each 100 µm thickness, have the largest share in the HTS tape architecture. Therefore, only the temperature-dependent thermal conductivity of these two materials is considered for the heat input by thermal conduction. Figure 4.11 shows the thermal conductivity of the substrate material Hastelloy C-276 in a temperature range from 4 K to 200 K according to [180]. With the thermal conductivity of Hastelloy and assuming Cu RRR 50 from fig. 4.8 as the copper in the stabilization layer, the total heat load for the HTS current leads between 77 K and 30 K, compared to resistive current leads, is reduced to 0.89 W.

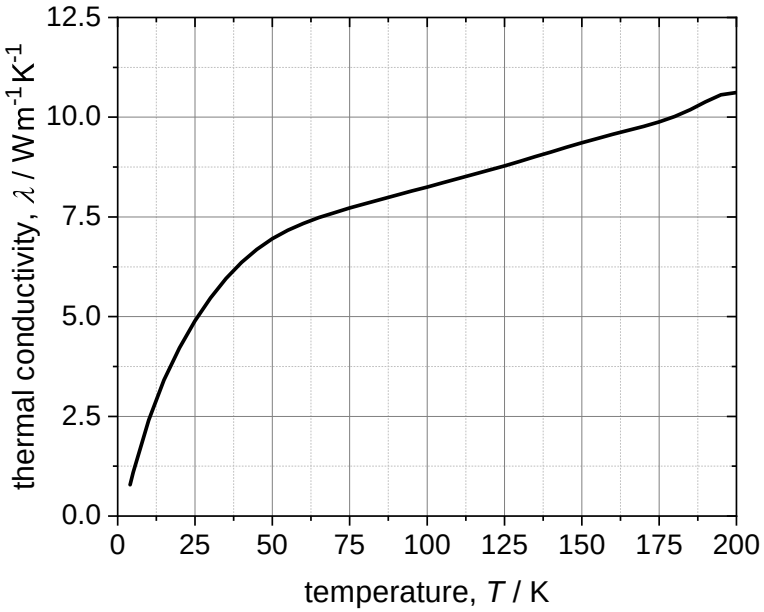

Figure 4.11: Thermal conductivity as a function of the temperature of Hastelloy C-276 [180]

4.2.3 Conductive heat load

In cryogenic systems, mechanical support structures are usually required to take the forces occurring in the low temperature region and to transfer them to components at ambient temperature [181]. This thermal connection between the different temperature levels means a further heat load on the cryogenic system according to equation 4.14. Therefore, the design of the mechanical components must take into account both the structural integrity and the reduction of heat input. The

geometrical design as well as the material properties regarding thermal conductivity λ and yield stress have to be considered in particular. In this section only the thermal properties will be discussed. The mechanical design is further explained in section 4.3.

The two materials used for the mechanical support structure are glass fiber reinforced plastic (G10) and stainless steel 304. The thermal conductivity of both materials for a temperature range from 5 K to 300 K is shown in figure 4.12 [182]. G10 is an anisotropic material and has a slightly higher thermal conductivity in the direction parallel to the glass fiber layers. Since the processing of the material makes it difficult to consider the actual alignment of the glass fiber layers in a three-dimensional geometry, the thermal conductivity parallel to the glass fiber layer was used for the following calculations to take into account the worst case.

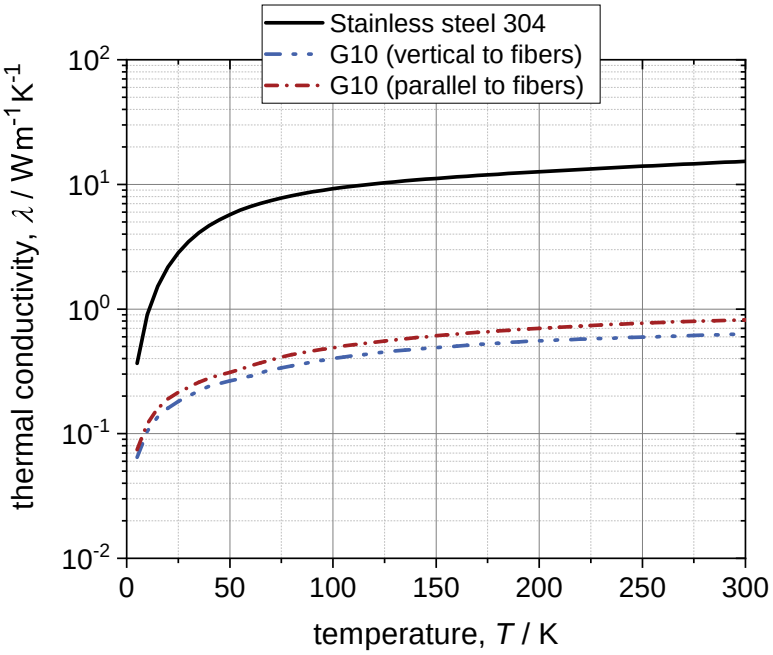

Figure 4.12: Thermal conductivity as a function of the temperature of stainless steel 304 and G10 in vertical and parallel direction of fibers [182]

Figure 4.13 shows the mechanical support structures between the individual temperature levels for a section of two stator coils. The main components of the mechanical support system are made of G10, as it has a much lower thermal conductivity than stainless steel. The superconducting stator system is mechanically stabilized with a G10 ring, which connects the outer cryostat structure at ambient temperature to the cryogenic system. The G10 structure is cooled by the thermal shield at the first cooling stage to reduce the heat input to the coil system at the second cooling stage. In order to increase the total thermal resistance R_{th} of the mechanical support system, the G10 structures are designed to have the longest possible thermal path between the temperature levels, while maintaining sufficient stability. Another G10 support ring, not shown in Figure 4.13, is located at the

rear of the generator to provide additional support and hold the thermal shield in position. This support forms a thermal link only between the ambient temperature and the first cooling stage.

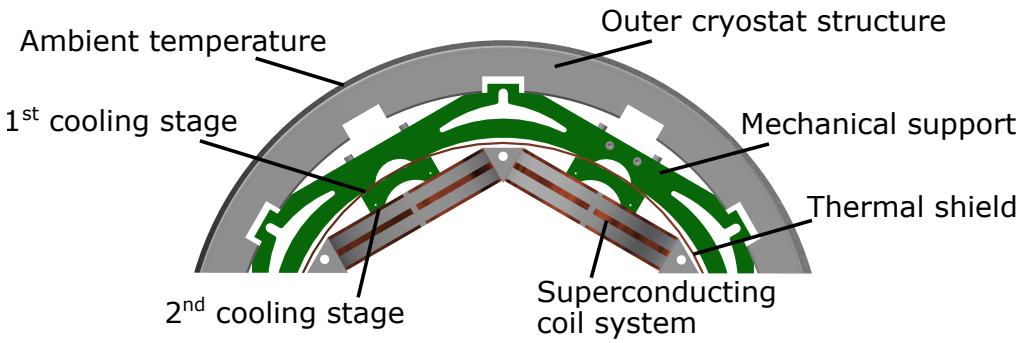

Figure 4.13: Mechanical support structure for a section of two stator coils, connecting cryogenic regions with ambient temperature

The heat input to the two cooling stages caused by the mechanical support structure is calculated with a thermal-stationary model by the FE software *Ansys Workbench* [183]. To take the designed structure sufficiently into account, a three-dimensional (3D) model, of the respective mechanical support, is considered. The temperature dependent material data from figure 4.12 is used for the calculation. Dirichlet temperature boundary conditions with fixed temperatures of 300 K, 77 K and 30 K are assumed for the different temperature levels. The temperature boundary conditions are applied to the contact surfaces of the mechanical support structures with the respective cooling stages. Figure 4.14 shows the results of the 3D calculations for the different G10 support structures. Subfigure a) displays one-third of the support structure for the thermal shield and subfigure b) one third of the support structure for the superconducting coil system. Structure a) and b) have a material thickness of 6 mm and 15 mm respectively. Both structures form the thermal link between the ambient temperature at 300 K and the first cooling stage at 77 K. Subfigure c) shows the second part of the coil support structure between the first and second cooling stage at 30 K. Structure c) has a material thickness of 15 mm. On the left side of the figure the temperature distribution is displayed and on the right side a vectorial representation of the heat flow ϕ is shown.

The calculated heat inputs refer to one of the presented components respectively. However, some of the mechanical support structures are used several times in the generator design. The heat load into the first cooling stage through the entire structure a) and b) is 1.78 W and 6.55 W respectively. Structure b) is designed twice in the generator system and thus the heat input for b) is doubled to 13.11 W. The heat input into the second cooling stage through structure c) is 0.11 W. Each coil has two such support structures. With six stator coils in total, the heat load of one component with 0.11 W is multiplied by 12 which result in a overall heat load of 1.36W for structure c).

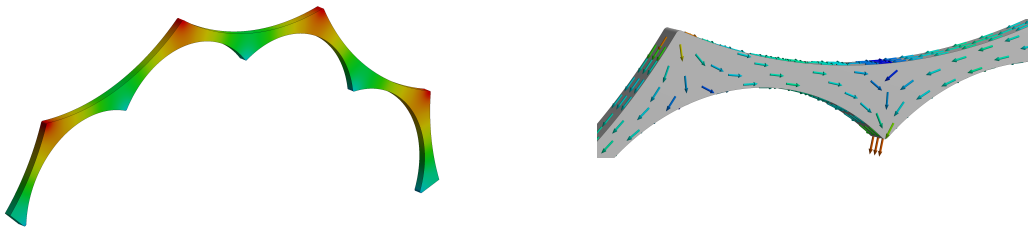

a) Thermal shield support between ambience and 1st cooling stage

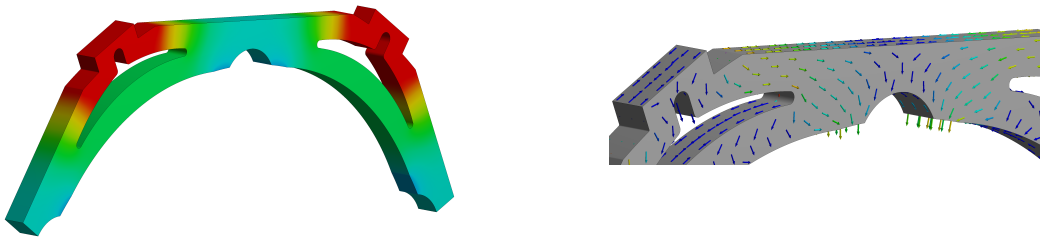

b) Coil support between ambience and 1st cooling stage

c) Coil support between 1st and 2nd cooling stage

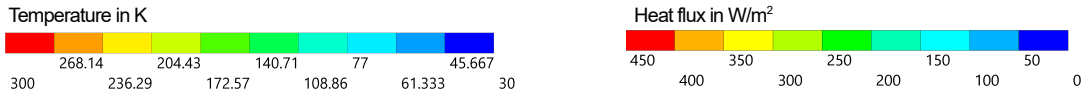

Figure 4.14: a), b): One-third of the G10 support structures between the ambient temperature and the first cooling stage.
c): G10 support structure between the first and second cooling stage. The left side shows the temperature distribution. The right side shows the heat flux

The superconducting coil system with its surroundings is inserted vertically into the cryostat during assembly. Therefore, both the thermal shield and the coil system have to be fixed vertically in addition to the horizontal mechanical G10 support. The thermal shield is attached to the cryostat lid with 12 threaded rods and the coil system with six threaded rods illustrated in figure 4.15. The rods for the thermal shield and coil system are marked in green and blue respectively. A threaded rod of the thermal shield forms a direct thermal link between the temperature levels of 300 K and 77 K over a length of 935 mm, with a cross section of 28.27 mm^2. The threaded rods of the coil system connect the temperatures of 300 K and 30 K over a length of 586 mm, with a cross section area of 50.27 mm^2.

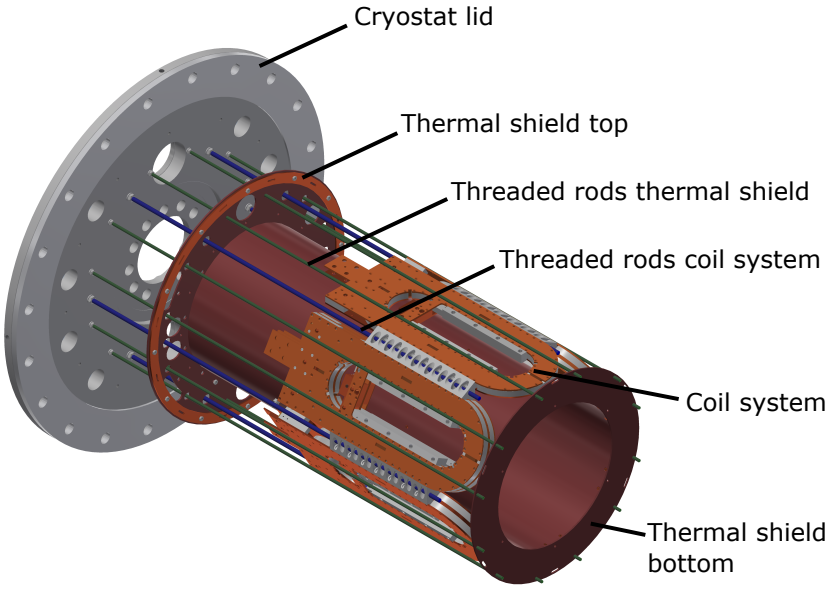

Figure 4.15: Vertical mechanical suspension connecting the cryostat lid to the thermal shield and coil system

The heat input calculations for the vertical suspension were also carried out with the software *Ansys Workbench*. The material used for the threaded rods was assumed to be stainless steel 304 from figure 4.12. G10 was not used for the threaded rods because the relatively long length and small cross section leads to an acceptable heat input into the two cooling stages. The heat input into the first cooling stage through a threaded rod of the thermal shield is 0.082 W. For a mechanical suspension with a total of 12 threaded rods, this results in a total heat input of 0.98 W. The heat load into the second cooling stage, caused by a threaded rod, is 0.25 W, resulting in a total heat input of 1.53 W.

A summary of the heat loads by conduction, into the two cooling stages through the different mechanical support structures is given in table 4.4.

Table 4.4: Summary of conductive heat loads into the cooling stages due to different mechanical supports

Support structure	Number of components	Heat load per component	Total heat load
	1^{st} cooling stage at 77 K		$\sum$ 15.87 W
G10 support a)	1	1.78 W	1.78 W
G10 support b)	2	6.55 W	13.11 W
Threaded rod thermal shield	12	0.082 W	0.98 W
	2^{nd} cooling stage at 30 K		$\sum$ 2.89 W
G10 support c)	12	0.11 W	1.36 W
Threaded rod coil system	6	0.25 W	1.53 W

4.2.4 Radiation heat

Every body with a temperature above 0 K radiates energy in the form of electromagnetic waves, which is also partly absorbed by other bodies. This type of heat transfer must be taken into account in a cryogenic system and can be described simplified by the following equation [184]:

$$\dot{Q}_{Rad} = \epsilon \cdot \sigma \cdot A \cdot (T_{hot}^4 - T_{cold}^4) \tag{4.16}$$

with the emissivity of the material ϵ, the Stefan-Boltzmann constant σ, the surface of the body A and the temperatures of the radiant bodies T_{hot} and T_{cold}.

According to equation 4.16, the heat input to the lower temperature level is significantly influenced by the temperature of the warmer body. In the following, the heat input to the second cooling stage at 30 K through a radiant body at 300 K and 77 K are compared:

$$\dot{Q}_{30K\ Rad}^{300K} = \epsilon \cdot \sigma \cdot A \cdot (300^4 - 30^4) \tag{4.17}$$

$$\dot{Q}_{30K\,Rad}^{77K} = \epsilon \cdot \sigma \cdot A \cdot (77^4 - 30^4) \tag{4.18}$$

Equating 4.17 and 4.18 and assuming the same emissivity and surface results in:

$$\dot{Q}_{30K\ Rad}^{300K} = 235.83 \cdot \dot{Q}_{30K\,Rad}^{77K} \tag{4.19}$$

With a radiant body at 77 K, the radiant heat at the 30 K level can be reduced by a factor of 235.83 compared to a directly radiant body at room temperature. Therefore, an actively cooled thermal shield is placed between the ambient temperature and the cold temperature level to trap the heat at an intermediate cooling stage. The thermal shield is connected to the first cooling stage and consists of copper for a homogeneous temperature distribution over the entire surface. The emissivity ϵ of the used material has a direct linear effect on the incident radiant heat and can vary greatly depending on the surface condition. According to [181, 185], polished copper has an emissivity between 0.01 and 0.05. In order to better estimate the maximum possible heat input, the higher value with 0.05 is assumed for the following considerations. The emissivity of the surface can be further reduced by using uncooled inter layers of so called multilayer insulation (MLI). The MLI consists of several layers of aluminized films which are separated from each other by a spacer material with poor thermal conductivity. The number of layers N_{MLI} influences the total emissivity according to [186, 187] as follows:

$$\epsilon_{total} = \epsilon \cdot \epsilon^{*} = \epsilon \cdot \frac{1}{N_{MLI} + 1} \tag{4.20}$$

Usually, 20 layers of MLI are used in cryostat systems, as this achieves a relatively low emissivity and a further increase in the number of layers has only a minor effect. However, since the installation space in the generator prototype is limited, only 10 layers are assumed. With the emissivity of polished copper of 0.05, the total emissivity ϵ_{total} according to equation 4.20 is therefore 4.55×10^{-3}. The total surface area of the thermal shield A_{TS} is 1.98 m^2. Assuming an ambient temperature of 300 K and a homogeneous temperature distribution of 77 K over the entire surface of the thermal shield, this results for the radiative heat to the first cooling stage, according to equation 4.16, in:

$$\dot{Q}_{Rad_{77K}} = 4.55 \times 10^{-3} \cdot \sigma \cdot 1.98 \cdot (300^4 - 77^4) = 4.11\,\mathrm{W} \tag{4.21}$$

The value agrees with the specification of 1 W/m^2 - 2 W/m^2 for a thermal shield with MLI according to [188].

This simplified consideration can be only made under the assumption of a homogeneous temperature distribution of the thermal shield. In order to check the design of the thermal shield, a 3D thermal-stationary calculation of half of the shield is carried out in *Ansys Workbench*. For this purpose, the heat inputs to the first cooling stage determined from the previous chapters 4.2.2 and 4.2.3 are assumed as additional boundary conditions in the model.

The calculated total heat input into the first cooling stage is 62.59 W. Figure 4.16 shows the cooling curves of the first and second cooling stages of the used cryogenic cooler from the company *Advanced Research System* [189]. The two cooling stages form an interdependent overall system and can therefore not be considered separately. The cooling system of Advanced Research Systems consists of a cold-head of the model DE210S driven by a compressor of the model ARS-10HW. In total two such cold-heads and compressors are provided for cooling the cryogenic system. Thus the heat input to the first stage of a cold head is 31.3 W. The expected temperature of the first cooling stage at a heat load of 31.3 W is about 60 K according to figure 4.16.

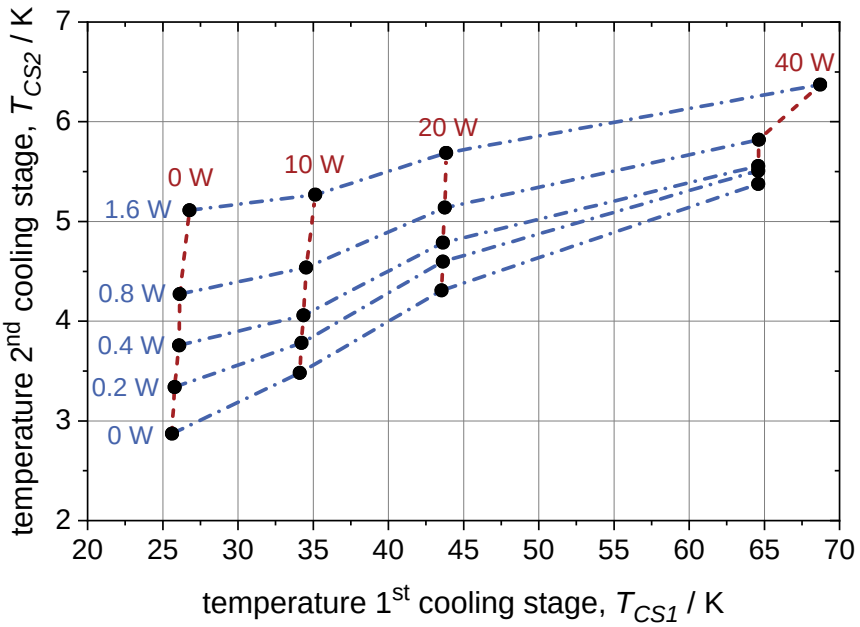

Figure 4.16: Cooling curves of the first and second cooling stages of the cold-head DE210S [189]

Figure 4.17 shows the boundary conditions for the calculation of the temperature distribution of the thermal shield. The design drawing is greatly simplified for the calculations. All partial components are joined together as a single coherent component. The boundary conditions are applied on distinct surfaces to further simplify the calculation. Figure 4.17 a) shows half of the thermal shield with the calculated heat input of the G10 supports on the first cooling stage as boundary conditions. The embossed surfaces for the boundary conditions are shown in green. Figure 4.17 b) shows the top side of the thermal shield. The connection of the first cooling stage of the cold-head is assumed on the blue surface with a temperature boundary condition of 60 K. The red area represents one current lead terminal, thermally connected with the top of the thermal shield. An additional thermal connection between the cold-head connection and the current lead terminal ensures a better dissipation of the heat introduced by the current

lead. According to chapter 4.2.2, a heat load of 21.29 W for one current lead is defined on this surface. In Figure 4.17 c) the heat input caused by the threaded rod suspension on the lower side of the thermal shield is illustrated. The boundary condition is assumed for the areas marked in yellow. Furthermore, a thermal radiation boundary condition is assumed for the remaining surfaces of the thermal shield for an ambient temperature of 300 K. The emissivity for the polished copper surface with MLI is set to 4.55×10^{-3}.

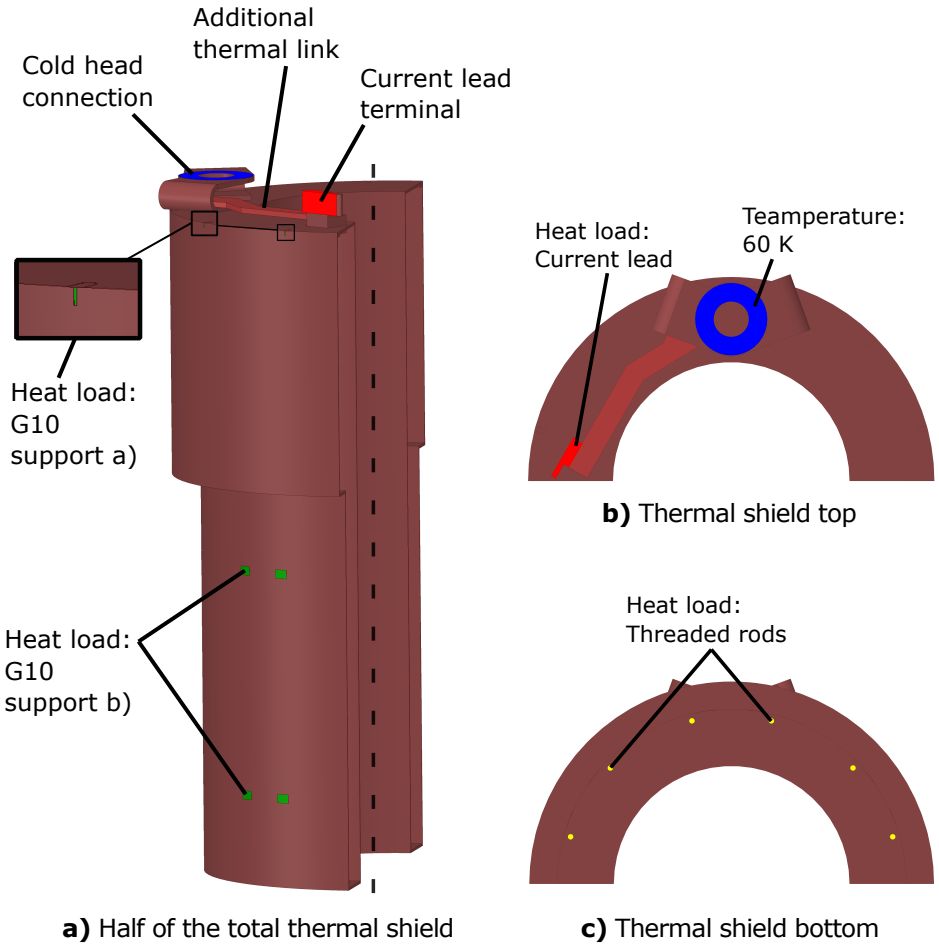

Figure 4.17: Boundary conditions of the thermal shield model
a): Half model of the thermal shield. Green surfaces indicate heat flow boundary conditions of G10 support structures.
b): Top of the thermal shield. Temperature boundary condition on blue surface. Red surface indicates current lead terminal with heat flow boundary condition.
c): Bottom of the thermal shield. Yellow surfaces indicate the heat flow boundary conditions of the threaded rods suspension.

The thermal shield has a thickness of 2 mm over a total length of 766 mm. Top and bottom are made with 3 mm thick copper plates. The maximum outside diameter is 484 mm and the minimum outside diameter is 418 mm. The inner diameter is

282 mm. The material thickness of the cold-head connection and the additional connection between cold-head and current lead terminal is 6 mm each.The cold-head connection is designed with flexible strip material to mechanically decouple the cold-head and the remaining cryogenic system. For the thermal analysis Cu RRR 50 from figure 4.8 is assumed as shield material.

Figure 4.18 shows the temperature distribution of the thermal shield. Figure 4.18 a) shows the temperatures over the entire surface of half of the thermal shield. The temperatures on the top side of the shield with the cold head connection and the current lead terminal are represented by figure 4.18 b). Figure 4.18 c) shows the bottom side furthest away from the cold-head connection.

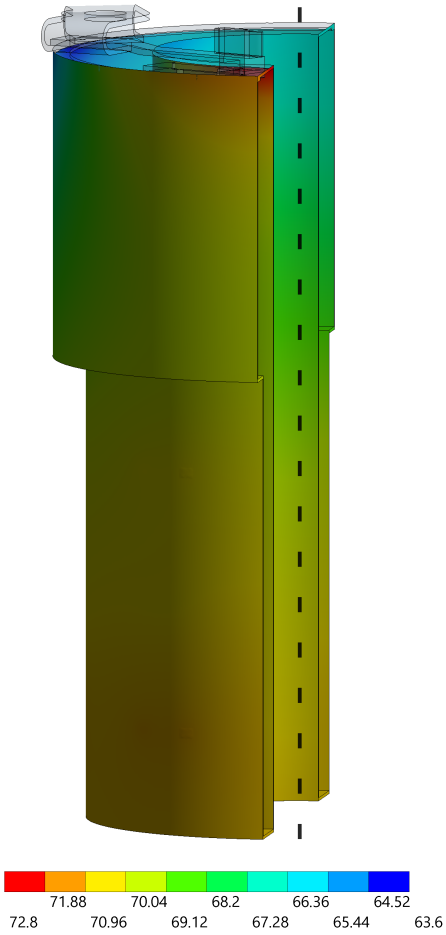

a) Half of the thermal shield

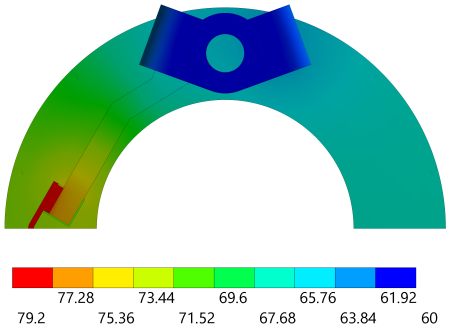

b) Thermal shield top

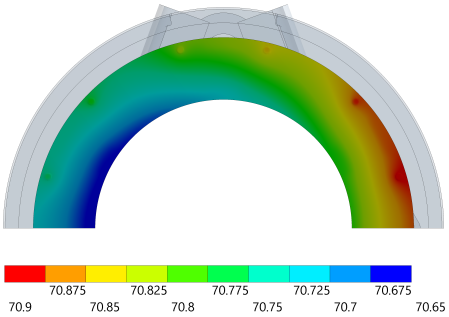

c) Thermal shield bottom

Figure 4.18: Temperature distribution of a) half of the thermal shield, b) top of the thermal shield and c) bottom of the thermal shield

The average temperature of the total surface of the thermal shield is 68.66 K with a maximum temperature at the bottom with 70.86 K. The direct connection of the resistive current lead to the current lead terminal on the first cooling stage has a maximum temperature of 79.19 K. However, the joint at the first cooling stage of the

HTS part of the binary current lead has a sufficient current carrying capacity at an average temperature of 72.45 K. The cryogenic system is thus sufficiently designed for stable thermal operation. The second cooling stage has a very low total heat load of 3.78 W and should reach very low temperatures according to Figure 4.16. For this reason, a detailed consideration of the temperature distribution is not presented here.

4.2.5 Heat loads summary

In table 4.5, all heat inputs to the two cooling stages, caused by the current leads, mechanical supports and heat radiation, are summarized. The total heat input to the first cooling stage and to the second cooling stage is 64.63 W and 3.78 W respectively.

Table 4.5: Summary of heat loads into the two cooling stages

Heat load	1^{st} cooling stage 77 K		2^{nd} cooling stage 30 K	
Current leads $\dot{Q}_{CL}$	44.64 W	69.1 %	0.89 W	32.5 %
Support structures $\dot{Q}_{SP}$	15.87 W	24.6 %	2.89 W	76.5 %
Radiation $\dot{Q}_{Rad}$	4.12 W	6.4 %	0 W	0 %
Total	64.63 W		3.78 W	

By using the total heat input of the two cooling stages in equation 4.12 from chapter 4.2.1, the required electrical power of the cryogenic system is obtained to:

$$\begin{aligned} P_{el_{300K}} &= \epsilon_{real_{77K}} \cdot \dot{Q}_{77K} + \epsilon_{real_{30K}} \cdot \dot{Q}_{30K} \\ &= 57.92 \cdot 64.63\,\mathrm{W} + 180.0 \cdot 3.78\,\mathrm{W} \\ &= 3.74\,\mathrm{kW} + 0.68\,\mathrm{kW} = 4.42\,\mathrm{kW} \end{aligned} \tag{4.22}$$

With the required electrical power of the cryogenic system, in relation to the rated power of the generator of 10 kW, sufficient efficiency cannot be achieved. However, it must be taken into account that a technology demonstrator is investigated and that with the selected cryogenic cooling system scaling effects only occur at generator powers of 3 MW and more [143].

4.3 Mechanical design

In an electrical machine, axial, tangential and radial electromagnetic forces occur, whereas in radial flux machines only the tangential force component can be used for torque generation. In externally excited electrical machines without permanent excitation, two basic electromagnetic forces must be taken into account.

According to [190], equation 4.23 describes the force effect due to a spatial permeability change:

$$f = -\int_0^H H \cdot grad\,\mu \cdot dH \tag{4.23}$$

with the magnetic field strength H and the permeability μ.

This force component causes an attraction between the stator and the rotor of an electrical machine as a normal force acting on the surface. It consists of a constant mechanical preload and a radial tension wave with double fundamental wave periodicity and can be expressed as:

$$f_n(x,t) = \frac{(\hat{B}_{\delta r}^2 - \hat{B}_{\delta t}^2)}{4 \cdot \mu_0} + \frac{(\hat{B}_{\delta r}^2 - \hat{B}_{\delta t}^2)}{4 \cdot \mu_0} \cdot \cos\left(\frac{2 \cdot \pi \cdot x}{\tau_p} - 2 \cdot \omega \cdot t\right) \tag{4.24}$$

with the radial air gap magnetic flux density $B_{\delta r}$, the tangential air gap magnetic flux density $B_{\delta t}$, the magnetic field constant μ_0, the circumferential location x, the pole pitch τ_p, the angular frequency ω and the time t.

During nominal operation the maximum of the tensile stress acting on the circumference is:

$$\hat{f} = \frac{(\hat{B}_{\delta r}^2 - \hat{B}_{\delta t}^2)}{2 \cdot \mu_0} = 124.34\,\mathrm{kN/m^2} \tag{4.25}$$

However, assuming a centric rotor position and a theoretically symmetry of the electric machine, these forces cancel each other at the diametrical point of the circumference. According to [168], the overlayed rotating tension wave which lead to mechanical vibrations in the electric machine, can be neglected in machines with a power class below 500 kW.

The Lorentz force is the force effect of a current-carrying conductor in a magnetic field, which is expressed as follows:

$$f_L = j \times B \tag{4.26}$$

with the current density j and the magnetic flux density B.

The force acting on the superconducting coils is influenced by the geometry and the materials used in the machine design. Figure 4.19 shows the different field and therefore force distribution in the tooth and slot of a slotted winding.

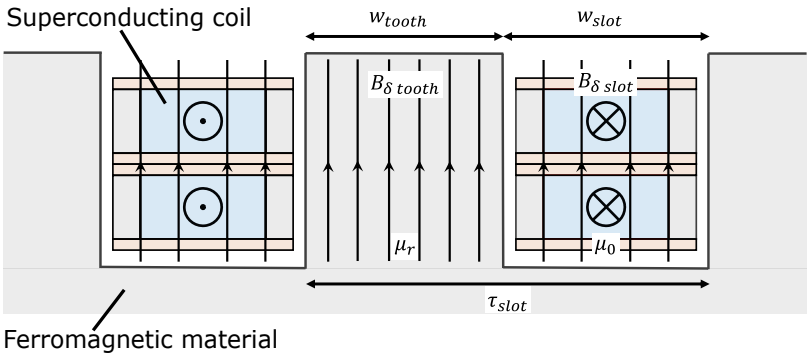

Figure 4.19: Field distribution in the tooth and slot of a slotted winding

In slotted windings, the magnetic air gap flux density is divided into the magnetic flux density of the teeth $B_{\delta tooth}$ and the slots $B_{\delta slot}$ as follows [168]:

$$B_{\delta tooth} = B_\delta \cdot \frac{\tau_{slot}}{w_{tooth} + w_{slot} \cdot \left(\frac{\mu_0}{\mu_r}\right)} \tag{4.27}$$

$$B_{\delta slot} = B_\delta \cdot \frac{\tau_{slot}}{w_{slot} + w_{tooth} \cdot \left(\frac{\mu_r}{\mu_0}\right)} \tag{4.28}$$

with the air gap magnetic flux density B_δ, the slot pitch τ_{slot}, the tooth width w_{tooth} and the slot width w_{slot}.

The teeth which are usually made of a highly permeable material such as iron carry the majority of the flux. According to [168], the tangential force on a slotted winding is only 2 % of the total force per slot pitch τ_{slot}. In the case of an air-gap winding, however, the coil is penetrated by the total magnetic flux density and thus experiences a greater force. For this reason, a 3D static electromagnetic model in *Ansys Maxwell* was used to investigate the mechanical stress on the superconducting winding in axial, tangential and radial directions. Figure 4.20 shows the 3D representation of a superconducting pole designed as a double pancake (DPC). The lower pancake (PC) is defined as the coil positioned closer to the rotor, while the upper pancake is located closer to the stator iron. In principle, a pancake is strained to its outward in the axial and tangential directions. Since the resulting total force is zero, the two pancakes are divided into sub components for a detailed consideration of the mechanical loads on the superconducting tapes.

For the tangential force components F_t, the two straight parts along the effective length l_{ef} are divided into a left and a right volume, to determine the integral total force. For the integral axial force component F_a, a pancake is cut in halves in the axial direction and divided into a front and back volume element. The calculation of the radial force components F_r applies to the complete volume of a pancake.

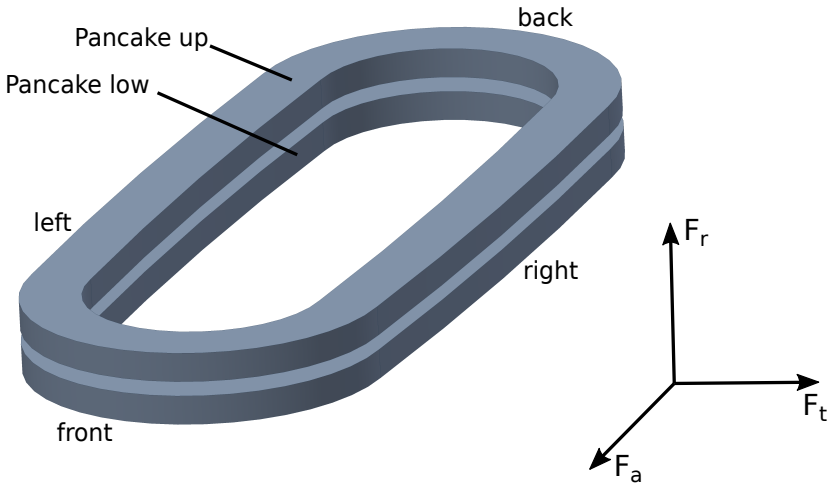

Figure 4.20: Three-dimensional view of lower and upper pancake in a double pancake configuration

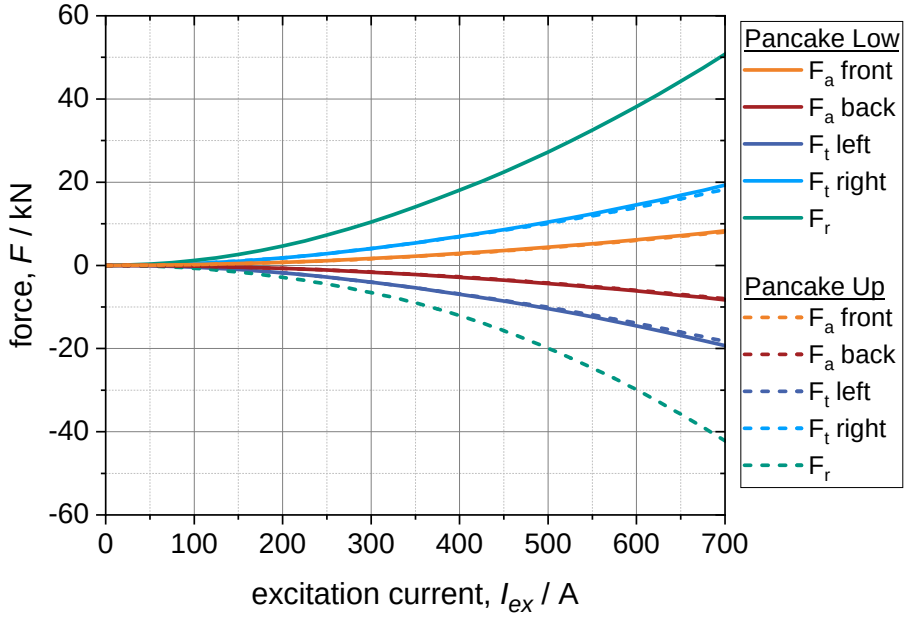

Figure 4.21: Axial, tangential and radial forces on lower and upper pancake in a double pancake configuration as a function of excitation current

The resulting forces on the corresponding volumes as a function of the excitation current I_{ex} are shown in figure 4.21. The axial and tangential force components

show relatively symmetrical curves for both pancakes and thus almost balance each other with respect to the entire coil. The radial forces are oriented such that both coils attract each other. However, the radial force on the lower pancake tends to have a higher magnitude, resulting in an total outward radial force on the entire coil system. For the operating point at 450 A, the radial force applied to the lower pancake with 22.45 kN and to the upper pancake with −15.69 kN results in a total outward force for one double pancake of 6.67 kN. The maximum magnitude of the axial and tangential loads of the partial volumes per pancake, at the operating point are 3.57 kN and 8.60 kN, respectively. The individual double pancake stator poles are mechanically connected to each other in the generator as a hexagon. The hexagonal structure absorbs the resulting outward radial forces. Under load conditions, additional tangential forces occur on the superconducting coils due to the torque of the generator. The mechanical G10 support structure presented in figure 4.13 transfers the additional forces from the cryogenic region of the superconducting coils to the outer cryostat wall. With a rated torque of 250 N m and a lever arm of 159 mm, the tangential force per stator pole is 262.05 N. This tangential force is transmitted from the four G10 supports directly attached to a double pancake to the rest of the mechanical support structure.

5 Development and preliminary tests of the superconducting coils

In this chapter, the two 2G HTS tapes used in the superconducting coils are first introduced and characterized in terms of their architecture, critical current and turn-to-turn resistance. Then, the design and manufacturing of the superconducting coils is described and their performance in liquid nitrogen and under conduction-cooled conditions is investigated.

5.1 Characterization of the HTS tapes

The superconducting coils developed in this work are designed with two 2G HTS tapes from different manufacturers. In the following, the superconductors used are referred to as tape 1 and tape 2.

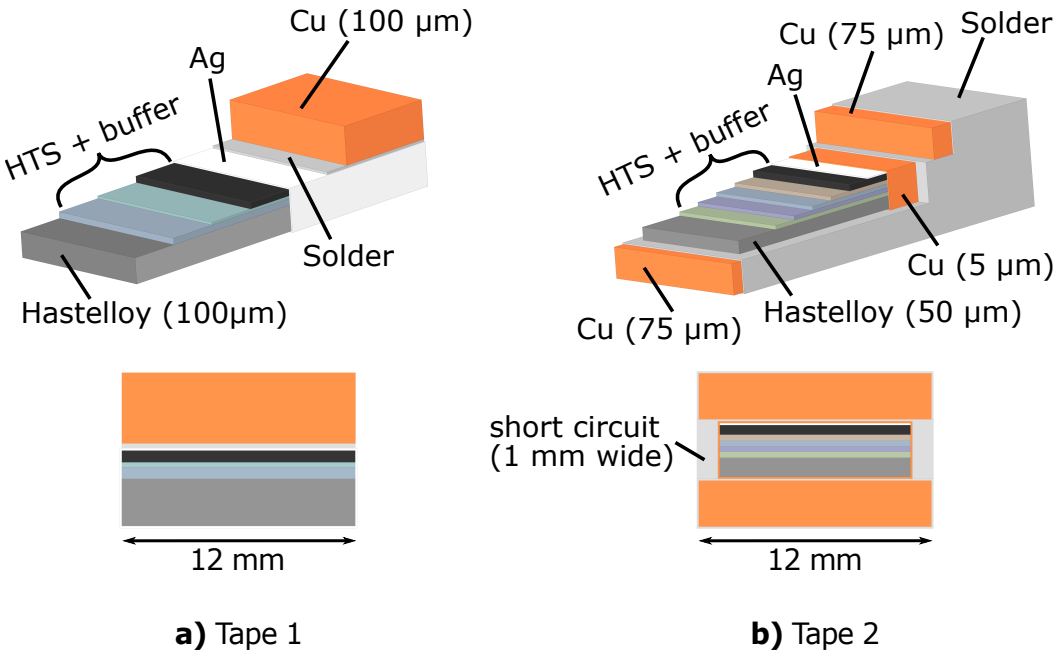

a) Tape 1 **b)** Tape 2

Figure 5.1: Architecture with cross-sectional view of the two HTS tapes used in the coils

A fundamental difference is the width of the superconducting layer and the thickness of the substrate layer of the two tapes. The width for tape 1 and tape 2 is 12 mm and 10 mm and the thickness of the substrate 100 µm and 50 µm respectively. However, for a uniform coil design both HTS tapes must be as identical as possible in terms of their geometric dimensions. For this reason, tape 2 has a special architecture in which the entire width and thickness of the HTS tape is adjusted by laminating 12 mm wide and 75 µm thick copper tape on both sides as a stabilization layer. The basic architecture of the two tapes with the different layers and their cross-section is shown in figure 5.1. Tape 1 and tape 2 both have a total average width of around 12 mm and a average thickness of 0.212 mm and 0.190 mm respectively. By laminating 12 mm wide stabilization layers on a 10 mm wide HTS tape, 1 mm wide areas filled with solder are created on both sides of the tape. The two 1 mm wide areas represent a direct short circuit between the two copper stabilization layers.

5.1.1 Critical current

In order to characterize the superconductors, a short sample from each of the two manufacturers is examined with regard to the critical current-carrying capacity. The critical current I_c is measured according to equation 2.1 with a $1\,\mu V\,cm^{-1}$ criterion at different temperatures, magnetic flux densities and orientation of the magnetic flux density. The measurement system includes a helium gas flow cryostat to generate the cryogenic temperatures in the area of the HTS probe. With a heater attached to the tape sample, stable temperatures between 1.8 K and 200 K can be achieved. The background field is generated by a superconducting split coil which achieves magnetic flux densities of up to 6 T. The sample holder can accommodate tapes with a maximum width of 15 mm and a maximum length of 90 mm and is exposed to the magnetic field in a 64 mm bore. It can be rotated about its own axis with a resolution of 0.5° to change the orientation of the magnetic flux density on the HTS tape. The current leads of the set-up are designed for a current of up to 1000 A. Figure 5.2 shows the basic design of the rotatable sample holder in a cryogenic environment with a magnetic background field. A more detailed description of the measurement system can be found in [191].

Figure 5.3 shows the measured critical currents per centimeter with the $1\,\mu V\,cm^{-1}$ criterion at temperatures between 20 K and 77 K and magnetic flux densities from 0 T to 5 T. The orientation of the magnetic flux density is fixed according to the orientation with the minimum current carrying capacity. Figure 5.3 a) shows the measurement of a 12 mm wide tape sample of tape 1 with a field orientation of 35°. The critical currents of a 5 mm wide tape sample of tape 2 at an angle of 0° are shown in figure 5.3 b). The sample of tape 2 is cut to a width of 5 mm to reduce the total critical current. This allows a broader measurement range for tape 2, since the maximum total current is limited to 1000 A by the measurement setup. For better comparability of the two tape samples, the critical currents per centimeter are given. It can be seen that at relatively high temperatures around 77 K and low

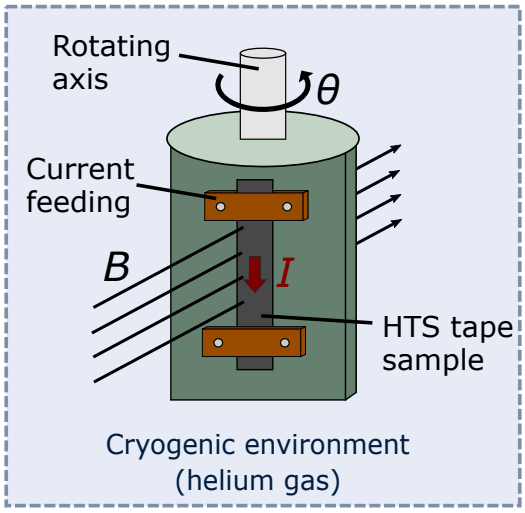

Figure 5.2: Schematic diagram of the measurement setup to determine the critical current of HTS samples as a function of temperature, magnetic flux density and orientation of the magnetic flux density

field, tape 1 has higher critical currents. However, tape 2 can reach similar or even higher critical currents at lower temperatures and higher fields.

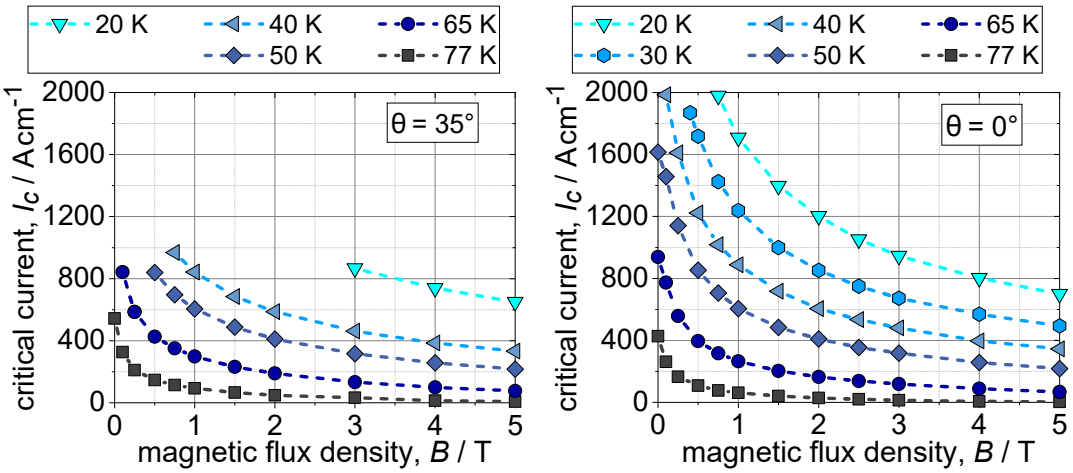

a) Tape 1 **b)** Tape 2

Figure 5.3: Measured critical current per centimeter of the two HTS tapes according to the 1 µV cm^{-1} criteria, at variable temperature and magnetic flux density. The angle of the magnetic flux density is fixed according to the orientation with the minimum current carrying capacity. a) tape 1 with a tape width of 12 mm at an angle of 35° b) tape 2 with a tape width of 5 mm at an angle of 0°

The measurements shown above refer to short tape samples only. However, hundreds of meters of HTS tape are used in superconducting coil systems. Therefore, the homogeneity of the critical current I_c over the entire tape length also plays

an important role. In total, 1 km and 0.4 km of tape 1 and tape 2 are used in the coils presented in this work. The I_c data for the entire tape length is provided by the manufacturers at a measuring distance of 0.2 m for tape 1 and 0.1 m for tape 2, at 77 K, self-field with a 1 µV cm^{-1} criterion. The average critical current I_c for tape 1 and tape 2 with their 12 mm and 10 mm wide ReBCO layers is 674 A and 315 A respectively, while the maximum deviation from the average critical current of 44 % for tape 1 is much higher than that for tape 2 with 14 %. In addition to the inhomogeneity of the critical current I_c, the geometric dimensions also have a tolerance range due to the manufacturing process. The data regarding I_c and the geometric dimensions with the respective minimum and maximum values for the tapes used are summarized in table 5.1.

Table 5.1: Critical current and geometrical data of the used HTS tapes

Parameter	Tape 1	Tape 2
Average I_c	674 A	315 A
Minimum I_c	380 A	275 A
Maximum I_c	880 A	360 A
(@ 77 K, self-field, 1 µV cm^{-1})		
Maximum deviation of I_c	44 %	14 %
Tilt of ReBCO layer	30°	-
(with respect to substrate normal)		
ReBCO layer width	12 mm	10 mm
Copper stabilizer width	12 mm	12 mm
Average tape width	12.17 mm	12.00 mm
Minimum tape width	12.00 mm	11.90 mm
Maximum tape width	12.45 mm	12.10 mm
Hastelloy^{TM} C276 thickness	100 µm	50 µm
Copper stabilizer thickness	100 µm	2 x 75 µm
Average tape thickness	0.212 mm	0.190 mm
Minimum tape thickness	0.190 mm	0.178 mm
Maximum tape thickness	0.230 mm	0.202 mm
Total length of used tape	1.0 km	0.4 km

5.1.2 Turn-to-turn resistance

As described in section 2.3, the contact resistance between the HTS tapes used, significantly influences the dynamic behavior of no insulation coils. Therefore, the contact resistivity ρ_c between two short tape samples is investigated in a preliminary test. The samples lie on top of each other and overlap at a length of 40 mm with a contact surface of 480 mm^2. The side of the tape facing the substrate is called the back side, while the side with the ReBCO layer is defined as the face side. In order to obtain the same contact configuration as in the wound coils, only face to back contacts are examined in this measurement. The measurements are performed in a bath of liquid nitrogen (LN2) at a temperature of approximately 77 K to ensure superconductivity. Using a hand-lever press, a pressure of up to 100 MPa can be applied to the contact surface. The forces that occur are recorded with two load cells. A DC current of 10 A is applied to both ends of the tapes and the voltage drop across the contact area is measured at different pressures. The basic measurement setup is shown in figure 5.4.

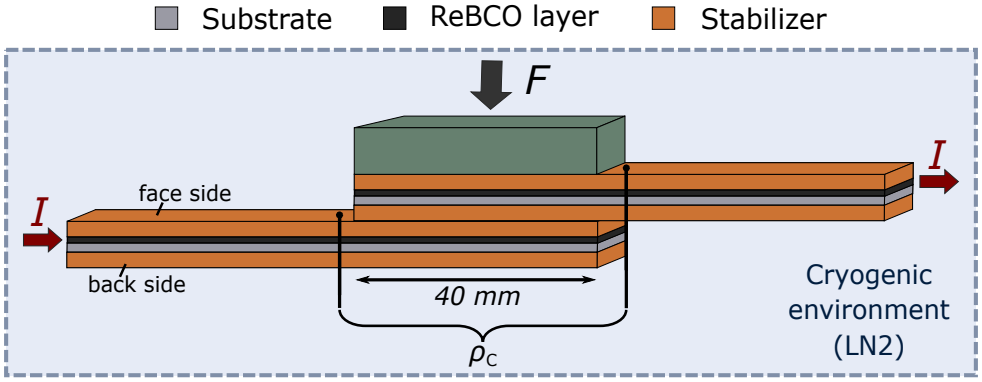

Figure 5.4: Measurement setup for determining the turn-to-turn resistance between two tape samples at variable contact pressure in LN2 at 77 K

The influence of mechanical load cycles is considered by six load cycles per sample arrangement. Cycle 0 describes the first measurement without any plastic deformation of the two HTS tapes involved. A total of 10 contact configurations with two overlapping HTS tapes each are investigated. Figure 5.5 a) to d) shows four contact configurations in which two samples of tape 1 lie directly on top of each other. Figure 5.6 a) to b) similarly shows two direct contact junctions between tape 2. It can be seen that the contact resistivity ρ_c between samples of tape 2 is orders of magnitude smaller than for tape 1. This can be explained by the direct short circuit caused by the 1 mm wide solder-filled outer areas of tape 2, as shown in figure 5.1. To achieve similar turn-to-turn resistance for the coils wound with tape 2, a 25 µm thick and 12 mm wide Hastelloy^{TM} C276 tape is used to artificially increase the contact resistivity between the tapes. Four further contact measurements with tape 2 and the intermediate metal tape are shown in figure 5.7 a) to d). By using the metal tape, the contact resistivity ρ_c for tape 2 can be significantly increased and reaches similar magnitudes as bare contacts with

tape 1. All contacts show a reduction of the contact resistivity ρ_c at increasing contact pressure with an asymptomatic behavior to a minimum value. With a sufficiently high contact pressure, the bare contacts with tape 1 and the contacts with tape 2 and intermediate metal tape both achieve a contact resistivity in the range of 500 $\mu\Omega\,cm^{-2}$ m. After the initial plastic deformation, mechanical cycling has only a minor effect on most sample contacts. However, the various contacts show a very large variation in resistivity due to the different surface properties of the contacts.

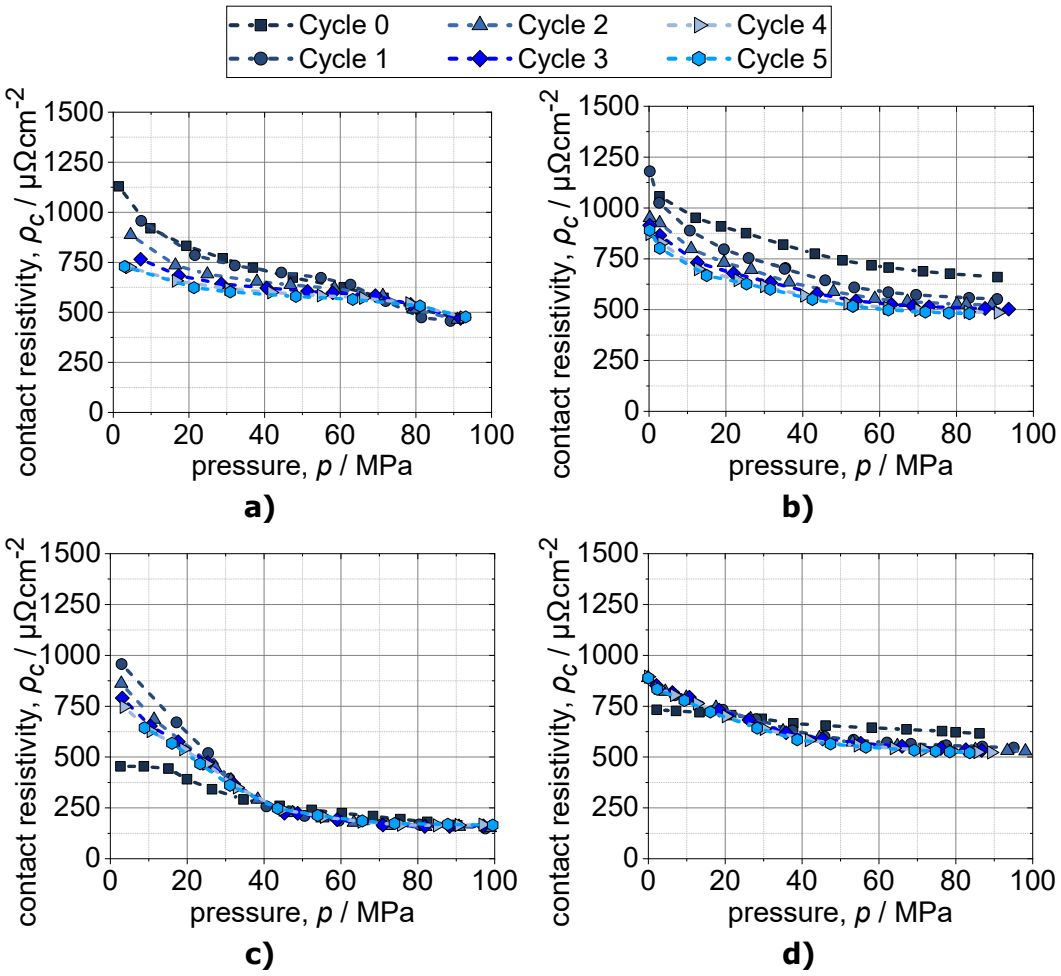

Figure 5.5: Measured turn-to-turn resistivity in LN2 for different applied pressures with a total of six load cycles. a) - d) 4 samples of tape 1

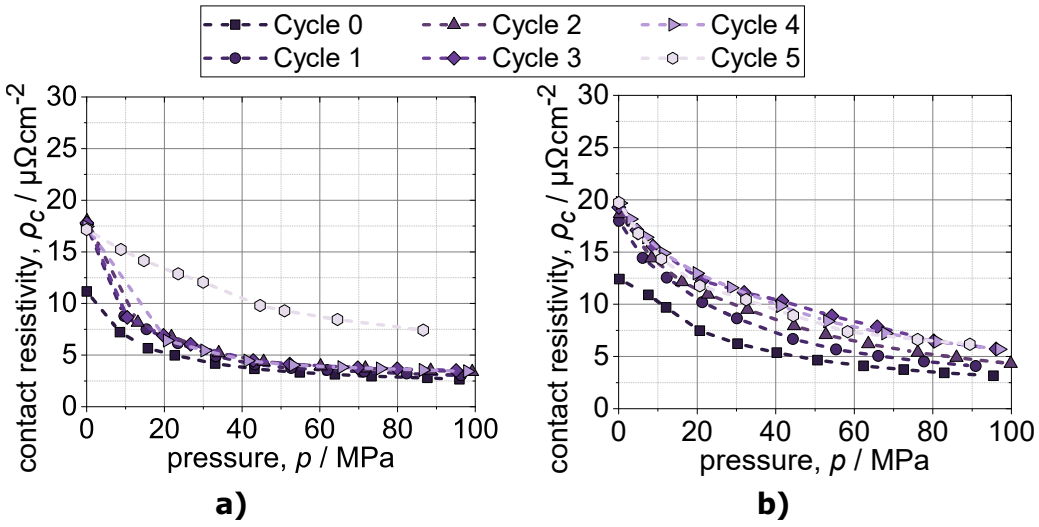

Figure 5.6: Measured turn-to-turn resistivity in LN2 for different applied pressures with a total of six load cycles. a) - b) 2 samples of tape 2

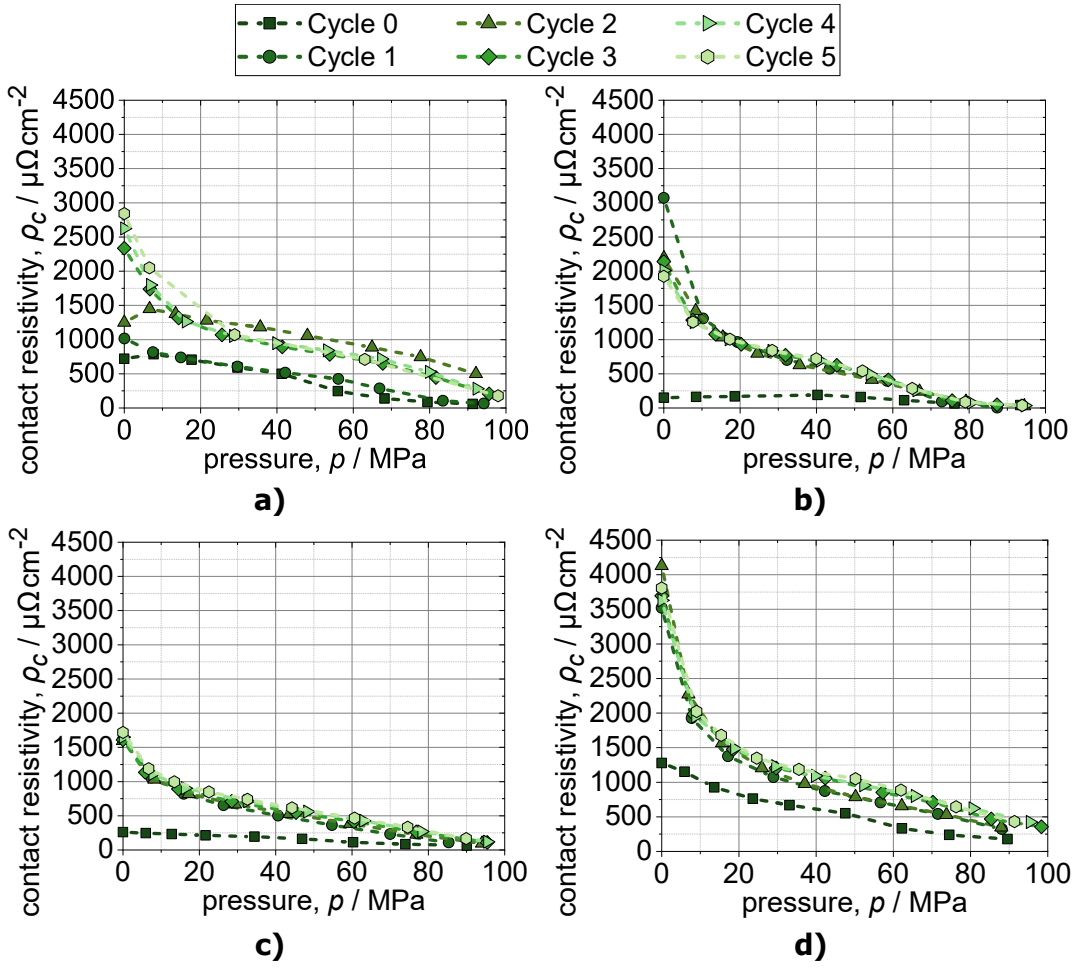

Figure 5.7: Measured turn-to-turn resistivity in LN2 for different applied pressures with a total of six load cycles. a) - d) 4 samples of tape 2 with intermediate 25 µm thick Hastelloy^{TM} C276 tape

5.2 Design and manufacturing of the coils

The superconducting coils in this work are designed as pancake coils in a racetrack shape as introduced in section 2.3 and are wound without electrical insulation between the turns. The design is developed according to the electromagnetic, thermal and mechanical requirements in the 10 kW generator technology demonstrator. Each pancake is wound around a 6 mm wide and 12 mm high stainless steel coil former. The superconducting winding is kept in the racetrack shape by the coil former and no additional potting or resin is used. Copper plates with a thickness of 3 mm press on the top and bottom of the pancake winding to provide conduction cooling. The copper plates are electrically insulated with a thin Kapton® foil and vacuum grease is used for better thermal contact between the plates and superconducting winding. On the back of each pancake a copper conduction cooling terminal acts as a thermal link to the cryogenic cooling system. The G10 mechanical support is later attached to the inner coil former to transmit the coil forces to the outer structures. The thermal and electrical connection terminals are designed to allow separate tests on individual pancakes. Each pancake is wound with a total of 100 m of continuous HTS tape, resulting in 115 turns.

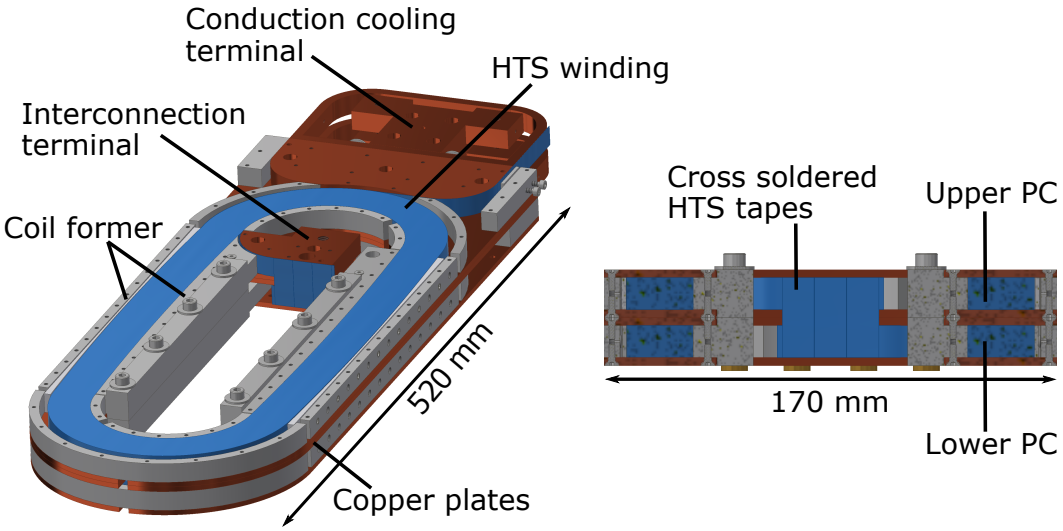

Figure 5.8: Total view and a cross-sectional view of the basic double pancake design. In the total view the top copper plate is removed for a better representation

One magnetic pole in the generator demonstrator consists of a double pancake. Therefore, two individual pancakes are stacked and are electrically connected in series. The electrical connection is realized by a cross-connection of three HTS tapes at the interconnection terminal in the center of the coil. Figure 5.8 shows a total view and a cross-sectional view of the basic double pancake design. For a better representation, the top copper plate is not shown in the total view. The basic parameters of a pancake and an interconnected double pancake are listed in the table 5.2. The design of the double pancake coils was first presented in [192].

Table 5.2: Coil parameter

Parameter	Pancake	Double pancake
Total length	520 mm	-
Effective length	420 mm	-
Total width	170 mm	-
Winding height	12 mm	-
Copper plates height	3 mm	-
Total height	18 mm	36 mm
Inner radius	43 mm	-
Outer radius	85 mm	-
Number of turns	115	2 x 115 (series connected)
HTS tape length	100 m	200 m
Inductance	5.6 mH	18.8 mH

According to the contact resistivity measurement from section 5.1.2, increased mechanical pressure helps to homogenize the turn-to-turn resistance in NI coils. Therefore, additional pressure is applied to the superconducting winding via seven setscrews in the outer stainless steel former on the straight sides of the NI coils. To ensure constant pressure, self-locking M5 screws specially developed for the cryogenic temperature range are used [193]. Figure 5.9 shows the straight side of a double pancake with the setscrews, to apply the additional mechanical pressure. For a better overview, the setscrew are marked in red and the outer stainless steel former of the upper pancake is transparent.

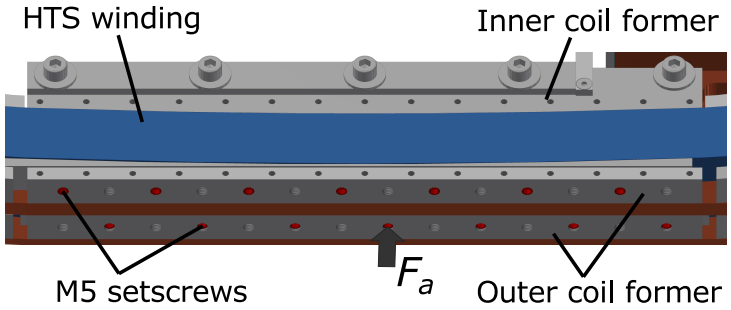

Figure 5.9: Straight part of a DPC with red marked setscrews to apply additional mechanical pressure on the HTS winding. The upper copper plate is removed for better visibility

The screws are tightened with a defined torque of 3.4 N m. According to [194], the axial force with which an M5 setscrew presses on the HTS winding results in:

$$F_a = \frac{2 \cdot M}{d_{sidewall} \cdot tan(\upsilon + \nu)} = 25.55kN \tag{5.1}$$

with a tightening torque of M = 3.4 N m, a sidewall diameter of $d_{sidewall}$ = 4.48 mm, a pitch angle of υ = 3.25° and a friction angle of ν = 0.15° for a bare stainless steel screw and thread [194].

In order to transfer the axial forces of the screws to the entire straight section of the winding, an additional stainless steel plate is placed in between. Thus, the total contact pressure, with seven setscrews over an area of 2880 mm^2, results in 62.1 MPa.

In total, 14 pancake coils are manufactured in this work, each with 100 m wound HTS tape. Ten of the coils are wound with tape 1 and the remaining four with tape 2. The coils with tape 1 are designed as no insulation (NI) coils, while the coils with tape 2, according to the preliminary measurements from subsection 5.1.2, are co-wound with a 25 µm thick Hastelloy^{TM} C276 tape and are thus carried out as metal insulation (MI) coils.

To obtain good resistive contacts on the spiral path of the coil, all electrical connections are soldered. The reduction in dissipated heat during current supply is particularly important under conduction cooled conditions below 77 K. To avoid high temperatures during the soldering process and thus degradation of the HTS, In-Ag (97%-3%) solder with a melting temperature of 143 °C is used. The 432 mm^2 contact areas are prepared with Spirflux 330®. Due to the good thermal coupling and large thermal mass of the coils, the heat required for the soldering process is provided as locally as possible. Therefore, heating cartridges are inserted directly at the soldering point and the temperature is monitored and controlled by a temperature sensor. For a good soldering result, the temperature is adjusted to a maximum of 165 °C and the soldering surface is additionally exposed to mechanical pressure by using screws. For the individual measurements of the pancakes, the HTS tapes are first soldered to the copper blocks at the center and back terminals. Later, the solder contacts are removed and reused to connect the pancake to a double pancake at the central terminal and the double pancake to the entire coil system at the back terminal. The interconnection of the coils is realized by three parallel cross-soldered HTS tapes.

At the beginning of the winding process, the lower copper plate of a pancake, the inner coil former and the central interconnection terminal are initially mounted. The HTS tape is then soldered to the central interconnection terminal and subsequently wound around the inner coil former. The coil former is rotated by a stepper motor which counts the number of coil turns. The HTS tape is unwound from a supply spool and a second motor puts the tape under tension by a counter-rotating motion. When winding with tape 2, a second supply spool is used, which enables co-winding of the metal tape. After the required number of turns has been reached, the winding is mechanically tensioned with the outer coil former and the soldering is performed at the back terminal. Finally, the upper copper plate

is mounted and the setscrews on the straight part of the coil are tightened to the specified torque of 3.4 N m.

Figure 5.10 depicts the manufacturing process of no insulation (NI) and metal insulation (MI) coils. In figure 5.10 a) the coil winding set-up in the case of an MI winding with tape 2 is shown. Figure 5.10 b) illustrates the soldering at the central terminal with the heating cartridge and the temperature sensor inserted in an additional copper block. The start of the winding of tape 2 is represented in figure 5.10 c). The HTS tape is already soldered and mechanically fixed at the central terminal. Figure 5.10 d) is a picture of a no insulation pancake with tape 1 and the top copper plate removed. Figure 5.10 e) displays a close-up of two pancake windings without the upper copper plate. On the left is a no insulation coil with tape 1 and on the right a metal insulation coil with tape 2 and co-wound metal tape.

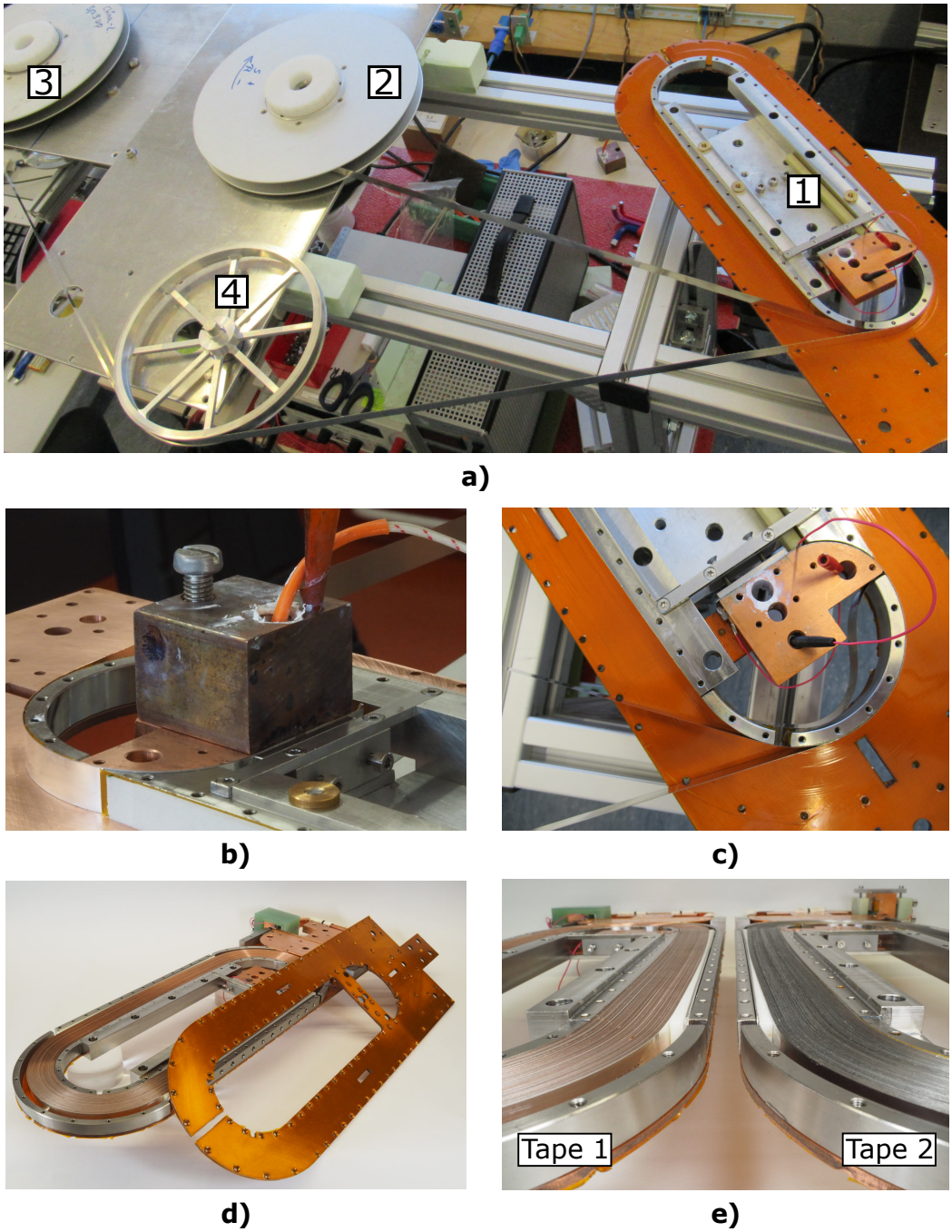

Figure 5.10: a) Coil winding set-up with the target coil former 1, the spool of the HTS tape 2, the spool of the Hastelloy^{TM} C276 tape 3 and a deflection pulley 4 to align the co-wound Hastelloy^{TM} C276 tape. When winding with tape 1, 3 and 4 are not needed
b) Soldering of the center joint at the interconnection terminal
c) Start of coil winding around the inner coil former. The HTS tape is mechanically fixed at the interconnection terminal.
d) Total view of a wound PC with the upper copper plate removed. The PC is wound with tape 1
e) Two wound pancakes without upper copper plate. Left: Pancake wound with tape 1. Right: Pancake wound with tape 2 and Hastelloy^{TM} C276

5.3 Measurements in liquid nitrogen

5.3.1 Critical current of the coils

Estimation of the critical coil current

To estimate the critical current I_c of the no insulation and metal insulation coils, the load line method [195] is used. Therefore, the distribution of the magnetic flux density B in a pancake and double pancake arrangement is determined using the 3D static electromagnetic model already presented in section 4.3. Figure 5.11 shows the magnetic flux density distribution of a pancake and double pancake arrangement, in a total view and cross-sectional view, at an excitation current of 450 A.

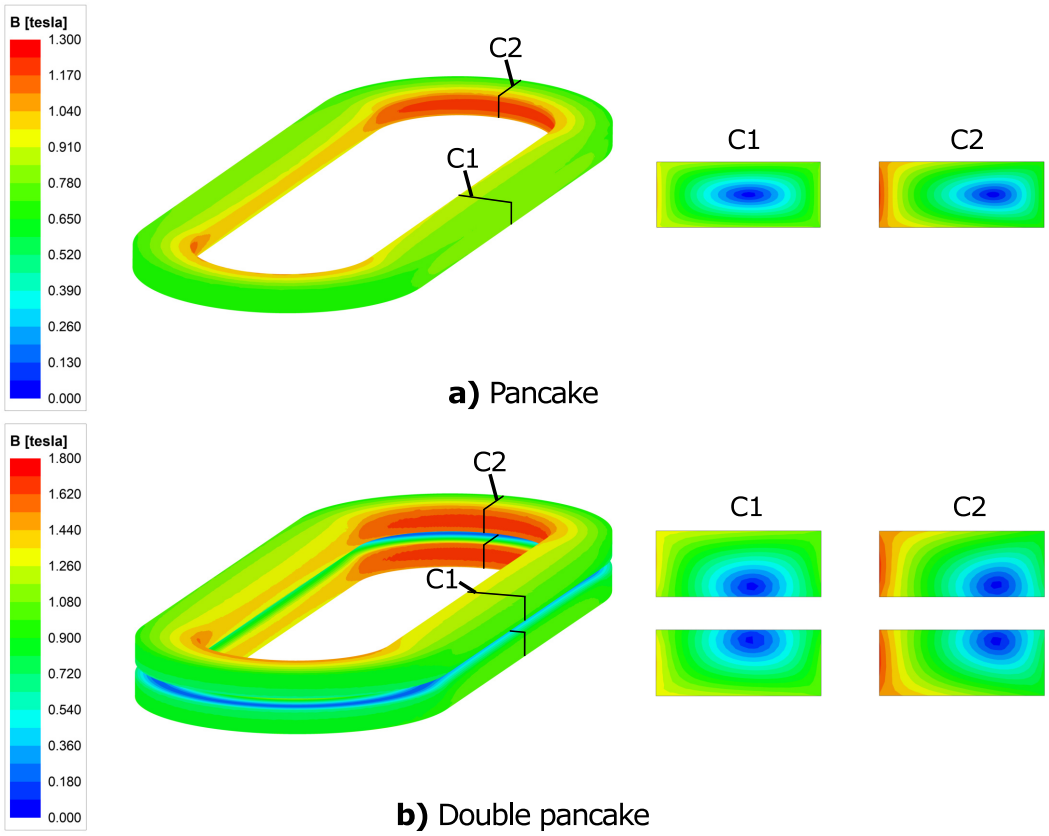

Figure 5.11: Total view and cross-sectional view of the distribution of magnetic flux density in a pancake and double pancake at a supply current of 450 A

It can be seen that especially the innermost coil turns in the curved part of the coils are exposed to the highest magnetic flux densities. Furthermore, the maximum flux density in the double pancake arrangement is higher due to the higher number of turns. The maximum flux density B_{max} in the superconducting coils can be expressed as a linear function of the excitation current and compared with

the critical current measurements of the two tape samples from section 5.1. The simulated linear curve of the maximum magnetic flux density of the coil is plotted against the critical current I_c measurement curves of the tape samples at various temperatures and magnetic field loads. From the resulting intersection points of the curves, an estimation of the I_c of the superconducting coils is obtained. Figure 5.12 shows the overlays of the tape measurement curves and the simulated maximum flux density in the coils according to the load-line method. Figure 5.12 a) shows the measurement curves of tape 1 and figure 5.12 b) the measurement curves of tape 2. The currents are now given in absolute critical current I_c values for HTS tapes with a 12 mm and 10 mm wide ReBCO layers respectively. The measured I_c of the 5 mm wide sample of tape 2 is extrapolated to a ReBCO layer width of 10 mm. The angle of the magnetic flux density is fixed according to the orientation with the minimum current carrying capacity with 35° and 0° respectively. To determine the critical current I_c of both a pancake and double pancake arrangement, the maximum magnetic flux density B_{max} curves for both coil configurations are given.

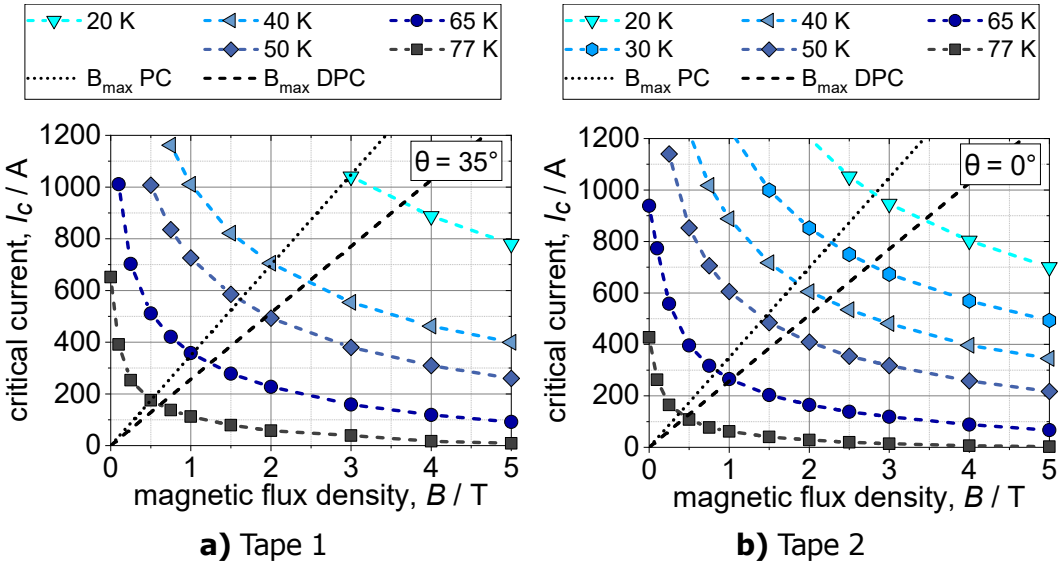

Figure 5.12: Measured critical current of the two HTS tapes according to the 1 µV cm^{-1} criteria, at variable temperature and magnetic flux density. The angle of the magnetic flux density is fixed according to the orientation with the minimum current carrying capacity. a) tape 1 with a tape width of 12 mm at an angle of 35° b) tape 2 with a tape width of 5 mm at an angle of 0°. The measured critical current of tape 2 is extrapolated to a ReBCO layer width of 10 mm. The maximum magnetic flux density in a pancake and double pancake coil as a function of the current is superimposed

The critical current I_c for the no insulation coils with tape 1, at a temperature of 77 K results in 175.7 A and 157.8 A for a pancake and double pancake respectively. For the I_c of the metal insulation coils wound with tape 2, 134.3 A for a pancake and 117.6 A for a double pancake are obtained at 77 K. The determined critical currents

of the superconducting coils correspond to the $1\,\mu V\,cm^{-1}$ criterion. It should be noted that the assumptions made, regarding the minimum current-carrying capacity of the tape samples at the corresponding angles of field orientation and the maximum magnetic flux density occurring in the superconducting coils, represent an estimation of the minimum critical current I_c for the no insulation and metal insulation coils.

Measurement of the critical coil current

All pancake and double pancake coils are pre-tested in a bath of liquid nitrogen (LN2) at around 77 K. The instrumentation for the intended measurements is shown in figure 5.13.

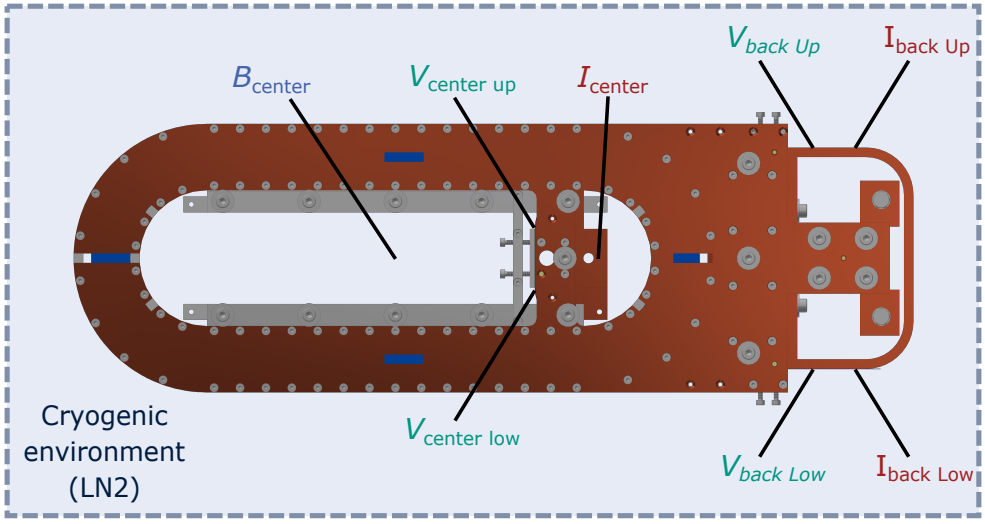

Figure 5.13: Instrumentation of a pancake or double pancake coil during measurements in LN2 at 77 K

The coils are supplied with a DC current via the corresponding connection terminals and the voltages and the magnetic flux density are recorded. The magnetic flux density is measured at the exact center of a pancake or double pancake with a Hall sensor specially calibrated for cryogenic temperatures (B_{center}). The voltage is tapped through soldered contacts at the beginning and end of each pancake or double pancake winding. If a single pancake is measured, current feeding and voltage measurements are performed at a back terminal and at the center terminal of the upper or lower pancake respectively (I_{center},V_{center} + I_{back},V_{back}). When measuring a double pancake, both back terminals are used on the upper and lower pancake for the current feeding ($I_{back\,Low}$ + $I_{back\,Up}$), while all voltage taps are used for the recording. At the position of each voltage tap, both the potential directly on the superconductor and the potential of the copper block from the electrical connection terminal are tapped. This allows, the additional measurement of the resistance of the soldered contacts.

To measure the critical current I_c of the no insulation and metal insulation coils, a DC current with a defined amplitude and slew rate is supplied. After the induced voltage U_{ind} due to the current change has decayed, the voltage drop across the pure spiral superconductor path of a pancake is measured. The voltage-current curve obtained is fitted with a power law fit according to equation 2.1. Some of the coils show a resistive component R_s on the spiral coil path. The power law fit is extended by this resistive component and the absolute voltage U and current I are used to evaluate the measurement results:

$$U(I) = U_c \cdot \left(\frac{I}{I_c}\right)^n + I \cdot R_s \tag{5.2}$$

For a safe test of the coils and to avoid unnecessary damage, the 0.1 µV cm^{-1} criterion is used to determine the critical current in the measurements. With a tape length of 100 m per pancake, this results in a critical voltage limit U_c per pancake of 1 mV. The critical current I_c measurements of all 14 pancake and seven double pancake coils in liquid nitrogen at 77 K are shown in figure 5.14.

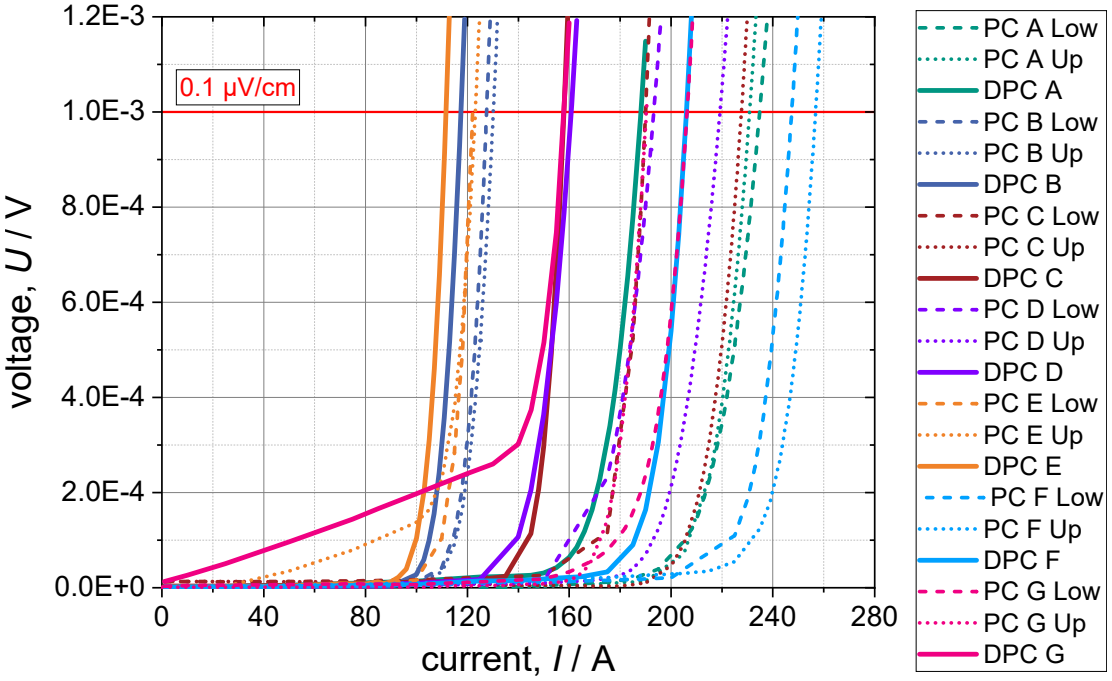

Figure 5.14: Critical current measurements of the NI and MI pancake and double pancake coils in LN2 at 77 K. The critical voltage per pancake is 1 mV according to the 0.1 µV cm^{-1} criterion

The seven double pancake coils are labeled with the letters A to G and are additionally subdivided into the lower and upper pancake, named as low and up respectively. For the measurement of the critical current I_c of a double pancake, the weaker pancake is considered in each case. The obtained values from the

measurement curves with the fit from equation 5.2 are listed in table 5.3. The critical current values for the 1 µV cm^{-1} criterion are determined by extrapolation of the measurement curves. Furthermore, the deviation of the measured critical current I_c values from the estimated I_c values is shown in table 5.3.

Table 5.3: Data of the critical current measurements of the no insulation and metal insulation pancake and double pancake coils in liquid nitrogen at 77 K

Coil	Tape	I_c (A) 0.1 µV cm^{-1}	I_c (A) 1 µV cm^{-1}	Diff. estimated I_c (%) 1 µV cm^{-1}	n-value	R_s (nΩ)
PC A Low	1	234.8	270.6	35.1	16.2	-
PC A Up	1	230.9	260.4	32.5	19.2	-
DPC A	1	188.2	216.8	27.2	16.3	370
PC B Low	2	127.6	144.1	6.8	19.0	-
PC B Up	2	130.2	149.5	10.2	16.7	-
DPC B	2	117.6	133.7	12.0	18.0	-
PC C Low	1	190.2	208.6	15.8	24.9	120
PC C Up	1	227.6	254.9	31.1	20.3	-
DPC C	1	158.1	175.2	9.9	22.4	-
PC D Low	1	193.2	228.1	23.0	13.9	-
PC D Up	1	219.3	253.7	30.7	15.8	-
DPC D	1	160.8	188.5	16.3	14.5	-
PC E Low	2	122.4	138.2	2.8	19.0	-
PC E Up	2	124.0	143.0	6.1	16.2	912
DPC E	2	111.6	126.4	7.1	18.6	-
PC F Low	1	247.5	275.1	36.1	21.8	24
PC F Up	1	257.1	283.6	38.0	23.5	84
DPC F	1	206.2	229.4	31.2	21.5	55
PC G Low	1	206.7	234.6	25.1	18.5	131
PC G Up	1	190.1	211.4	16.9	21.7	-
DPC G	1	160.9	178.9	11.8	21.8	1930

The measurements show that basically all coils demonstrate superconducting behavior. However, some coils also have a pronounced resistive component on the spiral coil path and are therefore not perfectly superconducting. As expected, all coils with tape 1 have a higher critical current due to the higher current carrying capacity of the tape. Double pancake E wound with tape 2 shows the lowest critical current I_c according to the $1\,\mu V\,cm^{-1}$ criterion with 126.4 A. Furthermore, the critical currents of the double pancakes are reduced due to the higher magnetic field exposure compared to the single pancakes. But the double pancakes with tape 2 experience a smaller average reduction in critical current I_c of 8.3 %, while the I_c of the double pancakes with tape 1 is reduced by 17.2 % on average. It can also be seen that especially the coils with tape 1 show a significant variation in the measured critical current I_c. For the $1\,\mu V\,cm^{-1}$, the I_c of the pancakes with tape 1 varies between a minimum value of 208.6 A and a maximum value of 283.6 A. The maximum deviation from the average critical current for the pancakes with tape 1 and tape 2 is 16 % and 4 %, respectively. The deviation of the measured critical currents of the coils can be attributed to the inhomogeneity of the two HTS tapes used. There is also a significant difference between the measured and the, according to the load-line method, estimated critical current values of the coils. For coils with tape 1, the measured average critical current I_c at a $1\,\mu V\,cm^{-1}$ criterion is 72.4 A and 40 A higher than the estimated values for a pancake and double pancake, respectively. For coils with tape 2, the values between the average measured and estimated critical currents are 9.4 A higher for a pancake and 12.5 A higher for a double pancake. The measured values are therefore generally higher than the estimated values and coils with tape 1 show a greater deviation. The deviation can be attributed to the simplified method of estimation using the load-line approach. In this method, only a maximum field load is used for the estimation, without taking into account the more complex distribution of the magnetic flux on the individual HTS tapes in the coil turns. Thus, only a worst case estimation for a minimum expected critical current of the coils can be made. More detailed simulation models for estimating the I_c of superconducting coils are presented in [195]. However, for practical use in the stator system, all superconducting coils produced in this work are measured with respect to their current-carrying capacity anyway. Therefore, these more advanced models will not be considered in the context of this work. Furthermore, the HTS tapes used, and tape 1 in particular, exhibit an inhomogeneity of the critical current over the total length. In fact, the critical current I_c estimation is based on the measurements of a small tape sample. Thus, the inhomogeneity of the tapes also affects the critical current estimation of a pancake winding with a total of 100 m HTS tape.

5.3.2 Dynamic charging and discharging

To investigate the dynamic behavior of the no insulation and metal insulation coils, a series of measurements with defined charging and discharging currents are performed. The supply current varies in its amplitude and slew rate. As shown in figure 5.13, the magnetic flux density is measured in the center of the coils and the delay of the field generation τ is determined by measurement as described in section 2.3. The magnetic flux density of the coils is recorded with hall sensors of type HHP-VP, specially designed for cryogenic temperatures, from the company *AREPOC* [196]. All no insulation pancake and double pancake coils are fed with a maximum current of 150 A and positive and negative slew rates of 1 A s^{-1}, 10 A s^{-1}, 50 A s^{-1} and 100 A s^{-1}. Due to their lower critical current, the metal insulation coils are fed with the same slew rates but only up to a maximum current of 100 A. In addition, sudden discharge measurements are carried out, where the supply is abruptly interrupted at different maximum, steady-state currents by using a switch. The no insulation coils are respectively interrupted at steady-state currents of 150 A, 100 A, 50 A, and 25 A. The sudden discharge tests of the metal insulation coils are performed at currents of 100 A, 75 A, 50 A and 25 A, respectively. This results in 12 measurements per coil with eight different slew rates and four sudden discharge measurements at different start currents. Figure 5.15 shows exemplary the measured magnetic flux density of all pancake and double pancake coils at a slew rate of 10 A s^{-1} and a sudden discharge test at a start current of 100 A. Due to the different amplitudes of the supply currents, the magnetic flux density is normalized to the maximum steady-state magnitude for better representation. Furthermore, all measurements are standardized to a common start time of the current ramp or sudden discharge.

The measured delay in the generation of the magnetic flux density can be quite different for the coils, due to their different turn-to-turn contact conditions. As already explained in section 2.3, the contact resistivity ρ_c is influenced by various factors such as surface properties like oxidation and roughness, contact pressure, temperature, mechanical and thermal cycling and the layer structure of the HTS tapes [79, 80]. Moreover, it can be seen that even with various measurements on the same coil, slightly different time constants τ are achieved. It is possible that the contact conditions in the coils change due to thermal and mechanical cycling. Furthermore, the time constant τ itself is dependent on the slew rate. Due to the increased induced voltage U_{ind} with a faster current increase dI/dt, a larger radial current I_r flows through the turn-to-turn contacts. This leads to more involved turn-to-turn contacts, resulting in a larger total radial resistance R_r. According to equation 2.4 a larger radial resistance R_r thus results in a shorter time constant τ under the assumption of constant inductance L. The results of the dynamic charging, discharging and sudden discharge measurements for all no insulation and metal insulation pancake and double pancake coils are summarized in table 5.4. The minimum, maximum and average time constants of all measurements are given. The measured time constants range from 4.69 s to 46.32 s. Coil D exhibits by far the largest delay in the buildup of the magnetic flux

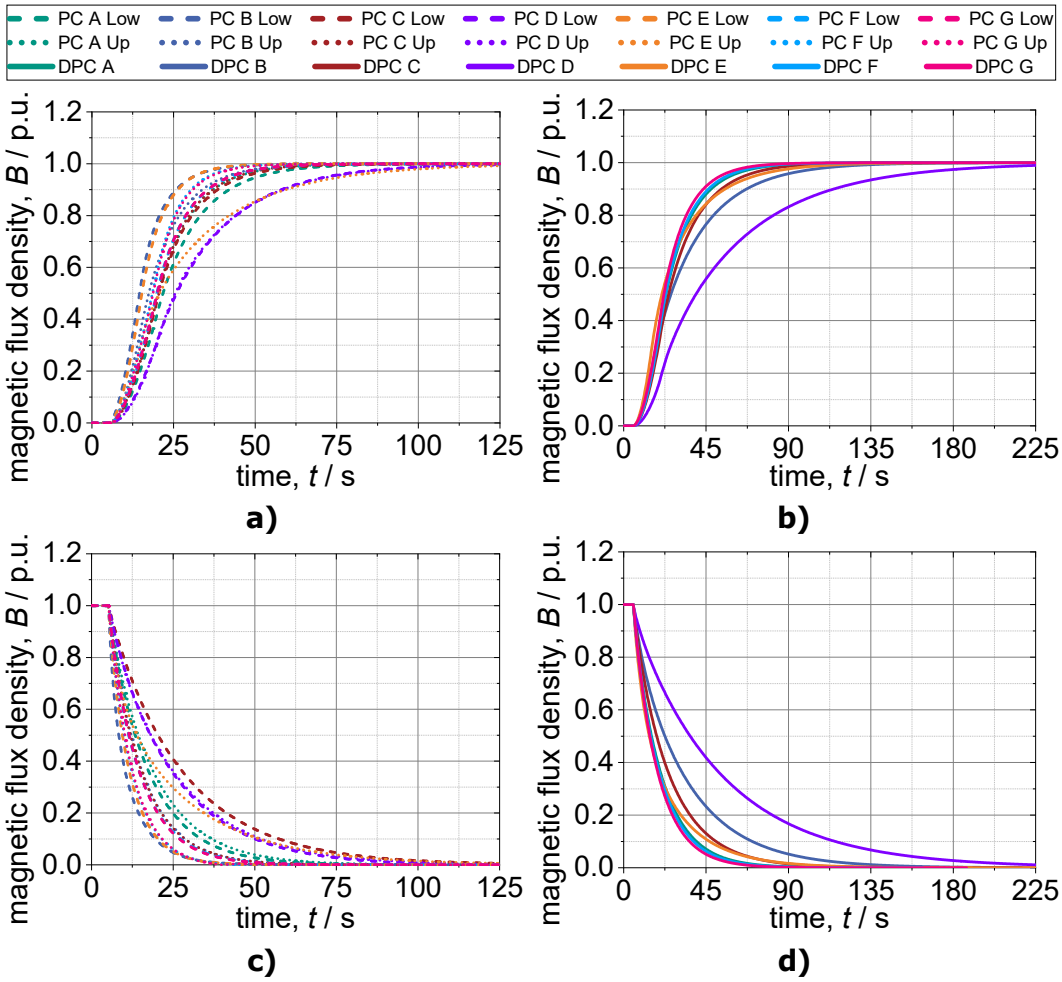

Figure 5.15: Measured center magnetic flux density of the no insulation and metal insulation pancake and double pancake coils in liquid nitrogen at 77 K. For a better overview, the measurements are standardized to a common start time and normalized to the respective steady-state magnetic flux density.
a) No insulation pancake coils with a 10 A s^{-1} current ramp up to a maximum current of 150 A and metal insulation pancake coils with a 10 A s^{-1} current ramp up to a maximum current of 100 A.
b) No insulation double pancake coils with a 10 A s^{-1} current ramp up to a maximum current of 150 A and metal insulation double pancake coils with a 10 A s^{-1} current ramp up to a maximum current of 100 A.
c) Sudden discharge of the no insulation and metal insulation pancake coils at a current of 100 A.
d) Sudden discharge of the no insulation and metal insulation double pancake coils at a current of 100 A

density. Furthermore, due to the increased inductance, the double pancakes show an increased time constant compared to their two individual pancakes in most cases. According to equation 2.4 the resulting radial resistance R_r is calculated

based on the averaged time constant τ_{avg} and the respective inductance for a pancake or double pancake. With the radial resistance R_r the average contact sensitivity ρ_c can be obtained by using equation 2.8.

Table 5.4: Data of the dynamic charging and discharging measurements of the no insulation and metal insulation pancake and double pancake coils in liquid nitrogen at 77 K

Coil	Tape	τ_{min} (s)	τ_{max} (s)	τ_{avg} (s)	R_r (µΩ)	ρ_c (µΩ cm^2)
PC A Low	1	11.04	13.36	12.05	464.65	213.85
PC A Up	1	10.08	13.29	11.27	496.74	228.62
DPC A	1	14.18	16.62	14.86	632.73	291.21
PC B Low	2	4.94	7.22	6.33	884.18	406.93
PC B Up	2	9.82	10.18	9.99	560.48	257.95
DPC B	2	23.00	26.74	24.70	380.53	175.13
PC C Low	1	9.33	21.74	14.14	396.05	182.28
PC C Up	1	9.57	11.12	10.02	558.96	257.26
DPC C	1	16.69	20.11	17.69	531.50	244.62
PC D Low	1	18.00	19.86	18.78	298.23	137.26
PC D Up	1	17.11	20.56	18.95	295.49	136.00
DPC D	1	40.22	46.32	43.15	217.85	100.26
PC E Low	2	6.22	7.54	6.65	842.08	387.56
PC E Up	2	14.89	24.97	18.89	296.42	136.42
DPC E	2	13.86	22.23	17.21	546.17	251.37
PC F Low	1	9.15	10.32	9.51	589.04	271.10
PC F Up	1	5.65	7.72	6.94	807.11	371.47
DPC F	1	13.79	15.85	14.18	662.83	305.06
PC G Low	1	9.07	10.74	9.45	592.90	272.88
PC G Up	1	4.69	8.63	7.11	787.32	362.36
DPC G	1	12.67	13.34	13.08	718.65	330.75

The contact resistivity ρ_c varies between a minimum and maximum value of 100.26 µΩ cm^2 to 406.93 µΩ cm^2 and is thus smaller than the contact transitions determined from the preliminary measurements of the individual tape samples

from the figures 5.5 and 5.7. Nevertheless, as already shown in the preliminary measurements, similar turn-to-turn contact ratios can be created in the MI coils by co-winding the Hastelloy^{TM} C276 tape. Further, the additional mechanical pressure of the outer setscrews homogenized the contact transitions in the individual coils, resulting in an overall similar dynamic behavior of all 14 pancake coils.

5.3.3 Performance under overcritical conditions

The superconducting stator system consists of a total of six magnetic poles. However, seven double pancakes are produced. Double pancake G is not used in the stator system and can therefore be subjected to overcritical measurements that risk degradation or destruction of the superconducting windings. To test the passive self-protection of the developed no-insulation coils, double pancake G is exposed to currents above its critical current of 160.9 A with 0.1 µV cm^{-1}. As in the measurements for determining the critical current, the coil is fed with a DC current with a defined amplitude and slew rate. After the induced voltage has decayed, the magnetic flux density in the center of the double pancake coil and the voltage drop across the two pancake coils are recorded for a period of 10 minutes. The averaged values from the measured data are shown as a function of the supply current in figure 5.16.

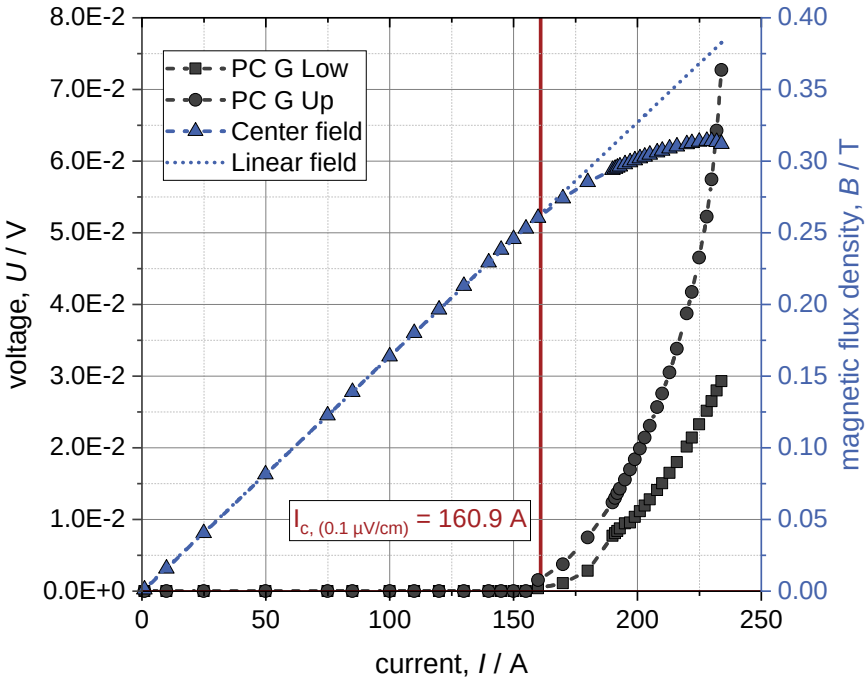

Figure 5.16: Measurement of double pancake G with up to 1.5 times of the critical current in liquid nitrogen at 77 K

At currents below the critical value, no significant voltage drop can be detected on the spiral superconducting path in the steady-state. The measured magnetic

flux density increases linearly with the injected DC current in accordance with the coil constant. As in the measurements for determining the critical current I_c of the coil, pancake G Up has the lower critical current and thus a faster increase in the measured voltage drop. With 72.7 mV, almost 73 times of the defined critical voltage according to the 0.1 µV cm^{-1} criterion is reached and the coil can be operated stable with almost 1.5 times of its critical current I_c. In the sub-critical case, after the induced voltage has decayed, the complete current flows in the spiral coil path I_s and thus contributes to the field generation. When the critical current is exceeded, parts of the spiral coil path become resistive and the current is diverted into the radial coil path via the turn-to-turn contacts. The proportion of the radial current I_r increases with higher coil current and thus no longer contributes to the field generation. As a result, the magnetic flux density saturates and does not increase linearly any further. An insulated coil would continue the linear increase of the magnetic flux density after reaching the critical current I_c until its local thermal destruction.

5.4 Measurements under conduction cooled conditions

5.4.1 Measurement set-up

Since the developed coils are operating at temperatures below 77 K via conduction cooling, additional pre-testing under these cryogenic conditions is performed. However, only measurements on individual coils are carried out, since the effort required is significantly greater compared to measurements in liquid nitrogen. The basic structure of the measuring system with its individual components is shown in figure 5.17 and is presented in the following. For the cooling of the sample and the substructures in the system, two two-stage cryocooler systems are used. In addition, cooling is realized by a liquid nitrogen (LN2) reservoir inside the vacuum measurement chamber. The LN2 directly cools a thermal shield to approximately 77 K to reduce the radiant heat on the sample at lower temperatures. Furthermore, a cold nitrogen gas flow can be forced by means of an LN2 heater to pre-cool the current leads to a temperature of about 100 K. The warmed nitrogen gas is released to the atmosphere by a pipe system. The first cooling stage of the cold heads is also connected to the current leads for pre-cooling and further cools the mechanical support structures to reduce heat input by conduction to the lower temperature levels. However, the forces occurring during the individual coil tests are completely absorbed by the coil former and cancel out each other. This eliminates the need for complex mechanical support in the cryogenic region. The continuation of the current leads and the second cooling stage is connected to a thermal anchor point. At this position, heaters can be used to set an arbitrary temperature below 77 K by a PID control.The thermal coupling and current lead connection both take place on the back of the test coil. Thus, similar thermal

conditions are achieved for the coils as later in the generator setup. Measurements under conduction-cooled conditions of the coils were first published in [192].

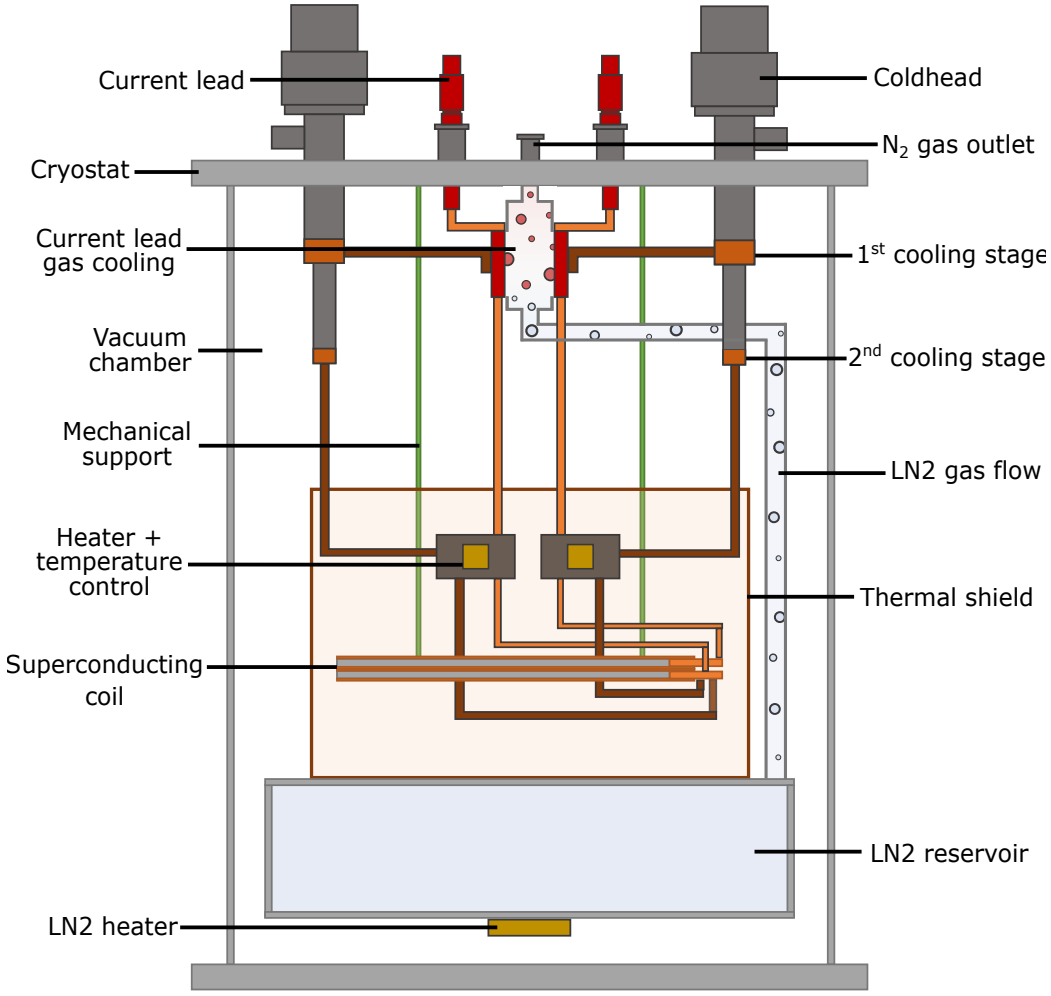

Figure 5.17: Measurement set-up for testing superconducting components under conduction cooled conditions at variably adjustable temperatures below 77 K

5.4.2 Critical current of the coils

Measurements of the critical current at different temperatures are performed for pancake G Up. The measurements are conducted as described for the critical current measurements in subsection 5.3.1. In order to reproduce the result from the liquid nitrogen tests, the temperature in the set-up is first adjusted to 77 K. Further temperatures at which the critical current I_c of the pancake is determined are 65 K, 50 K and 40 K.

Due to the increased current-carrying capacity of the coils at lower temperatures, a thermal equilibrium cannot be achieved in the set-up because of the associated

increased heat input. Therefore, only the I_c measurement results down to a minimum temperature of 40 K are shown. The measured critical current I_c of pancake G Up for the different temperatures under conduction-cooled conditions is shown in figure 5.18 a). For reference, the measured critical current I_c in liquid nitrogen is additionally plotted. Further, the estimated critical current I_c for a no insulation pancake and double pancake wound with tape 1 are shown according to the load line method from figure 5.12. In addition, the estimated critical currents at different temperatures for the metal insulation pancake and double pancake coils wound with tape 2 are given in figure 5.18 b).

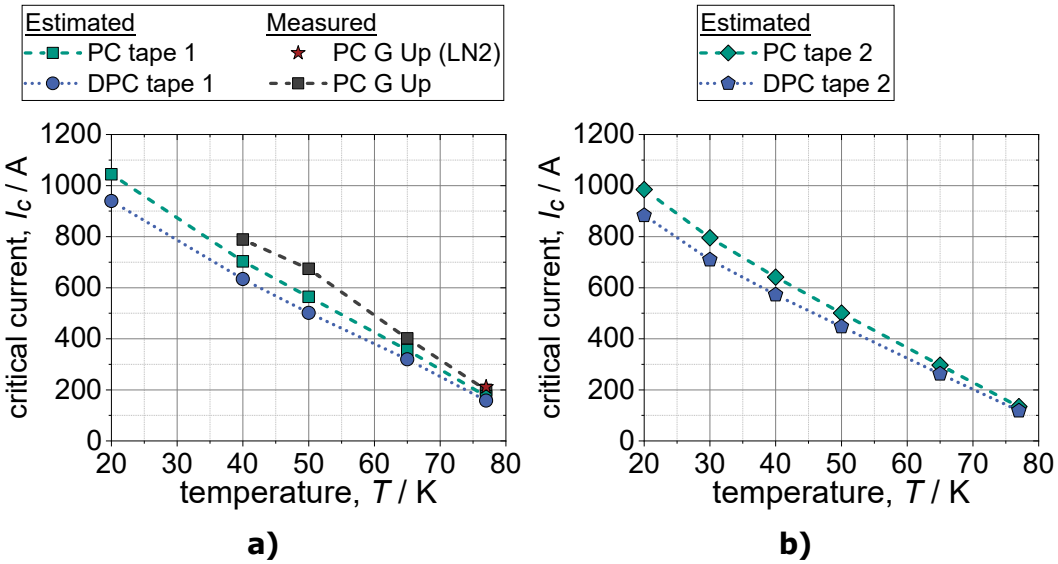

Figure 5.18: Estimated and measured critical current at different temperatures below 77 K according to the 1 µV cm^{-1} criterion.
a) Estimated critical current of the NI pancake and double pancake coil. Measured critical current of pancake G Up in LN2 and under conduction cooled conditions
b) Estimated critical current of the MI pancake and double pancake coil

However, no measurements are carried out in the described set-up with metal insulation coils. All estimated and measured values refer to the 1 µV cm^{-1} criterion. The measured critical current I_c at 77 K in liquid nitrogen and under conduction-cooled conditions is 211.4 A and 199.6 A, respectively. The deviation may be due to locally different temperature distributions under conduction-cooled conditions, whereas in a bath of liquid nitrogen, the cryogenic liquid ensures a homogeneous temperature. Both the estimated and measured critical currents show an approximately linear increase with decreasing temperature. This is due to the increased current carrying capacity of the tapes at lower temperatures and the corresponding increase in magnetic field exposure due to the self-field of the coils at higher supply currents. Similar to the liquid nitrogen measurements, the estimated and measured critical currents show an average deviation of about 14.6 %. This can again be attributed to the inhomogeneous critical current distribution of

the superconducting tapes and the fact that the applied estimation with the load line method represents an estimation for the expected minimum coil I_c. Critical currents above the rated current of 450 A at a temperature in the generator of 30 K are achieved with the coils from both tapes.

5.4.3 Dynamic charging and discharging

In order to investigate the dynamic behavior under conduction-cooled conditions, measurements are carried out on pancake G Low with defined charging and discharging currents at different temperatures. The temperatures are adjusted to 77 K, 65 K, 50 K and 30 K. Pancake G Low is fed with a maximum current of 150 A and slew rates of 1 A s^{-1}, 10 A s^{-1}, 50 A s^{-1}, and 100 A s^{-1}, as with the no insulation coil tests in liquid nitrogen. The sudden discharge measurements at steady-state currents of 150 A, 100 A, 50 A and 25 A are also repeated under conduction-cooled conditions. Figure 5.19 shows an example of the measured magnetic flux density of pancake G Low with a slew rate of 10 A s^{-1} and for a sudden discharge test at a start current of 100 A for the different temperatures.

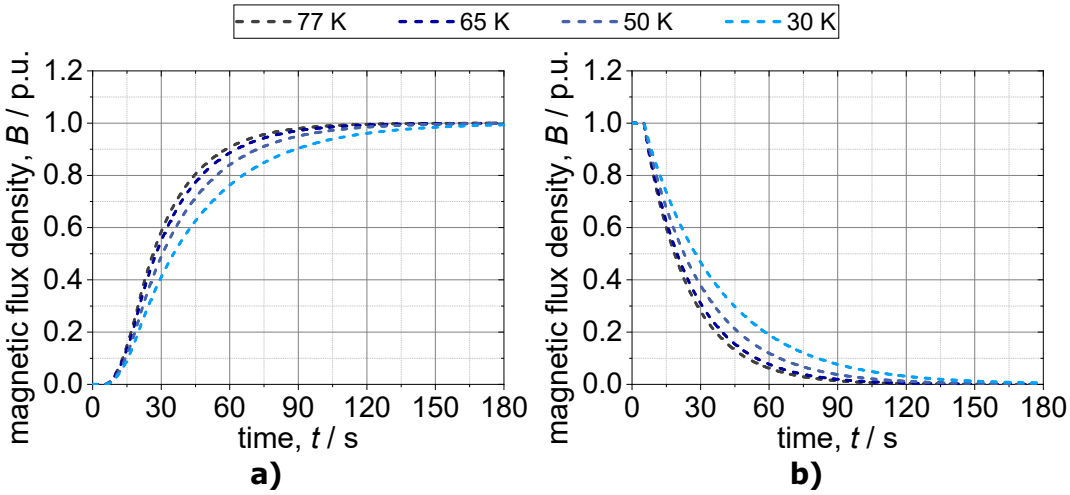

Figure 5.19: Measured center magnetic flux density of pancake G Low at variable temperatures. For a better overview, the measurements are standardized to a common start time and normalized to the respective steady-state magnetic flux density.
a) 10 A s^{-1} current ramp up to a maximum current of 150 A.
b) Sudden discharge at a current of 100 A

The results of the dynamic charging, discharging and sudden discharge measurements of pancake G Low are summarized in table 5.5. The minimum, maximum and average time constants as well as the for the average time constant resulting radial resistance and contact resistivity at the different temperatures are given. The time constant of pancake G Low under conduction cooled conditions is significantly larger at 77 K than for the measurements in liquid nitrogen. This could be

due to a change in the contact conditions in pancake G Low caused by the cooling and warm-up cycles or due to a fundamentally different turn-to-turn contact behavior in the liquid nitrogen bath. Further, an almost linear increase of the time constant at lower temperatures can be observed. This can be partly explained by a linear reduction in the electrical resistivity of the materials mainly involved in the turn-to-turn contact, such as Hastelloy^{TM} C276 and copper. According to [175] and [180], the electrical resistivity of a combination of Cu RRR 50 and Hastelloy^{TM} C276 decreases from 77 K to 30 K by 41.8 %, whereas the measured contact resistivity ρ_c of pancake G Low decreases by 40.0 % in this temperature range. Such a decrease in contact resistivity is already reported in [80], for the contact measurements on HTS tape samples.

Table 5.5: Data of the dynamic charging and discharging measurements of pancake G Low at different temperatures

T (K)	τ_{min} (s)	τ_{max} (s)	τ_{avg} (s)	R_r (µΩ)	ρ_c (µΩ cm^2)
77	18.82	19.66	19.20	291.67	134.24
65	20.72	21.30	21.02	266.36	122.59
50	24.86	25.24	25.06	223.48	102.86
30	31.61	32.34	32.00	175.00	80.54

5.4.4 Turn-to-turn losses

As presented in section 2.3, the radial current I_r in no insulation or metal insulation coils causes additional losses across the resistive turn-to-turn contacts during dynamic processes. These turn-to-turn losses are particularly important at lower temperatures under conduction-cooled conditions. Due to the low coil temperatures and the resulting increased current carrying capacity, particularly high supply currents are possible. As a result, high turn-to-turn losses P_{turn} occur during a ramp process. Furthermore, the heat dissipated in the coil can be removed much more slowly under conduction-cooled conditions than in a bath of liquid nitrogen. Finally, the materials involved in the HTS tape and coil have a reduced specific heat capacity c_p at low temperatures which leads to a greater temperature increase when turn-to-turn losses occur. Therefore, further measurements are performed on pancake G Low at a controlled starting temperature of 30 K with very high amplitudes and slew rates of the supply current. In addition to the instrumentation shown in figure 5.13, temperatures are measured directly on the superconducting tape with temperature sensors placed on the surface of the winding. For the environment with high magnetic flux density and for measuring cryogenic temperatures, *Cernox® CX-AA* temperature sensors [197] are used. The positions of the temperature sensors on the pancake coil are shown in figure 5.20.

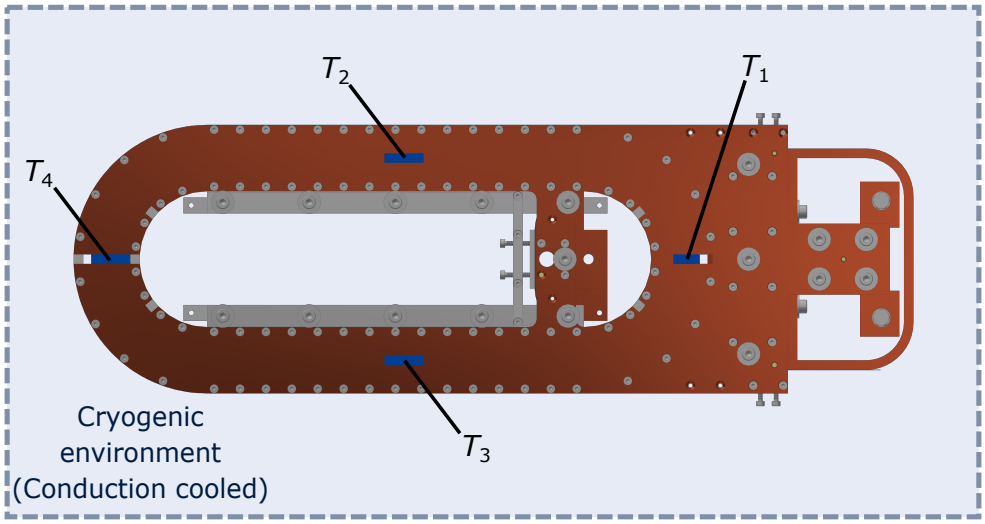

Figure 5.20: Instrumentation of the temperature sensors on pancake G Low during measurements under conduction cooled conditions

In order to better interpret the results of the measurements, a transient 1D thermal-electrical model is developed in *Matlab Simulink* [176]. For this purpose, the simplified equivalent circuit diagram of a no insulation (NI) coil from figure 2.8 is linked to the thermal mass of the pancake coil. The temperature increase of the NI pancake coil due to the heat dissipated in the radial resistance in dynamic processes can thus be estimated. A temperature dependent radial resistance $R_r(T)$ is assumed with a linear fit of the measurement results of pancake G Low from table 5.5. For better representation of the conditions in the measurement environment, the cooling power provided by the entire system is also integrated in the model. To measure the cooling curve, the heating power of the temperature control system presented in figure 5.17 is recorded at thermal equilibrium at different temperatures between 20 K to 75 K. The cooling capability of the overall system for different temperatures is shown in figure 5.21 a).

In addition, the temperature dependent specific heat capacity of the main materials involved is taken into account in the model. The specific heat capacity c_p for Hastelloy^{TM} C276 and Cu RRR 50 as a function of temperature from [175, 180] between 20 K to 75 K are given in figure 5.21 b). The principle relationship between the electrical and thermal part of the 1D model with the temperature dependent quantities is presented in figure 5.22. The inductance and the total mass of a pancake coil are 5.6 mH and 6.41 kg, respectively. The average measured initial temperature from the sensors T_1 to T_4 is used as the start temperature in the model.

The pancake coil G Low is fed at an average measured starting temperature of 30.14 K with a maximum charge current of 450 A at a slew rate of 650 A s^{-1}. In addition to the current, the voltage over the entire pancake winding, the magnetic flux density in the center of the coil and the temperatures directly on the winding are recorded during the charging process. The measured values are shown as solid

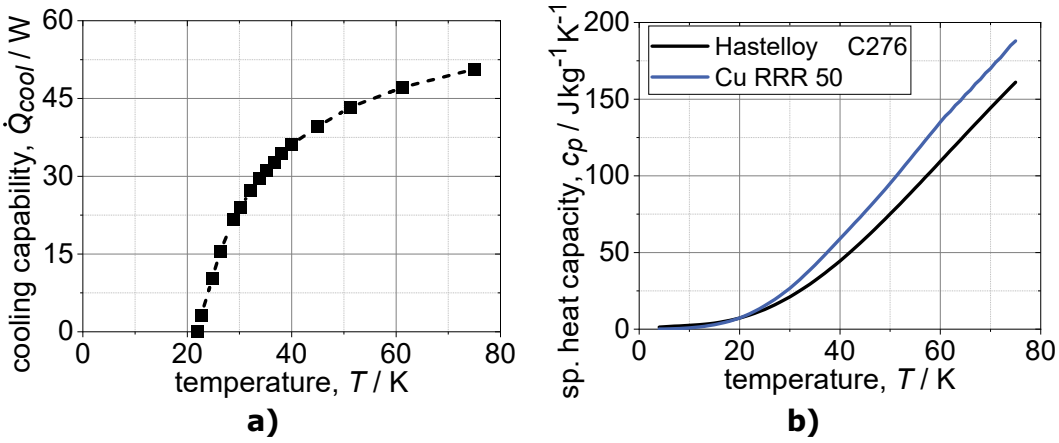

Figure 5.21: a) Measured cooling capability of the overall system as a function of temperature.
b) Specific heat capacity of Hastelloy^{TM} C276 and Cu RRR 50 as a function of temperature [175, 180]

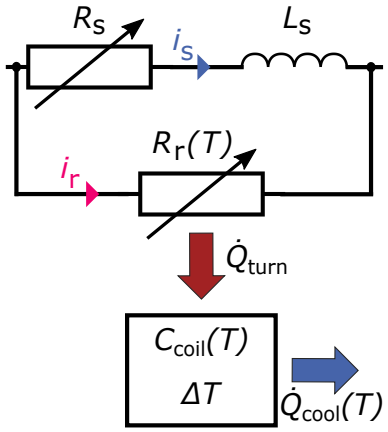

Figure 5.22: Illustration of the transient 1D thermal-electrical model for an NI PC coil

lines in figures 5.23 a) and c). The results from the transient 1D thermal-electrical model are displayed as dashed lines in the figures. The simulated magnetic flux density is the product of the modeled spiral current I_s and the coil constant. In addition to the measured quantities, the radial current I_r and the resulting losses can be calculated with the model. The curves of both quantities are plotted in figure 5.23 b). The measurement shows the typical behavior of a no insulation coil with the induced voltage during the current ramp and the delayed magnetic flux density. Furthermore, a temperature increase of the pancake coil during the ramp process can be observed. The measured average temperature increases from 30.14 K by 2.06 K to a maximum value of 32.20 K. It should be noted that the coil does not cool back to the output temperature of approximately 30 K after the charging process. This is due to the additional heat load from the current leads at a continuous supply current of 450 A.

The simulated voltage of the coil as well as the magnetic flux density show a good agreement with the measured values. However, the simulated temperature demonstrates a similar behavior to the measured values only in the rise phase, but the re-cooling phase shows a different behavior. This can be explained by the fact that in the re-cooling phase, both the heat load of the current leads and the cooling behavior of the entire system have a greater influence on the coil temperature. In order to better take into account the re-cooling of the coil, the thermal masses and the thermal-electrical relationships of the entire system must be better integrated into the model. Furthermore, the additional heat load caused by the current leads is not taken into account.
Nevertheless, the transient 1D model provides a good estimate of the maximum temperatures to be expected during the charging process of a no insulation coil. The modeled radial current I_r in figure 5.23 b) shows a similar curve to the induced voltage and slowly decays after the peak is reached. In this decay phase, more and more current flows into the spiral path of the coil and contributes to the generation of the magnetic flux density. Consequently, the turn-to-turn losses P_{turn} also exhibit a similar curve. The total energy supplied to the coil by the charging process is represented by the area below P_{turn} and equals to 562 J.

In [198], it is reported for the first time how an adjusted supply current can reduce the magnetic flux density delay in NI coils. Therefore, a second measurement is performed where the supply current is first set to a maximum current of 650 A with a slew rate of 650 A s^{-1}. The current of 650 A is kept for 37 s and then adjusted to the final current of 450 A with a negative current ramp of 450 A. The measured and simulated quantities are shown similarly in figure 5.24 for a direct comparison with the previous measurement. The magnetic flux density no longer shows the typical delay behavior with the changed supply current, but exhibits an almost linear increase. The measured time constant τ can thus be reduced from 29.77 s to 16.95 s compared to the first experiment. The induced voltage and the radial current also show a different curve and higher peak values due to the changed supply current. The modeled quantities show again good agreement with the measured electrical quantities. However, due to the changed supply current ramp, more current flows in the radial coil path, causing higher turn-to-turn losses. The total energy supplied to the coil by the charging process is now 1058 J. With the increased energy supply higher maximum temperatures develop during the charging process of the coil. The average measured start temperature of 30.04 K increases by 4.03 K to a maximum average temperature of 34.07 K. In comparison, the model shows a maximum coil temperature of 34.30 K.

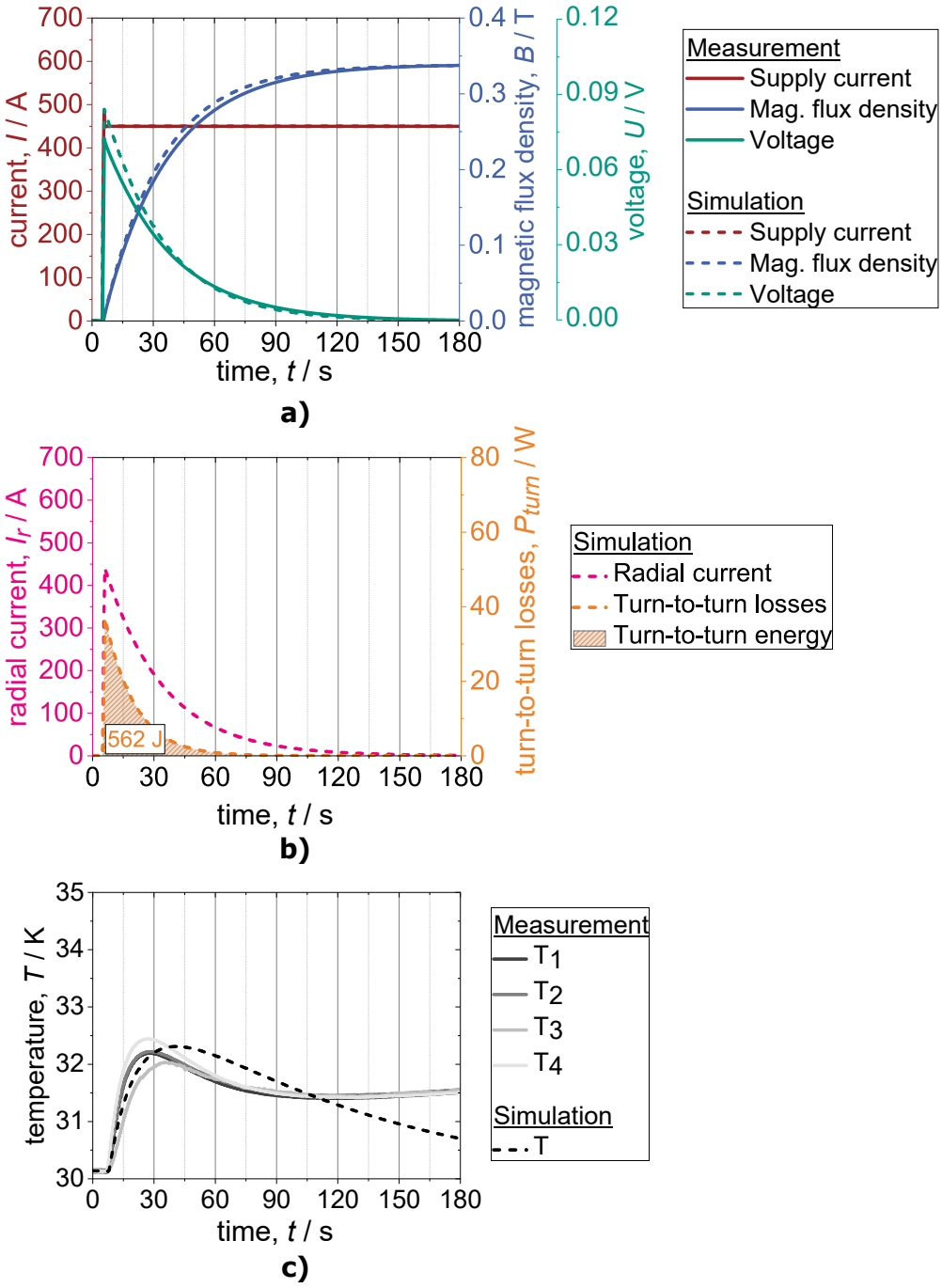

Figure 5.23: Measurement and simulation of pancake G low under conduction cooled conditions at initially 30 K with a current ramp of 650 A s^{-1} to a maximum current of 450 A.
a) Measured and simulated supply current, pancake voltage and central magnetic flux density.
b) Simulated radial current with resulting turn-to-turn losses and total energy supplied to the pancake coil.
c) Measured and simulated temperatures of the pancake coil

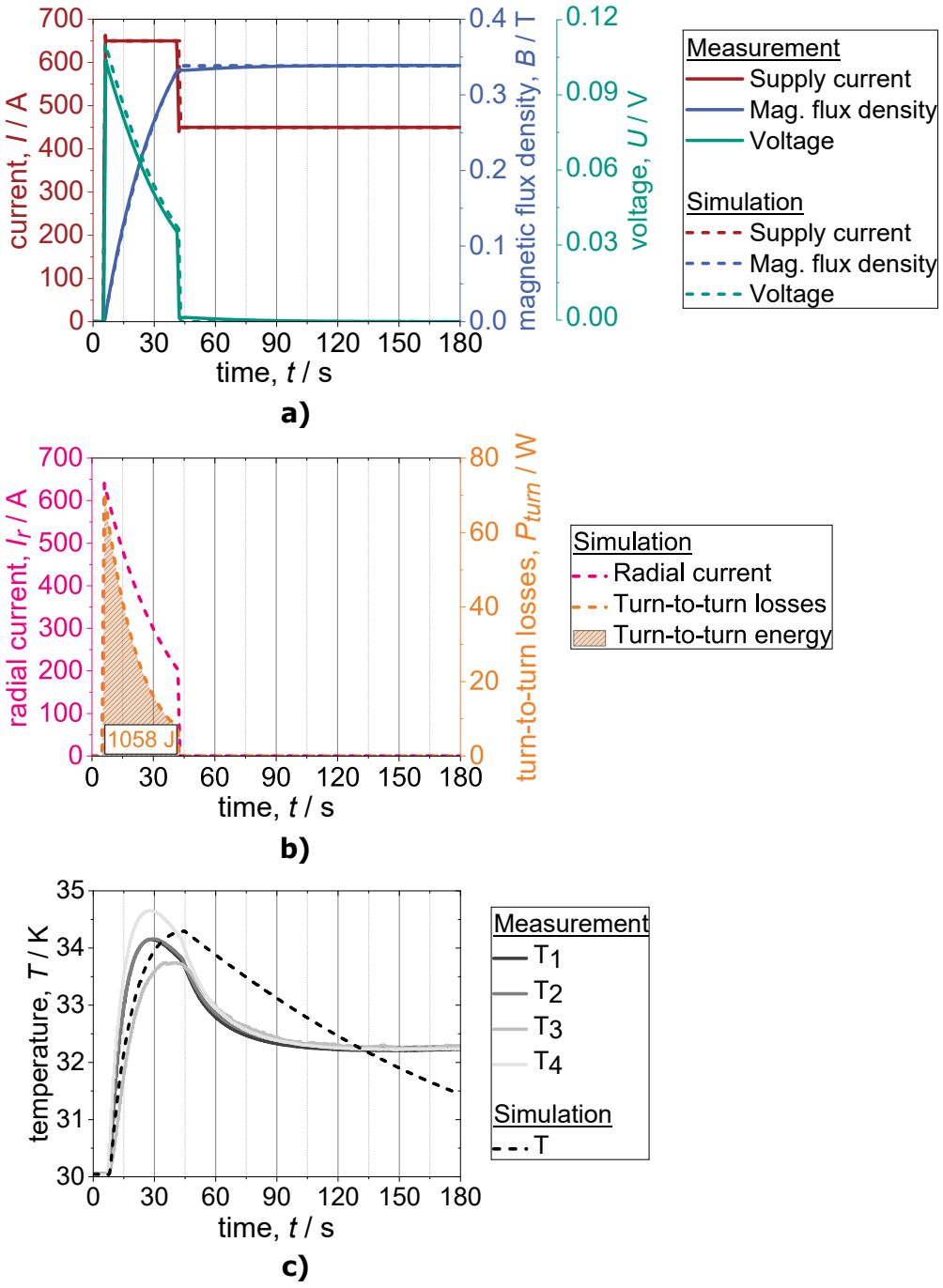

Figure 5.24: Measurement and simulation of pancake G low under conduction cooled conditions at initially 30 K. First current ramp with 650 A s^{-1} to a maximum current of 650 A. The current of 650 A is maintained for 37 s and then ramped to the final value of 450 A with −200 A.
a) Measured and simulated supply current, pancake voltage and central magnetic flux density.
b) Simulated radial current with resulting turn-to-turn losses and total energy supplied to the pancake coil.
c) Measured and simulated temperatures of the pancake coil

6 Assembly and test of the generator demonstrator

The following chapter discusses the assembly and testing of the superconducting generator technology demonstrator. First, the set-up and preliminary test of the six-pole stator system in liquid nitrogen is presented. Finally, the installation of the stator system in the cryostat and its performance under conduction-cooled conditions is described.

6.1 Instrumentation of the stator system

The double pancake coils A to F described in chapter 5 are connected together to form a six-pole stator system which is shown in figure 6.1.

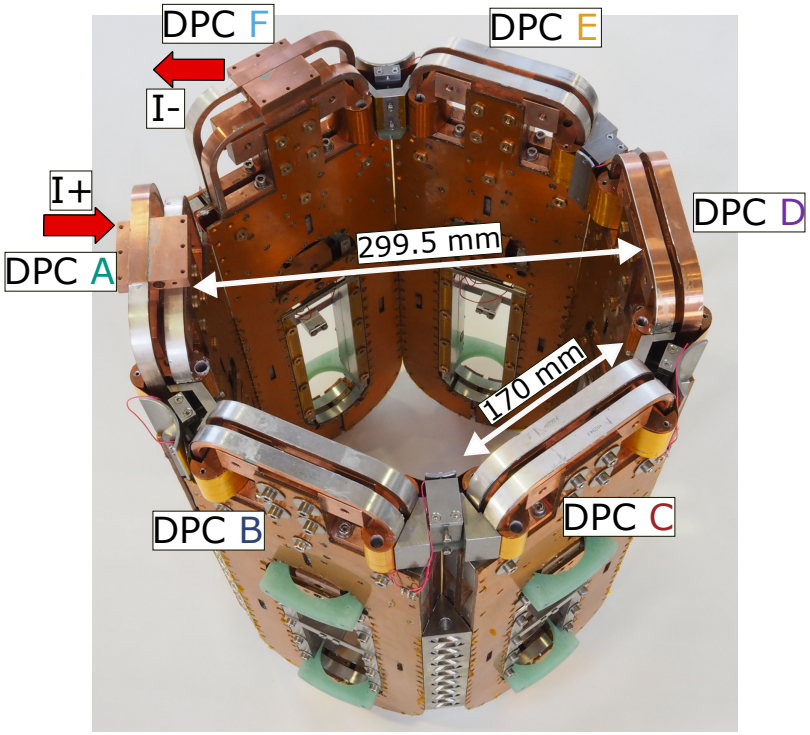

Figure 6.1: Overview of the six-pole stator system with the location of the individual double pancakes and current feeds at coil A and F

Mechanically, the double pancakes are connected to each other with a v-shaped stainless steel connector on the straight coil sides over the effective length l_{ef}. Electrically, the coils are series connected, with current feed points at double pancake A and F, later attached to the binary current leads presented in subsection 4.2.2. For the measurements in liquid nitrogen, the current feed points are contacted directly at double pancake A and F, without intermediate binary current leads. The electrical interconnections of the stator system are made with three parallel HTS tapes. To keep the resistive components as low as possible, all electrical joints are soldered. The same soldering method is used as already described in section 5.2. Alternating magnetic poles are required between the stator and rotor for the operation of electrically rotating machines. Due to the identical constructional design of the pancake coils, all coils show the same winding direction. Therefore, the current path in the respective neighboring double pancake coils must be reversed to generate alternating poles. For the correct contacting of the coils, the HTS tape of the individual pancake winding is redirected to the next contact via a copper bow on the rear side of the pancake coil. This ensures alternating contacting between the lower and upper pancake coils and, as a result, alternating magnetic poles in the stator system. A more detailed view of the connection systems between the individual coils can be seen in figure 6.2. The stator system and the tests in liquid nitrogen were first presented in [199].

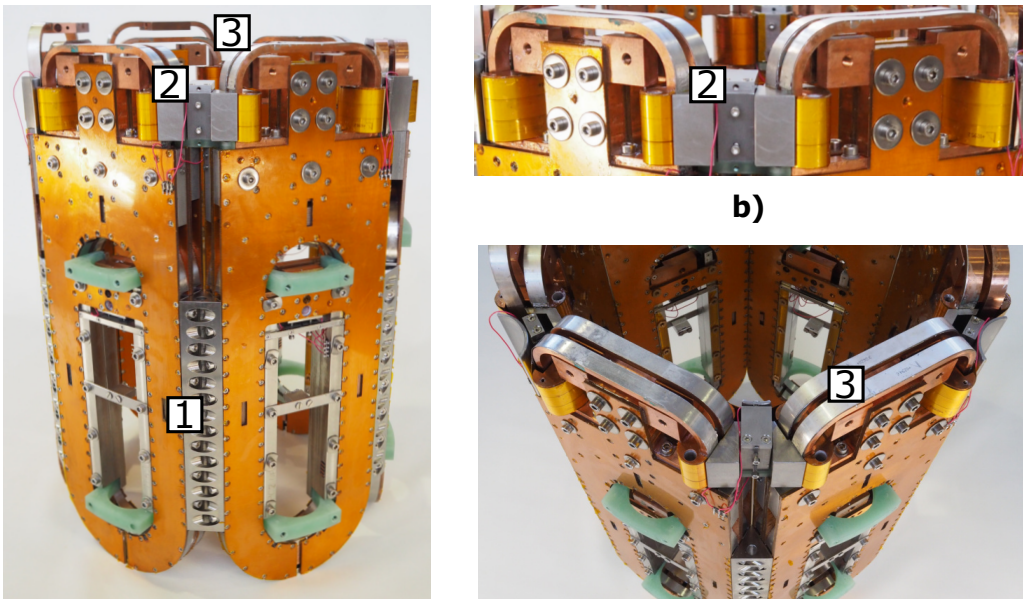

Figure 6.2: a) Side view of the total stator system with the v-shaped mechnical connection 1
b) Side view of the electrical interconnection with three parallel HTS tapes 2
c) Top view of the copper bow with the HTS tapes of the pancake windings 3 for alternating current paths

In order to determine the individual resistive components in the entire stator system, appropriate voltage taps are attached. Furthermore, the magnetic flux density of each double pancake is recorded directly in its center with hall sensors. An illustration of the current path with the alternating interconnections and feed points at different temperature levels, as well as the position of the voltage taps and hall sensors with the corresponding direction of magnetic flux density is shown in figure 6.3.

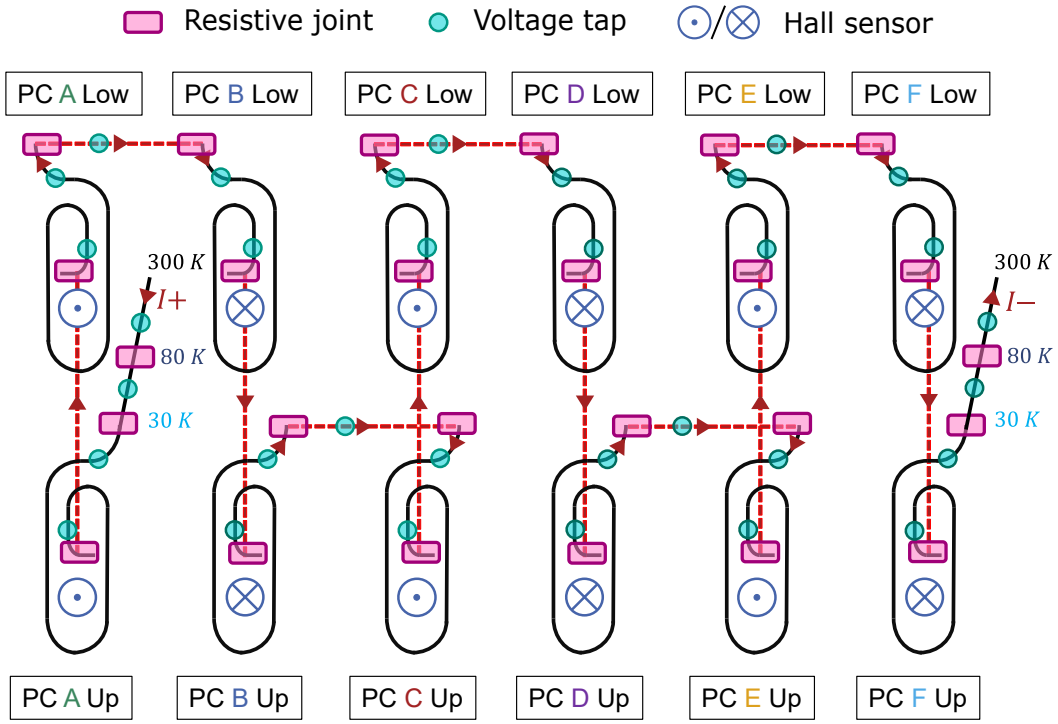

Figure 6.3: Illustration of the interconnection of the stator system with current path and position of the resistive connections, voltage taps and hall sensors

6.2 Measurements of the stator system in liquid nitrogen

6.2.1 Critical current and resistive components of the stator system

The measurement of the critical current is carried out as described in subsection 5.3.1. The plotted voltages and magnetic flux densities describe the steady state of the coils after the induced voltages U_{ind} have decayed due to the change in current over time. Figure 6.4 a) shows the critical current I_c measurement with the 0.1 µV cm^{-1} criteria. For better visibility, the plot shows the voltages of the lower

pancake coils with negative values and the voltages of the upper pancake coils with positive values.

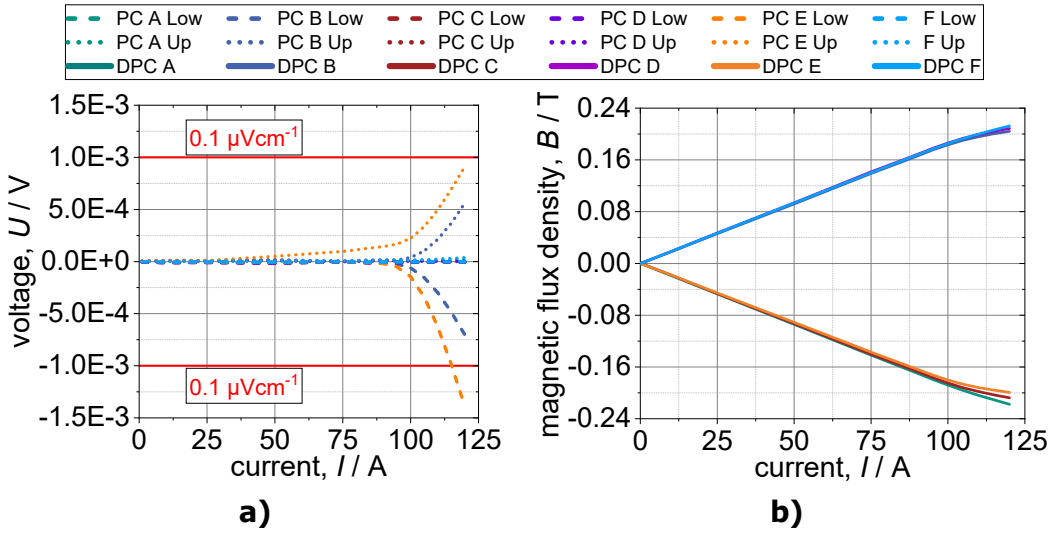

Figure 6.4: Measurements of the total stator system in liquid nitrogen at 77 K
a) Critical current measurement with a critical voltage per pancake of 1 mV according to the 0.1 µV cm^{-1} criterion
b) Measured magnetic flux density in the center of each double pancake coil

The pancake coils B and E wound with tape 2 show a voltage increase at about 100 A while the other coils with tape 1 do not demonstrate a significant voltage increase at these current levels due to the higher critical current I_c of the tape. As already shown in the previous measurements, double pancake E has the lowest critical current I_c of about 115.9 A and thus defines the critical supply current for the series-connected coil system as the weakest coil. The measured magnetic flux density in the center of each double pancake coil is displayed in figure 6.4 b). A linear increase of 1.86 mT A^{-1} can be seen until the critical currents are reached. After that, the saturation of the magnetic flux density typical for no insulation and metal insulation coils due to the alternative radial current paths can already be recognized. The lower the previously measured critical current I_c of the coils, the more current is diverted via the radial path and the more pronounced is the observed saturation. Furthermore, the formation of alternating magnetic poles can be seen due to the previously described interconnection of the pancake coils. Double pancake A, C and E have a negatively directed magnetic field, while poles B, D and F show a positive field. The resistive components of the entire system are also recorded. A distinction is made between the resistive part on the spiral coil path R_s from subsection 5.3.1 and the soldered joints shown in figure 6.3. The resistive joints are further subdivided into the connection between two pancakes to a double pancake in the center of the coils R_c and the interconnection of the individual double pancakes R_{int} to form the entire stator system. The restive components for each double pancake are summarized in figure 6.5. The soldered contacts show a greater deviation and in particular the interconnection between

double pancake D and E as well as the central contact of double pancake F show particularly high values. The total resistance of the stator system is 6.64 µΩ. With a nominal excitation current I_{ex} of 450 A, the total power dissipation at the second cooling stage caused by the resistive components in the system is 1.34 W.

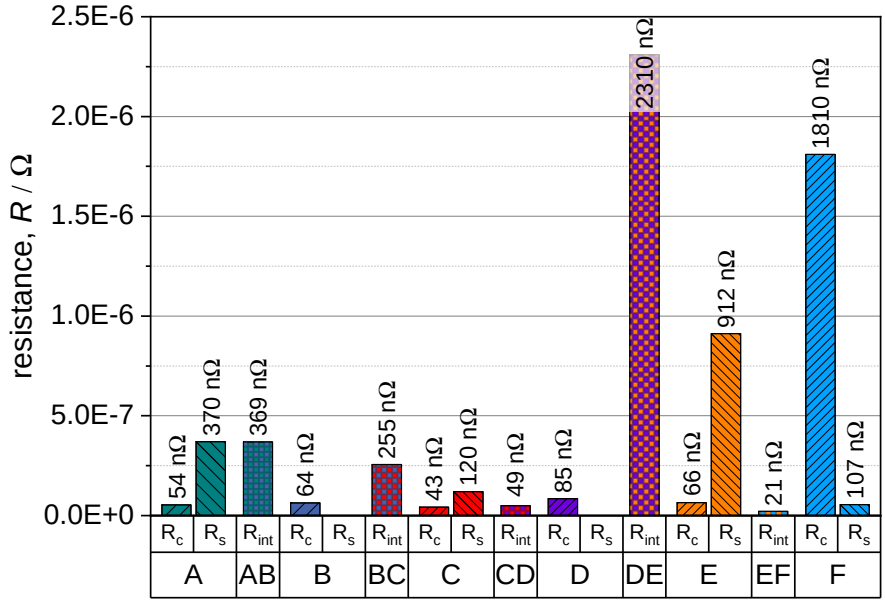

Figure 6.5: Resistive parts of the stator system divided into the resistive part of the spiral coil path R_s, the central contact for connecting the two pancakes to a double pancake R_c, and the interconnection of two double pancakes R_{int}

6.2.2 Dynamic charging and discharging of the stator system

As with the individual measurements of the different pancake and double pancake coils, the dynamic behavior of the coils connected together to the stator system is investigated. The stator system is supplied with defined charging and discharging currents, as already described in subsection 5.3.2. A maximum current of 100 A is supplied to the stator system with positive and negative slew rates of 1 A s^{-1}, 10 A s^{-1}, 50 A s^{-1}, and 100 A s^{-1}. To avoid possible damage to the entire coil system, no sudden discharge tests are performed in this test series. Figure 6.6 a) shows exemplary the measured magnetic flux density in the center of the double pancakes for a slew rate of 10 A s^{-1} up to a maximum current of 100 A. The interconnected coil system shows at all slew rates a fundamentally different dynamic behavior than the individual pancakes and double pancakes from figure 5.15.

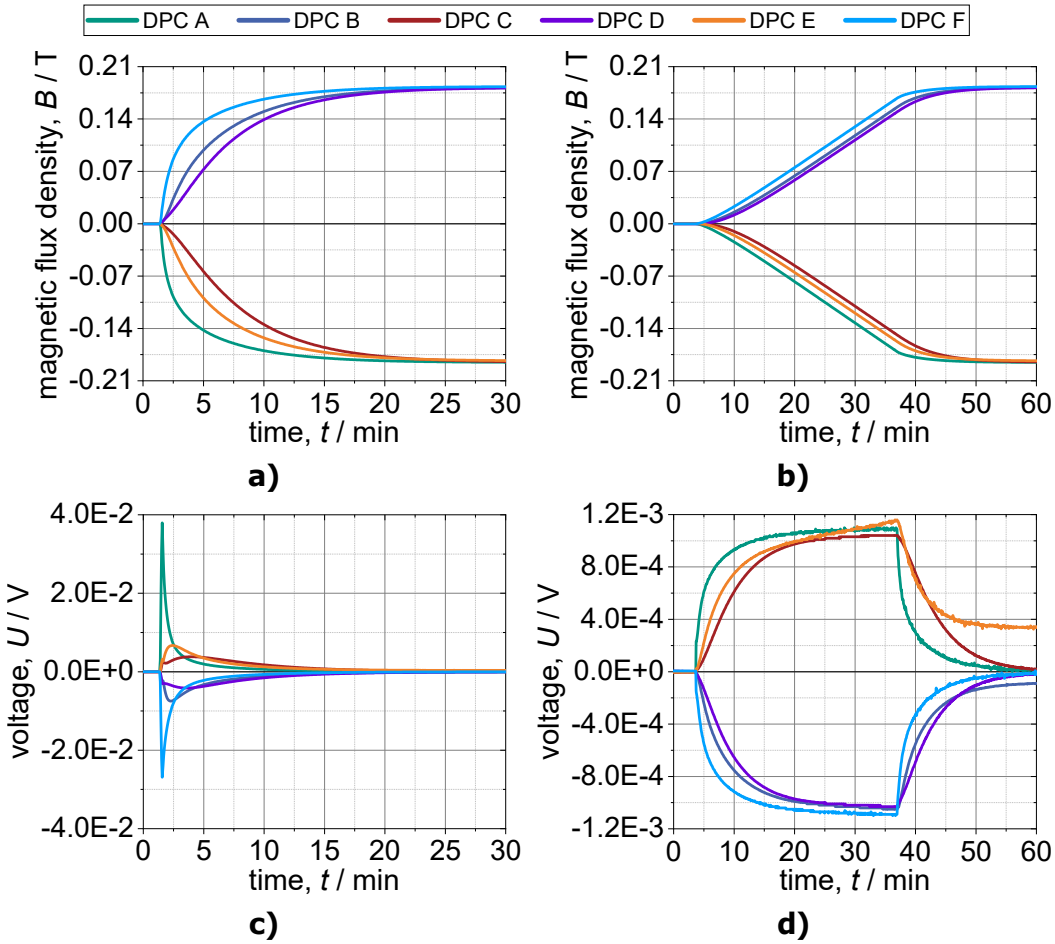

Figure 6.6: Measured center magnetic flux densities and induced voltages of the double pancakes in the assembled stator configuration in liquid nitrogen at 77 K
a) Magnetic flux density with a 10 A s^{-1} current ramp up to a maximum current of 100 A
b) Magnetic flux density with a 0.05 A s^{-1} current ramp up to a maximum current of 100 A
c) Induced voltage with a 10 A s^{-1} current ramp up to a maximum current of 100 A
d) Induced voltage with a 0.05 A s^{-1} current ramp up to a maximum current of 100 A

The stator system exhibits a type of pattern in which the double pancakes directly at the feeding points A and F show the shortest time delay in the generation of the magnetic flux density. The double pancakes C and D, which are located furthest away from the feeding points, have the greatest delay, while the poles B and E show an average delay in comparison. Furthermore, all double pancakes in the stator assembly show a significantly larger time constant τ than in the dynamic charging measurements of the single pancakes and double pancakes. The minimum, maximum and average time constants of the dynamic charging

and discharging measurements are summarized in table 6.1.

Table 6.1: Time constants of the dynamic charging and discharging measurements of the double pancake coils in the assembled stator configuration in liquid nitrogen at 77 K

Coil	τ_{min} (s)	τ_{max} (s)	τ_{avg} (s)
DPC A	137.0	206.9	157.6
DPC B	261.0	272.3	266.2
DPC C	365.4	387.5	379.6
DPC D	334.1	357.6	349.6
DPC E	257.0	268.7	262.9
DPC F	148.5	203.2	163.8

The induced coil voltages U_{ind} during the dynamic charging with a slew rate of 10 A s^{-1} show a similar pattern and are displayed in figure 6.6 c). Double pancake A and F show a particularly high peak in the induced voltage, while the magnitude of the induced voltage decreases with distance from the feeding points. This behavior cannot be explained with a series connection of the usual equivalent circuit diagram of no insulation or metal insulation coils shown in figure 2.8. To investigate the phenomenon further, another measurement is performed with a very slow slew rate of 0.05 A s^{-1}. Figure 6.6 b) shows the measured magnetic flux density in the center of the double pancakes for a slew rate of 0.05 A s^{-1} up to a maximum current of 100 A. In principle, the same pattern can be seen as for the other current ramps, but due to the very slow current feeding, the magnetic flux density curves show a behavior that is closer to a linear increase. The induced coil voltages during the dynamic charging with a slew rate of 0.05 A s^{-1} are displayed in figure 6.6 d). Due to the very slow current change dI/dt, the induced voltage reaches its maximum within the charging process. All double pancake coils reach a maximum induced voltage U_{ind} of about 1 mV. The same maximum induced voltages indicate that the inductance of the individual double pancakes must be equal and that a symmetrical field distribution can be assumed. Thus, field coupling effects of the stator coil system can be excluded as explanation for the changed dynamic behavior.

It is assumed that the changed dynamic behavior can be explained by additional, parasitic resistive connections R_{Par} during the assembly of the stator system. Due to the design as a conduction cooled system, good thermal contacts must be realized, which may not represent perfect electrical insulation. Thus, the coil system is not only thermally connected to each other, but further additional electrical connections are created between the no insulation and metal insulation coils, which influence the equivalent circuit and thus the dynamic behavior of the stator system.

For this reason, the equivalent circuit shown in figure 6.9 is simulated in *Matlab Simulink* [176]. For the coil inductance L and the radial resistances R_r the values from the tables 5.2 and 5.4 are applied. For the parasitic interconnections R_{Par} a resistance value of 1 µΩ is assumed. The simulated magnetic flux densities and voltages, according to the equivalent circuit diagram from figure 6.9, are shown in figure 6.7.

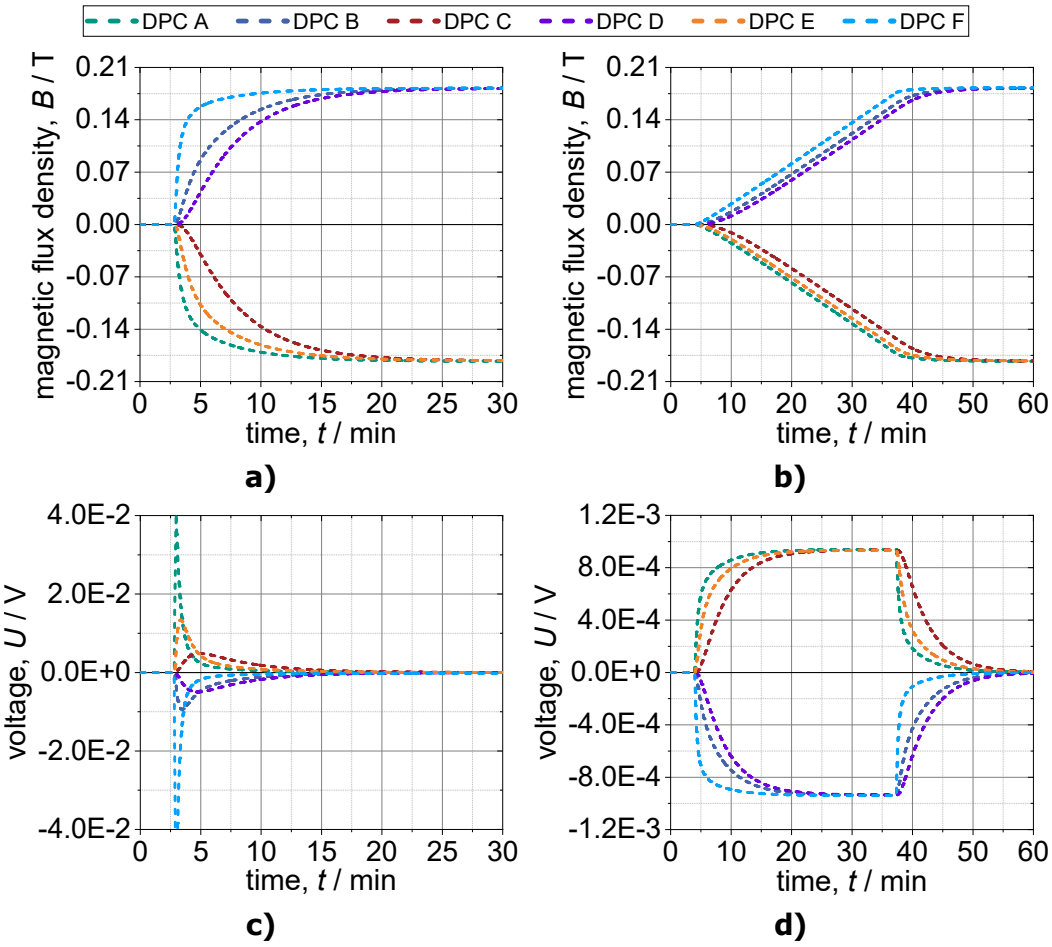

Figure 6.7: Simulated center magnetic flux densities and induced voltages of the double pancakes in the assembled stator configuration
a) Magnetic flux density with a 10 A s^{-1} current ramp up to a maximum current of 100 A
b) Magnetic flux density with a 0.05 A s^{-1} current ramp up to a maximum current of 100 A
c) Induced voltage with a 10 A s^{-1} current ramp up to a maximum current of 100 A
d) Induced voltage with a 0.05 A s^{-1} current ramp up to a maximum current of 100 A

To display the simulated magnetic flux density, the modeled spiral current I_s is multiplied by the coil constant. Figure figure 6.7 a) and figure 6.7 c) show respectively the simulated magnetic flux densities and induced voltages for a 10 A s^{-1}

current ramp up to a maximum current of 100 A. The simulated magnetic flux densities and induced voltages for a 0.05 A s^{-1} current ramp up to a maximum current of 100 A are shown in figure 6.7 b) and figure 6.7 d). It can be seen that the simulated equivalent circuit shows similar behavior to the measurements. Thus, the observed changed dynamic behavior and the significantly increased time constant τ of the coil system can be explained by parasitic resistive interconnections. However, it is not possible to quantify the resistive interconnections in the assembled stator system and therefore only a resistance value can be assumed that simulates the measured behavior as well as possible. In principle, it can be observed from the model that as the resistance value of R_{Par} decreases, the systematic behavior is more pronounced, whereas as the resistance value of R_{Par} increases, the systematic pattern diminishes.

Furthermore, figure 6.8 shows the simulated radial currents I_r in the double pancakes for both current ramps. While at a very slow current ramp of 0.05 A s^{-1} in figure 6.8 b) the maximum radial currents I_r are not higher than 10 A, a current ramp of 10 A s^{-1} in figure 6.8 a) already shows very high radial currents. In particular, the double pancakes A and F at the current feeding terminals show significantly higher radial currents compared to the remaining double pancakes.

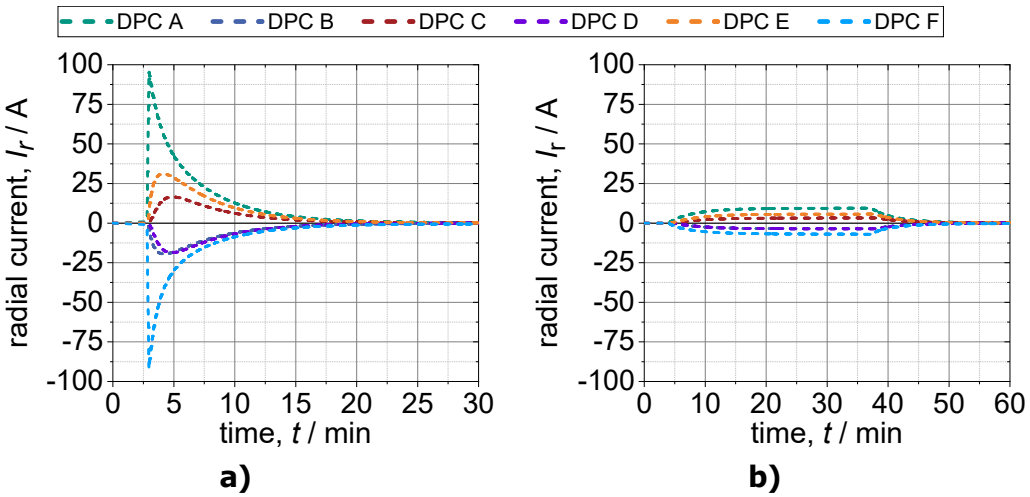

Figure 6.8: Simulated radial currents of the double pancakes in the assembled stator configuration
a) Radial current with a 10 A s^{-1} current ramp up to a maximum current of 100 A
b) Radial current with a 0.05 A s^{-1} current ramp up to a maximum current of 100 A

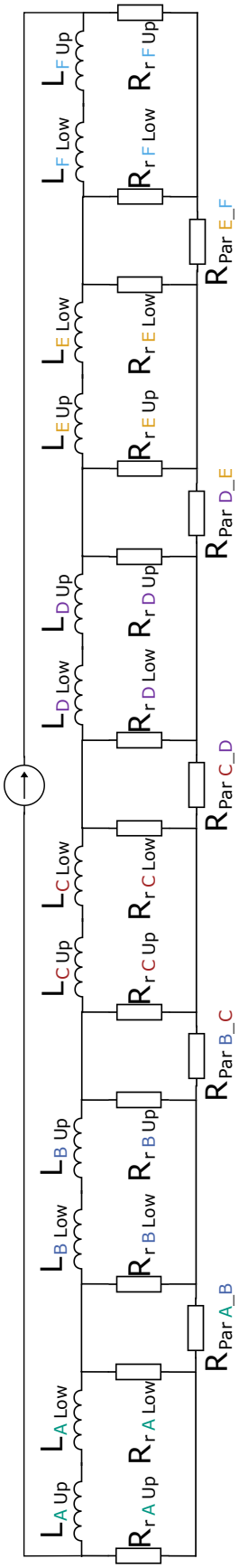

Figure 6.9: Equivalent circuit of the assembled stator configuration with parasitic resistive interconnections

6.3 Assembly and instrumentation of the generator system

The entire generator system is assembled in the vertical direction. As a first step, the feedthroughs from the atmospheric side to the vacuum chamber are installed on the upper cryostat lid. This includes the two cold heads, the two current leads, the supply lines for the heating elements and the measuring lines. Next, the inner thermal shield and the stator system are attached to the cryostat top lid with threaded rods. A total view of the inner thermal shield and stator system hanging from the cryostat top lid with the assembled feedthroughs is shown in figure 6.10 a). Figure 6.10 b) shows a close-up of the connection of the first and second cooling stages to one of the cold heads. The first cooling stage is connected to the lid of the thermal shield, while the second cooling stage is in contact with the stator system. To avoid mechanical loads on the cold heads, both cooling stages are connected with flexible copper connectors consisting of several 0.2 mm thick individual sheets from the company *Druseidt* [200].

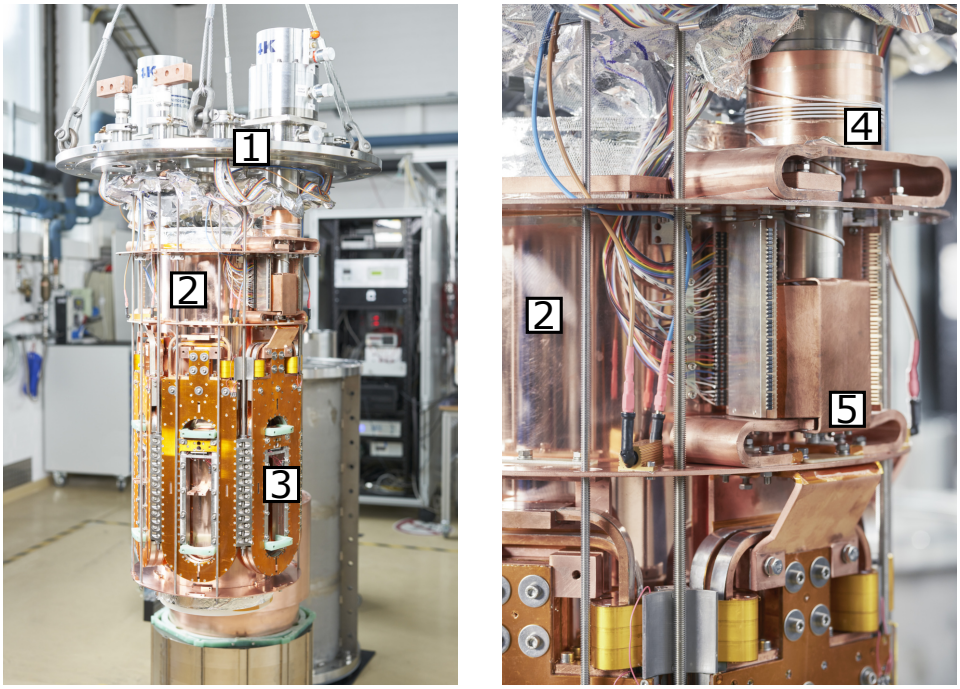

a) **b)**

Figure 6.10: a) Total view of the stator system 3 and the inner thermal shield 2 attached to the cryostat top lid 1 *(Ref.: Amadeus Bramsiepe)*
b) Close-up of the connections of the thermal shield and the stator system to the first cooling stage 4 and second cooling stage 5 *(Ref.: Amadeus Bramsiepe)*

After the assembly of the inner thermal shield and the stator system on the cryostat top lid, the other components are combined. The individual components of the

generator system before assembly are presented in figure 6.11. First, the outer thermal shield is applied and wrapped with multilayer insulation (MLI). The MLI of the outer thermal shield is not shown in the picture. The stator iron is then suspended from the cryostat lid with threaded rods and is positioned so that it covers the effective length l_{ef} of the coils. It is designed as a stack of electrical steel with the designation M235-35A delivered by the company *LCD LaserCut* [201]. After the complete thermal shield, stator coil system and stator iron are attached to the upper cryostat lid, everything can be inserted vertically into the outer cryostat and screwed together. Next, the entire structure consisting of the outer cryostat and the top lid with the interior is lifted and put over the inner cryostat. Once the inner cryostat has been aligned and fastened to the top cryostat lid, the complete generator system can be placed in the horizontal position. Finally, the bottom cryostat lid is attached to the horizontal generator system to create a sealed vacuum chamber.

Figure 6.11: Individual components of the generator before assembly. Stator system and inner thermal shield attached to the cryostat top lid [1], outer thermal shield (without MLI) [2], stator iron [3], outer cryostat [4], inner cryostat [5] *(Ref.: Amadeus Bramsiepe)*

With this arrangement, the vacuum system, the cryogenic system and the superconducting coils can already be tested, therefore the rotor assembly takes place subsequently. To install the rotor, the entire stator system is returned to the vertical position and the rotor is inserted upright into the center bore on the atmospheric side. The rotor shaft is supported by means of a floating bearing and a fixed bearing, which is attached to the top and bottom cryostat lid respectively. The shaft coupling and the connection to the slip ring system are located on the side with the bottom cryostat lid.

In addition to the instrumentation for measuring the voltages and magnetic flux densities of the stator system shown in figure 6.3, the generator system in the cryostat is equipped with temperature sensors. For the areas where low magnetic flux densities and temperatures greater than or equal to the temperature of the first cooling stage are expected, *Pt100* sensors [202] are used. For the temperature ranges below the first cooling stage and for areas with increased magnetic field exposure *Cernox® CX-AA* temperature sensors [197] are applied. In order to control the temperature of the superconducting coils, additional heating elements are mounted on the thermal link of the stator system. The position of the temperature sensors and heaters are shown in figure 6.12. Figure 6.12 a) displays the two cryocoolers (CC) A and CC F, as well as the substructures of the generator measured with *Pt100* sensors. The sensors $T_{CL\,A0}$ and $T_{CL\,F0}$ monitor the start temperatures of the current feedthroughs in the vacuum space of the generator, respectively. Directly after this measuring point, the resistive current leads described in subsection 4.2.2 are connected. Further, the temperatures at the top and bottom of the thermal shield and stator iron are measured with the sensors $T_{TS\,Up}/T_{TS\,Low}$ and $T_{Iron\,Up}/T_{Iron\,Low}$, respectively. Figure 6.12 b) shows the position of the temperature sensors of the binary current lead from subsection 4.2.2 in detail. The start of the binary current leads is electrically connected to the end of the resistive current leads and thermally attached to the top of the thermal shield. The start temperatures of the binary current leads are monitored with the sensors $T_{CL\,A1}$ and $T_{CL\,F1}$. Furthermore, the intermediate temperatures are measured with the sensors $T_{CL\,A2}$ and $T_{CL\,F2}$ and the temperatures at the connection terminals to double pancake A and F are measured with the sensors $T_{CL\,A3}$ and $T_{CL\,F3}$. The position of the heaters H A1 to H F2 for temperature control and the sensors for monitoring the temperatures of the double pancakes are shown in figure 6.12 c). For a better visualization of the thermal link between the coils and the connection to the cryocoolers CC A and CC F, the hexagonal coil system is presented as a two-dimensional (2D) illustration. The temperatures of the coils are measured at the front of each double pancake and thus at the position most distant from the cooling connection, with the sensors $T_{DPC\,A}$ to $T_{DPC\,F}$.

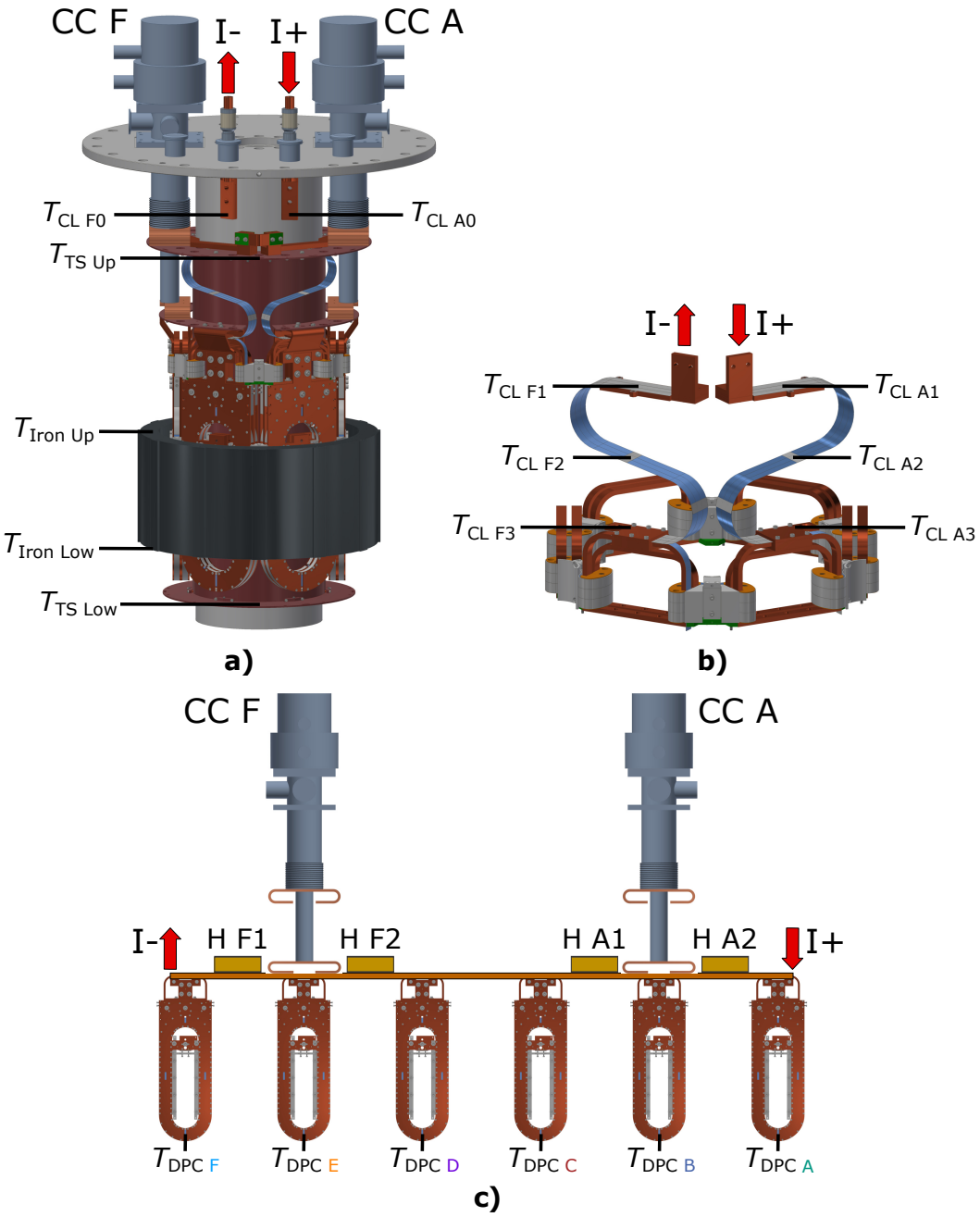

Figure 6.12: a) Position of temperature sensors (*Pt100*) of the substructures
b) Position of temperature sensors (*Cernox*) of the binary current leads
c) Position of heaters and temperature sensors (*Cernox*) of the stator system. For better visualization the stator system with thermal connection is shown as 2D illustration

6.4 Performance of the generator stator system

6.4.1 Cooldown of the conduction cooled cryogenic system

The cooldown of the entire generator system is shown in figure 6.13 and displays a cooling time slightly less than 48 h to reach thermal equilibrium. The vacuum pressure in the cryostat for the cooling process is around 6.65×10^{-5} mbar. The measured temperatures correspond to the sensor positions given in figure 6.12.

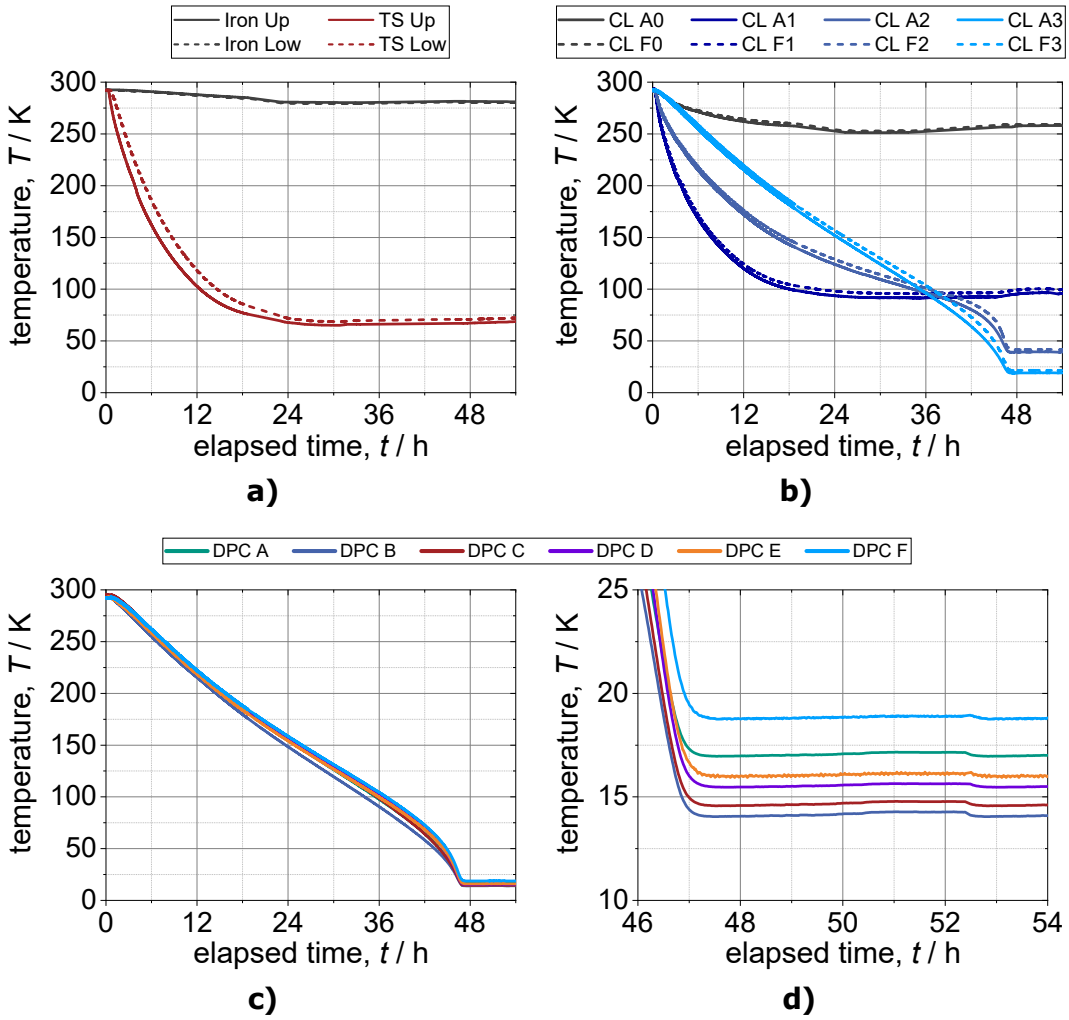

Figure 6.13: Cooldown of the generator system
a) Temperatures of the substructures
b) Temperatures of the current leads
c) Temperatures of the double pancakes
d) Zoomed temperatures of the double pancakes in thermal equilibrium

Figure 6.13 a) shows the cooling behavior of the substructures of the system. The stator iron, as warm iron design, shows a good thermal insulation to the cryogenic

temperature regions with a minimum temperature of about 280 K. The sensors at the upper and lower part of the thermal shield show sufficiently low temperatures of 66 K and 70 K, respectively. A temperature difference of 4 K also indicates a homogeneous temperature distribution of the thermal shield. Figure 6.13 b) shows the temperatures of the current leads. As expected, the sensors $T_{CL\,A0}$ and $T_{CL\,F0}$, directly after the atmospheric feeding terminals, show relatively high temperatures of around 260 K, while the subsequent temperatures of the current leads become continuously colder. It is noticeable that current lead A not only cools faster, but also reaches lower steady-state end temperatures than current lead F. However, the two sensors $T_{CL\,A1}$ and $T_{CL\,F1}$ with 96 K and 100 K do not reach the required temperatures. As a link between the resistive and binary current leads, this position should reach temperatures well below the critical temperature T_c of about 93 K. Thus, no excitation current can be supplied under these conditions. Figure 6.13 c) and d) show respectively the cooling behavior of the double pancakes and a zoomed image of the coil temperatures in thermal equilibrium. All double pancakes reach temperatures below 20 K. Figure 6.12 c) shows the distance between the individual double pancakes and the respective cryocoolers. In principle, the temperature distribution of the coils can be assigned to their geometrical arrangement in the thermal link. Thus, double pancake B with the shortest distance to cryocooler A is the coldest, followed by double pancake C. Double pancake A with an additional heat input through the current lead is the warmest in this arrangement. However, this temperature distribution is not observed for double pancakes D to F below cryocooler F. Furthermore, the double pancakes in this arrangement exhibit systematically higher temperatures, similar to current lead F, which is cooled with cryocooler F. The temperature distribution in the system suggests that cryocooler F is not providing the required cooling capacity. This assumption is confirmed by further measurements and is discussed in more detail in appendix A.

6.4.2 Critical current of the stator system with pre-cooling of the current leads by liquid nitrogen

Since no temperatures below the critical temperature T_c of the binary current leads are reached at positions $T_{CL\,A1}$ and $T_{CL\,F1}$, it is not possible to feed the system with an excitation current I_{ex} without further measures. However, since the double pancakes and the remaining structures in the system reach the required temperatures, the current leads are pre-cooled on the atmosphere side with liquid nitrogen in order to carry out further measurements. This takes the heat load off the current leads and makes it possible to feed in an excitation current.

To adjust different temperatures of the stator system by PID control, the heaters H A1 to H F2 shown in figure 6.12 c) are used. As described above, the cooling capacity of cryocooler F is reduced, causing an unbalanced temperature distribution of the double pancakes. Therefore, the control of the heaters is also used to

achieve more homogeneous temperatures for the coils. The stator system is adjusted to the temperatures 77 K, 50 K and 30 K respectively. Since double pancake E has the lowest critical current from the preliminary measurements, the temperature measured by this sensor is used as the control temperature. By pre-cooling the resistive current leads with liquid nitrogen and due to the low heat input of the binary current leads, very stable temperatures are achieved which are only slightly influenced by the supplied excitation current. Table 6.2 lists the respective steady-state coil temperatures and the corresponding heater outputs.

Table 6.2: Adjusted temperatures of the double pancakes and the respective heating power of the temperature control system

T_{ref} (K)	A1+A2 (W)	F1+F2 (W)	DPC A (K)	DPC B (K)	DPC C (K)	DPC D (K)	DPC E (K)	DPC F (K)
77	24.4	14.7	80.3	77.0	80.6	80.1	77.0	79.8
50	20.7	11.0	53.0	50.4	52.4	52.0	50.7	52.5
30	14.1	6.0	31.7	29.7	31.0	30.8	30.3	32.1

Figure 6.14 a) shows the measured critical currents of the stator system for the three adjusted temperatures according to the 0.1 µV cm^{-1} criterion.

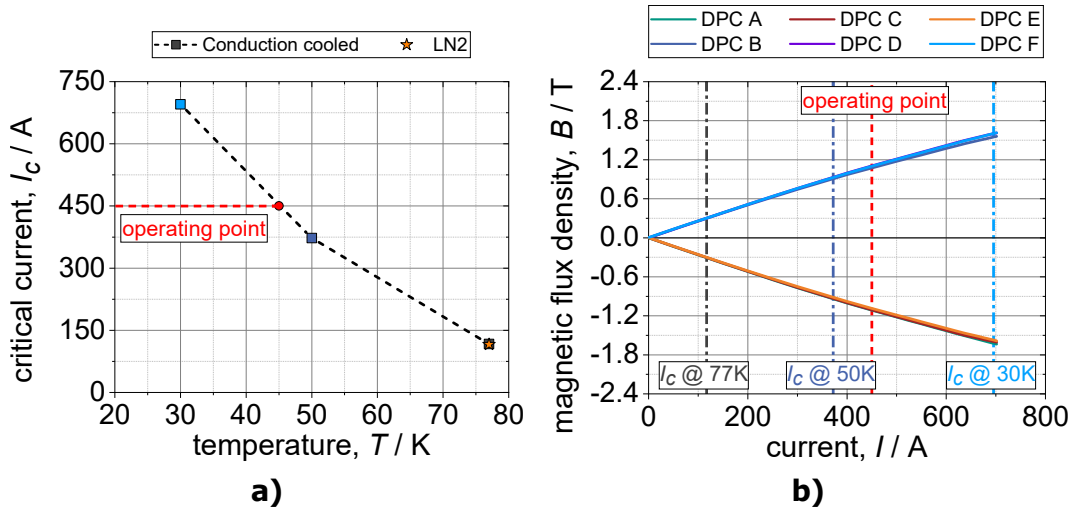

Figure 6.14: a) Critical current of the double pancake with the lowest current carrying capacity in the stator system at different temperatures under conduction cooled conditions and in liquid nitrogen at 77 K. Critical current is defined according to 0.1 µV cm^{-1} criterion
b) Measured magnetic flux density in the center of each double pancake coil

The critical current I_c of around 116.9 A at 77 K corresponds to the pre-measurement

of the stator system in liquid nitrogen. The critical currents at 50 K and 30 K are 372.3 A and 695.4 A, respectively. While at 77 K and 50 K, as expected, double pancake E represents the coil with the lowest critical current, at 30 K double pancake C is the first to reach its critical value. This can be attributed to the lower lift factor of tape 1 shown in figure 5.2. At lower temperatures, the coils with tape 2 outperform the coils with tape 1 and double pancake C, which has the lowest critical current of the coils wound with tape 1, is now responsible for the critical current of the entire coil system. However, at the design temperature of 30 K, the coil system reaches more than the rated current of 450 A. The measured average magnetic flux density in the center of the double pancakes at different excitation currents is shown in figure 6.14 b). The formation of alternating magnetic poles and a linear increase of the flux density with 2.58 mT A^{-1} is observed. However, the linear progression does not continue above a current level of approximately 300 A. This can be attributed to both the behavior of the no insulation and metal insulation coils and to increasing iron saturation. In addition, the surface area of the thermal contact of the resistive current lead to the first cooling stage is increased. For this purpose, the current lead is thermally connected to the additional thermal link shown in figure 4.17. The last step is to manually increase the frequency of the compressor of cryocooler F. In the first cooldown, it was determined that the frequency of the compressor is below the target frequency. The manual increase is expected to improve the cooling performance of cryocooler F.

6.4.3 Dynamic charging and discharging of the stator system with pre-cooling of the current leads by liquid nitrogen

As with the measurements of the stator system in liquid nitrogen, the dynamic behavior at different slew rates is investigated. The stator system is supplied with a maximum current of 100 A at positive and negative slew rates of 1 A s^{-1}, 10 A s^{-1}, 50 A s^{-1} and 100 A s^{-1}. The dynamic charging and discharging measurements of the stator system are performed at 77 K, 50 K and 30 K, respectively. To avoid possible damage to the entire coil system, no sudden discharge tests are performed in this test series. The minimum, maximum and average time constants of the dynamic charging and discharging measurements for the different temperatures are summarized in table 6.3. In principle, the same systematic pattern can be observed as already presented in figure 6.6. As with the measurements on double pancake G, a temperature dependence of the time constant τ is recognized, which can be attributed to the temperature dependence of the involved resistances. However, while the double pancakes A and F at the feeding points experience only a slight increase in the time constant τ with reduced temperature , the time constant of the remaining double pancakes in particular increases significantly. Furthermore, double pancake B has a much higher time constant compared to the liquid nitrogen measurements. Figure 6.15 shows the average time constants τ_{avg} of the double pancake coils from the measurements in liquid nitrogen and under conduction cooled conditions at different temperatures.

Table 6.3: Time constants of the dynamic charging and discharging measurements of the double pancake coils in the assembled stator configuration at 77 K, 50 K and 30 K

Coil	τ_{min} (s)	τ_{max} (s)	τ_{avg} (s)
77 K			
DPC A	138.6	222.5	166.8
DPC B	342.1	364.3	350.4
DPC C	357.1	377.6	367.4
DPC D	330.8	355.8	342.2
DPC E	274.4	300.3	287.2
DPC F	143.5	212.2	169.2
50 K			
DPC A	142.6	214.5	167.6
DPC B	401.9	414.7	407.3
DPC C	493.6	518.9	505.9
DPC D	394.4	410.0	399.8
DPC E	298.1	312.0	304.5
DPC F	163.1	218.7	180.2
30 K			
DPC A	155.0	219.0	175.5
DPC B	411.2	429.2	419.7
DPC C	523.2	540.7	531.7
DPC D	422.7	440.0	429.6
DPC E	314.8	333.0	323.0
DPC F	172.8	223.9	188.2

The significant increase of the time constants of the double pancakes B to E can be explained by the equivalent circuit shown in figure 6.9. A decrease of the involved resistances at lower temperatures in the model, also shows an increase of the time constants especially for the coils furthest away from the feeding points.

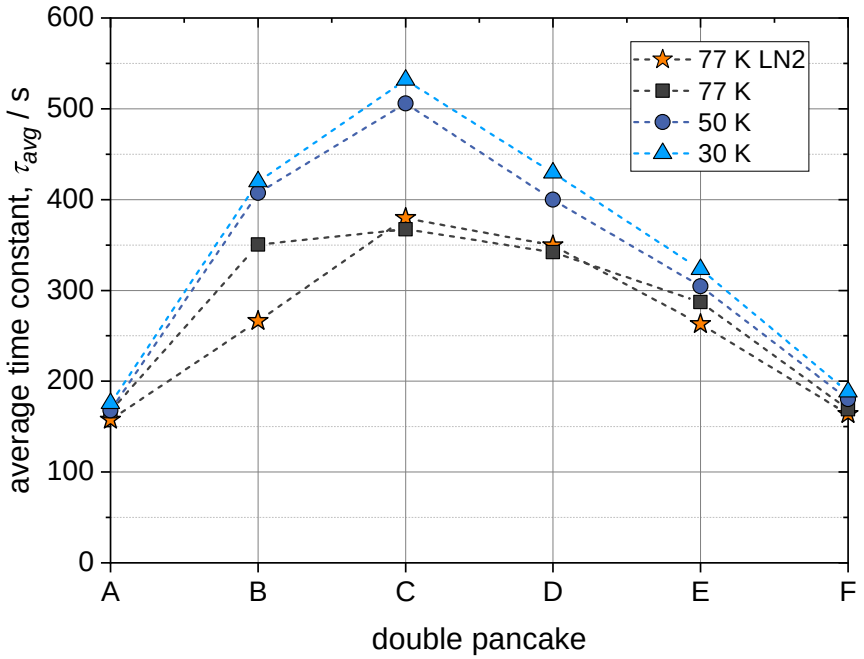

Figure 6.15: Measured average time constant of the double pancake coils in the assembled stator configuration in liquid nitrogen at 77 K and under conduction cooled conditions at 77 K, 50 K and 30 K

During the dynamic charging and discharging measurements, a temperature increase of the double pancakes is detected. This temperature increase can be attributed to the turn-to-turn losses P_{turn} during a current change dI/dt presented in section 2.3. As already explained in subsection 5.4.4, the turn-to-turn losses P_{turn} can lead to a significant temperature increase of the no insulation and metal insulation coils, especially at low temperatures under conduction-cooled conditions and during a dynamic charging or discharging process with a high maximum current and a high current change rate dI/dt.

Therefore, another experiment is performed at a controlled coil temperature of 30 K, with a positive current ramp of 100 A s^{-1} to the rated current of 450 A and a discharge to 0 A with a current ramp of −450 A s^{-1} after almost 2 h. The supplied current and the magnetic flux density measured at the center of the coils are shown in figure 6.16 a) and the measured coil temperatures are displayed in figure 6.16 b). Figure 6.16 b) shows that all double pancakes exhibit an increase in temperature at the time of the current change dI/dt. In particular, the double pancakes A and F at the feeding points show a more pronounced temperature increase compared to the other coils.

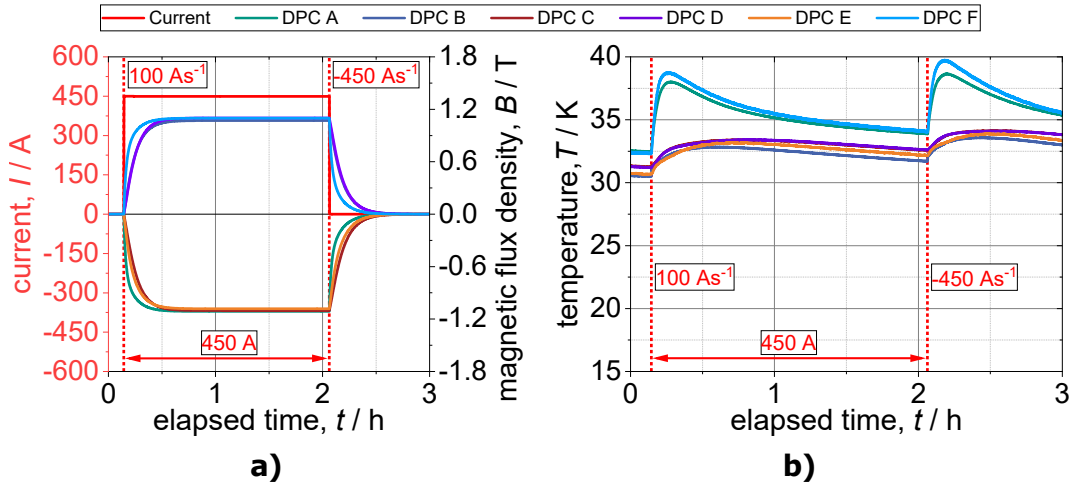

Figure 6.16: Measured double pancake center magnetic flux densities and temperatures during current supply with 450 A. Current ramp at 0.15 h to a maximum current of 450 A with 100 A s^{-1}. Current ramp at 2.1 h to a current of 0 A with 450 A s^{-1}.
a) Supply current and center magnetic flux densities of the double pancakes
b) Temperatures of the double pancakes

In order to reproduce the temperature rise of the coil system under conduction-cooled conditions, the electro-thermal model from figure 5.22 and the equivalent circuit diagram of the coil system presented in figure 6.9 are coupled with each other. For the simulation, the same current ramps are assumed as in the measurement from figure 6.16. For the thermal mass of the double pancakes, the temperature dependent specific heat capacities of Hastelloy^{TM} C276 and Cu RRR 50 shown in figure 5.21 b) are assumed. To simulate the thermal behavior and to get an estimation of the expected peak temperatures, the initial temperatures in the model are defined as the measured temperatures and a cooling curve is chosen to sufficiently reproduce the measured recooling of the coils. Figure 6.17 shows the simulated magnetic flux densities, temperatures and radial currents of the double pancake coils. The simulated temperatures in figure 6.17 b) are comparable to the measured temperatures and in particular the pronounced temperature increases of the double pancakes A and F at the feeding points can be reproduced. The temperature increases can be explained by the radial currents I_r shown in figure 6.17 c). Due to the parasitic resistive connections R_{Par} and the resulting equivalent circuit from figure 6.9, significantly higher radial currents occur especially in the double pancakes A and F at the feeding points. As a result, the turn-to-turn losses P_{turn} are particularly high in these two double pancakes, which leads to an increased temperature rise ΔT. The similar temperature rises for both current ramps show that the dissipated turn-to-turn losses P_{turn} already reach a maximum at a current ramp of 100 A s^{-1} and that increasing the current ramp from 100 A s^{-1} to 450 A s^{-1} does not increase the losses any further.

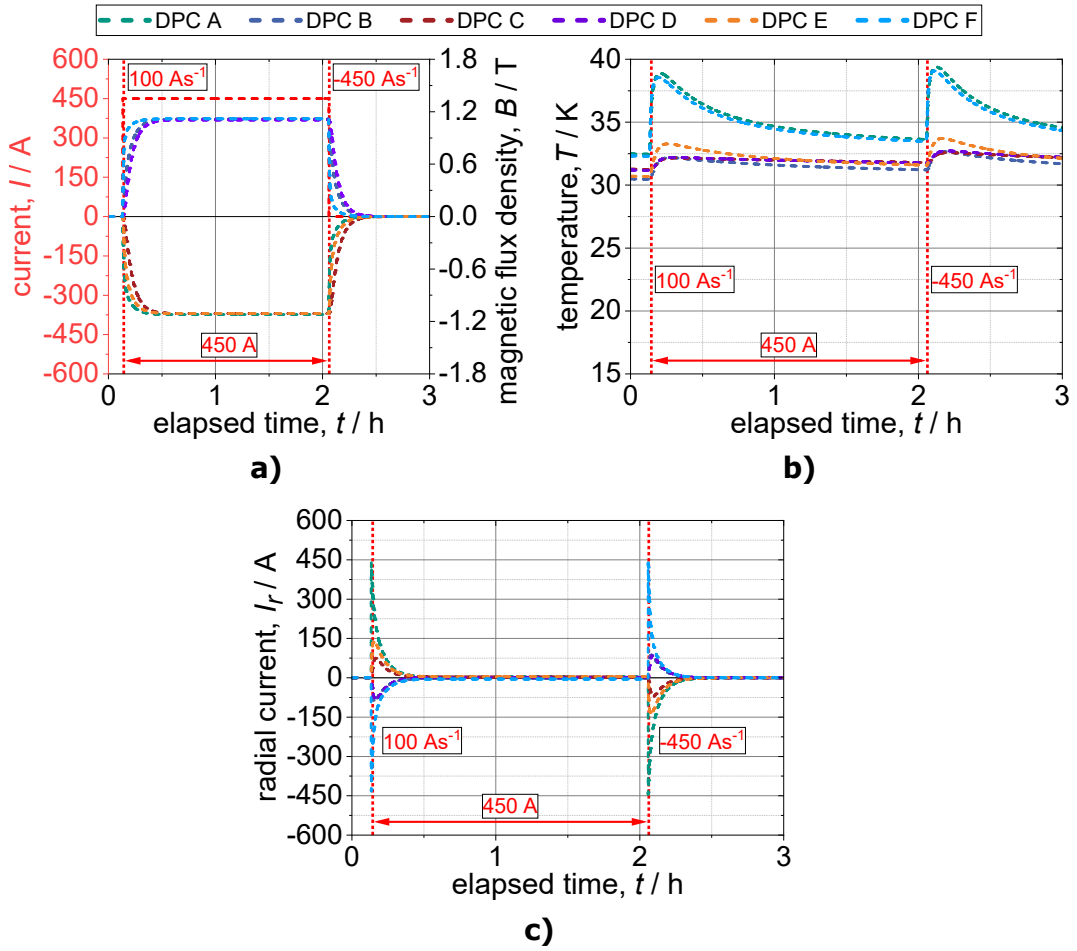

Figure 6.17: Simulated double pancake center magnetic flux densities, temperatures and radial currents during current supply with 450 A. Current ramp at 0.15 h to a maximum current of 450 A with 100 A s^{-1}. Current ramp at 2.1 h to a current of 0 A with 450 A s^{-1}.
a) Supply current and center magnetic flux densities of the double pancakes
b) Temperatures of the double pancakes
c) Radial currents of the double pancakes

Table 6.4 lists the average measured and simulated temperature rises of the double pancakes for the two current ramps. In addition, the simulated total dissipated energy in the double pancakes E_{turn} is given. As already mentioned, the individual resistance values for the equivalent circuit in figure 6.9 cannot be determined quantitatively. Nevertheless, table 6.4 shows that the expected peak temperatures of the double pancakes can be sufficiently estimated with the given model.

Table 6.4: Measured temperature rise, simulated temperature rise and simulated total dissipated energy of the double pancakes

Coil	Measured ΔT (K)	Simulated ΔT (K)	Simulated E_{turn} (J)
DPC A	5.52	6.91	8724.47
DPC B	2.31	2.16	1403.13
DPC C	2.11	1.31	751.00
DPC D	2.11	1.52	871.10
DPC E	2.47	3.00	2331.64
DPC F	6.36	6.75	8178.47

6.4.4 Cooldown of the modified conduction cooled cryogenic system

In order to test the system without the pre-cooling by liquid nitrogen, some changes are made to the current leads and further the operating point of cryocooler F is changed. As explained in subsection 4.2.2, the resistive current leads are designed for the expected maximum critical current of approximately 700 A at 30 K. Therefore, the previous resistive current leads are replaced by current leads optimized for a current of 450 A. This reduces the direct heat load on the interface between the resistive and binary current leads by 6.4 W. In addition, the thermal connection of the resistive current leads to the first cooling stage is improved. For this purpose, a further contact to the additional thermal link displayed in figure 4.17 is realized, in order to increase the total surface of the thermal connection between the resistive current leads and the first cooling stage. As a last measure, the frequency of the compressor of cryocooler F is increased manually. In the first cooldown, it was observed that the operating frequency of the compressor is below the target frequency. By manually increasing the frequency, it is intended to improve the cooling capacity of cryocooler F.

The cooling curves of the second cooldown are shown in figure 6.18. The temperature sensors $T_{CL\,A0}$ and $T_{CL\,A1}$ may have been damaged during the modifications and unfortunately do not show any signals in this measurement. The vacuum pressure in the cryostat for the cooling process is around 8.30×10^{-4} mbar and thus significantly higher than during the first cooldown. Although thermal equilibrium is reached about 4 h earlier, the double pancakes, as illustrated in figure 6.18 c) and figure 6.18 d), only reach temperatures above 30 K. In general, it can be seen that the cooling behavior of the entire system is fundamentally different compared to the first cooldown. Nevertheless, the temperature sensor $T_{CL\,F1}$ in figure 6.18 b) reaches a temperature of 70 K compared to the previous temperature of 100 K. This shows that the measures taken to improve the interface between the

resistive and binary current leads are successful and that it is possible to feed in excitation current without pre-cooling by liquid nitrogen.

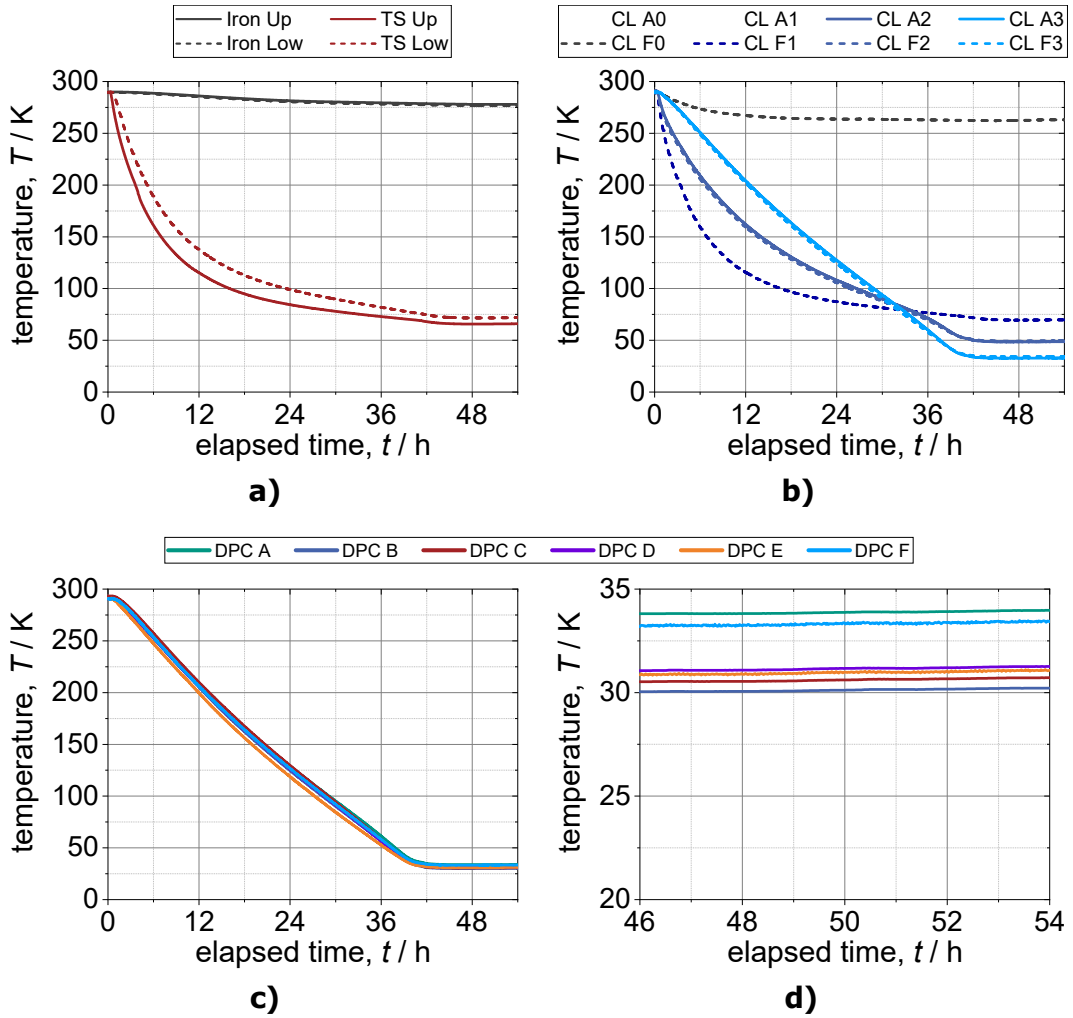

Figure 6.18: Cooldown of the generator system
a) Temperatures of the substructures
b) Temperatures of the current leads
c) Temperatures of the double pancakes
d) Zoomed temperatures of the double pancakes in thermal equilibrium

6.4.5 Continuous current supply without pre-cooling of the current leads by liquid nitrogen

To check the stability of the generator system without pre-cooling with liquid nitrogen, the stator system is supplied with an excitation current for several hours. The system is measured at steady state minimum thermal equilibrium and no additional heating power is used for temperature control. Figure 6.19 c) shows

the supplied current and the magnetic flux density in the center of the double pancakes for a maximum current of 350 A. The stator system is charged and discharged after 0.5 h and 5.8 h respectively at a slew rate of 0.5 A s^{-1}. Thus, a continuous current of 350 A over more than 5 h can be achieved. Due to the additional heat load from the excitation current and the absence of pre-cooling with liquid nitrogen, the thermal shield and current leads in the system heat up. Figure 6.19 a) displays the temperatures of the substructures. While the stator iron shows no temperature change due to the thermal decoupling to the cryogenic system, a slight temperature increase of the thermal shield can be observed. In particular, the upper thermal shield experiences a temperature increase due to the direct connection to the resistive current leads. In figure 6.19 b) the temperatures of the current leads are presented. The temperature sensors $T_{CL\,A0}$ and $T_{CL\,A1}$ are still damaged and do not show any signals. The sensors $T_{CL\,F0}$ and $T_{CL\,F1}$, which are located at the start and end of the resistive current lead, exhibit a temperature rise during the supply with the excitation current. The critical interface between the resistive and binary current lead, measured by sensor $T_{CL\,F1}$, reaches a maximum temperature of almost 80 K. Thus, the binary current lead remains below the critical temperature of the superconductor T_c of 93 K during a continuous current supply of 350 A. The temperatures of the double pancakes are displayed in figure 6.19 d) shows. The double pancakes B to E have a starting temperature of less than 30 K. The slightly lower temperature compared to the cooldwon in figure 6.18 can be explained by a further manual increase of the compressor frequency of cryocooler F. A temperature rise can be seen, resulting from the current change dI/dt of 0.5 A s^{-1} at 0.5 h and 5.8 h, caused by the turn-to-turn losses presented in section 2.3. As already displayed in figure 6.16, the double pancakes A and F exhibit the highest temperature rise, with an average temperature increase ΔT of 1.87 K and 2.39 K, respectively, while the remaining coils show a temperature increase of only 0.88 K on average. The start temperature of the binary current lead at sensor $T_{CL\,F1}$ with 80 K, during a continuous current of 350 A is already relatively high. The current carrying capacity of the HTS tapes of the binary current leads could be greatly reduced at temperatures above 80 K, which would result in a burnout of the binary current leads. Therefore, it was decided to perform the test with the rated current of 450 A directly on the rotation test bench.

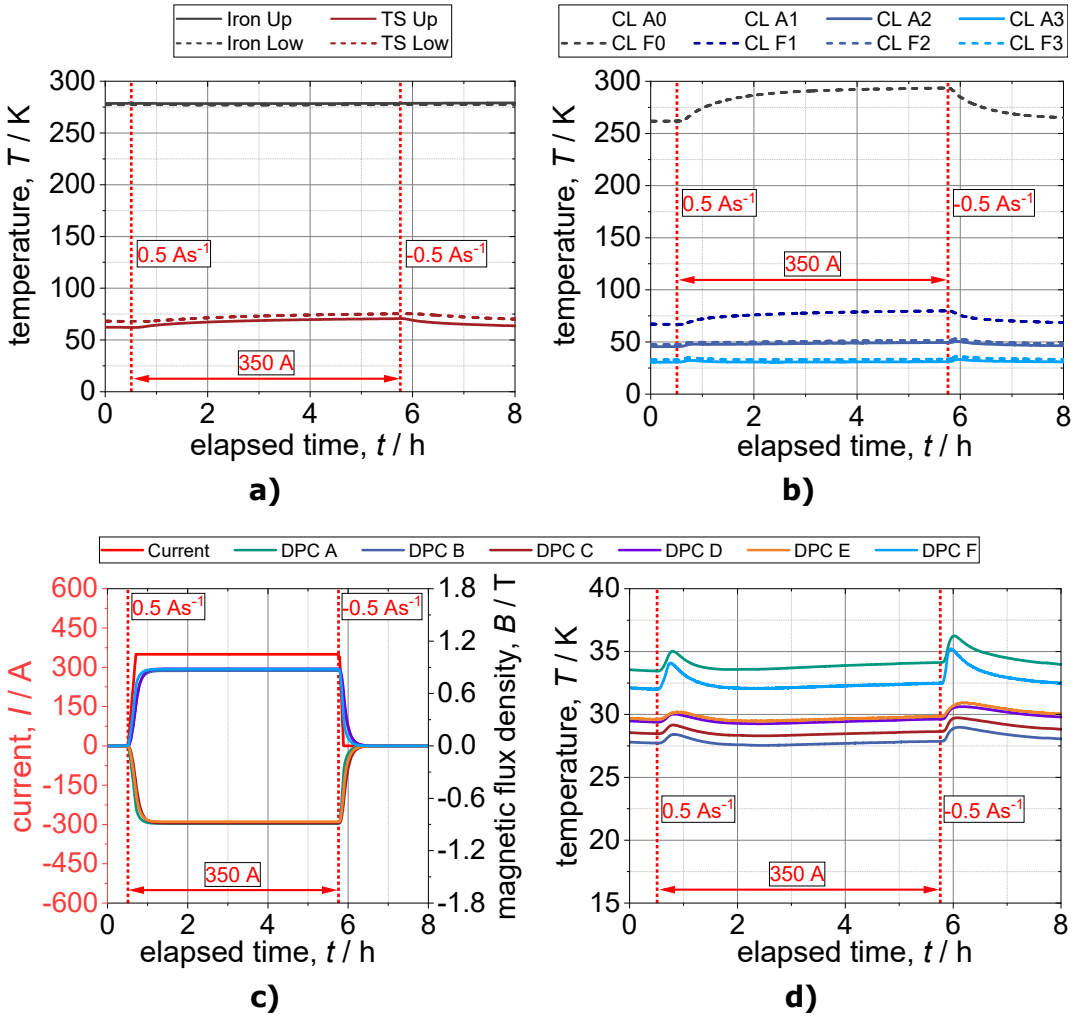

Figure 6.19: Measured temperatures and center magnetic flux densities during a continuous current supply. Current ramp at 0.5 h to a maximum current of 350 A with 0.5 A s^{-1}. Current ramp at 5.8 h to a current of 0 A with −0.5 A s^{-1}.
a) Temperatures of the substructures
b) Temperatures of the current leads
c) Supply current and center magnetic flux densities of the double pancakes
d) Temperatures of the double pancakes

6.5 Assembly of the generator demonstrator on the rotation test bench

To test the complete generator demonstrator under rotation, the shaft of the rotor is connected to a drive motor on a rotation test bench. The complete set-up with the superconducting generator demonstrator, the drive motor and the shaft coupling is presented in figure 6.20 a). Due to the poor vacuum conditions in

the cryostat, vacuum is continuously pumped via a vacuum hose. Figure 6.20 b) displays a close-up of the cryostat bottom lid with the rotor shaft including the shaft coupling and the vacuum connection. The two cold heads A and F with connected helium hoses, the current feedthroughs with connected high-current cables and the remaining feedthroughs for the measurement instrumentation are shown in the close-up of the upper cryostat lid in figure 6.20 c).

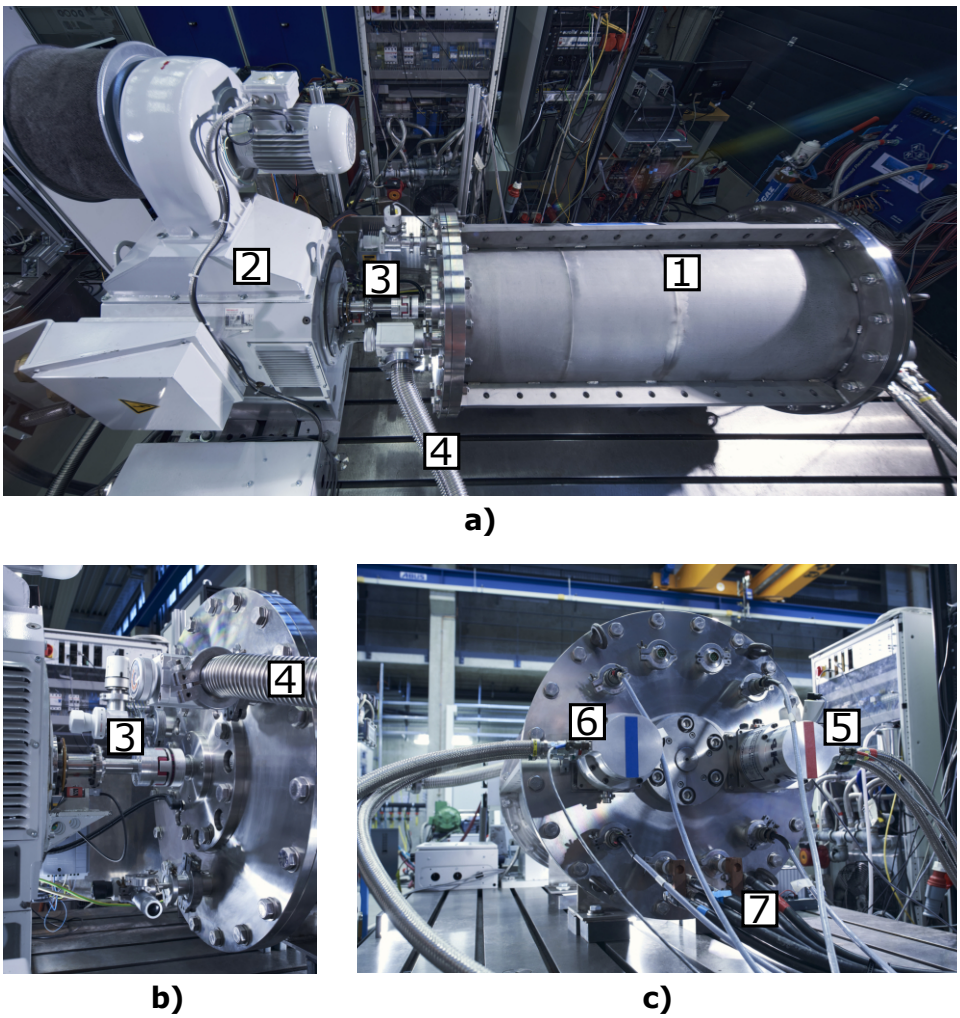

Figure 6.20: a) Top view of the rotation test bench with the generator demonstrator [1], the drive motor [2], the shaft coupling [3] and the vacuum hose [4] *(Ref.: Amadeus Bramsiepe)*
b) Close-up of the cryostat top lid with the shaft coupling [3] and the vacuum hose [4] *(Ref.: Amadeus Bramsiepe)*
c) Close-up of the cryostat bottom lid with cold head A [5] and cold head F [6] with assembled helium hoses and the current feedthrough [7] with assembled with assembled high-current cables *(Ref.: Amadeus Bramsiepe)*

During the third cooldown process on the rotating test bench, only a vacuum of 6.30×10^{-2} mbar could be achieved. A vacuum leakage test showed that the vacuum chamber in the generator is contaminated with helium gas. The reduced cooling capacity of cryocooler F, which is considered in more detail in appendix A, the reduced frequency of the compressor of cryocooler F, as well as the helium gas in the generator, lead to the conclusion that the cold head of cryocooler F has a helium leakage in the vacuum space of the generator. The leakage in cold head F could be confirmed with a further test. The temperatures in the cryostat during this test are shown in figure 6.21.

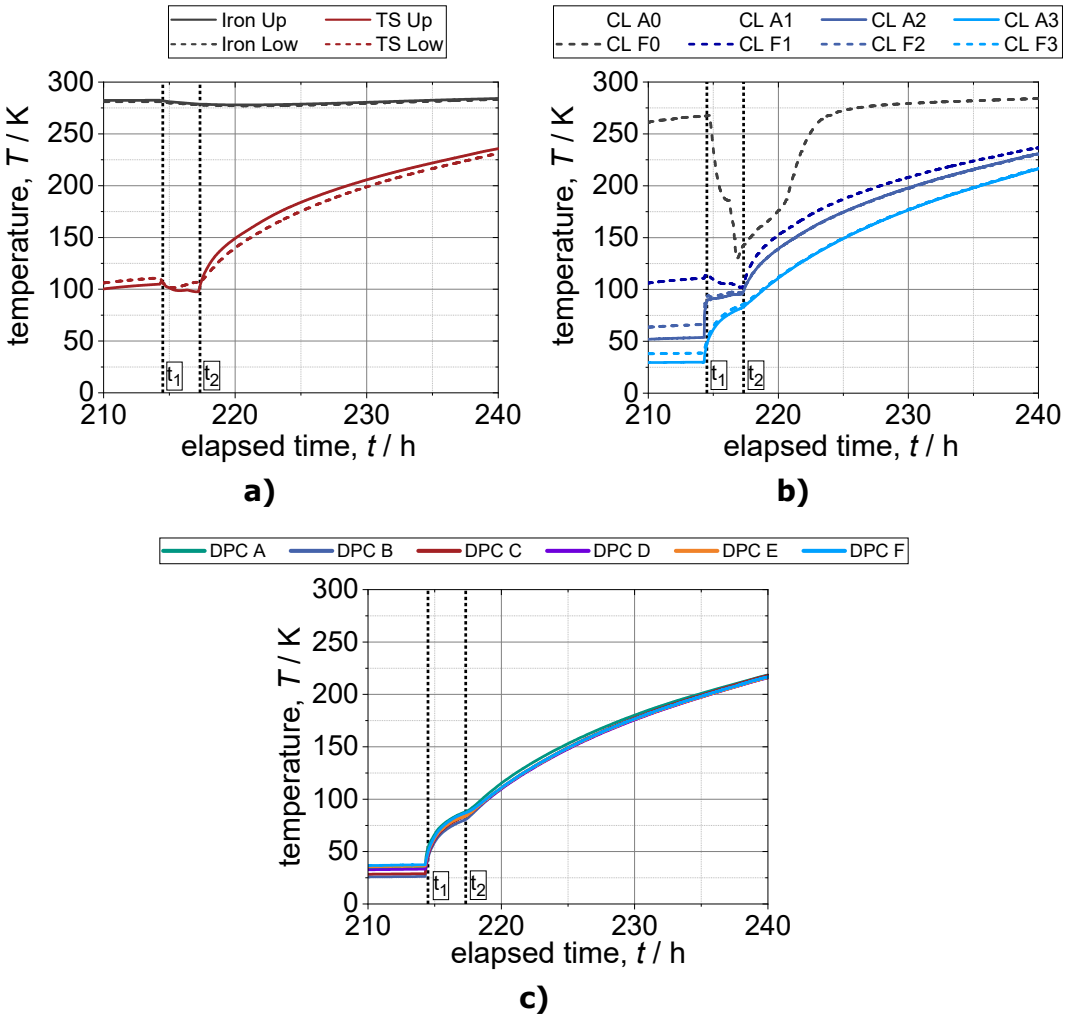

Figure 6.21: Measured temperatures during cooldown process on the rotating test bench. Pre-cooling of the current leads with liquid nitrogen and restart of cryocooler F at t_1. Shutdown of both cryocoolers at t_2
a) Temperatures of the substructures
b) Temperatures of the current leads
c) Temperatures of the double pancakes

Cryocooler F is shut down and the helium supply lines from the compressor to the cold head are disassembled. Thus, there is no longer a connection between the helium reservoir in the compressor and the cold head mounted on the cryostat. Until time t_1, only cryocooler A operates. By this time, due to the lack of connection to compressor F, the vacuum pressure can recover from an initial pressure of 6.30×10^{-2} mbar to 7.05×10^{-5} mbar within seven days. However, sensor T_{CLF1} in figure 6.21 b) shows that the cooling capacity of only one cryocooler is not enough to achieve a sufficiently low temperature at the interface of the resistive to the binary current leads. Even an additional pre-cooling of the current leads with liquid nitrogen and only one operating cryocooler is not sufficient to reach temperatures below the critical temperature T_c of the HTS tapes at the start of the binary current leads. Therefore, at time t_1, two measures are carried out simultaneously. Firstly, the current feedthroughs are pre-cooled on the atmosphere side with liquid nitrogen. Secondly, the helium hoses are reconnected to cold head F and cryocooler F is put back into operation. Due to the restart of cryocooler F, the vacuum pressure increases again abruptly to 5.1×10^{-2} mbar. As a result, two general trends can be observed. The temperatures of the first cooling stage, such as T_{CLF0}, T_{CLF1}, T_{TSUp}, and T_{TSLow} shown in figure 6.21 a) and 6.21 b), first decrease, due to the liquid nitrogen pre-cooling of the current leads. In particular, T_{CLF0}, as the closest sensor to the current feedthroughs, experiences a very fast cooldown. However, the double pancakes as well as the temperature sensors of the binary current lead show a sudden increase in temperature, displayed in figure 6.21 b) and 6.21 c). Due to the contamination of the vacuum chamber with helium gas, there is an additional heat input by convective heat transfer between the cryogenic system and the outer cryostat walls. Furthermore, convective heat exchange between the two cooling stages of the cryogenic system may occur. The lack of vacuum insulation together with the reduced cooling capacity of cryocooler F finally make cryogenic operation and further test of the generator under rotational conditions impossible. Therefore, at time t_2 both cryocoolers are switched off to warm up the system.

It is likely that this failure existed before the cryocooler was installed in the generator system, and that the leakage was exacerbated by the multiple cooling and warm-up phases. However, the acquisition of a replacement cryocooler and its installation in the cryogenic system of the superconducting generator demonstrator are not in the scope of this work.

7 Summary and outlook

To address the continuing increase in weight and volume of wind turbine generators due to the demand for higher turbine power ratings, this thesis addresses the potential and feasibility of superconducting generators for the wind industry. For this purpose, the design, development and testing of a generator technology demonstrator with field coils from high temperature superconductors is described. The no insulation winding method is applied with the aim of achieving particularly robust superconducting coils.

An introduction to the second generation superconductors (2G HTS) used in this work is given in chapter 2. The typical layer structure of the 2G HTS tapes as well as the parameters limiting the superconducting state such as the critical temperature T_c, the critical magnetic flux density B_c and the critical current density j_c are presented. An overview of the current state of 2G HTS technology from the most important manufacturers is given. Current 2G HTS tapes typically reach critical currents at 77 K in self-field between 400 A cm^{-1} and 600 A cm^{-1}, corresponding to an engineering current density j_e of around 500 A mm^{-2}. At 30 K and 3 T, which are typical operating conditions for superconducting electrical machines, a record engineering current density of up to 7068 A mm^{-2} can be reported. Due to their physical properties, 2G HTS are particularly susceptible to local hots spots with very high peak temperatures. For this reason, the stability criteria of these superconductors are further discussed and the current state of research regarding detection and protection of propagating normal conductive zones, known as quench, is presented. No insulation winding technique as passive self-protection against local hot spots is introduced as a possibility for robust superconducting field coils in electrical machines. The typical properties of no insulation coils such as the charging and discharging delay, the turn-to-turn resistance and the turn-to-turn losses occurring under dynamic operation are defined.

In chapter 3, the current developments in the wind industry are first described. In 2019, the global installed capacity is 651 GW and the compound annual growth rate (CAGR) until 2050 is given as 7.2 % and 11.5 % for onshore and offshore wind, respectively. In order to reduce the levelized cost of energy, there is a trend towards larger wind turbines and wind farms. The average offshore turbine capacity in the european union increased from around 2 MW to 8 MW between 2000 and 2020, while an average wind farm in 2020 has a total capacity of about 800 MW. First prototype turbines with a rated power of 14 MW and higher are expected in the years 2021 and 2022. Furthermore, the most common generator classes and drive train concepts and their future market share are presented. It is expected

that maintenance intensive high-speed gearboxes with induction generators will be increasingly displaced by medium-speed or direct drive permanent magnet synchronous generators.
In the second part of chapter 3, the effects and implementation options of superconductors in wind generators are discussed to enable a classification of the design concepts of superconducting machines. Due to the high current carrying capacity of superconductors, air gap windings are a possible alternative to save heavy ferromagnetic structures, to realize air gap flux densities above iron saturation and to reduce harmonics in the air gap, while maintaining a relatively low number of turns per winding. Nevertheless, the superconducting windings are exposed to higher electromagnetic and mechanical stress, which leads to an by a factor of 1.5 to 34 increased superconductor requirement for air gap winding designs. Furthermore, the concept of stationary superconducting field coils without a complex rotating cryogenic system as well as the concept of a partial superconducting machine with normally conducting three-phase winding and fully superconducting machine with a superconducting stator and rotor are discussed. For a comprehensive classification, the different cryogenic cooling concepts for superconducting rotating machines are further presented. The cooling concepts can basically be divided into open loop and closed loop and into remote and direct cryogenic cooling. Finally, a power density comparison of partial and fully superconducting wind generators with direct drive permanent magnet synchronous generators, as the most competitive conventional system, is given. For the data from direct drive permanent magnet synchronous generators, an average torque to weight ratio of 35 kN m t^{-1} is found whereas the designs of partial and fully superconducting machines reach average values of 79 kN m t^{-1} and 204 kN m t^{-1}, respectively.

Regarding the classification from chapter 3, a demonstrator design of a partial superconducting synchronous generator with stationary superconducting, no insulation field coils and a rotating, normally conducting three-phase winding is chosen. Stator and rotor iron are designed as air gap windings and the cryogenic temperatures in the stator are achieved by a direct conduction cooled cryogenic cooling system.
In chapter 4 the detailed electromagnetic, thermal and mechanical design of the generator technology demonstrator is presented. The electromagnetic calculations are based on a transient, two-dimensional (2D) finite element model. The rated power of the demonstrator is 10 kW at a rotational speed of 389 min and a torque of 250 N m. The average magnetic flux density in the air gap is 0.63 T at a rated excitation current I_{ex} of the superconducting field coils of 450 A. The thermal calculations are based on static 3D finite element models and analytical 1D models. The cryogenic system is cooled by direct conduction cooling with two cryocoolers. The cold heads of the cryocoolers have two cooling stages for which temperatures of 77 K and 30 K are assumed in the thermal models. The heat input of the current leads $\dot{Q}_{CL}$, the mechanical support structures $\dot{Q}_{SP}$ and the thermal radiation $\dot{Q}_{Rad}$ on the first cooling stage are respectively 44.64 W, 15.87 W and 4.12 W and to the second cooling stage 0.89 W, 2.89 W and 0 W. This corresponds to a total required electrical power of the cryogenic cooling system of 4.42 kW at room

temperature. The calculations for the mechanical design are based on transient 2D and static 3D finite element models. The maximum forces acting on the individual superconducting coils at rated excitation of 450 A in the axial, tangential, and radial directions are 3.57 kN, 8.60 kN, and 22.45 kN, respectively.

In this work, 2G HTS tapes from two different manufacturers are used. Therefore, in chapter 5 the architectures of both tapes are presented and a characterization regarding the critical current I_c and the turn-to-turn contact resistivity ρ_c is performed. The critical currents are measured for a minimum temperature of 20 K and maximum magnetic flux densities of 5 T, while the determination of the contact resistivity takes place in liquid nitrogen at 77 K. Furthermore, the design and the manufacturing process of the superconducting field coils are explained. Due to the very different contact resistivity ρ_c of the two HTS tapes, the coils with tape 1 are designed as no insulation coils and the coils with tape 2 are co-wound with a metal tape and therefore referred to as metal insulation coils. A total of 14 individual pancake coils are manufactured which are then assembled into seven double pancake coils. Both pancake and double pancake coils are successfully pretested in liquid nitrogen at 77 K. All coils reach the expected minimum critical current but especially coils with tape 1 show a large scatter in the measured values. The critical current for pancakes with tape 1 ranges from 208.6 A to 283.6 A, while pancakes with tape 2 range from 122.4 A to 130.2 A. The range of the time constant τ of the double pancakes measured in the dynamic charging and discharging tests is between 13.1 s and 43.2 s. The coil which is not to be used in the generator technology demonstrator is investigated in further measurements under conduction-cooled conditions with regard to the critical current, the dynamic behavior and the thereby occurring turn-to-turn losses. To successfully demonstrate the improved stability of the designed no insulation coils in liquid nitrogen, this coil is further supplied with 1.5 times the critical current without any damaging.

Finally, chapter 6 describes the assembly and testing of the generator technology demonstrator. Six of the double pancake coils are joined together in a hexagon, electrically connected in series and pretested in liquid nitrogen at 77 K. In this first test, a critical current I_c of the whole coil system of 115.9 A is reached and the generation of alternating magnetic poles is confirmed. Furthermore, a total resistance of 6.64 µΩ can be determined caused by resistive components in the coil path and by resistive interconnections. This results in additional Joule heating of 1.34 W on the second cooling stage at a rated current of 450 A. In addition, dynamic charging and discharging tests reveal a systematic pattern that leads to significant increases in coil time constants, ranging from 157.6 s to 379.6 s. This behavior is probably caused by parasitic resistive interconnections due to insufficient electrical insulation. Next, the installation of the superconducting coil system in the stator cryostat of the generator demonstrator is described. For this purpose, the cryogenic cooling system, the coil system and the stator iron are suspended vertically from the cryostat top lid, inserted into the cryostat vessel and finally placed in the horizontal position. The generator stator system is then tested with respect to the performance of the conduction-cooled cryogenic cooling system and superconducting coil system. The cooldown of the entire system to thermal

equilibrium takes almost 48 h and all double pancake coils reach a temperature below 20 K. However, the current leads do not reach the required low temperatures and are therefore precooled on the atmospheric side with liquid nitrogen for a current supply. Thus, the superconducting coil system can be measured under conduction-cooled conditions at controlled temperatures of 77 K, 50 K and 30 K. The coil system reaches a critical current of 695.4 A at the operating temperature of 30 K, hence meeting the requirements for a rated current of 450 A. Furthermore, the dynamic charging and discharging and turn-to-turn losses are investigated at the different temperatures. It is shown that the previously observed pattern is temperature-dependent and that the double pancakes at the current feeding terminals show the largest temperature increase during dynamic operation. The maximum measured temperature rise ΔT, caused by turn-to-turn losses, at an initial temperature of 30 K is 5.52 K and 6.36 K for the two double pancakes. In a further step, the cryogenic cooling system is improved and an operation over more than 5 h with an excitation current of 350 A without the pre-cooling of the current leads with liquid nitrogen is achieved. However, during the final test of the generator technology demonstrator on the rotating test bench, the cryogenic cooling system fails and no measurements can be performed under rotating conditions. A defective cryocooler is suspected as the cause of the inadequate performance of the cooling system but the acquisition of a replacement cryocooler and its installation in the cryogenic system are not in the scope of this work.

Within the framework of this thesis, the development of a partial superconducting generator technology demonstrator is successfully realized. Thus, basic design approaches are worked out which contribute to the development of superconducting technologies for the wind industry. However, further projects with machine designs of higher power classes are needed to demonstrate the effects of superconducting materials in terms of increased power density and efficiency as well as an improved economic balance. The application of no insulation technology in electrical machines allows very robust field coils to be operated above the usual safety margins of superconducting coils, which could reduce the amount of required superconductor. Nevertheless, the principle use of such coils under rotating conditions in a generator environment could not be demonstrated due to the defective cooling system. Therefore, future work should be done to measure the entire generator system under rotating conditions. Not only the basic functionality of the system can be tested, but also the behavior of the no insulation coils under transient conditions such as a change in load. Finally, the potential of fully superconducting machines in wind turbines with regard to a significantly increased power density, as presented in this work, should be the subject of future research. However, the design and realization of a functional prototype poses a great challenge due to the complexity and stage of development of such machines. In addition to superconducting field coils, developments in superconducting armature coils and their detailed thermal and mechanical design are required. As a first step, individual prototype coils could be investigated with regard to alternating current losses and theoretical machine concepts with an enhanced focus on practical feasibility should be developed.

8 Bibliography

[1] J. Lee and F. Zhao. *Global wind report 2019*. Tech. rep. Global Wind Energy Council (GWEC), 2020.

[2] D. Gielen, R. Gorini, G. Prakash et al. *Future of wind: Deployment, investment, technology, grid integration and socio-economic aspects*. Tech. rep. International Renewable Energy Agency (IRENA), 2019.

[3] F. Selot, D. Fraile and G. Brindley. *Offshore Wind in Europe: Key trends and statistics 2018*. Tech. rep. WindEUROPE, 2019.

[4] L. Ramirez, D. Fraile and G. Brindley. *Offshore Wind in Europe: Key trends and statistics 2020*. Tech. rep. WindEUROPE, 2021.

[5] Siemens Gamesa Renewavle Energy. 2021. URL: https://www.siemensgamesa.com/products-and-services/offshore/wind-turbine-sg-14-222-dd.

[6] General Electric Renewable Energy. 2021. URL: https://www.ge.com/renewableenergy/wind-energy/offshore-wind/haliade-x-offshore-turbine.

[7] Vestas. 2021. URL: https://www.vestas.com/en/products/offshore%20platforms/v236_15_mw#!grid_0_content_0_Container.

[8] R. S. Semken, M. Polikarpova, P. Röyttä et al. "Direct-drive permanent magnet generators for high-power wind turbines: Benefits and limiting factors". In: *Renewable Power Generation* (2012). DOI: 10.1049/iet-rpg.2010.0191.

[9] K. S. Haran, S. Kalsi, T. Arndt et al. "High power density superconducting rotatingmachines—development status and technologyroadmap". In: *Superconductor Science and Technology* (2017). DOI: 10.1088/1361-6668/aa833e.

[10] P. Viebahn, O. Soukup, S. Samadi et al. "Assessing the need for critical minerals to shift the German energy system towards a high proportion of renewables". In: *Renewable and Sustainable Energy Reviews* (2015). DOI: 10.1016/j.rser.2015.04.070.

[11] S. Hahn, D. K. Park, J. Bascuñán et al. "HTS Pancake Coils Without Turn-to-Turn Insulation". In: *IEEE Transactions on Applied Superconductivity* (2011). DOI: 10.1109/TASC.2010.2093492.

[12] J. Bardeen, L. N. Cooper and J. R. Schrieffer. "Theory of Superconductivity". In: *Physical Review* (1957). DOI: 10.1103/PhysRev.108.1175.

[13] J. G. Bednorz and K. A. Müller. "Possible high Tc superconductivity in the BaLaCuO system". In: *Zeitschrift für Physik B Condensed Matter* (1986). DOI: 10.1007/BF01303701.

[14] P. J. Ray. "Structural investigation of La2-xSrxCuO4+y". MA thesis. Niels Bohr Institute, Faculty of Science, University of Copenhagen, 2015. DOI: 10.6084/m9.figshare.2075680.v2.

[15] P. Mele, K. Prassides, C. Tarantini et al. *Superconductivity*. Springer, Cham, 2020. DOI: 10.1007/978-3-030-23303-7.

[16] T. Matsushita. *Superconductivity and Electromagnetism*. Springer, Cham, 2021. DOI: 10.1007/978-3-030-67568-4.

[17] T. Hoshino, I. Muta, T. Itoh et al. "Preliminary Study on a Rotating Armature Type Superconducting Motor". In: *IEEE Transactions on Magnetics* (1994). DOI: 10.1109/20.305665.

[18] K. S. Haran, D. Loder, T. O. Deppen et al. "Actively Shielded High-Field Air-CoreSuperconducting Machines". In: *IEEE Transactions on Applied Superconductivity* (2016). DOI: 10.1109/TASC.2016.2519409.

[19] R. Fair, W. Stautner, M. Douglass et al. *Superconductivity for Large Scale Wind Turbines*. Tech. rep. General Electric - Global Research, 2012. DOI: 10.2172/1052970.

[20] R. M. Scanlan, A. P. Malozemoff and D. C. Larbalestier. "Superconducting materials for large scale applications". In: *Proceedings of the IEEE* (2004). DOI: 10.1109/JPROC.2004.833673.

[21] René Flükiger. *MgB2 Superconducting Wires*. WORLD SCIENTIFIC, 2016. DOI: 10.1142/9830.

[22] D. Uglietti. "A review of commercial high temperature superconducting materials for large magnets: from wires and tapes to cables and conductors". In: *Superconductor Science and Technology* (2019). DOI: 10.1088/1361-6668/ab06a2.

[23] I. Pallecchi, M. Eisterer, A. Malagoli et al. "Application potential of Fe-based superconductors". In: *Superconductor Science and Technology* (2015). DOI: 10.1088/0953-2048/28/11/114005.

[24] B. Holzapfel. "Supraleitung: Grundlagen, Effekte, Anwendungen". In: *ZIEHL VI, ivSupra*. 2018. URL: https://ivsupra.de/vi-ziehl-vortraege/.

[25] M. Bäcker. "Produktion supraleitender Drähte für die Energietechnik". In: *ZIEHL VI, ivSupra*. 2018. URL: https://ivsupra.de/vi-ziehl-vortraege/.

[26] M. Bauer. "Supraleiter für die Energietechnik". In: *ZIEHL VII, ivSupra*. 2020. URL: https://ivsupra.de/vii-ziehl-vortraege/.

[27] Victoria University of Wellington, Robinson Research Intitute. "HTS Wire database". In: (2021). DOI: 10.6084/m9.figshare.5331145.v2.

[28] F. Sirois and F. Grilli and A. Morandi. "Comparison of Constitutive Laws for Modeling High-Temperature Superconductors". In: *IEEE Transactions on Applied Superconductivity* (2019). DOI: 10.1109/TASC.2018.2848219.

[29] Y. Iwasa. *Case studies in superconducting magnets : design and operational issues*. Springer, 2009. DOI: 10.1007/b112047.

[30] G. Majkic, R. Pratap, A. Xu et al. "Over 15 MA/cm^2 of critical current density in 4.8 μm thick, Zr-doped (Gd, Y)$Ba_2Cu_3O_x$ superconductor at 30 K, 3 T". In: *Scientific Reports* (2018). DOI: 10.1038/s41598-018-25499-1.

[31] Theva Dünnschichttechnik GmbH. May 2021. URL: https://www.theva.de/produkte/#pro-line.

[32] Shanghai Superconductor Technology Co. May 2021. URL: http://www.shsctec.com/index.php?m=list&a=index&classid=62.

[33] Y. Zhao, J. Zhu, G. Jiang et al. "Progress in fabrication of second generation high temperature superconducting tape at Shanghai Superconductor Technology". In: *Superconductor Science and Technology* (2019). DOI: 10.1088/1361-6668/aafea5.

[34] G. Jiang, Y. Zhao, J. Zhu et al. "Recent development and mass production of high J e 2G-HTS tapes by using thin hastelloy substrate at Shanghai Superconductor Technology". In: *Superconductor Science and Technology* (2020). DOI: 10.1088/1361-6668/ab90c4.

[35] American Superconductor. May 2021. URL: https://www.amsc.com/gridtec/amperium-hts-wire/.

[36] S. Fleshler, K. DeMoranville, J. Gannon et al. "Development Status of AMSC Amperium®Wire". In: *Journal of Physics: Conference Series* (2014). DOI: 10.1088/1742-6596/507/2/022005.

[37] M. W. Rupich, X. Li, S. Sathyamurthy et al. "Second Generation Wire Development at AMSC". In: *IEEE Transactions on Applied Superconductivity* (2013). DOI: 10.1109/TASC.2012.2235495.

[38] SuperPower Inc. May 2021. URL: https://www.superpower-inc.com/specification.aspx.

[39] X. Zhang, Z. Zhong, J. Geng et al. "Study of Critical Current and n-Values of 2G HTS Tapes: Their Magnetic Field-Angular Dependence". In: *Journal of Superconductivity and Novel Magnetism volume* (2018). DOI: 10.1007/s10948-018-4678-8.

[40] Superconductor Technologies Inc. May 2021. URL: https://www.supetech.com/conductus/.

[41] J.-U. Huh, J. Cao, J. Chase et al. "Development of Low-Cost 2G HTS Coated Conductors at STI". In: *Electric Power Research Institute: Conference on Superconductivit*. 2013. URL: http://mydocs.epri.com/docs/PublicMeetingMaterials/MRNYPKPLTGV/01-PFEIFFER-STI_Low-Cost_Conductors.pdf.

[42] SuNam Co., LTD. May 2021. URL: http://www.i-sunam.com/wp/sunam1-2/.

[43] J.-H. Lee, J. Kim, H. Lee et al. "Status of HTS wire and magnet activities in SuNAM". In: *Workshop on Advanced Superconducting Materials and Magnets*. 2019. URL: https://conference-indico.kek.jp/event/62/contributions/1246/attachments/837/879/KEK_WS_SuNAM_Lee_rev.pdf.

[44] SuperOx Japan LLC. May 2021. URL: http://www.superox.jp/en/about-product/.

[45] A. Molodyk, S. Samoilenkov, A. Markelov et al. "Development and large volume production of extremely high current density YBa2Cu3O7 superconducting wires for fusion". In: *Scientific Reports* (2021). DOI: 10.1038/s41598-021-81559-z.

[46] S. Samoilenkov, A. Molodyk, S. Lee et al. "Customised 2G HTS wire for applications". In: *Superconductor Science and Technology* (2015). DOI: 10.1088/0953-2048/29/2/024001.

[47] Fujikura Ltd. May 2021. URL: https://www.fujikura.co.jp/eng/products/newbusiness/superconductors/01/2052504_12808.html.

[48] M. N. Wilson. *Superconducting magnets.* Clarendon Press, 1983.

[49] F. Trillaud, F. Ayela, A. Devred et al. "Quench propagation ignition using single-mode diode laser". In: *IEEE Transactions on Applied Superconductivity* (2005). DOI: 10.1109/TASC.2005.849381.

[50] M. Breschi, L. Trevisani, L. Bottura et al. "Comparing the thermal stability of NbTi and Nb3Sn wires". In: *Superconductor Science and Technology* (2009). DOI: 10.1088/0953-2048/22/2/025019.

[51] D. Colangelo and B. Dutoit. "Impact of the Normal Zone Propagation Velocity of High-Temperature Superconducting Coated Conductors on Resistive Fault Current Limiters". In: *EEE Transactions on Applied Superconductivity* (2015). DOI: 10.1109/TASC.2015.2396935.

[52] A. A. Armenio, A. Augieri, G. Celentano et al. "Stability Measurements on YBCO Coated Conductors". In: *IEEE Transactions on Applied Superconductivity* (2008). DOI: 10.1109/TASC.2008.920835.

[53] A. Ishiyama, Y. Nishio, H. Ueda et al. "Degradation Characteristics of YBCO-Coated Conductors Subjected to Overcurrent Pulse". In: *IEEE Transactions on Applied Superconductivity* (2009). DOI: 10.1109/TASC.2009.2018734.

[54] M. Marchevsky. "Quench Detection and Protection for High-Temperature Superconductor Accelerator Magnets". In: *Instruments* (2021). DOI: 10.3390/instruments5030027.

[55] T. Ariyama, T. Takagi, D. Nakayama et al. "Quench Protection of YBCO Coils: Co-Winding Detection Method and Limits to Hot-Spot Temperature". In: *IEEE Transactions on Applied Superconductivity* (2016). DOI: 10.1109/TASC.2016.2529838.

[56] M. Marchevsky, A. R. Hafalia, D. Cheng et al. "Axial-Field Magnetic Quench Antenna for the Superconducting Accelerator Magnets". In: *IEEE Transactions on Applied Superconductivity* (2015). DOI: 10.1109/TASC.2014.2374536.

[57] M. Marchevsky, Y. Xie and V. Selvamanickam. "Quench detection method for 2G HTS wire". In: *Superconductor Science and Technology* (2010). DOI: 10.1088/0953-2048/23/3/034016.

[58] K. Zhou, L. Ren, J. Shi et al. "Experimental Study of Fiber Bragg Grating Applied on Quench Detection of HTS Tapes". In: *IEEE International Conference on Applied Superconductivity and Electromagnetic Devices* (2020). DOI: 10.1109/ASEMD49065.2020.9276371.

[59] F. Scurti, S. Ishmael, G. Flanagan et al. "Quench detection for high temperature superconductor magnets: a novel technique based on Rayleigh-backscattering interrogated optical fibers". In: *Superconductor Science and Technology* (2016). DOI: 10.1088/0953-2048/29/3/03LT01.

[60] J. Jiang, Z. Wu, B. Liu et al. "Thermal Stability Study of a Solder-Impregnated No-Insulation HTS Coil Via a Raman-Based Distributed Optical Fiber Sensor System". In: *IEEE Transactions on Applied Superconductivity* (2019). DOI: 10.1109/TASC.2018.2890384.

[61] X. Zhang, Y. Lu, F. Wang et al. "Development of fully-distributed fiber sensors based on Brillouin scattering". In: *Photonic Sensors* (2010). DOI: 10.1007/s13320-010-0019-7.

[62] M. Marchevsky and S. A. Gourlay. "Acoustic thermometry for detectingquenches in superconducting coils andconductor stacks". In: *Applied Physics Letters* (2017). DOI: 10.1063/1.4973466.

[63] M. Marchevsky, E. Hershkovitz, X. Wang et al. "Quench Detection for High-Temperature Superconductor Conductors Using Acoustic Thermometry". In: *IEEE Transactions on Applied Superconductivity* (2018). DOI: 10.1109/TASC.2018.2817218.

[64] E. Ravaioli, M. Martchevskiia, G. Sabbi et al. "Quench Detection Utilizing Stray Capacitances". In: *IEEE Transactions on Applied Superconductivity* (2018). DOI: 10.1109/TASC.2018.2812909.

[65] E. Ravaioli, D. Davis, M. Marchevsky et al. "A new quench detection method for HTS magnets: stray-capacitance change monitoring". In: *Physica Scripta* (2020). DOI: 10.1088/1402-4896/ab4570.

[66] B. Chen, Y. Hu, J. Li et al. "Research on Quench Detection Method Using Radio Frequency Wave Technology". In: *IEEE Transactions on Applied Superconductivity* (2019). DOI: 10.1109/TASC.2019.2957195.

[67] S. S. Bang, G. S. Lee, G.-Y. Kwon et al. “Detection of Local Temperature Change on HTS Cables via Time-Frequency Domain Reflectometry”. In: *Journal of Physics: Conference Series* (2017). DOI: 10.1088/1742-6596/871/1/012100.

[68] N. Nanato, W. Asai and S. Murase. “Study on criterion for quench detection/protection of superconducting magnet based on active power method”. In: *Proceedings of the 24th International Symposium on Superconductivity* (2012). DOI: 10.1016/j.phpro.2012.03.499.

[69] N. Nanato and Y. Kobayashi. “Quench Detection and Protection for High Temperature Superconducting Transformers by Using the Active Power Method”. In: *Physics Procedia* (2014). DOI: 10.1016/j.phpro.2014.09.071.

[70] M. Breschi, L. Cavallucci, P. L. Ribani et al. “Modeling of Quench in the Coupled HTS Insert/LTS Outsert Magnet System of the NHMFL”. In: *IEEE Transactions on Applied Superconductivity* (2017). DOI: 10.1109/TASC.2017.2698214.

[71] J. van Nugteren, J. Murtomäki, J. Ruuskanen et al. “A Fast Quench Protection System for High-Temperature Superconducting Magnets”. In: *IEEE Transactions on Applied Superconductivity* (2019). DOI: 10.1109/TASC.2018.2848229.

[72] E. Ravaioli, V. I. Datskov, C. Giloux et al. “New, Coupling Loss Induced, Quench Protection System for Superconducting Accelerator Magnets”. In: *IEEE Transactions on Applied Superconductivity* (2013). DOI: 10.1109/TASC.2013.2281223.

[73] S. B. Kim, A. Saitou, J. H. Joo et al. “The normal-zone propagation properties of the non-insulated HTS coil in cryocooled operation”. In: *Physica C: Superconductivity and its Applications* (2011). DOI: 10.1016/j.physc.2011.05.209.

[74] Y. Wang, W. K. Chan and J. Schwartz. “Self-protection mechanisms in no-insulation (RE)Ba2Cu3Ox high temperature superconductor pancake coils”. In: *Superconductor Science and Technology* (2016). DOI: 10.1088/0953-2048/29/4/045007.

[75] Y.-G. Kim, S. Hahn, K. L. Kim et al. “Investigation of HTS Racetrack Coil Without Turn-to-Turn Insulation for Superconducting Rotating Machines”. In: *IEEE Transactions on Applied Superconductivity* (2012). DOI: 10.1109/TASC.2011.2181931.

[76] K. L. Kim, Y. H. Choi, D. G. Yang et al. “Analytical and empirical studies on the characteristic resistances of no-insulation GdBCO racetrack pancake coil under various operating currents”. In: *Current Applied Physics* (2015). DOI: 10.1016/j.cap.2014.10.029.

[77] X. Wang, S. Hahn, Y. Kim et al. "Turn-to-turn contact characteristics for an equivalent circuit model of no-insulation ReBCO pancake coil". In: *Superconductor Science and Technology* (2013). DOI: 10.1088/0953-2048/26/3/035012.

[78] D. G. Yang, S. Hahn, Y. Kim et al. "Characteristic Resistance of No-Insulation and Partial-Insulation Coils With Nonuniform Current Distribution". In: *IEEE Transactions on Applied Superconductivity* (2014). DOI: 10.1109/TASC.2013.2285103.

[79] J. Lu, J. Levitan, D. McRae et al. "Contact resistance between two REBCO tapes: the effects of cyclic loading and surface coating". In: *Superconductor Science and Technology* (2018). DOI: 10.1088/1361-6668/aacd2d.

[80] J. Lu, R. Goddard, K. Han et al. "Contact resistance between two REBCO tapes under load and load cycles". In: *Superconductor Science and Technology* (2017). DOI: 10.1088/1361-6668/aa5b05.

[81] H. Jeon, W. S. Lee, J. Kim et al. "Investigation of electrical characteristics of no-insulation coil wound with surface-processed HTS tape". In: *Physica C: Superconductivity and its Applications* (2017). DOI: 10.1016/j.physc.2017.06.003.

[82] Y. Wang, H. Song, D. Xu et al. "An equivalent circuit grid model for no-insulation HTS pancake coils". In: *Superconductor Science and Technology* (2015). DOI: 10.1088/0953-2048/28/4/045017.

[83] K. Kim, K. Kim, K. R. Bhattarai et al. "Quench behavior of a no-insulation coil wound with stainless steel cladding REBCO tape at 4.2 K". In: *Superconductor Science and Technology* (2017). DOI: 10.1088/1361-6668/aa6a8b.

[84] Z. Zhang, C. H. Kim, J. G. Kim et al. "An Experimental Investigation of the Transient Response of HTS Non-insulation Coil". In: *Journal of Superconductivity and Novel Magnetism volume* (2016). DOI: 10.1007/s10948-016-3824-4.

[85] Y. Liu, J. Ou, R. Gyuraki et al. "Study of contact resistivity of a no-insulation superconducting coil". In: *Superconductor Science and Technology* (2021). DOI: 10.1088/1361-6668/abd14d.

[86] H. Song. "Sudden-Discharge Cycling Characteristics and Millisecond Dynamic Behaviors of a HTS Stainless-Steel Insulated Double-Pancake Coil With Thin Copper Plates". In: *IEEE Transactions on Applied Superconductivity* (2020). DOI: 10.1109/TASC.2020.2975770.

[87] T. Lécrevisse and Y. Iwasa. "A (RE)BCO Pancake Winding With Metal-as-Insulation". In: *IEEE Transactions on Applied Superconductivity* (2016). DOI: 10.1109/TASC.2016.2522638.

[88] Y. H. Choi, S. Hahn, J. B. Song et al. "Partial insulation of GdBCO single pancake coils for protection-free HTS power applications". In: *Superconductor Science and Technology* (2011). DOI: 10.1088/0953-2048/24/12/125013.

[89] Y. Wang, H. Song, W. Yuan et al. "Ramping turn-to-turn loss and magnetization loss of a No-Insulation (RE)Ba2Cu3Ox high temperature superconductor pancake coil". In: *Journal of Applied Physics* (2017). DOI: 10.1063/1.4978593.

[90] International Energy Agency (IEA). *Renewables*. 2021. URL: https://www.iea.org/fuels-and-technologies/renewables.

[91] L. Cozzi, B. Wanner, C. Donovan et al. *Offshore Wind Outlook 2019*. Tech. rep. International Energy Agency (IEA), 2019.

[92] H. Guo, K. Rudion, C. Heyde et al. "Stability Studies of Offshore Wind Farms". In: *International Conference on Critical Infrastructure* (2010). DOI: 10.1109/CRIS.2010.5617503.

[93] C. Kost, S. Shammugam, V. Jülich et al. *Levelized cost of electricity renewable enery technologies*. Tech. rep. Frauenhofer institute for solar energy systems (ISE), 2018.

[94] K. Cory and P. Schwabe. *Wind Levelized Cost of Energy: A Comparison of Technical and Financing Input Variables*. Tech. rep. National Renewable Energy Laboratory (NREL), 2009.

[95] I. Komusanac, G. Brindley, D. Fraile et al. *Wind energy in Europe: 2020 Statistics and the outlook for 2021-2025*. Tech. rep. WindEUROPE, 2021.

[96] R. Fischer. *Elektrische Maschinen*. Hanser, 2013. DOI: 10.1007/978-3-322-92691-3_4.

[97] E. Hau. *Windkraftanlagen: Grundlagen, Technik, Einsatz und Wirtschaftlichkeit*. Springer Vieweg, 2016. DOI: 10.1007/978-3-662-53154-9.

[98] W. Hu. *Advanced Wind Turbine Technology*. Springer Vieweg, 2018. DOI: 10.1007/978-3-319-78166-2.

[99] Y. Feng, P. J. Tavner and H. Long. "Early experiences with UK round 1 offshore wind farms". In: *Proceedings of the Institution of Civil Engineers: energy* (2010). DOI: 10.1680/ener.2010.163.4.167.

[100] W. Erdmann and J. Keller. "The DOE Next-Generation Drivetrain for Wind Turbine Applications: Gearbox, Generator, and Advanced Si/SiC Hybrid Inverter System". In: *EEE Energy Conversion Congress & Exposition* (2016). DOI: 10.1109/ECCE.2016.7855499.

[101] D. Bang, H. Polinder, G. Shrestha et al. "Review of Generator Systems for Direct-Drive Wind Turbines". In: *Conference: European Wind Energy Conference* (2008).

[102] S. Sumathi, L. A. Kumar and P. Surekha. *Solar PV and WindEnergy Conversion Systems*. Springer Vieweg, 2015. DOI: 10.1007/978-3-319-14941-7.

[103] R. Schürhuber, B. R. Oswald, L. Fickert et al. "Verhalten von Windkraftanlagen mit doppelt speisenden Asynchrongeneratoren (DFIG) bei Kurzschlüssen und anderen Netzfehlern". In: *e & i Elektrotechnik und Informationstechnik* (2020). DOI: 10.1007/s00502-020-00829-2.

[104] F. K. Moghadam and A. R. Nejad. "Evaluation of PMSG-based drivetrain technologies for 10-MW floating offshore wind turbines: Pros and cons in a life cycle perspective". In: *Wind Energy* (2020). DOI: 10.1002/we.2499.

[105] V. Fernandez. "Rare-earth elements market: A historical and financial perspective". In: *Resources Policy* (2017). DOI: 10.1016/j.resourpol.2017.05.010.

[106] S. Alshibani, V. G. Agelidis and R. Dutta. "Lifetime Cost Assessment of Permanent Magnet Synchronous Generators for MW Level Wind Turbines". In: *IEEE Transactions on Sustainable Energy* (2014). DOI: 10.1109/TSTE.2013.2271781.

[107] Siemens Gamesa Renewavle Energy. 2021. URL: https://www.siemensgamesa.com/en-int/products-and-services/offshore/wind-turbine-sg-8-0-167-dd.

[108] General Electric Renewable Energy. 2021. URL: https://www.ge.com/renewableenergy/wind-energy/offshore-wind/offshore-turbine-haliade-150-6mw.

[109] Vestas. 2021. URL: https://www.vestas.com/en/products/offshore-platforms/v164_10_0_mw#!grid_0_content_0_Container.

[110] H. H. Woodson, Z. J. J. Stekly and E. Halias. "A Study of Alternators with Superconducting Field Windings: I-Analysis". In: *IEEE Transactions on Power Apparatus and Systems* (1966). DOI: 10.1109/TPAS.1966.291667.

[111] H. Sung, M. Park and I. Yu. "Designs of 10 MW Air-core and Iron-core HTS Wind Power Generators". In: *Journal of Electrical Engineering and Technology* (2015). DOI: 10.5370/JEET.2015.10.2.545.

[112] P. Breining, M. Veigel, M. Doppelbauer et al. "Iron loss measurement of nonoriented silicon and cobalt iron electrical steel sheets at liquid nitrogen temperature using ring specimen". In: *IEEE International Electric Machines and Drives Conference* (2017). DOI: 10.1109/IEMDC.2017.8002327.

[113] X. Lv, D. Sun and L. Sun. "Determination of Iron Loss Coefficients of Ferromagnetic Materials Used in Cryogenic Motors". In: *International Conference on Electrical Machines and Systems* (2019). DOI: 10.1109/ICEMS.2019.8922160.

[114] Y. Guan, Z. Q. Zhu, Z. Azar et al. "Comparison of Electromagnetic Performance of 10MW Superconducting Generators with Different Topologies for Offshore Direct-Drive Wind Turbines". In: *IEEE Transactions on Applied Superconductivity* (2017). DOI: 10.1109/TASC.2017.2732289.

[115] Y. Terao, M. Sekino and H. Ohsaki. "Comparison of Conventional and Superconducting Generator Concepts for Offshore Wind Turbines". In: *IEEE Transactions on Applied Superconductivity* (2013). DOI: 10.1109/TASC.2012.2237223.

[116] H. Ohsaki, L. Quéval and Y. Terao. "Design and Characteristic Analysis of 10 MW Class Superconducting Wind Turbine Generators with Different Types of Stator and Rotor Configurations". In: *IEEE International Conference on Applied Superconductivity and Electromagnetic Devices* (2015). DOI: 10.1109/ASEMD.2015.7453437.

[117] H. Karmaker, M. Ho, E. Chen et al. "Direct Drive HTS Wind Generator Design for Commercial Applications". In: *International Conference on Electrical Machines* (2014). DOI: 10.1109/ICELMACH.2014.6960225.

[118] J.-T. Erikssom, R. Mikkonen, J. Paasi et al. "A HTS Synchronous Motor at Different Operating Temperatures". In: *IEEE Transactions on Appiled Superconductivity* (1997). DOI: 10.1109/77.614556.

[119] N. Deb, S. Mishra, T. A. Lipo et al. "A HTS Synchronous Machine with Rotating Armature for Wind Power Applications". In: *IEEE Texas Power and Energy Conference* (2018). DOI: 10.1109/TPEC.2018.8312049.

[120] S. H. Park, Y. Kim, S. Lee et al. "Characteristics of Rotating Armature Type HighTemperature Superconducting Generators WithDual Field Windings for the Wind Turbine". In: *IEEE Transactions on Applied Superconductivity* (2014). DOI: 10.1109/TASC.2014.2369472.

[121] M. Iwakuma, A. Tomioka, M. Konno et al. "Development of a 15 kW Motor With a Fixed YBCO Superconducting Field Winding". In: *IEEE Transactions on Applied Superconductivity* (2007). DOI: 10.1109/TASC.2007.898480.

[122] J. Sun, S. Sanz, A. León et al. "Development of a rotary union for Gifford-McMahon cryocoolers utilized in a 10 MW offshore superconducting wind turbine". In: *IOP Conference Series: Materials Science and Engineering* (2017). DOI: 10.1088/1757-899X/278/1/012067.

[123] B. Felder, M. Miki, K. Tsuzuki et al. "Cryogenic Rotary Joints Applied to the Coolingof Superconducting Rotating Machinery". In: *IEEE Transactions on Applied Superconductivity* (2013). DOI: 10.1109/TASC.2013.2241382.

[124] G. Snitchler, B. Gamble and C. K. andPeter Winn. "10 MW Class Superconductor Wind Turbine Generators". In: *IEEE Transactions on Applied Superconductivity* (2011). DOI: 10.1109/TASC.2010.2100341.

[125] A. Thomas and Z. Azar. *Summary Report for Work Package 3.1.2 Investigation of Super-Conducting Direct Drive Generator*. Tech. rep. Technical University of Denmark (DTU), 2016.

[126] P. H. Jensen, T. Chaviaropoulos, A. Natarajan et al. *LCOE reduction for the next generation offshore wind turbines*. Tech. rep. Technical University of Denmark (DTU), 2017.

[127] I. Marino. *SUPRAPOWER: Superconducting, reliable, lightweight, and more powerful offshore wind turbine Final report*. Tech. rep. Energy and Environmental Division, TECNALIA, 2017.

[128] A. Bergen, R. Andersen, M. Bauer et al. “Design and in-field testing of the world’s first ReBCO rotor for a 3.6 MW wind generator”. In: *Superconductor Science and Technology* (2019). DOI: 10.1088/1361-6668/ab48d6.

[129] X. Song, C. Bührer, A. Mølgaard et al. “Commissioning of the World’s First Full-ScaleMW-Class Superconducting Generator on a DirectDrive Wind Turbine”. In: *IEEE Transactions on Energy Conversion* (2020). DOI: 10.1109/TEC.2020.2982897.

[130] T. Ida, Z. Li, D. Zhou et al. “Materials preparation and magnetization of Gd-Ba-Cu-O bulk high-temperature superconductors”. In: *Superconductor Science and Technology* (2016). DOI: 10.1088/0953-2048/29/5/054005.

[131] A. Patel, A. Baskys, T. Mitchell-Williams et al. “A trapped field of 17.7 T in a stack of high temperature superconducting tape”. In: *Superconductor Science and Technology* (2018). DOI: 10.1088/1361-6668/aad34c.

[132] D. Zhou, M. Izumi, M. Miki et al. “Superconductor Science and TechnologyTOPICAL REVIEWAn overview of rotating machine systems withhigh-temperature bulk superconductors”. In: *Superconductor Science and Technology* (2012). DOI: 10.1088/0953-2048/25/10/103001.

[133] P. Cheng, G. Wang, P. Qin et al. “Design and Simulation Analysis of HTS Wind Generator”. In: *Applied Mechanics and Materials* (2013). DOI: 10.4028/www.scientific.net/AMM.312.138.

[134] M. Zhang, W. Wang, Y. R. Chen et al. “Design Methodology of HTS Bulk Machine for Direct-Driven Wind Generation”. In: *IEEE Transactions on Applied Superconductivity* (2012). DOI: 10.1109/TASC.2011.2179696.

[135] X. Feng, G. Gao, K. Davey et al. “Radial Flux High Temperature Superconductor Motor using Bulk Trapped Field Magnets ”. In: *IEEE International Electric Machines and Drives Conference* (2009). DOI: 10.1109/IEMDC.2009.5075246.

[136] M. Hirakawa, S. Inadama, K. Kikukawa et al. “Developments of superconducting motor with YBCO bulk magnets”. In: *Physica C: Superconductivity* (2003). DOI: 10.1016/S0921-4534(03)01213-9.

[137] K. Suzuki, J. Matsuda, M. Yoshizumi et al. “Development of a laser scribing process of coated conductors for the reduction of AC losses”. In: *Superconductor Science and Technology* (2007). DOI: 10.1088/0953-2048/20/8/017.

[138] S. Miura, M. Iwakuma and T. Izumi. “Lightweight Design of Tens-MWFully-Superconducting Wind Turbine GeneratorsWith High-Performance REBa2Cu3Oy Wires”. In: *IEEE Transactions on Applied Superconductivity* (2020). DOI: 10.1109/TASC.2020.2979157.

[139] F. Herzog, T. Kutz, M. Stemmle et al. “Cooling unit for the AmpaCity project – One year successful operation”. In: *Cryogenics* (2016). DOI: 10.1016/j.cryogenics.2016.04.001..

[140] R. T. Jacobsen, S. G. Penoncello and E. W. Lemmon. *Thermodynamic Properties of Cryogenic Fluids*. Springer US, 1997. DOI: 10.1007/978-1-4899-1798-0.

[141] M. D. Atrey, ed. *Cryocoolers Theory and Applications*. Springer, Cham, 2020. DOI: 10.1007/978-3-030-11307-0.

[142] L. Bai, L. Zhang, G. Lin et al. "Development of cryogenic loop heat pipes: A review and comparative analysis". In: *Applied Thermal Engineering* (2015). DOI: 10.1016/j.applthermaleng.2015.06.010..

[143] B. Maples, M. Hand and W. Musial. *Comparative Assessment of Direct Drive High Temperature Superconducting Generators in Multi-Megawatt Class Wind Turbines*. Tech. rep. National Renewable Energy Laboratory (NREL), 2010. DOI: 10.2172/991560.

[144] L. Sethuraman and K. Dykes. *GeneratorSE: A Sizing Tool for Variable-Speed Wind Turbine Generators*. Tech. rep. National Renewable EnergyLaboratory (NREL), 2017. DOI: 10.2172/1395455.

[145] H. Sung, G. Kim, K. Kim et al. "Practical Design of a 10 MW Superconducting Wind Power Generator Considering Weight Issue". In: *IEEE Transactions on Applied Superconductivity* (2013). DOI: 10.1109/TASC.2013.2245175.

[146] H. Polinder, D. Bang, R. P. J. O. M. van Rooij et al. "10 MW Wind Turbine Direct-Drive Generator Design with Pitch or Active Speed Stall Control". In: *IEEE International Electric Machines Drives Conference* (2007). DOI: 10.1109/IEMDC.2007.383632.

[147] X. Zhu and M. Cheng. "Design and Analysis of 10 MW Class HTS Exciting Double Stator Direct-Drive Wind Generator With Stationary Seal". In: *IEEE Access* (2019). DOI: 10.1109/ACCESS.2019.2911298.

[148] L. Sethuraman, M. Maness and K. Dykes. "Optimized Generator Designs for the DTU 10-MW Offshore Wind Turbine using Generator SE". In: *National Renewable Energy Laboratory (NREL)* (2017). DOI: 10.2514/6.2017-0922.

[149] J. Lloberas-Valls, G. Benveniste Pérez and O. Gomis-Bellmunt. "Life-Cycle Assessment Comparison Between 15-MW Second-Generation High-Temperature Superconductor and Permanent-Magnet Direct-Drive Synchronous Generators for Offshore Wind Energy Applications". In: *IEEE Transactions on Applied Superconductivity* (2015). DOI: 10.1109/TASC.2015.2493121.

[150] Y. Xu, N. Maki and M. Izumi. "Electrical Design Study of 10-MW Salient-Pole Wind Turbine HTS Synchronous Generators". In: *IEEE Transactions on Applied Superconductivity* (2014). DOI: 10.1109/TASC.2014.2338300.

[151] B. Go, H. Sung, M. Park et al. "Design and Comparative Analysis of Performance Evaluation Systems for a Large-Scale HTS Generator". In: *IEEE Transactions on Applied Superconductivity* (2019). DOI: 10.1109/TASC.2019.2908605.

[152] Y. Xu, N. Maki and M. Izumi. "Overview Study on Electrical Design of Large-Scale Wind Turbine HTS Generators". In: *IEEE Transactions on Applied Superconductivity* (2018). DOI: 10.1109/TASC.2018.2815918.

[153] J. Wang, R. Qu, Y. Liu et al. "Comparison Study of Superconducting Wind Generators With HTS and LTS Field Windings". In: *IEEE Transactions on Applied Superconductivity* (2015). DOI: 10.1109/TASC.2014.2379697.

[154] H. J. Sung, R. A. Badcock, B. S. Go et al. "Design of a 12-MW HTS Wind Power Generator Including a Flux Pump Exciter". In: *IEEE Transactions on Applied Superconductivity* (2016). DOI: 10.1109/TASC.2016.2539220.

[155] H. Sung, M. Park, B. Go et al. "A study on the required performance of a 2G HTS wire for HTS wind power generators". In: *Superconductor Science and Technology* (2016). DOI: 10.1088/0953-2048/29/5/054001.

[156] Y. Xu, L. An, B. Jia et al. "Study on Electrical Design of Large-Capacity Fully Superconducting Offshore Wind Turbine Generators". In: *IEEE Transactions on Applied Superconductivity* (2021). DOI: 10.1109/TASC.2021.3061903.

[157] M. Saruwatari, K. Yun, M. Iwakuma et al. "Design Study of 15-MW Fully Superconducting Generators for Offshore Wind Turbine". In: *IEEE Transactions on Applied Superconductivity* (2016). DOI: 10.1109/TASC.2016.2535315.

[158] Y. Liang, M. D. Rotaru and J. K. Sykulski. "Electromagnetic Simulations of a Fully Superconducting 10-MW-Class Wind Turbine Generator". In: *IEEE Transactions on Applied Superconductivity* (2013). DOI: 10.1109/TASC.2013.2277778.

[159] D. Liu, U. Hasanov, C. Ye et al. "Design Considerations and Short-Circuit Characteristics of Fully Superconducting Wind Turbine Generators". In: *12th IEEE PES Asia-Pacific Power and Energy Engineering Conference* (2020). DOI: 10.1109/APPEEC48164.2020.9220445.

[160] D. Kostopoulos, D. Liu, G. Genani et al. "Feasibility Study of a 10 MW MgB2 Fully Superconducting Generator for Offshore Wind Turbines". In: *European Wind Energy Association Offshore Conference* (2013). URL: http://resolver.tudelft.nl/uuid:42184015-8cac-4be2-8084-a221744d0452.

[161] S. Grieco, Y. D. Nyanteh and P. J. Masson. "Monte Carlo Design Space Exploration of Superconducting Wind Generator Using MgB2 and YBCO Conductors". In: *IEEE Transactions on Applied Superconductivity* (2016). DOI: 10.1109/TASC.2016.2524563.

[162] T. Hoang, L. Quéval, C. Berriaud et al. "Design of a 20-MW Fully Superconducting Wind Turbine Generator to Minimize the Levelized Cost of Energy". In: *IEEE Transactions on Applied Superconductivity* (2018). DOI: 10.1109/TASC.2018.2810309.

[163] Y. Liu. "Design of a superconducting DC wind generator". PhD thesis. Karlsruher Institute of Technology, Department of Electrical Engineering and Information Technology, 2018.

[164] D. Xing, J. Patel, Q. Sun et al. "AC Loss Comparison Between Multifilament and Nonstriated YBCO Coils Designed for HTS Propulsion Motors". In: *IEEE Transactions on Applied Superconductivity* 27.4 (2017), pp. 1–5. DOI: 10.1109/tasc.2017.2669156.

[165] M. D. Sumption, P. N. Barnes and E. W. Collings. "AC Losses of Coated Conductors in Perpendicular Fields and Concepts for Twisting". In: *IEEE Transactions on Appiled Superconductivity* 15.2 (2005), pp. 2815–2818. DOI: 10.1109/tasc.2005.848233.

[166] *Antriebssysteme Faurndau*. Nov. 2021. URL: https://www.faurndau.de/de/.

[167] ANSYS, Inc. *Ansys Electronics Destkop 2019 R3*. Comp. software. 2019. URL: https://www.ansys.com/de-de/products.

[168] A. Binder. *Elektrische Maschinen und Antriebe*. Springer vieweg, 2017. DOI: 10.1007/978-3-540-71850-5.

[169] H. Karmaker, M. Ho, D. Kulkarni et al. "Design Studies for a 10 MW Direct Drive Superconducting Wind Generator". In: *IEEE Industrial Electronics Society* (2014). DOI: 10.1109/IECON.2014.7048546.

[170] N. Mijatovic. "Superconducting wind turbine generators". PhD thesis. Technical University of Denmark, Department of Electrical Engineering., 2014.

[171] A. B. Abrahamsen, D. Liu and H. Polinder. *Direct drive superconducting generators for INNWIND.EU wind turbines*. 2017.

[172] H. Harwig, C. Kautz and A. Moschallski. *Technische Thermodynamik*. Springer Vieweg, 2016. DOI: 10.1007/b112047.

[173] F. Schreiner. "Design of a three-stage cooled Current Lead for Superconducting High Current DC Busbars". PhD thesis. Technischen Universität Kaiserslautern, Fachbereich Elektrotechnik und Informationstechnik, 2019.

[174] T. Arndt. "High Temperature Superconductors (HTS) as Enabling Technology for Sustainable Mobility and Energy Efficiency". In: *Applied Superconductivity Conference*. Applied Superconductivity Conference. 2018. URL: https://ieeetv.ieee.org/conference-highlights/high-temperature-superconductors-hts-sustainable-mobility-energy-efficiency.

[175] E. E. Inc. *CryoComp Vers. 5.2*. 2012. URL: http://www.eckelsengineering.com/.

[176] *MATLAB R2019a*. MathWorks. URL: https://www.mathworks.com/products/matlab.html.

[177] R. Heller, W. H. Fietz, R. Lietzow et al. "70 kA High Temperature Superconductor Current Lead Operation at 80 K". In: *IEEE Transactions on Appiled Superconductivity* (2006). DOI: 10.1109/TASC.2006.871275.

[178] E. Rizzo. "Simulations for the optimization of High Temperature Superconductor current leads for nuclear fusion applications". PhD thesis. Karlsruher Institute of Technology, Department of Electrical Engineering and Information Technology, 2013.

[179] A. Bellarino. *Large-Capacity Current Leads*. Tech. rep. European Organization for Nuclear Research, Laboratory for Particle Physics, 2008. URL: https://cds.cern.ch/record/1081336/files/at-2008-001.pdf.

[180] J. Lu, E. S. Choi and H. D. Zhou. "Physical properties of Hastelloy® C-276^{TM} at cryogenic temperatures". In: *Journal of Applied Physics* (2008). DOI: 10.1063/1.2899058.

[181] S. W. V. Sciver. *Helium Cryogenics*. Springer, 2012. DOI: 10.1007/978-1-4419-9979-5.

[182] National Institute of Standards and Technology (NIST), U.S. Department of Commerce. *Material Measurement Laboratory, Applied Chemicals and Materials Division*. URL: https://trc.nist.gov/cryogenics/materials/materialproperties.htm.

[183] ANSYS, Inc. *Ansys Workbench 2019 R3*. Comp. software. 2019. URL: https://www.ansys.com/de-de/products.

[184] H. D. Baehr and K. Stephan. *Wärme- und Stoffübertragung*. Springer, 2016. DOI: 10.1007/978-3-662-58441-5.

[185] V. Musilova, P. Hanzelka, T. Kralik et al. "Low temperature radiative properties of materials used in cryogenics". In: *Cryogenics* 45.8 (2005), pp. 529–536. DOI: 10.1016/j.cryogenics.2004.11.010.

[186] H. Karmaker, M. Ho, E. Chen et al. "Direct Drive HTS Wind Generator Design for Commercial Applications". In: *International Conference on Electrical Machines* (2014). DOI: 10.1109/ICELMACH.2014.6960225.

[187] J. G. Weisend. *Cryostat Design, Case Studies, Principles and Engineering*. Springer, 2016. DOI: 10.1007/978-3-319-31150-0.

[188] T. M. Flynn. *Cryogenic Engineering, Revised and Expanded*. Marcel Dekker, 2005.

[189] *Advanced Research Systems, Closed cycle cryocoolers*. May 2020. URL: https://www.arscryo.com/de-210.

[190] E. Kallenbach, R. Eick, P. Quendt et al. *Elektromagnete: Grundlagen, Berechnungen, Entwurf und Anwendung*. Vieweg+Teubner, 2012. DOI: 10.1007/978-3-8348-8297-4.

[191] M. Lao, J. Hänisch, S. Kauffmann-Weiss et al. "High current variable temperature electrical characterization system for superconducting wires and tapes with continuous sample rotation in a split coil magnet". In: *Review of Scientific Instruments* (2019). DOI: 10.1063/1.5078447.

[192] F. Schreiner, Y. Liu, Y. Zhang et al. "Development of No-Insulation Racetrack Coils Wound With 2nd Generation HTS Tapes for a Stator System for Wind Generators". In: *IEEE Transactions on Applied Superconductivity* (2020). DOI: 10.1109/TASC.2020.2969112.

[193] all-tight® GEWINDESICHERN & DICHTEN GmbH. June 2021. URL: https://all-tight.de/produkte/thermo-tight/.

[194] H. Hinzen. *Maschinenelemente 1*. De Gruyter Oldenbourg, 2017. DOI: 10.1515/9783110540871.

[195] Y. Liu, J. Ou, F. Grilli et al. "Comparison of 2D simulation models to estimate the critical current of a coated superconducting coil". In: *Superconductor Science and Technology* (2019). DOI: 10.1088/1361-6668/aae960.

[196] *AREPOC spol. s.r.o.* Jan. 2020. URL: http://www.arepoc.sk/.

[197] Lake Shore Cryotronics. July 2021. URL: https://www.lakeshore.com/products/categories/overview/temperature-products/cryogenic-temperature-sensors/cernox.

[198] S. Kim, S. Hahn, K. Kim et al. "Method for generating linear current-field characteristics and eliminating charging delay in no-insulation superconducting magnets". In: *Superconductor Science and Technology* (2017). DOI: 10.1088/1361-6668/aa56ff.

[199] F. Schreiner, Y. Liu and M. Noe. "Investigation of a Six-Pole Stator System Using No-Insulation 2nd Generation HTS Coils for a 10 kW Generator Demonstrator". In: *IEEE Transactions on Applied Superconductivity* (2021). DOI: 10.1109/TASC.2021.3064513.

[200] *P. Druseidt Elektrotechnische Spezialfabrik GmbH & Co. KG*. Nov. 2021. URL: https://www1.druseidt.de/deutsch/produkte/produkte.html.

[201] *LCD LaserCut AG*. Nov. 2021. URL: https://www.lcd-lasercut.ch/de/home.

[202] *RS Components GmbH*. Nov. 2021. URL: https://de.rs-online.com/web/p/rtd-sensoren/6117873.

List of publications

1. F. Schreiner, Y. Liu and M. Noe. "Investigation of a Six-Pole Stator System Using No-Insulation 2nd Generation HTS Coils for a 10 kW Generator Demonstrator". In: *IEEE Transactions on Applied Superconductivity* (2021). DOI: 10.1109/TASC.2021.3064513

2. Y. Liu, J. Ou, Y. Cheng et al. "Investigation of AC loss of superconducting field coils in a double-stator superconducting flux modulation generator by using T-A formulation based finite element method". In: *Superconductor Science and Technology* (2021). DOI: 10.1088/1361-6668/abef7e

3. Y. Liu, J. Ou, R. Gyuraki et al. "Study of contact resistivity of a no-insulation superconducting coil". In: *Superconductor Science and Technology* (2021). DOI: 10.1088/1361-6668/abd14d

4. Y. Cheng, R. Qu, Y. Gao et al. "Comparison of electromagnetic performance of 10-MW HTS double-stator flux modulation wind generators with different topologies". In: *IEEE Transactions on Applied Superconductivity* (2020). DOI: 10.1109/TASC.2020.2975153

5. F. Schreiner, Y. Liu, Y. Zhang et al. "Development of No-Insulation Racetrack Coils Wound With 2nd Generation HTS Tapes for a Stator System for Wind Generators". In: *IEEE Transactions on Applied Superconductivity* (2020). DOI: 10.1109/TASC.2020.2969112

6. R. Gyurák, F. Schreiner, T. Benkel et al. "Fluorescent thermal imaging of a quench in insulated and non-insulated REBCO-wound pancake coils following a heater pulse at 77 K". in: *Superconductor Science and Technology* (2019). DOI: 10.1088/1361-6668/ab6dc0

7. R. Gyuráki, T. Benkel, F. Schreiner et al. "Fluorescent thermal imaging of a non-insulated pancake coil wound from high temperature superconductor tape". In: *Superconductor Science and Technology* (2019). DOI: 10.1088/1361-6668/ab38f2

8. Y. Liu, J. Ou, F. Grilli et al. "Comparison of 2D simulation models to estimate the critical current of a coated superconducting coil". In: *Superconductor Science Technology* (2018). DOI: 10.1088/1361-6668/aae960

9. Y. Liu, J. Ou, F. Schreiner et al. "Design of a Superconducting DC Demonstrator for Wind Generators". In: *IEEE Transactions on Energy Conversion* (2018). DOI: 10.1109/TEC.2018.2846721

10. F. Schreiner, B. Gutheil, M. Noe et al. “Design and Manufacturing of a Multistage Cooled Current Lead for Superconducting High Current DC Busbars in Industrial Applications”. In: *IEEE Transactions on Applied Superconductivity* (2017). DOI: 10.1109/TASC.2017.2655108.

A Performance of the cryocoolers

To test the performance of the two cryocoolers, cryocooler A and F are switched on and off alternately after the cooldown presented in figure 6.13. Figure A.1 shows the double pancake temperatures during this operation. Up to the time t_1 the cryocoolers A and F are switched on. Between t_1 and t_2, only cryocooler A operates, resulting in a rise of the coil temperatures to an average value of 29.38 K. Both cryocoolers are working again between t_2 and t_3 and it can be seen that the same minimum temperatures are reached as during the initial cooldown. After t_3 only cryocooler F remains switched on and the coil temperatures increase to an average temperature of 50.06 K. It shows that in single operation with cryocooler F, a considerably greater heating takes place. In addition to the findings already described in section 6.4, this behavior suggests a reduced cooling capacity of cryocooler F.

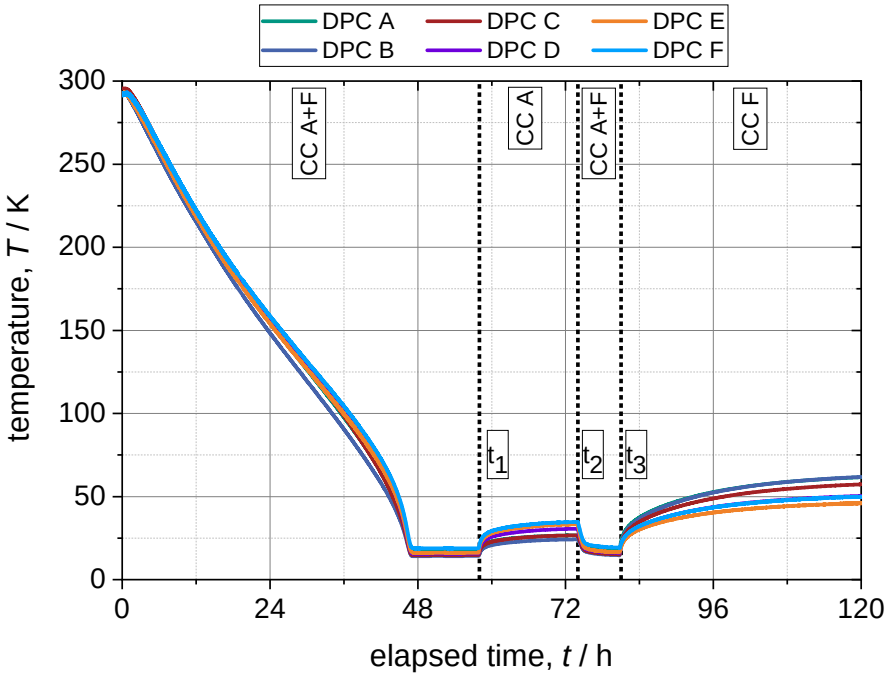

Figure A.1: Measured double pancake temperatures during combined and single operation of cryocooler A and F

List of Figures

List of Tables